

**PhD Thesis**

**Department of Civil and Environmental Engineering**

**University of Strathclyde**

---

**Utilizing Microseismic Monitoring in the Investigation of  
Brownfield Sites**

---

**By:**

**Gheith Abdulraheem Mohamed Alfakri**

---

A thesis presented in fulfilment of the requirements for the degree of Doctor of  
Philosophy

April 2025

## **Declaration**

This thesis is the result of the author's original research. It has been composed by the author and has not been previously submitted for examination which has led to the award of a degree.

The copyright of this thesis belongs to the author under the terms of the United Kingdom Copyright Acts as qualified by the University of Strathclyde Regulation 3.50. The due acknowledgment must always be made of the use of any material contained in, or derived from, this thesis.

*Signed:*

*Date: 01/11/ 2024*

Gheith

## **Abstract**

Technical difficulties in the redevelopment of brownfield sites stem mainly from the uncertainties in the shallow subsurface. Often the use of the site has not been adequately documented. Unmapped buried infrastructure, e.g. concrete or steel tanks, can pose delays to site remediation works and incur significant, unexpected costs. Traditionally, in assessing brownfield sites for redevelopment, intrusive investigations are carried out. Such investigations are expensive and can only provide information at discrete locations. Non-intrusive methods, including electrical resistivity/conductivity and ground penetrating radar (GRP), have also been applied to brownfield sites. Their ability in detecting pollution e.g. buried canisters, is often restricted due to unfavourable on-site conditions (clay soils or concrete surface layers). Seismic could overcome such challenges but their application for the shallow subsurface suffers from time consuming surveys, poor signal to noise ratios and high computational and expert elicitation requirements for processing and interpretation of the acquired data which is done later in the office. These are prohibiting factors, often to the expense of the site investigation efforts.

This thesis explores this research and technology gap by proposing a different methodology approach for identifying the presence of buried objects of dimensions down to 1 m x 1m x1m and at depths between 1 and 3 m. The workflow is based on active microseismic recordings and the principle of seismic wave reflection but the analysis and interpretation are different to traditional seismic reflection surveys.

Using numerical simulations in FLAC<sup>3D</sup>, this study investigated the changes in surface seismic wave amplitude and frequency over distance from the active source, as the seismic wave interacts with a heterogeneous subsurface and how these changes can be used to map what lies beneath.

The numerical simulation results revealed higher wave amplitudes at monitoring stations positioned above or approximately 2 to 4m in lateral distance from the buried objects. Spectral analysis highlighted concentrated seismic energy at these locations and this was quantified by calculating the area under the Power Spectral Density (PSD) curve. The area above and around the buried object exhibited consistently the maximum seismic energy while the actual value of this concentrated energy differed based on the material of the object, which for this research was either (a) concrete, (b) steel or (c) PVC. Results were validated through available historical

field data and a field experiment specifically designed and executed to verify the numerical simulations at a chosen site with made soil.

The results in this thesis show that the workflow is simpler, easy to implement, computationally faster and considerably cheaper than existing geophysical methods for site investigation. The workflow in this thesis was carried out manually but it can be easily automated and can be used for real-time preliminary site investigation of brownfield sites to identify areas that require a more comprehensive assessment, ensuring effective environmental and industrial site management.

## **Acknowledgements**

I would like to express my heartfelt gratitude to all those who have played an instrumental role in my academic journey, without whom the completion of my PhD would not have been possible.

The first and foremost appreciation goes to Dr. Stella Pytharouli, my first supervisor for this thesis. Dr. Stella provided invaluable guidance, support, and supervision throughout the entire research period. Her expertise, dedication, and mentorship were instrumental in shaping the direction and quality of this work. I am deeply grateful for the knowledge and skills I have gained from her, both academically and administratively. Dr. Stella's unwavering encouragement and constructive feedback have been pivotal in my academic journey, and I am sincerely thankful for her mentorship.

I extend my sincere appreciation to My former second supervisor, Dr. John Douglas, for his contributions to my research.

Gratitude and appreciation to the Ministry of Higher Education in Libya and the Libyan Embassy in London for their invaluable support of this project.

I would like to extend my gratitude to my former second supervisor, Dr. Emmanouil Parastatidis, for his mentorship and guidance in shaping my academic path.

Many thanks to ITASCA for generously providing me with the FLAC3D software

I would like to express my gratitude to the Libyan Embassy for their sponsorship and financial support during my PhD studies.

To my parents, their unwavering love, encouragement, and sacrifices have been our foundation. I owe our success to your constant support and belief in us. To my wife, Rugeia Alshwihdi, her steadfast support and understanding have been my strength throughout this journey, and I am deeply grateful. To my daughters, Haneen, Sereene, and Robeene, their joy, love, and understanding have inspired me throughout this journey. I am deeply grateful for their support, and I strive to make them proud. A heartfelt thanks also to my friends for their steadfast support and companionship.

Finally, to all those mentioned and to the countless others who have been a part of my academic journey, I offer my heartfelt thanks. Their contributions, whether big or small, have made a significant impact on my life and my research.

## Table of Contents

<b>Declaration .....</b>	<b>i</b>
<b>Abstract .....</b>	<b>ii</b>
<b>Acknowledgements.....</b>	<b>iv</b>
<b>Table of Contents .....</b>	<b>v</b>
<b>List of figures.....</b>	<b>ii</b>
<b>List of Tables.....</b>	<b>xiii</b>
<b>List of Symbols:.....</b>	<b>xviii</b>
<b>Chapter 1 : Introduction.....</b>	<b>20</b>
1.1 The Importance of Brownfield Sites: .....	22
1.2 Thesis Aim .....	22
1.3 Research Question .....	22
1.4 Objectives: .....	23
1.5 Layout of the thesis.....	23
<b>Chapter 2 : Literature Review.....</b>	<b>26</b>
2.1 Introduction.....	26
2.2 Geophysical methods for imaging the subsurface and near-surface .....	26
2.3 Application of Geophysical Techniques for Detecting Shallow Subsurface Materials (Steel Pipes, Concrete, Plastic Drums).....	30
2.3.1 Locating Steel Pipes Using Geophysical Techniques.....	30
2.3.2 Identifying Concrete Structures Underground .....	35
2.3.3 Detecting Plastic Drums in the Subsurface .....	37
2.4 Research gap .....	37
<b>Chapter 3 Background theory and method .....</b>	<b>39</b>
3.1 Seismic Reflection Theory.....	39
3.1.1 Principles of Seismic Reflection.....	39
3.1.2 Seismic waves Propagation Through the Earth.....	40
3.2 Methodology of analysis steps .....	43
3.3 Numerical modelling of seismic waves propagation.....	44
3.3.1 Numerical modelling tool -FLAC <sup>3D</sup> .....	44
3.3.2 Setting up numerical model in FLAC <sup>3D</sup> .....	45
3.3.3 Governing Equation.....	46
3.3.4 Time Step .....	47
3.3.5 Boundary conditions .....	47
3.3.6 Dynamic load:.....	52

## *Table of Contents*

---

3.3.7 Element size.....	53
3.4 Numerical modelling of the propagation of a sine wave .....	54
3.4.1 Generation and analysis of synthetic data (Step2 & Step3):.....	55
3.4.2 Model 1 .....	57
3.4.3 Model 2 – Brownfield soil (lower threshold for seismic velocity range) .....	62
3.4.4 Model 3– Brownfield soil (upper threshold for seismic velocity range) .....	63
3.4.5 Model 4 – Brownfield soil (end threshold for seismic velocity range) .....	64
3.5 Analysis of seismic velocity data .....	65
3.5.1 Time-Domain Seismic Analysis: Understanding Wave Interactions and Attenuation .....	65
3.5.2 Spectral Analysis of Seismic Waves .....	65
3.6 Validation and verification of numerical models (Step 4).....	68
<b>Chapter 4 : Numerical simulation of seismic waves propagation through media .....</b>	<b>69</b>
4.1 Introduction.....	69
4.2 Models set up .....	69
4.3 Model 2.....	71
4.3.1 Material properties.....	71
4.3.2 Dynamic input: .....	72
4.3.3 Results for site A. ....	73
4.3.4 Model 2 with buried object .....	76
4.3.5 Wave Propagation in Homogeneous and Heterogeneous Media: Travel Time, Amplitude, and Frequency Alterations.....	85
4.3.6 Results for site B.....	88
4.3.7 Site B: Model 2 with buried object.....	88
4.3.8 Seismic power variation.....	90
4.3.9 Discussion of results (model 2) .....	94
4.4 Model 3.....	95
4.4.1 Material properties.....	95
4.4.2 Dynamic input .....	96
4.4.3 Results .....	96
4.4.4 Results for site A. ....	97
4.4.5 Model with buried object .....	97
4.4.6 Result for site B. ....	98
4.4.7 Model with buried object .....	99
4.4.8 Seismic power variation.....	100
4.4.9 Discussion of results (model 3) .....	102

## *Table of Contents*

---

4.5 Model 4.....	103
4.5.1 Material properties.....	103
4.5.2 Dynamic input:.....	103
4.5.3 Results.....	104
4.5.4 Results site A.....	104
4.5.5 Model with buried object.....	105
4.5.6 Results for site B.....	106
4.5.7 Model with buried object.....	106
4.5.8 Seismic power variation.....	107
4.5.9 Discussion of results (model 4).....	108
4.6 Summary of Seismic Wave Simulation.....	108
4.7 Further investigations based on numerical simulations (model 2).....	109
4.7.1 How does the size of an object impact the reflection and transmission of seismic energy?.....	109
4.7.2 What is the maximum depth at which objects can be identified or captured through the study of seismic wave properties?.....	111
4.7.3 Can objects be detected at lateral monitoring stations, and what is the maximum distance at which they can be detected?.....	115
4.7.4 Can concrete objects be detected in brownfield areas, and how does concrete affect the properties of seismic waves?.....	120
4.7.5 The relationship between object depth and the quantity of reflected energy.....	123
4.7.6 How do the mechanical properties of objects (concrete and steel) influence the amount of seismic energy reflected from them?.....	124
4.7.7 What is the most suitable source of seismic waves to be utilized for shallow subsurface investigations in brownfields?.....	125
<b>Chapter 5 : Validation of numerical modelling results.....</b>	<b>127</b>
5.1 Introduction.....	127
5.2 Field experiment.....	127
5.2.1 Instrumentation.....	127
5.2.2 Experiment BP: Buried PVC Pipe.....	127
5.2.3 Experiment BB: Buried bucket.....	129
5.2.4 Spectral analysis of seismic waves.....	130
5.3 Simulation of the objects (PVC pipe and a JCB bucket) that used in Heriot Watt experiment study.....	132
5.3.1 Simulation of PVC pipe.....	132
5.3.2 Simulation of JCB bucket.....	135
5.4 Comparative Study of Simulation Versus Field Data Results.....	138

<b>Chapter 6 : Brownfield site investigation: Pilot study .....</b>	<b>139</b>
6.1 Introduction .....	139
6.2 Field site.....	139
6.3 Seismic Source .....	141
6.4 Seismic nodes.....	141
6.5 Experimental Set-Up: .....	142
6.6 Sensors’ geometry .....	143
6.7 Geometrical characteristics of buried objects. ....	143
6.8 Experimental Procedure.....	144
6.9 Data collection.....	146
6.10 Data Pre - processing .....	147
6.11 Methodology .....	147
6.12 Baseline data .....	148
6.12.1 Seismic source (JCB) at SA .....	149
6.12.2 Seismic source (JCB) located at SB.....	150
6.13 Vertical component (Seismic Source located at SA).....	151
6.13.1 Concrete block experiment.....	151
6.13.2 Steel drum experiment .....	153
6.13.3 Plastic drum experiment.....	156
6.14 Vertical component (Seismic Source located at SB).....	159
6.14.1 Concrete experiment .....	159
6.14.2 Steel drum experiment .....	161
6.14.3 Plastic drum experiment.....	163
6.15 Summary of Vertical Component Results .....	165
6.16 East – West component (Seismic Source located at SA).....	167
6.16.1 Concrete experiment .....	167
6.16.2 Steel drum experiment .....	169
6.16.3 Plastic drum experiment.....	171
6.17 East – West component (Seismic Source located at SB).....	173
6.17.1 Concrete experiment .....	173
6.17.2 Steel experiment .....	175
6.17.3 Plastic drum experiment.....	177
6.18 Summary of E - W Component Results.....	179
6.19 North – South component (Seismic Source located at SA) .....	180
6.19.1 Concrete experiment .....	180

## *Table of Contents*

---

6.19.2 Steel drum experiment .....	183
6.19.3 Plastic drum experiment.....	185
6.20 North – South component (Seismic Source located at SB) .....	188
6.20.1 Concrete experiment .....	188
6.20.2 Steel experiment .....	190
6.20.3 Plastic drum experiment.....	191
6.21 Summary of N - S Component Results.....	193
6.22 Response of Various Materials to Seismic Waves .....	195
<b>Chapter 7 : Discussion .....</b>	<b>197</b>
7.1 Introduction .....	197
7.2 Comparison of developed microseismic reflection methodology vs existing geophysical technologies .....	197
7.3 Numerical simulation of seismic waves propagation through media.....	199
7.3.1 Data Analysis approach.....	199
7.4 Pilot study (chapter 6).....	201
7.5 Key contributions of this Research.....	204
7.6 Application of developed Microseismic approach as a Complementary Tool in Site Investigations: practical considerations.....	204
7.6.1 Favourable Cases: .....	207
7.6.2 Less favourable/not recommended Use: .....	207
7.7 Where would it be particularly valuable? .....	208
7.8 Future work .....	208
Depth Determination Methods .....	208
<b>Chapter 8 : Conclusion .....</b>	<b>210</b>
<b>References.....</b>	<b>212</b>
<b>Appendix .....</b>	<b>221</b>

## List of figures

<b>Figure 1.1:</b> Aerial View of a Brownfield Area ( <a href="https://theconstructor.org/construction/protect-buildings-brownfield-land/21711/">https://theconstructor.org/construction/protect-buildings-brownfield-land/21711/</a> ) .....	20
<b>Figure 1.2:</b> Symbolic representation of the path taken to complete the PhD research. ....	25
<b>Figure 3.1:</b> P- wave and S-wave (Murthy, 2002).....	40
<b>Figure 3.2:</b> Reflected and transmitted seismic waves which generated by normal incident (ASIM HASHIMI, 2011) .....	41
<b>Figure 3.3:</b> Obliquely incident seismic waves produce both reflected and refracted waves (Mari, 2019).....	42
<b>Figure 3.4:</b> (a) Seismic wave front pattern during wave propagation over kilometres scale, (b) Zoomed in section close to seismic source (within 10 m depth) where the incident angle can be regarded almost vertical. ....	43
<b>Figure 3.5:</b> The timestep in Itasca software (Itasca Consulting Group, 2017).....	47
<b>Figure 3.6:</b> Free Field Boundary Mechanisms in FLAC <sup>3D</sup> (Itasca Consulting Group, 2017).50	
<b>Figure 3.7:</b> Basic 3D geometry of numerical model with the free field boundary. ....	51
<b>Figure 3.8:</b> Illustrates the quiet boundary. Modified after (Itasca Consulting Group, 2017). 52	
<b>Figure 3.9:</b> Dynamic input direction (applied on second, third, and four model). ....	53
<b>Figure 3.10:</b> A cross section in 2D, the shape of the element, which is a square, and the size of the element, which is 1m in all axes, this shape and size of the element is applied to all models. ....	54
<b>Figure 3.11:</b> The origin of the coordinate system and a homogeneous model's geometry. The conditions at the free-field boundary are represented by the "extended walls". ....	57
<b>Figure 3.12:</b> Monitoring points deployed at the surface of the model 1. ....	58
<b>Figure 3.13:</b> Velocity history in X-direction at monitoring stations V1, V2 and V3 .....	60
<b>Figure 3.14:</b> Velocity history in Y-direction at monitoring stations V1, V2 and V3 .....	61
<b>Figure 3.15:</b> Velocity history in Z-direction at monitoring stations V1, V2 and V3.....	61
<b>Figure 3.16:</b> model dimensions and monitoring stations on the model surface .....	62
<b>Figure 4.1:</b> Site A and B locations on the model. The distances between the monitoring stations are 2m s in both horizontal directions with the monitoring points placed on the surface.....	71
<b>Figure 4.2:</b> Numbering of the monitoring stations at site A and site B on the model's surface. ....	71

**Figure 4.3:** **a)** The sinusoidal wave dynamic source applied to model 2 in along Z-direction, **b)** PSD of seismic source. .... 72

**Figure 4.4:** Homogenous model: Velocity history at stations: 11–15, 11, **(b)** 6 – 10. The stations closest to the source, has the largest wave amplitudes. Also shown are the PSDs for stations **(c)** 11 – 15 and **(d)** 6 – 10 . .... 74

**Figure 4.5:** Velocity history recorded at monitoring stations s1, s2, s3, s4, and s5 from the homogenous model. .... 75

**Figure 4.6:** PSD of the velocity history recorded at monitoring stations s1, s2, s3, s4, and s5 in the homogeneous model. .... 75

**Figure 4.7:****a)** Model 2 with buried object at 1m depth. Velocity histories at stations 11–15 show Station 13 with the largest wave amplitude, indicating higher seismic energy due to the buried object **b)** Station 8, influenced by the nearby object, had the highest wave amplitude among stations 7–10.**c)** Station 13, directly above the object exhibits the highest PSD value. **d)** Station 8 had a higher PSD peak value than the other three stations (s7, s9, s10) due to the nearby object. S6 has a high PSD because it’s the closest station to source amongst all stations along the line s6 – s10. .... 77

**Figure 4.8:** Model 2 with buried object at 1m depth. Velocity history recorded at monitoring stations s1, s2, s3, s4, and s5. .... 78

**Figure 4.9:** Model 2 with buried object at 1m depth .PSD of the velocity history at monitoring stations s1, s2, s3, s4, and s5 ..... 78

**Figure 4.10:** **a)** Model 2 with buried object at 2m depth. Velocity history comparison at stations 11–15 shows Station 13, directly above the object, with the highest wave amplitude **b)** Station 8, 2 meters away, has a higher wave amplitude than stations 7, 9, and 10, reflecting the largest energy amount **c)** The highest PSD value was recorded at Station 13 **d)** Station 8 recorded a higher PSD than stations 7, 9, and 10 dues to the nearby object. .... 80

**Figure 4.11:** Model 2 with buried object at 2m depth. Velocity history recorded at monitoring stations s1, s2, s3, s4, and s5 from the homogenous model. .... 81

**Figure 4.12:** Model 2 with buried object at 2m depth .PSD of the velocity history recorded at monitoring stations s1, s2, s3, s4, and s5 ..... 81

**Figure 4.13:** **a)** Model 2 with buried object at 3m depth .Velocity histories at stations 11–15 show Station 13, directly above the object, still affected by its presence **b)** Station 8, 2 meters away, has a larger wave amplitude than stations 7, 9, and 10, detecting the object at this distance **c)** The highest PSD value was recorded at Station 13.**d)** Station 8 recorded a higher PSD than other stations due to the nearby object. .... 83

**Figure 4.14:** Velocity history recorded at monitoring stations s1, s2, s3, s4, and s5 from the homogenous model. .... 84

**Figure 4.15:** PSD of the velocity history recorded at monitoring stations s1, s2, s3, s4, and s5 ..... 84

**Figure 4.16:** Model 2: The velocity history results at station 13 recorded from the homogenous model (The red dot on the graph marks the maximum peak velocity observed at station s13, occurring at approximately 0.089 seconds)..... 86

**Figure 4.17:** Model 2 with a buried object: The velocity history results at station 13 recorded from the homogenous model with the object at 1 m depth (The red dot on the graph marks the maximum peak velocity observed at station s13, occurring at approximately 0.095 seconds) ..... 87

**Figure 4.18:** The sinusoidal wave dynamic source applied to model 3 in the Z-direction. ... 96

**Figure 4.19:** The sinusoidal wave dynamic source applied to the model in the Z-direction. .... 104

**Figure 4.20:** Maximum of PSD amplitude at monitoring station s13..... 111

**Figure 4.21:** Maximum PSD value at station s11 – s15. Station s13, positioned directly above the object, displays the highest values among most stations. However, station s11 records the highest overall value due to its closer proximity to the seismic source. (The object is 1m depth). .... 112

**Figure 4.22:** Maximum PSD value at station s11 – s15. Station s13, positioned directly above the object, displays a decrease in PSD value. (object at 2m depth)..... 112

**Figure 4.23:** Maximum PSD value at station s11 – s15. Station s13, positioned directly above the object, displays a decrease in PSD value. (object at 3m depth)..... 113

**Figure 4.24:** Maximum PSD value at station s11 – s15. Station s13, positioned directly above the object, displays a decrease in PSD value. (object at 1m depth)..... 114

**Figure 4.25:** Maximum PSD value at station s11 – s15. Station s13, positioned directly above the object, displays a decrease in PSD value. (object at 2m depth)..... 114

**Figure 4.26:** Maximum PSD value at station s11 – s15. Station s13, positioned directly above the object, displays a decrease in PSD value. (object at 3m depth)..... 115

**Figure 4.27:** Maximum PSD value at station s6 – s10..... 116

**Figure 4.28:** Maximum PSD value at station s1 – s5..... 117

**Figure 4.29:** This figure compares maximum PSD amplitude values at side stations (s6-s10) for homogeneous and object models. Station s8 shows the greatest PSD reduction, indicating the object's strong effect on wave propagation (1m depth)..... 117

**Figure 4.30:** The monitoring stations, located 4 m or more from the object, show a reduction in seismic energy as the distance from the source increases. Consequently, the object's presence at a depth of 1 m has no noticeable impact at these lateral stations..... 118

**Figure 4.31:** The monitoring stations are positioned about 2m or a little bit farther away from the object. Notably, Station s8 had the greatest PSD (Power Spectral Density) amplitude measurements that had ever been made. The important finding strongly implies that the object, which is located at a depth 1m, can be seen at a lateral distance of two metres from its position. .... 119

**Figure 4.32:** The monitoring stations are positioned 4m or somewhat farther away from object. As we go further away from the seismic source, the energy of the seismic waves decreases. As a result, the object's presence at these lateral monitoring stations, which is at a depth of 1m, has no obvious effect..... 119

**Figure 4.33:**The time domain comparison where we can see the monitoring station s13 which deployed over the object reflected with high amplitude. .... 121

**Figure 4.34:** The PSD (Power Spectral Density) maximum values are shown in the figure, which highlights an interesting finding. Station 13's PSD has the highest PSD values. .... 122

**Figure 4.35:** The PSD (Power Spectral Density) amplitude values displayed reveal an intriguing finding: the greatest PSD amplitudes are found at Station s8. .... 122

**Figure 4.36:** The monitoring stations are positioned 4m or somewhat farther away from the object. As we go further away from the seismic source, the energy of the seismic waves decreases. As a result, the object's presence at these lateral monitoring stations, which is at a depth of 1m, has no observable influence. .... 123

**Figure 4.37:** Monitoring station s13 shows a trend in Power Spectral Density (PSD) amplitude as the object depth increases. This decrease in PSD that seismic energy captured diminishes as the object is deeper (the object is steel)..... 124

**Figure 4.38:** Monitoring station s13 recorded the highest frequency spectrum density for both steel and concrete objects, with the PSD for the concrete object being higher than that of the steel object. .... 125

**figure 5.1: a)** Images illustrating the PVC pipe's condition, one when it was initially positioned in the trench (on the left), and the other after it had been buried (on the right), are provided. **b)** A visual representation is included, illustrating the different depths involved in Experiment BP (after Yfantis and Pytharouli 2015). .... 128

**Figure 5.2:** Deployment geometry of the seismometers, the area where the PVC pipe was buried as well as the location of the JCB (after Yfantis and Pytharouli 2015). ..... 129

**Figure 5.3:** **a)** JCB bucket used for this experiment. **b)** Cross section of buried bucket with elevation marks shown (after Yfantis and Pytharouli 2015). ..... 129

**Figure 5.4:** The description of the seismometer placement, the area where the JCB bucket was buried, and the positioning of the JCB vehicle (after Yfantis and Pytharouli 2015). ..... 130

**Figure 5.5:** PSD curves of all vertical traces of all sensors. All curves are almost identical except the curve corresponding to the 3D sensor Centre (for the frequencies between 30Hz and 55Hz) which is placed upon the buried PVC pipe (after Pytharouli 2015). ..... 131

**Figure 5.6:** PSD curves of all vertical traces for the time window analysed when the JCB bucket was buried. All traces are identical except the vertical trace of the 3D central seismometer, which is placed upon the buried JCB bucket. Its spectral amplitude is higher between frequencies 20Hz to 85Hz, with the differences more evident after 35Hz (after Pytharouli 2015). ..... 131

**Figure 5.7:** The figure illustrates the locations of the monitoring stations (A, B, C, D, and E) on the model surface, including the distances between them and from the seismic source. It also indicates the position of the object (PVC pipe), which is situated beneath stations B and C. .... 133

**Figure 5.8:** A comparison of velocity histories recorded at monitoring stations A, B, C, D, and E showed that stations B and C had the highest wave amplitudes, indicating that these two stations received the largest amount of seismic energy. .... 134

**Figure 5.9:** The PSD of seismic waves recorded at monitoring stations A, B, C, D, and E. Stations B and C, located directly above the PVC pipe, exhibit the highest power spectral density values, indicating they recorded the largest amount of reflected seismic energy. ... 134

**Figure 5.10:** The figure displays the locations of monitoring stations A, B, C, D, and E, along with the distances between them and from the seismic source. It also clearly identifies the position of the JCB bucket, which is situated beneath monitoring station B. .... 136

**Figure 5.11:** A comparison of the velocity histories recorded at monitoring stations A, B, C, D, and E revealed that the highest wave amplitude was noted at station B. .... 136

**Figure 5.12:** The PSD of seismic waves recorded at monitoring stations A, B, C, D, and E showed that station B, situated directly above the JCB bucket, exhibited the highest power spectral density values. This indicates that station B recorded the largest amount of reflected seismic energy. .... 137

**Figure 6.1:** Field experiment Site: Top left - Location map of the field site (created using Digimap, © Crown copyright and database rights “2025” Ordnance Survey (AC0000851941)). The field site is in Stepps, Glasgow. Top right - Aerial map of the site with the actual site indicated by a purple rectangle, created using Digimap (© Getmapping Ltd). Bottom - Panoramic View of the Experimental area with the locations of seismic nodes indicated by red flags (author's own photo). ..... 140

**Figure 6.2:** JCB used as seismic source. .... 141

**Figure 6.3:** a) Smart Solo Seismic sensor (Zeckra, 2022): b) Seismic sensor deployed on site ..... 142

**Figure 6.4:** Array of seismic sensors and locations of seismic sources. s0 to s25 indicate locations of the seismic sensors. S<sub>A</sub> and S<sub>B</sub> are the locations of seismic source (JCB digger). ..... 143

**Figure 6.5 :** Objects that were buried as part of the field experiments. a) Concrete block. b) Steel drum c) PVC drum. .... 144

**Figure 6.6:** Determination of sensor locations using GNSS receivers..... 145

**Figure 6.7:** Excavation for buried objects. .... 145

**Figure 6.8:** a) placement of concrete block inside the hole. b) Steel drum inside the hole. c) PVC drum inside the hole. d) Demonstrating the process of backfilling the hole and planting the sensor s13 on top of it. The vertical distance from the surface of these objects to the surface of the ground is about 1m. .... 146

**Figure 6.9:** The entire duration of the micro seismic recording period. .... 147

**Figure 6.10: No object:** PSD of 5 mins segments of data recorded at all monitoring stations when the seismic source (JCB) was at location SA. .... 149

**Figure 6.11:** Power spectral density curves of seismic waves recorded at all monitoring stations with the seismic source (JCB) positioned at location SB..... 150

**Figure 6.12:** A comparison of the PSD of seismic waves recorded vertically. The PSD at station No. s13 located above the object (concrete) differs from the others in the frequency range from 18 to 80 Hz..... 152

**Figure 6.13:** Station 13's PSD curve (red dashed line) shows significant peaks of frequency range from 20 Hz to 80 Hz, indicating strong reflections and resonances caused by the concrete object beneath it. In contrast, other stations (s1 to s25) exhibit lower and more uniform PSD peaks. These variations highlight the impact of the steel object on seismic wave propagation and energy distribution..... 153

- Figure 6.14:** The Power Spectral Density (PSD) of seismic waves recorded at monitoring stations (s11, s12, s13, s14, s15) illustrates varying levels of seismic energy. Notably, monitoring station s13, deployed directly above the steel drum, recorded the highest seismic energy. This peak corresponds to a frequency range from 20 to 120 Hz on the PSD - Frequency plot..... 154
- Figure 6.15:** The PSD curves depicting seismic waves recorded at all monitoring stations. It is clear that the PSD curve at s13 has the highest value. This notable peak occurs within two frequency ranges: approximately 20 to 70 Hz and 80 to 120 Hz, emphasizing that the largest amount of seismic energy detected at the s13, which is positioned above the steel drum. .... 155
- Figure 6.16:** Within the Power Spectral Density (PSD) - Frequency plot, which includes some monitoring stations, station s13 shows the peak PSD of seismic waves, with the maximum value recorded between 18 and 70 Hz. This indicates a high concentration of seismic energy in this specific frequency range throughout the monitoring sites..... 156
- Figure 6.17:** In the PSD - Frequency plot showing all monitoring stations, the PSD curves are almost identical, except for the PSD curve at monitoring station s13, located directly above the plastic, which showed a difference that recorded the highest value of the PSD which corresponds to a frequency interval between 18 and 50 Hz., highlighting a specific concentration of seismic energy..... 157
- Figure 6.18:** In the PSD - Frequency plot showing all monitoring stations, the PSD curves are almost identical, except for the PSD curve at monitoring station s13, located directly above the plastic, which showed a difference that recorded the highest value of the PSD which corresponds to a frequency interval between 18 and 50 Hz., highlighting a specific concentration of seismic energy..... 158
- Figure 6.19:** An examination of the Power Spectral Density (PSD) of vertically recorded seismic waves reveals distinct variations. Notably, at Station No. s13, situated directly above the object (concrete), the PSD diverges from the others within the frequency range spanning from 18 to 80 Hz..... 160
- Figure 6.20:** PSD curves of all vertical traces of all 25 sensors. Most of the curves are almost identical except for the curve corresponding to the monitoring station s13 (for the frequencies between 18 Hz and 75 Hz) which is placed upon the buried concrete. .... 161
- Figure 6.21:** The Power Spectral Density (PSD) of seismic waves recorded at monitoring stations s11, s12, s13, s14, and s15 indicates nearly identical PSD curves. However, there is an exception: the curve associated with monitoring station s13 (placed upon the steel drum), specifically in the frequency range between 18 Hz and 65 Hz, exhibits a distinct deviation. 162

**Figure 6.22:** This figure illustrates the PSD curves of seismic waves detected across all monitoring stations. Within the frequency range of 15 to 60 Hz, monitoring station s13, situated directly above the object, recorded the highest PSD, while the remaining curves exhibit mostly similar patterns with no noticeable distinctions. Beyond the 60 Hz threshold, differentiation between the PSD curves becomes less apparent and more challenging (steel drum)..... 163

**Figure 6.23:** The PSD of some seismic waves recorded in the vertical component. All PSDs curves are identical except for the curve, which represents the PSD recorded at monitoring station s13, which is located directly above the plastic. The largest amount of seismic energy was recorded at monitoring station s13, which corresponds to a frequency of 18 to 70 Hz. And this indicates the presence of the object. .... 164

**Figure 6.24:** Comparing the PSD of seismic waves recorded at all monitoring stations, the dashed line representing the monitoring station No. s13, which is situated above the object, showed the highest value within the frequency range of 18 to 55 Hz. All other PSD curves exhibit nearly identical patterns. .... 165

**Figure 6.25:** The PSD plot for seismic waves at monitoring stations s11-s15 displays different patterns, where station s13 stands out with high seismic energy across a wide frequency range (18 to 50 Hz). This signifies a more prominent influence from the underlying concrete..... 167

**Figure 6.26:** The PSD of all seismic waves detected by all monitoring stations. The maximum value of the spectral density curve was measured at monitoring station s13 over a frequency range of 15 to 27 Hz..... 168

**Figure 6.27:** This figure depicts the Power Spectral Density (PSD) curves of seismic waves recorded at monitoring station s11, s12, s13, s14, s15. The PSD of seismic waves recorded at monitoring station No. s13 is the highest compared to other stations. This indicates that the largest amount of seismic energy was reflected from the steel drum and recorded at station No. s13, which is located directly above the steel drum..... 170

**Figure 6.28:** This figure displays the Power Spectral Density (PSD) curves of seismic waves recorded at all monitoring stations, with station No. s13 recording the highest PSD values for seismic waves. .... 171

**Figure 6.29:** The PSD of the seismic waves recorded at monitoring stations s11, s12, s13, s14 and s15. I notice that the curve representing the PSD of the seismic waves recorded at monitoring station s13 records the highest value corresponding to the frequency period from 18 to 40 Hz. .... 172

**Figure 6.30:** Power Spectral Density (PSD) of seismic waves recorded at all monitoring stations. The curve depicting the PSD of seismic waves at monitoring station s13 recorded the highest value within the frequency range spanning from 20 to 25 Hz..... 173

**Figure 6.31:** Power Spectral Density (PSD) Curves for Seismic Waves at Monitoring stations s11 to s15: Notable Increase in PSD Values at Station 13 Over Concrete in the 18Hz to 55Hz Range..... 174

**Figure 6.32:** PSDs of the seismic waves that recorded at all monitoring stations, s13, which is placed upon the buried concrete. Its spectral amplitude is higher between frequencies 20Hz to 35Hz. .... 175

**Figure 6.33:** Power Spectral Density (PSD) curves of seismic waves recorded at monitoring stations s11, s12, s13, s14, and s15. The PSD of seismic waves at s13 reached its peak within the frequency range of 18 to 40 Hz. This indicates that seismic activity exhibited the highest energy concentration in this specific frequency band. .... 176

**Figure 6.34:** The Power Spectral Density (PSD) curves depict seismic waves recorded at all monitoring stations. Within the frequency range of 18 to 30 Hz, the PSD of seismic waves at station s13 attains its maximum value. This observation signifies that the concentration of seismic energy was highest within this particular frequency band..... 177

**Figure 6.35:** The PSD of seismic waves at some monitoring stations. Monitoring station s13 recorded the highest amount of energy corresponding to a frequency period from 18 to 35 Hz. .... 178

**Figure 6.36:** The PSDs curves depict the seismic waves recorded at all monitoring stations. Despite the monitoring station s13 with the highest energy being identified within a narrow frequency range of 25 to 27 Hz, distinguishing between the monitored stations remains challenging..... 179

**Figure 6.37:** PSDs of seismic waves recorded at monitoring stations s11, s12, s13, s14, and s15. It is clear that station No. s13, located directly above the concrete, recorded the highest value of the PSD corresponding to the frequency from 20 Hz to approximately 55 Hz. This confirms that the concrete still has an effect and can be detected from recording the seismic waves in the north-south component..... 181

**Figure 6.38:** PSDs of seismic waves were measured at all monitoring stations. It is obvious that station No. s13, placed directly above the concrete, recorded the maximum PSD value corresponding to the frequency range of 20 Hz to about 55 Hz. This demonstrates that the concrete still has an effect, which may be observed by measuring seismic waves in the north-south component (concrete block). .... 182

- Figure 6.39:** PSD of seismic waves recorded from the North-South Component distinctly reveals that station No. s13 recorded the highest PSD value. This observation signifies that the greatest amount of energy was detected at this particular station..... 184
- Figure 6.40:** The PSD of the seismic waves recorded from the North-South Component at all monitoring stations. It was noted that the highest value of the PSD was recorded at monitoring station No. s13. This is important evidence that the steel drum had an impact on the characteristics of the seismic waves..... 185
- Figure 6.41:** The Power Spectral Density (PSD) curves for monitoring stations s11, s12, s13, s14, and s15 show how seismic waves are affected by a plastic drum. Station 13 (red dashed line) exhibits prominent peaks between 20 Hz and 100 Hz, particularly around 20 Hz, 40 Hz, and 80 Hz, indicating strong reflections and resonances caused by the plastic drum directly below it. In contrast, the PSD curves for stations s11, s12, s14, and s15 display lower and more uniform peaks, suggesting less influence from the plastic drum object. .... 186
- Figure 6.42:** This figure illustrates the Power Spectral Density (PSD) of select recorded seismic waves. It is noteworthy that the maximum PSD value was observed at monitoring station s13, precisely positioned directly above the plastic drum. This peak PSD value corresponds to a frequency period ranging from 20 to 30 Hz. The results emphasize the significance of monitoring station s13 in capturing seismic energy within this specific frequency range and its direct correlation with the presence of the plastic drum. .... 187
- Figure 6.43:** PSDs curves for seismic waves recorded at monitoring stations s11, s12, s13, s14, and s15. The PSD of the seismic waves recorded at monitoring station s13, which is located above the concrete, recorded the highest value corresponding to the frequency from 20 to 40 Hz. .... 188
- Figure 6.44:** The Power Spectral Density (PSD) curves for seismic waves across all monitoring stations reveal that monitoring station No. s13 recorded the peak PSD value within the frequency range of approximately 20 to 35 Hz. .... 189
- Figure 6.45:** PSD of seismic waves recorded at these monitoring stations does not exhibit a consistent trend across all PSD - Frequency curves. It was observed that the PSD reached its peak at the monitored station s13 (deployed above the steel drum) within the frequency range of 25 to 35 Hz and from 70 to 85 Hz. .... 190
- Figure 6.46:** In the Power Spectral Density (PSD) - Frequency plot encompassing all monitoring stations, the PSD of seismic waves at station s13 reaches its peak, recording the highest value within the frequency period of 25 to 33 Hz. This indicates a notable concentration of seismic energy in that specific frequency range across the monitoring stations. .... 191

**Figure 6.47:** In this figure, the Power Spectral Density (PSD) of some recorded seismic waves is presented. Notably, monitoring station s13, situated directly above the plastic drum, exhibited the highest PSD value. This peak PSD value aligns with a frequency period ranging from 20 to 35 Hz. .... 192

**Figure 6.48:** The PSD of seismic waves detected across all monitoring stations generally does not allow for the determination of the object's location. However, there was a noticeable uptick in the spectral density curve at monitoring station number s13, specifically for frequencies between 20 to 45 Hz..... 193

**Figure 6.49:** power spectral density of the seismic waves recorded at Station No. s13 ..... 195

**Figure 7.1:** Fast Fourier Transform (FFT) of velocity history at s13 (Homogeneous model, Site A). .... 200

**Figure 7.2:** Power Spectral Density (PSD) of velocity history at s13 (Homogeneous model, Site A). .... 201

**Figure 7.3:** Seismic Source and Geophone Sensor Array ..... 206

## List of Tables

<b>Table 3.1:</b> Summarize the main characteristics of the models and the object. -----	56
<b>Table 4.1</b> Mechanical properties of steel material which represents the buried object . -----	69
<b>Table 4.2 :</b> Input material properties for model 2. -----	72
<b>Table 4.3:</b> Shows the parameters used for eq 3.22 for model 2. -----	72
<b>Table 4.4:</b> Shows the values for $\Delta t$ , $v$ , and the depth estimation ( $d$ ) -----	88
<b>Table 4.5:</b> Site A, Homogeneous model.-----	91
<b>Table 4.6:</b> Site A - Model 2 with object at 1m depth-----	91
<b>Table 4.7:</b> Site A - Model 2 with buried object at 2m depth-----	91
<b>Table 4.8:</b> Site A - Model 2 with buried object at 3m depth-----	92
<b>Table 4.9:</b> Site B, Homogeneous model. -----	93
<b>Table 4.10:</b> Site B- Model 2 with buried object at 1m depth -----	93
<b>Table 4.11:</b> Site B- Model 2 with buried object at 2m depth -----	94
<b>Table 4.12:</b> Site B- Model 2 with buried object at 3m depth -----	94
<b>Table 4.13:</b> Input material properties for model 3. -----	96
<b>Table 4.14:</b> Shows the parameters used for this case -----	97
<b>Table 4.15:</b> Site A - homogeneous model. -----	100
<b>Table 4.16:</b> Site A - Model 3 with buried object at 1m depth -----	101
<b>Table 4.17:</b> Site A - Model 3 with buried object at 2m depth -----	101
<b>Table 4.18:</b> Site A - Model 3 with buried object at 3m depth. -----	101
<b>Table 4.19:</b> Site B - homogeneous model. -----	101
<b>Table 4.20:</b> Site B - Model 3 with buried object at 1m depth. -----	102
<b>Table 4.21:</b> Site B - Model 3 with buried object at 2m depth. -----	102
<b>Table 4.22:</b> Site B - Model 3 with buried object at 3m depth. -----	102
<b>Table 4.23:</b> Input material properties for model 4. -----	103
<b>Table 4.24:</b> Shows the parameters used in this case -----	104
<b>Table 4.25:</b> Site A - Model 4 with buried object at 1m depth -----	107
<b>Table 4.26:</b> Site A - Model 4 with buried object at 2m depth -----	107
<b>Table 4.27:</b> Site B - Model 4 with buried object at 1m depth -----	107
<b>Table 4.28:</b> Site B - Model 4 with buried object at 2m depth -----	108
<b>Table 4.29:</b> Results of numerical simulations and the effect of seismic wave source locations on the wave characteristics with changing speeds and frequencies. Green colour signifies the	

potential to detect objects, red colour indicates the incapacity to identify objects. Black colour indicates that the object is not simulated at this depth. The orange colour indicates that the methodology followed in this chapter. ----- 108

**Table 4.30:** Shows the steel object dimensions. ----- 109

**Table 4.31:** Shows the mechanical properties of concrete. ----- 120

.....

**Table 5.1:** Mechanical properties of PVC pipe (De Martins, Freire and Hemadipour, 2009). ----- 132

.....

**Table 5.2:** The calculated area under the density curves is represented in Figure 5.9, High seismic energy is indicated by red, while low energy is represented by green. .... 135

**Table 5.3:** Mechanical properties of JCB bucket. .... 135

**Table 5.4:** The calculated area under the density curves is represented in Figure 5.12, High seismic energy is indicated by red, while low energy is represented by green ..... 137

.....

**Table 6.1:** Smart Solo IGU-16HR 3C technical specification (<https://smartsolo.com>). ---- 142

**Table 6.2 :**The calculated area under the PSD curves in figure 6.10 of seismic waves for all monitoring stations when JCB was at SA. No buried objects buried present. ----- 150

**Table 6.3:** Calculated area under the PSD curves of seismic waves for all monitoring stations when JCB was at SB (figure 6.11). ----- 151

**Table 6.4:** The area under the curves of the PSD of seismic waves recorded at stations s11 to s15 in figure 6.12. ----- 152

**Table 6.5:** The calculated area beneath each Power Spectral Density (PSD) curve in figure 6.13, for all recorded seismic waves at every monitoring station (concrete block). ----- 153

**Table 6.6:** In the table summarizing the calculated areas under the PSD curves in Figure 6.14, the highest value is attributed to station No. s13. This station, situated directly above the steel drum, recorded the largest amount of seismic energy, indicating a notable concentration of seismic energy in that specific frequency range (steel object). ----- 154

**Table 6.7:**The computed area under the Power Spectral Density (PSD) curves in Figure 6.15. Monitoring station s13 exhibits a significant value. However, some other monitoring stations recorded seismic energy levels exceeding those observed at s13. This is due to the local heterogeneity present in the soil. ----- 155

**Table 6.8:**The table presents the Power Spectral Density (PSD) values calculated from the areas under the PSD curves shown in Figure 6.16. It indicates that monitoring station No. s13 captured the highest amount of seismic energy compared to other stations (plastic drum).- 157

**Table 6.9:**The table provides the calculated area beneath the PSD curves depicted in Figure 6.17. Evidently, the highest value was recorded at monitoring station No. s13 (plastic drum). ----- 158

**Table 6.10:** The table provides the calculated area beneath the PSD curves depicted in Figure 6.18. Evidently, the highest value was recorded at monitoring station No. s13. ----- 159

**Table 6.11:** The area beneath each curve in figure 6.19, ranging from monitoring station No. s1 to Monitoring Station No. s25 (concrete block).----- 160

**Table 6.12:** The table presents the area under the Power Spectral Density (PSD) curves for all monitoring stations, as depicted in Figure 6.20. Monitoring station s13 exhibited the highest Power Spectral Density (PSD) value among all stations (concrete block).----- 161

**Table 6.13:** The area beneath each curve in figure 6.21, ranging from monitoring station No. s11 to Monitoring Station No. s15 (Steel drum).----- 162

**Table 6.14:** The numbers in the table correspond to the values beneath the power spectral density curves in the figure 6.22. Station No. s13 registered the maximum seismic energy among all the stations (steel drum).----- 163

**Table 6.15:** The calculated area under the PSD curves in the figure 6.23. It is clear that the monitoring station recorded the highest value compared to the other stations (plastic drum). ----- 164

**Table 6.16:** The calculated PSD value is shown under each curve in Figure 6.24. Comparison to all values at other stations, the station s13 showed the highest value (plastic drum). ----- 165

**Table 6.17:** The calculated area under the PSD curves in Figure 6.25. ----- 168

**Table 6.18:** This table represents the estimated area under the curves for the PSD of all seismic waves at all monitoring stations in figure 6.26. The calculated area under the PSD curve at monitoring station s13 recorded a high value compared to all other stations except for station No., which recorded the highest value (concrete object).----- 168

**Table 6.19:** The table outlines the areas under the Power Spectral Density (PSD) curves that were previously illustrated in Figure 6.27. Each entry in the table corresponds to a different monitoring station. It is noted that monitoring station No. s13 recorded the highest PSD value among all stations listed.----- 170

**Table 6.20:**The values in the table correspond to the area beneath the Power Spectral Density (PSD) curves presented in Figure 6.28. Station No. s13 recorded the highest seismic energy among all the stations.----- 171

- Table 6.21:**The calculated Power Spectral Density (PSD) values are depicted beneath each curve in Figure 6.29. Upon comparison with values from other stations, it is evident that station s13 exhibited the highest PSD value.----- 172
- Table 6.22:** The computed PSD value is shown under each curve in Figure 6.30. In comparison to all other stations, Station s13 has the greatest value. ----- 173
- Table 6.23:** Estimated area under PSDs curves (figure 6.31), the area value under PSD curve which recorded at monitoring station s13 is higher than the others. ----- 174
- Table 6.24:** This table shows the estimated PSD area under the curves for the seismic waves at all monitoring stations in figure 6.32. Concrete's had a little effect on seismic waves that recorded at monitoring station No. 13's which located above the concrete. ----- 175
- Table 6.25:** This table provides a quantitative analysis of the areas under the Power Spectral Density (PSD) curves as showed in Figure 6.33. It lists each monitoring station alongside the corresponding area values, calculated from their PSD curves. Notably, monitoring station No. s13 is highlighted for recording the highest PSD value, indicating a greater concentration of seismic energy across the frequency spectrum compared to other stations. ----- 176
- Table 6.26:** The calculated values are under the curves of the PSD curves in Figure 6.34. Since the PSD represents the amount of recording seismic energy, the highest value of the seismic energy was recorded at monitoring station No. s13. This is evidence of the presence of the object's influence on the characteristics of the seismic waves. ----- 177
- Table 6.27:** The calculated Power Spectral Density (PSD) values are depicted beneath each curve in Figure 6.35. it is difficult to identify the object based on the area under the PSDs curves.----- 178
- Table 6.28:** The calculated Power Spectral Density (PSD) values are depicted beneath each curve in Figure 6.36. When comparing with all other stations, it is apparent that the plastic drum cannot be detected through the East-West component. ----- 179
- Table 6.29:** This table represents the calculated area under the curves in the figure 6.37 for the PSD. It is clear that station No. s13 received the largest amount of seismic energy (concrete block).----- 182
- Table 6.30:** This table represents the calculated area under the curves in the figure 6.38 for the PSD. It is clear that station No. s13 received the largest amount of seismic energy compared to the majority of other stations, but it was noted that station No. s17 received the largest amount of seismic energy, and this may be the result of the local heterogeneity of the soil (concrete block).----- 183

**Table 6.31:** The table describes the areas under the Power Spectral Density (PSD) curves from Figure 6.39, showing that monitoring station No. s13 recorded the highest PSD value. This high value is linked to the station's location above a buried steel drum, suggesting significant alterations in seismic wave characteristics due to the steel drum's presence. This comparison highlights the influence of steel material on seismic data.----- 184

**Table 6.32:** The values derived from calculations are depicted beneath the PSD curves in Figure 6.40. The table highlights the highest calculated area under the curves, corresponding to the PSD recorded at station No. 13. This indicates that station No. s13 exhibited the most significant seismic energy among all the stations, as represented in the table. ----- 185

**Table 6.33:** This table represents the calculated areas under the PSD curves for seismic waves at monitoring stations s11 to s15 as shown in Figure 6.41.----- 187

**Table 6.34:** Figure 6.42 shows that station s13 did not record the highest PSD values compared to other stations, complicating the identification of the underlying object. ----- 188

**Table 6.35:** The estimated area under the PSDs curves in the figure. 6.43 As there is no effect of concrete on the monitoring station planted above the object according to this table. ----- 189

**Table 6.36:** The estimated area beneath the Power Spectral Density (PSD) curves in Figure 6.44 indicates that, according to the table, it is not possible to differentiate concrete based on the quantity of seismic energy recorded.----- 189

**Table 6.37:** The calculated area under each curve in the figure 6.45.----- 190

**Table 6.38:** shows the power spectral density value which calculated under the PSD curves in figure 6.46. ----- 191

**Table 6.39:** The Power Spectral Density (PSD) values are depicted below each curve in Figure 6.47.----- 192

**Table 6.40:** In Figure 6.48, the Power Spectral Density (PSD) values are presented below each curve. Upon comparison with all other stations, it becomes clear that detection of the plastic drum using the North-South component is not feasible. ----- 193

**Table 6.41:** The table provides a summary of how seismic components perform in detecting objects with different mechanical properties near the Earth's surface. It outlines the impact of each object on the recorded characteristics of seismic waves from each seismic component conclusions from the results obtained in the field experiment. ----- 196

## List of Symbols:

Symbol	Description	Unit
$A$	The amplitude of the wave	(m)
$A$	Area of influence of free field grid point	$m^2$
$C_s$	Speed of wave propagation through the medium	(m/s)
$d$	Depth	(m)
$dB$	Ratio of two values of the same physical meaning (usually power) expressed at a logarithmic scale.	
$E$	Young's modulus	Pascal
$F$	Force	(N)
$f$	Frequency	(Hz)
$f_s$	Sampling frequency	(Hz)
$f_g$	Gravity component	(N)
$f_s$	Source component	(N)
$G$	Shear modulus	pascal
$K$	Bulk modulus	pascal
$P$	Primary wave	(m/s)
$S$	Shear wave	(m/s)
$\nu$	Poisson's ratio	-
$v_x^m$	x - velocity of a grid point in the main grid at the side boundary	(m/s)
$v_y^m$	y- velocity of a grid point in the main grid at the side boundary	(m/s)
$v_z^m$	z- velocity of a grid point in the main grid at the side boundary	(m/s)
$v_x^{ff}$	x- velocity of grid point inside the free field	(m/s)
$v_y^{ff}$	y- velocity of grid point inside the free field	(m/s)
$v_z^{ff}$	z- velocity of grid point inside the free field	(m/s)
$F_x^{ff}$	Free-field grid point force	(N)
$\sigma_{xx}^{ff}$	Stresses of the free-field zones around the grid point.	(N/m <sup>2</sup> )
$\sigma_j \tau_{ij}$	Represents the divergence of the stress tensor.	(N/m <sup>2</sup> )
$\lambda$	The wavelength of a seismic wave	(m)
$\rho$	Material density	(Kg m <sup>-3</sup> )

## List of symbols

$\omega$	The angular frequency of the wave	(rad/s)
$\sigma_s$	Applied stress.	(N/m <sup>2</sup> )
$v_s$	Input particle velocity.	(m/s)
$v_n$	Component of normal wave velocity	(m/s)
$v_s$	Component of shear wave velocity	(m/s)
$t_n$	Viscous tractions in normal directions	(N/m <sup>2</sup> )
$t_s$	Viscous tractions in shear directions	(N/m <sup>2</sup> )
$\mathbf{x}$	Input signal vector	-
$\mathbf{u}$	Acceleration	(m/s <sup>2</sup> )

## List of Abbreviation

<b>2D</b>	Two dimensional
<b>3D</b>	Three dimensional
<b>EM</b>	Electromagnetic
<b>FLAC<sup>3D</sup></b>	Fast Lagrangian Analysis of Continua in 3 dimensions
<b>DFT</b>	Discrete Fourier Transfer
<b>Ff</b>	Free field boundary
<b>FDM</b>	Finite difference method
<b>FFT</b>	Fast Fourier Transform
<b>GPR</b>	Ground penetrating radar
<b>PFC</b>	Particle Flow Code
<b>PSD</b>	Power Spectral Density
<b>SI</b>	International Standard
<b>NFFT</b>	Number of points in the FFT
<b>P-wave</b>	Primary or pressure wave
<b>S-Wave</b>	Secondary wave
<b>s</b>	Station name

## Chapter 1 : Introduction

A **brownfield area** is often defined as land or structures that were formerly developed but are now unoccupied, decrepit, or underused.



**Figure 1.1:** Aerial View of a Brownfield Area (<https://theconstructor.org/construction/protect-buildings-brownfield-land/21711/>)

This may include unoccupied buildings, abandoned industrial sites, or other regions with the possibility for regeneration (Adams, de Sousa and Tiesdell, 2010). Brownfield sites are important because their redevelopment offers benefits, including urban revitalization, sustainable land use, economic growth, environmental improvement, community enhancement, historic preservation, and the promotion of smart growth principles (BenDor, Metcalf and Paich, 2011). Steel pipes and concrete structures buried at shallow depths (up to 3m) pose significant challenges for development and rehabilitation efforts in brownfield sites. These concealed objects may harbour subsurface utilities, hazardous substances, or remnants of past industrial activities, necessitating careful handling and management to mitigate risks effectively (CIRIA, 2018). Detailed site investigations and risk assessments can be a solution necessary for the detection and management of these buried objects to comprehend their position and potential effects on future development. To prevent delays during construction or redevelopment, it may be necessary to carefully arrange where subsurface infrastructure, such as utilities or pipes, are located. To preserve the site's safety and environmental integrity, it is also necessary to take the correct remediation steps when hazardous elements, such as polluted

soil or groundwater, are present. In the quest for accurate determination of the locations of objects buried near the surface of the earth within brownfield sites, geophysical methods like ground-penetrating radar (GPR), resistivity surveys, and borehole geophysics have been extensively utilized (Pringle *et al.*, 2024). However, these methods come with inherent limitations and are often constrained by factors such as cost, environmental impact, and the need for excavation. Intrusive studies are often carried out to evaluate contamination levels, examine geology, and comprehend hydrogeological conditions while evaluating brownfield areas for rehabilitation (Hammond *et al.*, 2021). However, these intrusive techniques are also expensive because they call for renting pricey machinery like drill rigs or excavators. Standing fees for renting out equipment can add up quickly, especially when the item is not in use. Furthermore, intrusive studies limit our comprehension of the entire site by only providing information for discrete sample windows.

Non-intrusive techniques have been used in the evaluation of brownfield sites to help overcome these difficulties. Ground-penetrating radar (GPR) and electrical resistivity/conductivity surveys are two methods that have been used to collect data over a larger area (Alamar *et al.*, 2020). These non-intrusive techniques have the benefit of collecting data over a wider area, giving a more thorough picture of the underlying conditions. However, unfavourable on-site circumstances may limit the efficacy of non-intrusive approaches in identifying forms of pollution, such as industrial chemicals or buried canisters. For instance, where a layer of clay, which is frequently used to cap landfills, or reinforced concrete is present, GPR could not be effective (Quinta-Ferreira, 2019). This makes it difficult to effectively detect subsurface anomalies because these materials can prevent radar pulses from penetrating and propagating. Non-intrusive techniques are nonetheless useful in the first evaluation and screening of brownfield sites despite these drawbacks. They provide a quick and affordable way to acquire basic data across a greater area, assisting in the detection of probable pollution hotspots and supplying information for ensuing focused intrusive investigations. Combining intrusive and non-intrusive techniques can give a complete image of the site's circumstances, allowing the redevelopment of brownfield sites and enabling informed decision-making.

This research project focuses on the use of microseismics in brownfield land site investigations and explores its ability in imaging the sub-surface. The idea originated from the application of Passive Seismic in the development of oil and gas fields (Likhacheva, Kashin and Mironychev, 2021). Fluid activities, including hydraulic fracturing, water injection, and fluid extraction, are the primary causes of passive seismicity in the development of oil and gas fields (Chen, 2014).

### 1.1 The Importance of Brownfield Sites:

- Collaton and Bartsch highlight the significant benefits of urban revitalization through built sites. These locations offer opportunities to regenerate neglected areas and transform them into lively and functional spaces. By reusing these sites, cities can enhance their visual appeal, stimulate economic growth, and create attractive urban environments that meet the needs of residents and businesses.
- Reclamation of damaged sites is consistent with the principles of sustainable development because it promotes the efficient use of existing infrastructure and resources. By revitalizing these areas, cities can mitigate urban sprawl, preserve green spaces, and reduce the environmental impact typically associated with developing new land (Doick *et al.*, 2006).

Social Benefits: Transforming brownfields can enhance social cohesion by providing new housing, recreational spaces, and community amenities. Redevelopment projects often prioritize affordable housing, community facilities, and public spaces, fostering inclusivity and improving the quality of life for residents (Miller, 2016)

### 1.2 Thesis Aim

The primary objective of this project is to create an innovative technology that complements the current geophysical survey methods used in Brownfield sites. This technology will address limitations in current methods, improve detection accuracy, and streamline site assessments. By integrating this new tool, the project aims to achieve better site characterization, reduce costs and time, and ensure safer and more effective remediation processes. This research project investigates the application of microseismic technology for assessing Brownfield sites, specifically targeting the detection of subsurface objects such as pipes and concrete structures located up to 3m deep. The study involves recording seismic signals and analyzing them in both the time and frequency domains to identify and characterize these objects. Significantly, following a comprehensive examination of global literature, no alternative approach possessing comparable qualities has been discovered.

### 1.3 Research Question

The central focus of this thesis is: Is it practical to use microseismic technology for investigating Brownfield sites to detect objects in the shallow subsurface layers of the earth, at depths of up to 3 meters?

#### 1.4 Objectives:

- a. Understand how changes in the energy of seismic signals when encountering a buried object are manifested in the seismic recordings (*numerical modelling*).
- b. Develop a start-to-end methodology for the analysis of seismic recordings for brownfield site investigations (*Analysis*).
- c. Application of findings on a pilot field study (*Validation*).

The redevelopment of brownfield sites offers significant benefits, including economic revitalization, environmental restoration, and efficient land use. However, several challenges hinder these efforts. One of the major obstacles is the uncertainty surrounding the locations of buried infrastructure, which complicates planning and construction. Additionally, soil contamination poses risks to both human health and the environment, further complicating redevelopment efforts.

Among these challenges, the detection of buried infrastructure is particularly problematic. Current practices for identifying underground structures include ground-penetrating radar (GPR), electromagnetic induction, and other geophysical techniques. However, these methods often face limitations such as reduced effectiveness in certain soil conditions, high costs, and difficulties in distinguishing between different types of buried materials.

This research aims to address some of these challenges by exploring the potential of microseismics for detecting buried infrastructure. Microseismic techniques, which utilize passive seismic signals, offer advantages such as deeper penetration, minimal site disturbance, and potential applicability in a variety of ground conditions. By leveraging these characteristics, this study seeks to improve the accuracy and efficiency of underground infrastructure detection, thereby contributing to the broader goal of facilitating brownfield site redevelopment.

#### 1.5 Layout of the thesis

The thesis structure is built based on the research approach, which consists of six separate phases and is shown in Figure 1.1. I have outlined each of these six phases briefly below.

**Chapter 1 and 2:** This phase encompasses the introductory section, outlining the purpose of the research, formulating the research question and objectives, and presenting an overview of the thesis structure and literature review chapter which discuss as the importance of brownfield site investigation methods.

**Chapter 3:** In this chapter, the seismic wave theory explains how waves generated by earthquakes or artificial sources travel through the Earth's layers. It distinguishes between different types of waves—primary (P) waves, which are compressional, and secondary (S) waves, which are shear. The theory also covers how these waves interact with various geological materials, influencing their speed and direction. The numerical model theory is established, outlining the fundamental principles and equations that govern the simulation of seismic waves. An appropriate numerical technique, the finite difference method, is chosen to model wave propagation. Additionally, the boundary conditions of the numerical model are defined to reflect real-world scenarios. Furthermore, the methodology encompasses the spectral analysis of seismic waves. This involves analysing the frequency content of the recorded seismic data to identify specific patterns and characteristics that can provide valuable insights into shallow subsurface objects.

**Chapter 4:** The focus is on simulating seismic waves by constructing various numerical models that represent the conditions found in brownfield sites. The study involves applying a source of seismic waves to these models, considering the specific mechanical properties typically encountered in the soil of brownfields. Additionally, objects such as steel and concrete, which are commonly present in these areas, are incorporated into the simulations. The objective is to examine the feasibility of detecting and differentiating these objects through the simulation of seismic waves.

**Chapter 5:** The primary purpose was to verify the numerical model developed in chapter 4.

**Chapter 6:** Field experiments were conducted at Stepps area in Glasgow to verify and expand understanding of the mechanics of propagation and properties of seismic waves.

**Chapter 7:** The discussion chapter includes an explanation of how to analyse and interpret the research findings, addresses the study questions and objectives, and places the results within the broader framework of existing knowledge in the field. It is an important component of the thesis that explains the significance of the research, analyses ramifications, makes conclusions, and frequently offers future research options.

**Chapter 8:** The conclusion chapter summarise the results and includes suggestions for future work.

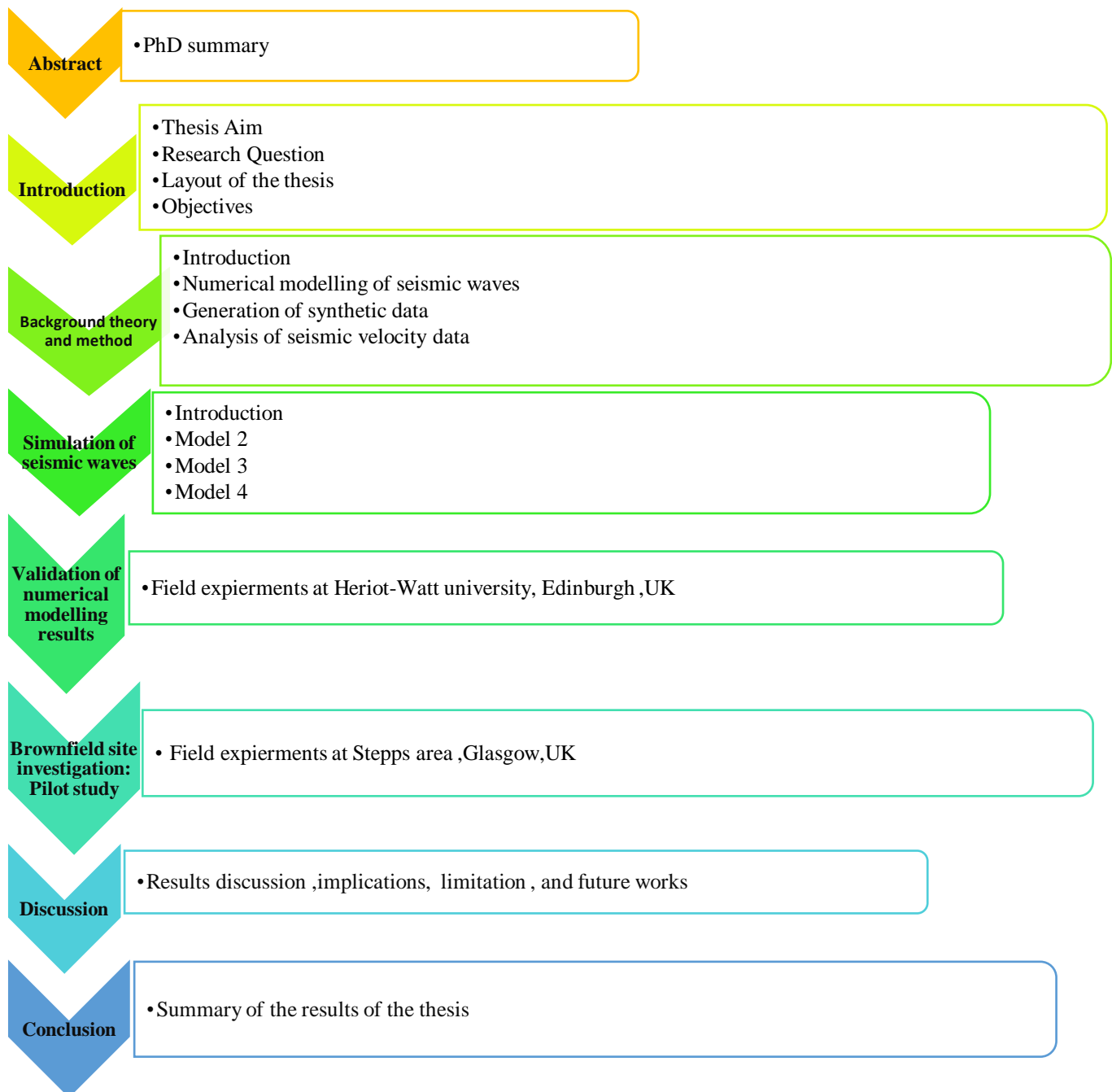


**Figure 1.2:** Symbolic representation of the path taken to complete the PhD research.

## Chapter 2 : Literature Review

### 2.1 Introduction

This literature review examines various geophysical methods, including electrical resistivity, ground-penetrating radar, and seismic imaging, and assesses their effectiveness and limitations in brownfield site investigations. This review explores the potential of micro seismic technology as an innovative approach to address these challenges, informing the study's objective of integrating it with traditional methods for improved site assessment.

### 2.2 Geophysical methods for imaging the subsurface and near-surface

Geophysical techniques can provide insights into subsurface conditions, including those beneath brownfield sites, helping to identify buried objects, geological features, and potential contamination pathways. Methods, such as seismic refraction and reflection, gravity, magnetic, electric, GPR, and electromagnetic techniques, offer diverse applications across various industries. For example, seismic reflection, commonly used in oil and gas exploration, is also employed in environmental science for contamination assessments, in forensic science for locating buried evidence, in military intelligence for geospatial analysis, and in geotechnical and hydrogeological studies for subsurface characterization and groundwater analysis (Das and Skelton, 2020; Gisinier, 2016).

One widely used non-invasive geophysical technique for investigating brownfield sites is the electrical resistivity method, which can reveal underlying conditions close to the surface, such as contamination, fluid channels, and geological features. By injecting an electric current into the ground through two electrodes and measuring the resulting potential on the surface, variations in resistivity can be detected. Low resistivity values often indicate conductive materials like water or pollutants, while high resistivity values may suggest non-conductive materials such as clay or bedrock. The method is useful for environmental assessments due to its ability to produce comprehensive models of subsurface features. This method used mainly 2D and 3D models, with electrodes placed along the surface to measure subsurface resistivity variations. These methods, like Electrical Resistivity Imaging (ERI), can detect features such as faults, fractures, cavities, weak zones, groundwater, and soil-bedrock interfaces. The resolution depends on electrode spacing, allowing detection of features as small as 1 meter. Typically, these surveys explore depths from about 5 to 30 meters, making them ideal for environmental, geotechnical, and engineering applications. (Paul, 2022; Barago et al., 2021). Electrical resistivity tomography (ERT), a more advanced version of this method, has been

particularly effective in detecting buried foundations, although its data interpretation can be complicated by factors such as moisture content, material composition, and the presence of reinforcing materials (Eissa, 2021). Despite its advantages, ERT may struggle with ambiguous data interpretation, as similar resistivity values can correspond to different subsurface features. Additionally, factors such as highly conductive elements like metallic infrastructure or salty groundwater may create artifacts that obscure underlying structures (De Carlo *et al.*, 2013). The method also requires significant manual effort, particularly in deploying and retrieving electrodes (Usman *et al.*, 2020).

Magnetic surveys, based on the detection of anomalies in the Earth's magnetic field, can also be used to identify subsurface objects and metallic structures, which are common at brownfield sites. Magnetic surveys are quick, cost-effective, and efficient for covering large areas, and they have been widely used in mineral exploration, hazardous waste site investigations, and the detection of buried metallic objects such as tanks, pipes, and drums (Fkirin, Youssef and El-Deery, 2021). However, the method faces challenges due to "cultural noise" from human-built structures, such as steel pipelines and fences, which can interfere with the magnetic signal and reduce data accuracy (Adagunodo, Sunmonu and Adeniji, 2015). Furthermore, magnetic surveys cannot detect non-metallic materials like concrete, limiting their application in areas where these materials are prevalent (Bongiolo *et al.*, 2022).

Gravity surveys measure variations in the Earth's gravitational field to detect subsurface features. This technique is particularly useful for mapping large-scale geological structures, such as bedrock topography, sedimentary basins, and fluid reservoirs. In groundwater research, gravity surveys help locate potential aquifers and map subsurface density variations (Awad, Araffa and Pek, 2014). In this study, the depth and size of geological structures are estimated using the strength, shape, and gradient of gravity anomalies. Bandpass filters are applied to separate signals by depth: 1–5 km anomalies indicate shallow Quaternary deposits, 5–17.5 km correspond to Molasse and Mesozoic layers, and 20–40 km reveal deep Permo-Carboniferous troughs. However, the resolution of this method is not sufficient to detect smaller features such as narrow pipes or concrete structures. (Guglielmetti and Moscariello, 2019). Additionally, gravity surveys are less effective for detecting materials like steel and concrete, which do not produce significant gravitational anomalies (Coe *et al.*, 2018).

Ground-penetrating radar (GPR) uses electromagnetic pulses to scan the subsurface, producing high-resolution images of features such as soil stratigraphy, geological interfaces, and buried

objects. This non-destructive method is useful in various fields, including geology, environmental studies, and archaeology (Jol and Bristow, 2003). GPR's ability to collect real-time data makes it highly effective for site evaluations and infrastructure inspections. However, GPR's effectiveness is limited by soil conditions, especially in environments with high moisture content or high dielectric permittivity, which can attenuate radar signals and limit penetration depth. Additionally, GPR faces challenges in distinguishing between different subsurface materials and is less effective in detecting certain materials, such as plastic pipes or reinforced concrete, due to signal attenuation and low dielectric contrast (Baker, Jordan and Pardy, 2007). In brownfield sites, interference from urban clutter and complex soil conditions can further complicate data interpretation (Yang, Qin and Ren, 2015). To overcome these limitations, GPR is often combined with other geophysical methods to provide a more comprehensive subsurface investigation (Sigurdsson, 1992).

The electromagnetic (EM) method is a geophysical technique that investigates subsurface conductivity variations, providing valuable insights into geology and object detection by controlling the source array and frequencies during surveys. EM methods, particularly electromagnetic inductive methods, are effective for obtaining data on the electrical conductivities of the ground. These methods are divided into two categories: natural field methods and controlled-source methods (United States Environmental Protection Agency, 2016).

The primary advantages of the EM method in geophysical investigations lie in its ability to measure conductivity fluctuations non-invasively. It allows for flexible survey designs, rapid data collection, and real-time interpretation, making it ideal for a range of applications, such as mineral exploration (Gołębiowski *et al.*, 2017), groundwater studies, environmental assessments, and brownfield site investigations. The technique's flexibility allows it to be applied in diverse scenarios, and it's particularly effective in mapping soil conductivity, detecting contamination, buried objects, and infrastructure in brownfield areas. Additionally, electromagnetic induction (EMI) can detect metallic objects like pipes and tanks without the need for direct contact with the soil, which is particularly useful in compact or contaminated sites (Shin *et al.*, 2021).

However, interpreting EM data can be challenging due to the variables influencing responses. Subsurface conditions, geological formations, and the surrounding environment all impact data interpretation. EM methods are also limited by penetration depth and can be susceptible to

nearby noise sources, affecting accuracy. Furthermore, EMI is less effective at detecting non-metallic objects like plastic pipes or concrete structures, which do not create significant conductivity contrasts with surrounding soils (Routh and Oldenburg, 2000).

Seismic imaging methods, including seismic refraction and reflection, use acoustic waves to measure subsurface properties. These methods are valuable for studying geological structures and boundaries, as well as for mapping faults and stratigraphy (Beckel, 2022). Seismic reflection, in particular, involves sending sound waves into the ground, where they bounce off geological boundaries and return to the surface. The timing of these reflected waves is then analyzed to image subsurface structures, with varying angles of incidence affecting the wave travel paths and depth (Joshi *et al.*, 2020). Seismic waves provide crucial information on geological boundaries, such as depth variations, and aid in locating and mapping mineral resources (Heezen and Wilson, 2006).

Seismic reflection offers comprehensive imaging of subsurface structures, making it invaluable for site characterization, geological interpretation, and hydrocarbon exploration (Bruno, 2023). It can identify geological features and boundaries, aiding in resource exploration and groundwater studies (Anyanwu, 2021). However, seismic reflection can struggle when subsurface structures are complex, and interpreting data in areas with steeply dipping or discontinuous reflectors can be challenging (Roden *et al.*, 2017). Additionally, shallow-depth surveys or lower-frequency sources may limit seismic resolution for fine geological features.

Seismic interferometry, which involves cross-correlating seismic recordings to reconstruct wavefields, offers high-resolution imaging by using ambient seismic noise or controlled sources (Duguid, Halliday and Curtis, 2011). This passive, non-invasive approach is cost-effective and environmentally friendly, allowing for continuous subsurface monitoring without the need for specific seismic events (Dales, Audet and Olivier, 2017). Seismic interferometry can also monitor dynamic subsurface processes, enabling tracking of changes over time, such as in volcanic or reservoir monitoring (Ruigrok *et al.*, 2010). Nevertheless, it faces challenges related to data accessibility, resolution limitations, and the impact of near-surface anomalies on data quality (Duguid, Halliday, and Curtis, 2011).

Microseismic events, caused by both natural and human activities, provide valuable data for subsurface characterization, especially in industries like mining and oil and gas (Mitchell and Green, 2017). Monitoring microseismic activity helps assess rock stability, hydraulic fracturing

effectiveness, and earthquake risk. Microseismic data also enables real-time mapping of fractures and aids in understanding subsurface processes and fluid flow dynamics (Bohnhoff *et al.*, 2013). However, microseismic monitoring can be limited by factors such as surrounding noise, sensor placement, and the resolution of low-magnitude seismic events (Del Pezzo *et al.*, 2013).

Borehole geophysical methods involve inserting sensors into wells to measure subsurface properties, offering valuable insights into stratigraphy and hydrogeology (Miong, 2008). While borehole measurements provide detailed data along the well's length, they are limited by their confined spatial coverage and high costs (Killeen, 1997).

### **2.3 Application of Geophysical Techniques for Detecting Shallow Subsurface Materials (Steel Pipes, Concrete, Plastic Drums).**

This thesis is focusing on the detection of buried objects commonly found at brownfield sites: concrete foundations or tanks and plastic or steel drums. Such objects are usually found up to 3m depth from the surface and have dimensions usually >1m. Anything less than 1 m can be relatively easier to move as it is smaller than the dimensions of the bucket of excavators.

#### **2.3.1 Locating Steel Pipes Using Geophysical Techniques**

Buried pipes is common infrastructure at brownfield sites (Moss, 2003). They can be made of steel or plastic/PVC. Accurate detection enhances safety by lowering the risk of accidents during excavation and development projects.

A study by Karim *et al.*, (2015) used 2D Electrical Resistivity Imaging (ERI) and 1D Vertical Electrical Sounding (VES) to detect buried utilities and characterize subsurface soils. Electrical Resistivity Imaging (ERI) is a fast, non-invasive geophysical method used to map subsurface features by injecting electrical current into the ground and measuring voltage differences. A 2D ERI setup typically uses 64 electrodes with automated switching, allowing quick data collection over large areas. The data is processed using software like RES2DINV, which models the subsurface as rectangular blocks and adjusts resistivity values to match field measurements. The 2D ERI, employing a Wenner-Schlumberger array with 64 electrodes, provided detailed subsurface imaging, identifying pipes (of diameter 400–1200 mm) as low-resistivity zones (<1 ohm.m). In contrast, 1D VES, using 4 electrodes, offered quick but limited depth profiles. 2D ERI was more time-consuming due to extensive electrode setup but delivered superior lateral and vertical resolution. Vertical resolution in ERI refers to its ability

to distinguish layers at different depths. It's high near the surface but decreases with depth—deeper features may appear blurred unless they have strong resistivity contrasts. In the study, the method reached depths up to 26 meters. However, it faced challenges from soil salinity and moisture. 1D VES was faster but lacked detail. The study concluded that 2D ERI is better for comprehensive utility detection, while 1D VES serves as a supplementary method for calibration. Combining both improved accuracies, though 2D ERI remains the preferred choice for large-scale investigations (H. Karim, H. Ibrahim and A. H. Al-Rubaye, 2015).

Karim et al., (2015) also explored similar techniques in subsurface investigations, more specifically Electrical Resistivity Tomography (ERT). Their study evaluated Wenner and Dipole-Dipole (DD) arrays in detecting buried targets. Their analysis revealed distinct resistivity contrasts: metallic objects (steel drums, pipes) exhibited low resistivity ( $<0.1 \Omega\text{m}$ ), while non-metallic targets (plastic buckets, tiles) showed high resistivity ( $>11,000 \Omega\text{m}$ ), aligning with laboratory measurements. The Wenner array (48 electrodes, fixed spacing) achieved strong vertical resolution and signal clarity, detecting targets at 0.5–1.0 m depths but required iterative adjustments (1.0 m  $\rightarrow$  0.5 m  $\rightarrow$  0.25 m spacing) to resolve smaller or inclined objects. The DD array (48 electrodes, variable spacing) excelled in horizontal resolution, identifying lateral anomalies but missed vertical/small targets (e.g., 0.05 m pipes). Both methods produced inverted resistivity models using RES2DINV software, with RMS errors of 2.7–9.9% (Wenner) and 2.9–7.3% (DD), yet struggled with fine geometries and inclined structures. Combined use improved subsurface characterization, though limitations persisted in resolving features less than 10 cm in size. Fieldwork duration was longer for the Wenner array due to spacing iterations, while DD offered faster lateral profiling. The fieldwork took longer with the Wenner array (3 – 4 hrs) because it required multiple surveys with different electrode spacings (1.0 m, 0.5 m, 0.25 m) to improve resolution and detect smaller or deeper targets. In contrast, the Dipole-Dipole (DD) array (1 – 1.5 hr) allowed for faster data collection by providing good horizontal coverage in a single setup, making it more efficient for lateral profiling without the need for repeated measurements.

One of the key challenges in mapping soil resistivity around buried pipes in urban areas to assess corrosion risks is the interference caused by pipes, particularly uncoated or shallow ones, which can produce minor anomalies. Coated pipes, however, have minimal impact. This study compares electrical resistivity tomography (ERT) and capacitive electrostatic measurements (sliding carpet) to address these challenges. Synthetic modelling confirmed that standard pipe dimensions did not significantly affect results. Both methods effectively identified low-

resistivity layers ( $<50 \Omega \cdot \text{m}$ ) linked to corrosion risks and resolved lateral soil variations. While ERT faced logistical challenges such as invasive electrode installation and slow data acquisition. The sliding carpet method is an electrostatic resistivity technique employing capacitive coupling, using flat metal sheets or copper gauze as non-invasive poles ( $0.4 \times 0.80 \text{ m}^2$  for current injection,  $0.2 \times 0.80 \text{ m}^2$  for voltage measurement) embedded in a portable plastic array. Designed for urban environments, it enables rapid (e.g., 200 m in 10 minutes), non-destructive surveys by continuously pulling the carpet along paved surfaces, sampling data every 0.2 m (filtered to 0.5 m resolution) and inverting results via DC resistivity software (e.g., RES2DINV). Advantages include noise resilience through lateral filtering, speed, and shallow focus (0–3 m depth), though it lacks ERT's deeper resolution. Key findings indicate minimal pipe influence unless uncoated, large, or shallow ( $<1.5 \text{ m}$ ), validating its utility for mapping soil resistivity to assess corrosion risks around urban utilities despite subsurface complexity. This method provided rapid, non-destructive deployment with noise suppression, making it especially suitable for urban environments (Rejkjær *et al.*, 2021).

In a 1990 study by Schlinger, magneto metric and gradiometric surveys were employed at Hill Air Force Base to identify underground steel storage tanks. The methods involve using magnetometers and gradiometers to detect underground storage tanks (USTs) by measuring variations in Earth's magnetic field. Magnetometers (proton precession type) record total field strength, while gradiometers measure vertical gradients using paired sensors to cancel diurnal noise. Surveys are conducted along grids, with data corrected for temporal geomagnetic fluctuations and background values. Anomalies—strong positive signals (e.g., 3,000–6,000 nT) for steel tanks or subtle voids for nonmagnetic tanks—are mapped and interpreted based on amplitude, shape, and gradient decay rates. This approach successfully located a buried 42,000-liter steel tank at Hill Air Force Base, demonstrating its utility for targeted excavation in environmental remediation. The magnetometer assessed the total magnetic field intensity, revealing broad anomalies linked to deeper or larger tanks, while the gradiometer—utilizing two vertically aligned sensors—gauged the magnetic gradient, yielding sharper anomalies (1,200–4,000 nT/m) for shallow targets. Data were gathered along meticulously planned transects, adjusted for diurnal magnetic fluctuations, and visualized through spatial mapping to accurately locate the buried tanks.

The magnetometer was faster but less precise for shallow objects, whereas the gradiometer offered higher resolution but required more field time. The study conducted magnetometer and gradiometer surveys simultaneously using an EDA Omni Plus instrument, which recorded both

total field and gradient data at the same time. Fieldwork for both sites took 12 hours over two days, including setup, data collection, and land surveying. Both methods successfully located tanks, with the gradiometer pinpointing a 42,000-liter tank at 1 m depth. Combining the techniques improved accuracy, making them ideal for rapid, non-invasive site assessments. Limitations included sensitivity to cultural noise and power lines, with gradiometers being less effective for very deep targets (2 – 3 m) (Schlinger, 1990).

A study by Alao et al. (2024) examines magnetic anomaly detection for identifying buried objects in environmental and engineering applications. A 55m × 55m test site was used, measuring Total Magnetic Intensity (TMI) before and after burial, with signal enhancement techniques improving accuracy. Signal enhancement techniques in magnetic surveys improve anomaly detection by emphasizing subtle features, reducing noise, and highlighting target signals. Key methods include First Vertical Derivative (FVD) to enhance near-surface features, Analytical Signal (AS) for edge detection independent of magnetization direction, Euler Deconvolution to estimate source depths, and Residual Maps to isolate local anomalies from regional trends. These techniques offer greater sensitivity and clarity than conventional magnetic intensity maps for identifying buried objects and geological structures. The methodology included laboratory testing of magnetic susceptibility and data analysis using Euler Deconvolution and Analytical Signal processing. Results showed significant TMI variations, confirming the method's effectiveness. However, limitations include sensitivity to geological noise, controlled test conditions, and the potential for false detections. (Alao *et al.*, 2024) .

Ground-Penetrating Radar (GPR) with a 100 MHz antenna and SIR-3000 GSSI system was utilized to detect buried steel pipes in Sharm El-Sheikh and Qusier (Schlinger, 1990). Data acquisition in time mode with manual marking every 5 m allowed precise profiling. Processing involved bandpass filtering, noise removal, and the generalized Hough transform to calculate pipe diameters from hyperbolic reflections. In Sharm El-Sheikh, GPR identified 25-cm diameter steel pipes at 1–2 m depth, validated by excavations. At the survey in Qusier, a steel pipe was detected at 2.2 m depth. Advantages included high resolution for metallic targets and accurate depth/diameter estimation. Limitations included susceptibility to cultural noise and challenges in heterogeneous soils. The method required minimal field time but depended on optimal antenna frequency (100 MHz for deeper penetration) and parameter calibration. GPR proved highly effective for steel pipe detection, offering non-invasive, real-time imaging crucial for urban utility mapping (Schlinger, 1990).

Ékes et al. (2011) introduced Pipe Penetrating Radar (PPR) as a ground-breaking in-pipe application of ground-penetrating radar (GPR) for assessing underground non-ferrous pipe integrity. This study, alongside my research, highlights PPR's capability to detect defects such as wall thickness variations, voids, delamination, and reinforcing steel placement. Utilizing robotic or manned deployment of high-frequency GPR (12.5 MHz–4 GHz) in conjunction with advanced software (PP-RADIAN. Validated in case studies involving large sewers and tunnels, PPR effectively identifies structural anomalies and informs trenchless rehabilitation strategies. Results demonstrated precise detection of rebar, voids, and joint flaws, significantly enhancing asset management and repair prioritization. While PPR provides high-resolution insights, its limitations include restricted penetration depth (~3 meters), resolution constraints for sub-centimetre features, operational dependencies on pipe size/accessibility, and the necessity for expert interpretation to distinguish complex reflections.(Ékes *et al.*, 2011).

Gravity and magnetic surveys are less commonly used to locate objects like pipes. However, Li et al. (2019) explored how pipeline parameters such as spacing, depth, diameter ratio, density, and susceptibility impact detection. Both methods faced challenges in detecting pipelines parallel to the measurement line, and magnetic surveys were limited to detecting ferromagnetic materials, leaving non-magnetic materials like plastic undetectable. Detection accuracy decreases with smaller pipe spacing, greater depth, or non-ideal diameter ratios. The study assumed uniform density and susceptibility, overlooking real-world factors like corrosion. Gravity surveys were less sensitive to small pipe spacing or deep pipelines, and field tests revealed issues with noise and data fluctuations, making these methods less reliable for such applications (Li *et al.*, 2019).

The study conducted by Kumar, Pal, and Guha (2024) used a combined analysis of three geophysical methods—magnetics, electrical resistivity tomography (ERT), and very low frequency electromagnetic (VLF-EM) data—focusing on investigating kimberlite pipes. The primary objective was to assess the spatial distribution, depth, and subsurface characteristics of these pipes, which are crucial for mineral exploration.

By integrating these methods, the study sought to mitigate the limitations of each individual method and enhance the accuracy of the results. The findings revealed clear anomalies that matched the locations of kimberlite pipes at different depths, with high magnetic and resistivity anomalies identified. Depth estimates ranged from 5 to 100 meters, with a mean depth of 48

meters based on the Euler deconvolution method. Additionally, strong correlations were observed between the magnetic, VLF-EM, and ERT data, offering robust evidence for the kimberlite body locations.

However, the study also pointed out some limitations, especially the sensitivity of the methods to local electromagnetic interference, such as from power lines, which could affect data quality. VLF-EM data, in particular, were impacted by noise and required careful pre-processing. Furthermore, the weathering of kimberlite pipes could influence the anomalies, making the interpretation more complex. (Kumar, Pal and Guha, 2024).

Seismic reflection is commonly used to study subsurface features like tunnels and geological structures such as faults but is not typically applied for pipeline detection. The study by Xu and Li (2021) examined the use of the TSP-SK seismic reflection imaging system for tunnel geological prediction. The system generated elastic waves using explosives. The waves are detected by geophones and processed through filtering, wave picking, and velocity analysis. Field tests conducted in Sanming City, Fujian Province showed that low P-wave velocity indicated weak rock mass, while low S-wave velocity and high Poisson's ratio suggested potential water seepage risks. The system's predictions closely aligned with excavation findings, confirming its reliability. However, its accuracy depended on proper water sealing in boreholes and selecting optimal Q filtering values (15-30). While effective, it may not fully replace detailed drilling-based surveys (Xu, Wei and Li, 2021).

### **2.3.2 Identifying Concrete Structures Underground**

Geophysical methods for detecting concrete, such as Ground-Penetrating Radar (GPR), Electrical Resistivity Tomography (ERT), and Seismic Reflection/Refraction, each have limitations. GPR is effective for shallow concrete structures but struggles with depth, high moisture content, or interference from metal objects. ERT offers lower resolution and can be impacted by soil variability and high-water content, making concrete harder to detect at deeper levels. Seismic methods have lower sensitivity to concrete, especially in urban areas, and their resolution diminishes with depth. Overall, GPR is the most effective for shallow concrete detection, while ERT and seismic methods can provide complementary information but are less precise (Gehrig, 2004).

Ground Penetrating Radar (GPR) is a non-destructive method that uses electromagnetic waves to detect subsurface features in concrete (e.g., rebar, voids, utilities) by analyzing reflections at dielectric interfaces. It employs high-frequency antennas (e.g., 1.5 GHz) for shallow, high-

resolution scans (1–2 m depth) and monostatic setups for rapid fieldwork, producing radargrams with hyperbolic patterns for rebar or polarity shifts for voids. While GPR excels in speed, versatility (slabs, bridges), and avoiding damage, it struggles with metallic interference, conductive soils, and depth limitations. Post-processing converts time-domain data to depth, but interpretation requires expertise. Ideal for quick evaluations, GPR balances resolution and efficiency but trades off penetration for precision (Gehrig, 2004).

Electrical Resistivity Tomography (ERT) is adapted for Reinforced Concrete (RC) floors using a warm-start inversion to model the RC layer (wire mesh + cement) and underground electrodes via existing wells, overcoming current distortion from embedded metal. Warm-start inversion uses a realistic starting model to improve the speed and accuracy of data inversion, especially in complex settings like reinforced concrete. This hybrid approach resolves deep targets by combining surface and subsurface sensors, though fieldwork is longer due to drilling and multi-electrode setups. Advantages include non-destructive assessment and enhanced depth resolution, while drawbacks involve complexity and reliance on boreholes. Compared to conventional ERT (surface-only, faster but ineffective under RC), modified ERT uses 55 surface + 12 underground electrodes, proving ideal for urban/industrial sites with RC infrastructure (Yang, Yang and Yuan, 2024).

The shallow seismic refraction method, utilizing P-wave (2800–4500 m/s) and S-wave velocities (1600–2750 m/s) with 24 geophones per profile and hammer-generated sources, directly estimates geotechnical parameters (e.g., elastic moduli, bearing capacity) and identified two subsurface layers, deeming 86% of New Minia City suitable for construction. While effective for mechanical property analysis, it requires time-intensive field work (30 profiles, multiple shots/stacks) and has limited depth penetration. The study integrated shallow seismic refraction (30 lines, 46 m spreads) and reflection (92 m spreads, CMP gathers) to enhance subsurface characterization. Refraction provided velocity-depth models, while reflection imaging (NMO correction, migration) resolved low-velocity zones and detected fractures/voids. (Shebl *et al.*, 2019).

A study by Anderson and Akingbade (1997) focuses on the shallow seismic reflection technique at near-vertical incidence to map subsurface structures. The method uses a source (such as a hammer or small explosive) and geophones arranged in a linear spread to record seismic waves reflected from subsurface layers. The incident angle—the angle at which seismic energy strikes a boundary—is near vertical, meaning it is very small (close to 0°). This ensures

that the reflected angle is also near vertical, simplifying wave path calculations and enhancing the resolution of horizontal or gently dipping layers. The results demonstrate high-resolution imaging of shallow subsurface features, making the technique particularly effective for environmental and engineering site investigations. (Anderson and Akingbade, 1997).

Another study confirms the effectiveness of near-vertical incidence in seismic reflection analysis. In this approach, reflections primarily arise from vertical heterogeneities, and the method iteratively adjusts a deconvolution filter to accommodate the non-white reflectivity spectrum of a von Kármán stochastic model—enhancing both stability and accuracy over earlier techniques. Synthetic tests showed successful recovery of depth ( $az$ ) and velocity ( $v$ ) under noise-free conditions, though sensitivity to noise increased with greater deviation from vertical incidence. When applied to field data from the PASSCAL Basin and Range experiment, the method produced results of  $az \approx 277$  m and  $v \approx 0.26$ , aligning well with known crustal properties and validating its usefulness for near-vertical reflection datasets (Poppeliers, 2007).

### 2.3.3 Detecting Plastic Drums in the Subsurface

Similarly, no geophysical method, except GPR, can reliably detect plastic pipes. Plastic lacks the electrical or magnetic properties necessary for detection by other methods. ERT cannot detect plastic pipes, as their resistivity is too similar to the surrounding material. Magnetic and electromagnetic methods are also ineffective since plastic is neither conductive nor magnetic. Therefore, GPR is the only practical method for locating buried plastic pipes, as it can detect differences between the pipe and the surrounding soil.

The study by Ayala-Cabrera et al. (2011) explains how Ground-Penetrating Radar (GPR) detects plastic pipes, presenting a method that combines data transformation with a multi-agent system to automatically identify pipe locations. The method showed 95% accuracy in simple scenarios and 75% in complex ones. It offers advantages such as being non-destructive, effective for low-reflectivity plastic pipes, and not requiring expert operators. However, it is sensitive to soil conditions and may have reduced accuracy in complex environments. Using a single 1.5 GHz monostatic antenna, the method likely reduces fieldwork time compared to traditional interpretation methods due to its automated nature (Ayala-Cabrera *et al.*, 2011).

## 2.4 Research gap

The various geophysical methods discussed—Ground-Penetrating Radar (GPR), Electrical Resistivity Tomography (ERT), Seismic Refraction, and magnetic surveys—each provide

---

valuable advantages for subsurface detection but also come with inherent limitations. GPR is highly effective for detecting non-metallic objects like plastic drums and pipes but faces challenges with signal attenuation in moist environments and limited depth penetration (Wahab, 2013). ERT, while useful for mapping resistivity contrasts, offers lower resolution than GPR and can be affected by soil variability and slower data collection (Shahandashti *et al.*, 2021). Seismic methods, such as seismic refraction, are effective for assessing mechanical properties but suffer from limited depth penetration and require extensive fieldwork (Watts *et al.*, 2022). Magnetic methods, however, are restricted to detecting ferromagnetic materials, leaving non-metallic objects undetectable.

Microseismic methods offer a solution to these limitations by providing enhanced resolution for detecting small-scale subsurface anomalies. Such as pipes of both plastic and steel and concrete. This was also confirmed by conducting a series of laboratory experiments. Unlike traditional geophysical techniques, microseismic can detect even small object. Microseismic methods have shown strong potential to complement traditional techniques like Ground Penetrating Radar (GPR) and Electrical Resistivity Tomography (ERT), particularly in enhancing the detection of plastic and non-metallic objects. Their real-time, non-invasive nature makes them especially suitable for complex or urban environments where access is limited. These surveys are relatively quick to perform—typically taking around 4 to 5 hours in practical fieldwork—followed by straightforward data uploading and processing using accessible, non-licensed software. However, despite these advantages, there remain key gaps that this project aims to address. Specifically, there is a need for a geophysical method that is universally applicable across various soil types, easy to deploy, and simple to interpret without relying heavily on complex inversion models. Ideally, this method should allow near real-time analysis, reduce the need for expert interpretation, and be capable of detecting a wide range of buried objects regardless of their material. Collecting data in this way does not take much time, whether in simulations or in practical experiments.

## Chapter 3 Background theory and method

### 3.1 Seismic Reflection Theory

Seismic reflection works on the idea that seismic waves created by a controlled source travel into the Earth's subsurface and reflect off the borders of distinct geological strata. These reflections emerge as a result of acoustic impedance caused by rock density and seismic velocity differences. In Geophysics, one may use the time it takes for reflected waves to return to the surface to construct pictures of the subsurface at depths of 100s of meters. This approach is particularly useful for mapping stratigraphy, detecting fault zones, and discovering resources like as oil and gas (Ackman and Cohen, 1994). Samsudin, et al. (1999) showed that, seismic reflection can be utilized for shallow subsurface investigations (depths 10m to 60m). This potential is further explored in this thesis but for the near-surface (depths  $\leq 3$ m). This is a particularly challenging depth zone because the soil at such shallow depths is less compacted and dispersion of seismic waves is very high. Traditional analysis of reflective waves that utilises arrival times is not easy, if not impossible, to apply.

#### 3.1.1 Principles of Seismic Reflection

Seismic waves are created using controlled sources such as explosions, air guns, and seismic vibrators (Vibroseis truck)(Chelminski, Watson and Ronen, 2019) along the surface or the near-surface.

Seismic waves are generally divided into P-waves (Primary waves) and S-waves (Secondary waves) (Yang *et al.*, 2007). P-waves are compressional or longitudinal waves that travel by compressing and expanding the material in the same direction as the wave propagates. They are the quickest form of seismic wave, making them the first to be detected by seismographs. P-waves may pass through solids, liquids, and gases, making them useful for understanding the Earth's internal structure. S-waves, on the other hand, are shear or transverse waves that move particles perpendicular to the wave's propagation direction, resulting in a shearing effect. S-waves are slower than P-waves and come later. Importantly, S-waves can only travel through solids, revealing vital information about the Earth's fundamental composition, specifically that the outer core is liquid since S-waves do not pass through it (Kayal, 2006).

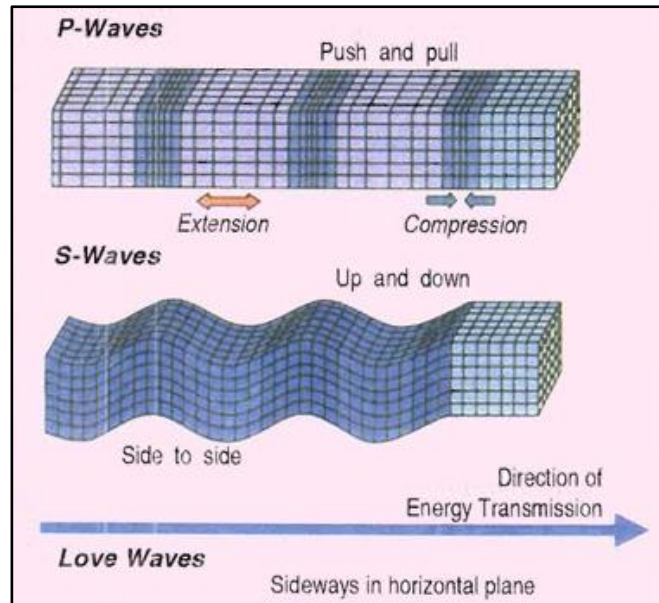


**Figure 3.1:** P- wave and S-wave (Murthy, 2002)

### 3.1.2 Seismic waves Propagation Through the Earth

Traditionally, the application of the seismic reflection is to measure the time it takes for a seismic wave to travel from a source down into the earth, where it is reflected back to the surface and detected by a receiver (geophone). The time that is measured is termed as two-way time (TWT) (Murthy, 2002).

At the boundary between two rock layers, seismic wave speeds often vary due to differences in the physical properties of the strata. When a seismic wave encounters a material boundary, its energy splits into transmitted and reflected waves. The magnitudes of the transmitted and reflected waves are determined by the velocities ( $V$ ), densities ( $\rho$ ), and the angle of incidence. The total energy of the transmitted and reflected waves must be equal to the energy of the incident ray (ASIM HASHIMI, 2011).

The reflection coefficient  $R$  is defined by the formula:

$$R = A_1 / A_0 \quad \text{Eq 3.1}$$

Here,  $A_0$  represents the amplitude of the incident wave, whereas  $A_1$  represents the amplitude of the reflected wave. The value of  $R$  may be determined for a wave that is incident at a normal angle.

$$R = \frac{\rho_2 v_2 - \rho_1 v_1}{\rho_2 v_2 + \rho_1 v_1} = \frac{Z_2 - Z_1}{Z_2 + Z_1} \quad \text{Eq 3.2}$$

The variables  $\rho_1$ ,  $v_1$ ,  $Z_1$  represent the density, P-wave velocity, and acoustic impedance of the first layer, whereas  $\rho_2$ ,  $v_2$ ,  $Z_2$  represent the same properties for the second layer (ASIM HASHIMI, 2011).

When a compressional wave hits the interface at a 90-degree angle (Fig.3.2), the transmitted wave passes through the interface in a straight line without any change in direction, while the reflected wave follows the same path as the incident wave. The total energy of the reflected and transmitted waves is equivalent to the energy of the incident wave.

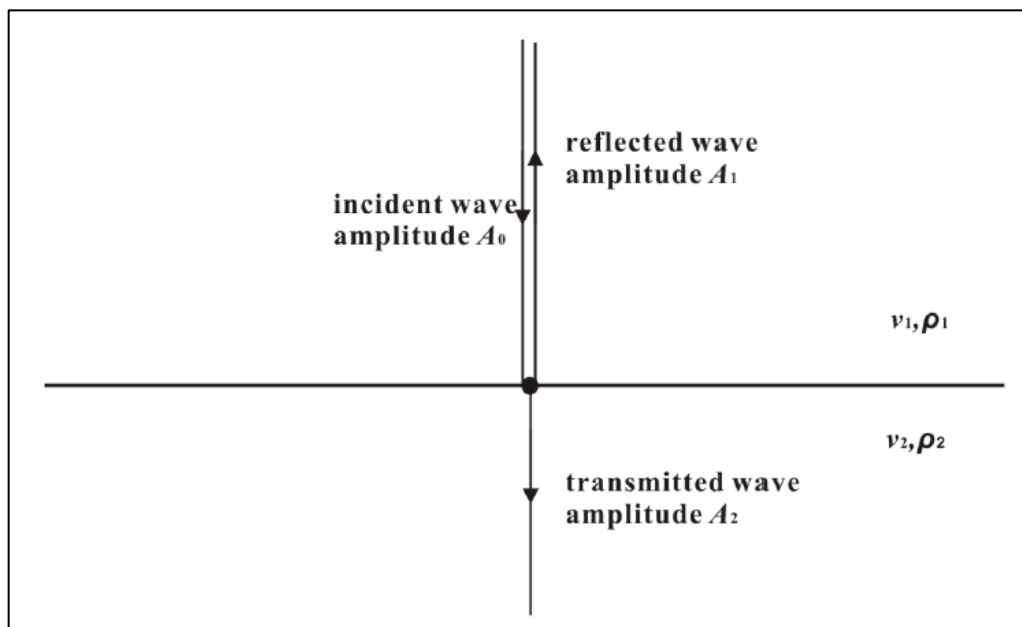


**Figure 3.2:** Reflected and transmitted seismic waves which generated by normal incident (ASIM HASHIMI, 2011)

As in the case of normally incidence, a seismic wave obliquely incident on the contact produces reflected and transmitted waves (Fig.3.3). Considered as a refracted wave, the transmitted wave moves in a different direction. Snell's law characterizes the link between the angles of incidence and refraction.

$$\frac{\sin \theta_1}{\sin \theta_2} = \frac{v_1}{v_2} \quad \text{Eq 3.3}$$

Where the refraction angle is  $\theta_2$  and the incidence angle is  $\theta_1$  correspondingly. Wave velocities in various materials are  $v_1$  and  $v_2$  (Mari, 2019).

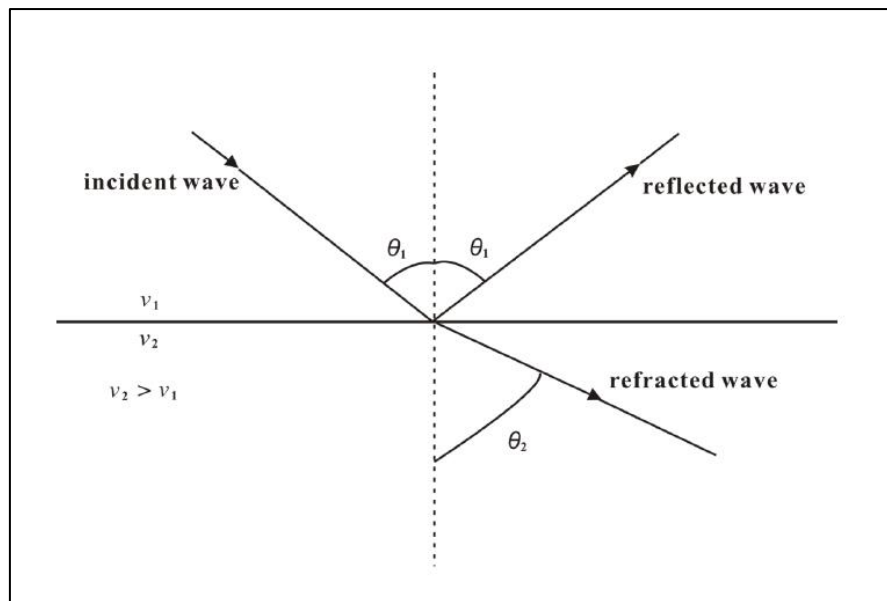


**Figure 3.3:** Obliquely incident seismic waves produce both reflected and refracted waves (Mari, 2019).

This figure (3.4) below consists of two figures, a and b. Figure a illustrates the mechanics of seismic wave propagation, with the area inside the red box representing wave propagation near the surface. Figure b depicts the incidence and reflection of seismic waves. In this study, the target depth ranges from 1 to 3 meters, while the horizontal distance does not exceed 60 meters. Under these conditions, the waves are incident and reflected vertically, as this represents only a very small portion of the initial stage of seismic wave propagation, limiting the extent of wave expansion (Anderson and Akingbade, 1997).

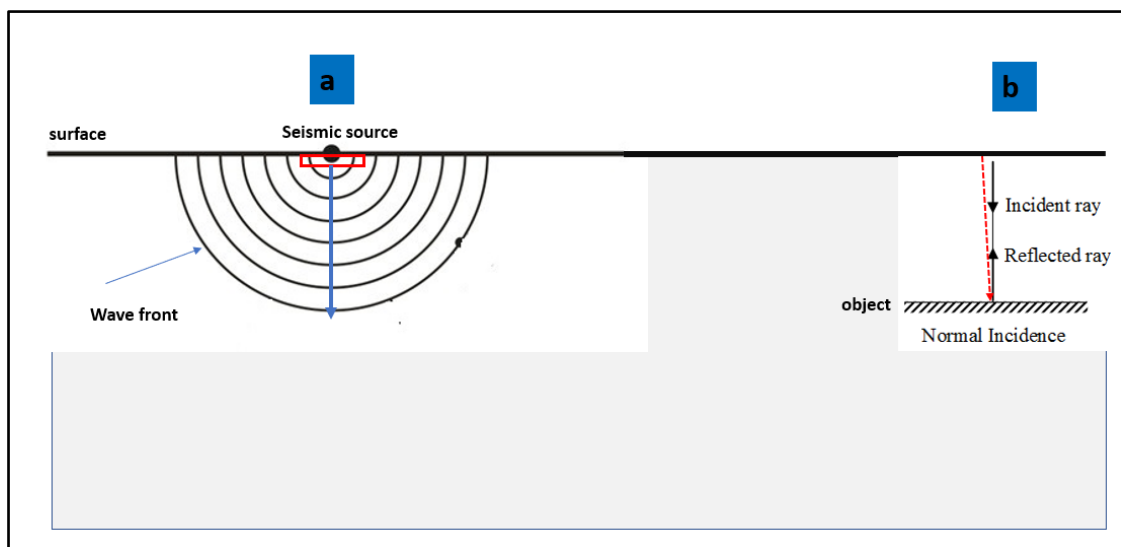


**Figure 3.4:** (a) Seismic wave front pattern during wave propagation over kilometres scale, (b) Zoomed in section close to seismic source (within 10 m depth) where the incident angle can be regarded almost vertical.

### 3.2 Methodology of analysis steps

To achieve the set objectives detailed in chapter 1, I followed the analysis steps /methods mentioned below, which are expanded on in greater detail in the next sections of this chapter.

**Step 1.** Application of numerical modelling to simulate seismic wave propagation on ground surface generated by a surface seismic source (objective 1).

**Step 2.** Analysis of synthetic velocity data generated by the numerical models (objective 2). For identification of a buried object.

**Step 3.** Synthesis of results from Step 2 to develop a site investigation methodology (objective 2).

**Step 4.** Verification and validation of the methodology developed in Step 3 using field data (objective 3).

### **3.3 Numerical modelling of seismic waves propagation**

This modelling approach seeks to shed light on several elements of seismic wave behaviour, such as velocity, amplitude, and dispersion patterns as they pass through diverse media. This included looking into changes in the time domain concerning wave amplitude and changes in the frequency domain addressing frequency variations caused by seismic waves interacting with shallow subsurface objects. (Adamo et al., 2020).

Several factors led me to utilise numerical modelling before field experiments. Helped me rapidly generate several controlled situations and scenarios. I could methodically study seismic waves attributes by modelling first.

When seismic waves encounter an object, they can undergo several interactions: part of the wave may reflect back, while another part may refract and change direction as it passes through the object. Additionally, waves can diffract around the object's edges, scatter in various directions if the object is irregular, or lose energy through absorption, reducing their amplitude. These effects depend on the wave's properties and the nature of the object.

#### **3.3.1 Numerical modelling tool -FLAC<sup>3D</sup>**

I obtained and was granted a license for the commercial software FLAC<sup>3D</sup> ((Fast Lagrangian Analysis of Continua in 3D). The FLAC<sup>3D</sup> is a highly effective software for seismic wave numerical modelling due to its ability for geomechanically simulations, nonlinear material behaviour handling, advanced constitutive models, and ability to simulate complex subsurface geometries. FLAC<sup>3D</sup> integrates static and dynamic seismic analysis, allowing for accurate modelling of the dynamic response of objects to seismic waves. Its industry acceptance makes it a popular choice for seismic wave modelling. The user-friendly interface and extensive technical support resources make it a favourable choice for researchers and engineers in numerical seismic wave and subsurface geomechanics (Itasca Consulting Group, 2017) .

It can address a range of challenges, including mechanical response to loads and deformations, failure assessment and progressive breakdown, safety factor calculations, and complex aspects of fluid flow under fully and partially saturated conditions (Guo et al., 2013). This programme was utilised in multiple research investigations to simulate seismic waves, such as fault simulations and tunnel simulations. And used in numerical investigation of the dynamic response of a horizontal layered-structure rock slope to a normally incident Sv wave (Zhan &

Qi, 2017), Numerical simulation of the seismic response of a rigid foundation on soft soil (Zhang & Wang, 2015). Numerical Simulation Method for Seismic Analysis of a Shallow Tunnel in Poor Ground Conditions (Zihong *et al.*, 2018).

The Finite Difference Method (FDM) is used in FLAC<sup>3D</sup> due to its accuracy and reliability in handling elastodynamics. FDM's strength lies in providing precise solutions for complex dynamic problems, making it a good tool for modelling seismic wave propagation. However, FDM is adapted to simpler geometries due to its grid-based discretization approach, which may face challenges in complex or irregular geological settings (Semblat, 2011).

Performing a dynamic analysis in FLAC<sup>3D</sup> involves a well-structured process to simulate how objects materials respond to dynamic loading, such as seismic waves. It begins with setting up the model, defining objects properties, and establishing boundary conditions. Accurately defining the dynamic load and creating a detailed mesh are essential for accurately modelling objects so that seismic waves can pass through them without interference. Dynamic analysis settings, including time step size, need to be carefully configured. The choice of the numerical solver and solution algorithm depends on the specific problem at hand.

### 3.3.2 Setting up numerical model in FLAC<sup>3D</sup>

To simulate seismic waves with FLAC<sup>3D</sup> within an elastic model, three material characteristics need consideration. Firstly, density ( $\rho$ ) is expressed as mass per volume unit. For measurements in the International Standard (SI) units, mass is quantified in kilograms. Secondly, the material's stiffness is captured in FLAC<sup>3D</sup> by attributing a bulk modulus ( $\mathbf{K}$ ) and shear modulus ( $\mathbf{G}$ ), both gauged in force per unit area. It's noteworthy that Young's modulus ( $\mathbf{E}$ ) and Poisson's ratio ( $\nu$ ) can be employed to deduce the bulk and shear moduli, as detailed in the FLAC<sup>3D</sup> Manual (Itasca Consulting Group, 2017).

Note: The following equations link the bulk modulus ( $\mathbf{K}$ ), shear modulus ( $\mathbf{G}$ ), Young's modulus ( $\mathbf{E}$ ), and Poisson's ratio ( $\nu$ ):

$$\mathbf{G} = \frac{\mathbf{E}}{2(1+\nu)} \quad \text{Eq 3.4}$$

or

$$\mathbf{E} = \frac{9\mathbf{K}\mathbf{G}}{3\mathbf{K}+\mathbf{G}} \quad \text{Eq 3.5}$$

$$\nu = \frac{3\mathbf{K}-2\mathbf{G}}{2(3\mathbf{K}+\mathbf{G})} \quad \text{Eq 3.6}$$

Based on these mechanical properties, the velocity of **P** and **S** wave through this medium, are given by:

$$v_p = \sqrt{\frac{(K + \frac{4}{3}G)}{\rho}} \quad \text{Eq 3.7}$$

$$v_s = \sqrt{\frac{G}{\rho}} \quad \text{Eq 3.8}$$

The wavelengths of these waves are characterized by two distinct equations, each providing information on aspects of wave propagation. The wavelength of a seismic wave ( $\lambda$ ) is determined by dividing the velocity ( $V$ ) that the wave travel through the medium by the frequency ( $f$ ) of the wave see the equation below (Itasca Consulting Group, 2017).

$$\lambda = \frac{V}{f} \quad \text{Eq 3.9}$$

### 3.3.3 Governing Equation

The momentum equation or the equation of motion for a continuum is solved for the ground response to seismic excitation (eq 3.10). Each component ( $u_i$ ,  $\tau_{ij}$ , and  $f_i$ ) is affected by both position ( $\mathbf{x}$ ) and time. The body force term  $\mathbf{f}$  frequently contains a combination of gravity ( $\mathbf{f}_g$ ) and a source component ( $\mathbf{f}_s$ ). Gravity has a substantial influence on very low frequencies in normal mode seismology, although it has less influence on calculations incorporating body and surface waves at regularly observable wavelengths. (Shearer, 2012).

$$\rho \frac{\partial^2 \mathbf{u}}{\partial t^2} = \sigma_j \tau_{ij} + \mathbf{f}_i \quad \text{Eq 3.10}$$

where  $\rho$  is the density and the term  $\sigma_j \tau_{ij}$  represents the divergence of the stress tensor, and it's important to note that this expression involves summation over the index  $j$ , which takes values from 1 to 3.

The commencement of wave propagation occurs when the initial state of equilibrium is stimulated through the imposition of a force, denoted as  $\mathbf{F}$ . This force is introduced at a specified location within the model, dictating a prescribed velocity. In essence, this implies that the constituent material particles within the model experience an excitation akin to seismic velocity (m/s) at a specific frequency.

The calculation procedure involves tracking deformations in a jointed block system over minute time intervals, allowing for dynamic propagation of applied forces and reactions. This methodology is advantageous for tracing deformation from the initial loading phase to equilibrium (Fairhurst, 2019).

### 3.3.4 Time Step

A step, often referred to as a "cycle," corresponds to a single iteration within the sequence. During the execution of equations of motion, forces remain constant for all elements. This approach is effective due to the underlying assumption in the explicit solution scheme that information propagation is limited to a distance no greater than a single element within a single timestep. Consequently, the duration of each timestep is contingent upon factors like material density, the stiffness of contacts or zones, and the dimensions of the elements (Itasca Consulting Group, 2017).

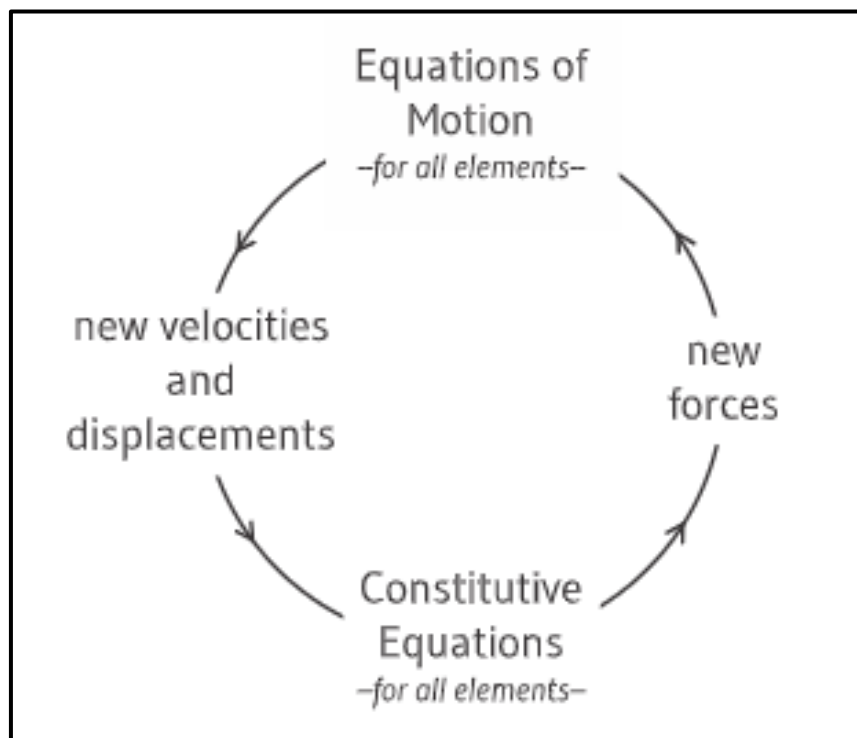


**Figure 3.5:** The timestep in Itasca software (Itasca Consulting Group, 2017).

### 3.3.5 Boundary conditions

Boundary conditions within a numerical model are defined by the field variables' values—such as stress, velocity, and displacement—at the model's numerical grid boundaries. In the context of this study, boundary conditions should prevent outward-propagating waves from reflecting

back into the model. Reflected seismic waves create destructive interference in a numerical model and can have serious consequences for simulation accuracy and reliability. When two or more waves of opposing phase collide and mix, they partially or fully cancel each other out, resulting in a diminution or complete nullification of the wave's amplitude. A strategy to mitigate this is by employing an expansive model size, effectively ensuring that the wave does not reach the boundary within the designated run time, hence averting reflections. However, this approach can prove computationally demanding when dealing with smaller element sizes. For my models, three distinct boundary condition types were under consideration:

- Free field boundary conditions governing the four vertical sides of the model, running parallel to the x and y axes.
- Quiet boundary conditions implemented along the model's lower boundary.
- Free-surface boundary conditions applied to the vertical sides of the model.

#### **3.3.5.1 The Free surface**

As stated by Robertson (2001), implementing the free-surface boundary condition is accomplished by applying zeroing functions along these boundaries, following the outlines of the mesh elements. When a gas and a solid or liquid come into contact, the interface between them is known as a free surface. As a result, the uppermost layer of the model has a free-surface boundary condition. The term "free" in this case refers to the significant difference in densities between air (gas) and solid (rock mass), which causes the distinction.(Robertson, 2001).

#### **3.3.5.2 Free-field boundary conditions**

Free-field boundaries find their application in simulating the medium's lateral extent. This is vital to facilitate accurate energy radiation. With the assignment of a free-field boundary to the model, modifications in properties within the main grid do not extend to the free-field zones. This approach effectively emulates an infinite lateral space while concurrently addressing the necessity for non-reflective boundaries (Ferrari, 2011).

By applying this kind of boundary conditions, the seismic waves propagating upwards do not suffer from any boundary distortion, because the grid of the free field provides conditions like those of an infinite space. To apply a free field boundary in  $FLAC^{3D}$ , the model should be oriented so that the bottom is perpendicular to the z-axis, and the model sides should be parallel to the z-axis with their normal along the x or y-axis. This kind of boundary condition is implemented in  $FLAC^{3D}$  as four-plane free field grids located on the model sides. At each

corner, the model has a column-free field grid. The planar grids are designed to match the main grid zones of the side boundaries so that there is a match between the grid points in the free field and the main grid. Figure 3.6 shows the free field boundary applied to model.

The main grid's lateral boundaries are interconnected with the free-field grid through viscous dashpots, which emulate a quiet boundary. The resultant imbalanced forces from the free field grid is exerted upon the boundary of the main grid. These two conditions are mathematically expressed in the subsequent set of three equations, which are applicable to the free-field boundary situated along one side boundary plane, with its normal aligned in the direction of the x-axis. Corresponding formulations can be devised for the other sides and corner boundaries (Itasca Consulting Group, 2017).

$$F_x = -\rho C_p (v_x^m - v_x^{ff})A + F_x^{ff} \quad Eq\ 3.11$$

$$F_y = -\rho C_s (v_y^m - v_y^{ff})A + F_y^{ff} \quad Eq\ 3.12$$

$$F_z = -\rho C_s (v_z^m - v_z^{ff})A + F_z^{ff} \quad Eq\ 3.13$$

Where;

$\rho$  = Density of material along the vertical model boundary.

$C_p$  = Primary wave speed at the side boundary.

$C_s$  = shear wave speed at the side boundary.

$A$  = Area of influence of free field grid point.

$v_x^m = x$  - velocity of a grid point in the main grid at the side boundary.

$v_y^m = y$ - velocity of a grid point in the main grid at the side boundary.

$v_z^m = z$ - velocity of a grid point in the main grid at the side boundary.

$v_x^{ff} = x$ - velocity of grid point inside the free field.

$v_y^{ff} = y$ - velocity of grid point inside the free field.

$v_z^{ff} = z$ - velocity of grid point inside the free field.

$F_x^{ff}$  = free-field grid point force with contributions from  $\sigma_{xx}^{ff}$  the stresses of the free-field zones around the grid point.

$F_y^{\text{ff}}$  = free-field grid point force with contributions from  $\sigma_{xy}^{\text{ff}}$  the stresses of the free-field zones around the grid point.

$F_z^{\text{ff}}$  = free-field grid point force with contributions from  $\sigma_{xz}^{\text{ff}}$  the stresses of the free-field zones around the grid point.

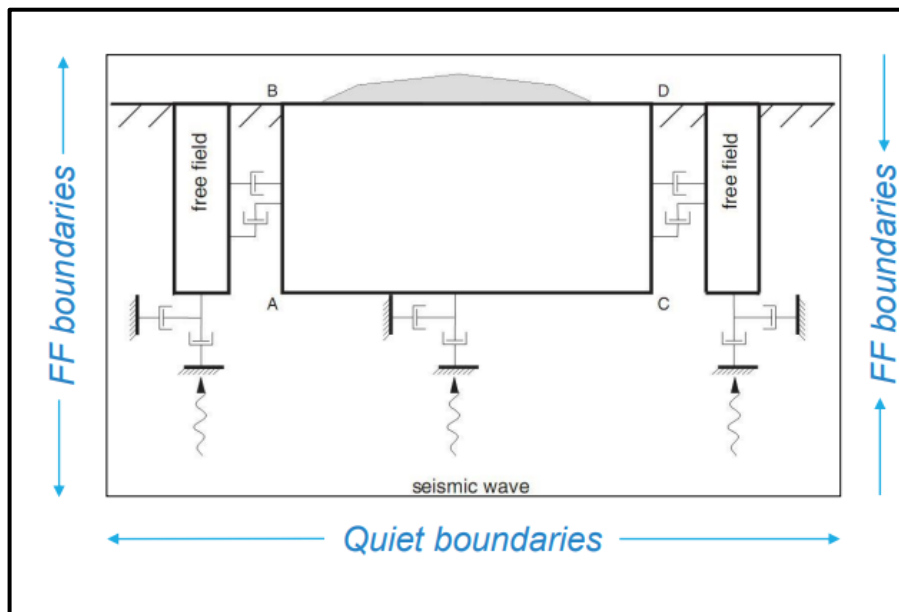


**Figure 3.6:** Free Field Boundary Mechanisms in FLAC <sup>3D</sup>(Itasca Consulting Group, 2017).

This boundary condition becomes indispensable when dealing with seismic sources that are defined by their velocity rather than stress or acceleration. When seismic waves are generated by velocity sources, such as vibrating machinery or surface motion, applying the correct boundary condition becomes paramount. This boundary condition ensures that the velocity at the boundary is maintained at the prescribed value, thus mimicking the characteristics of real seismic sources.

Figure 3.7 illustrates the model's geometry, including the model planes, monitoring stations, seismic wave emission location, and the object location.

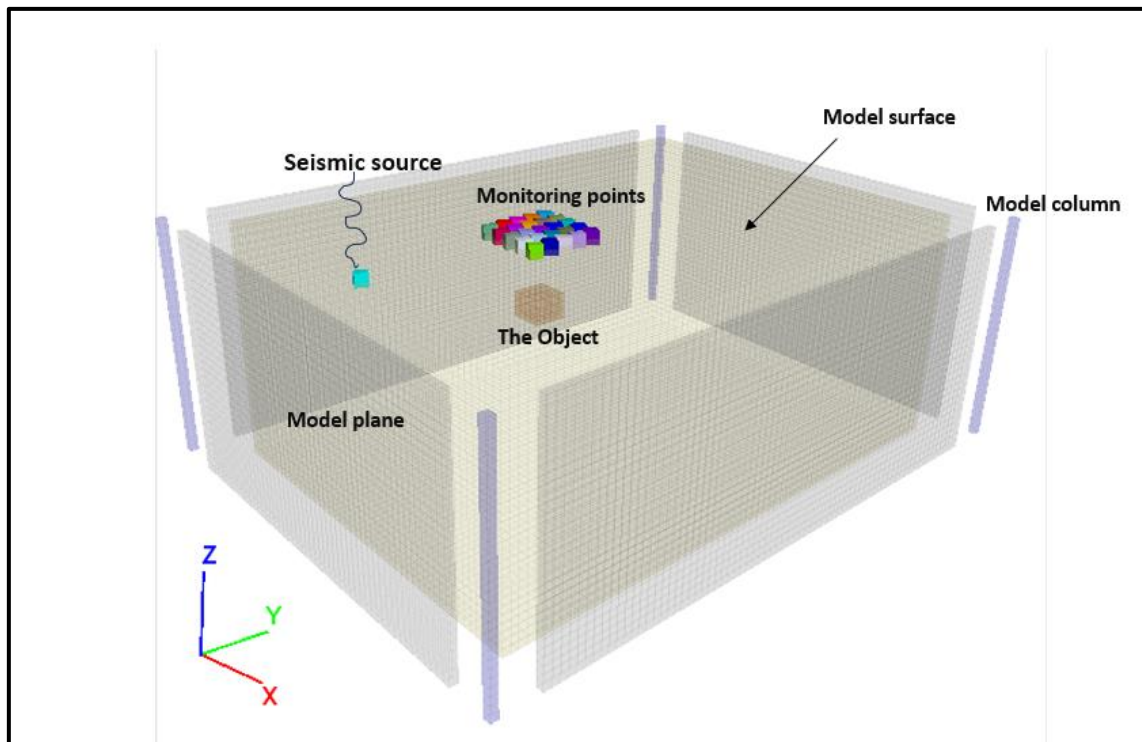


**Figure 3.7:** Basic 3D geometry of numerical model with the free field boundary.

### 3.3.5.3 Quiet boundary (viscous) boundary

An absorbent (viscous) boundary is used to prevent any reflection of seismic waves back into the model. The quiet-boundary approach utilizes separate dashpots that are connected to the boundary in both perpendicular and parallel directions (Itasca,2019). These dashpots serve to offer viscous tractions in both the normal and shear directions. The dashpots offer viscous normal and shear tractions given by using:

$$t_n = -\rho C_p v_n \quad \text{Eq 3.14}$$

$$t_s = -\rho C_s v_s \quad \text{Eq 3.15}$$

**Where:**  $v_n$  is the component of normal wave velocity and  $v_s$  component of shear wave velocity at the model boundary;  $\rho$  = material density;  $C_p$  and  $C_s$  are the primary and shear wave respectively.

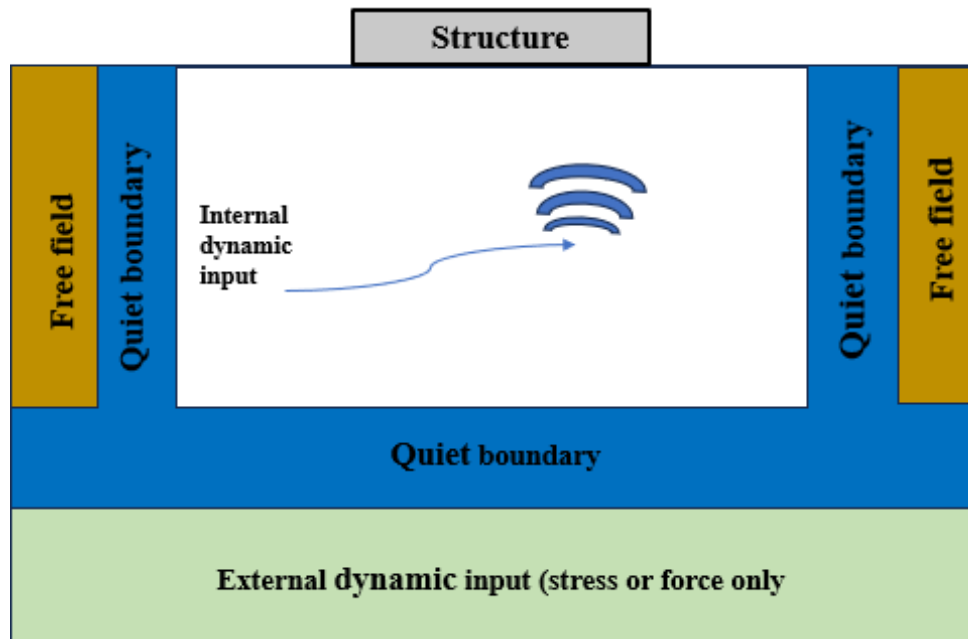


**Figure 3.8:** Illustrates the quiet boundary. Modified after (Itasca Consulting Group, 2017).

### 3.3.6 Dynamic load:

In all models, a sine wave (eq3.16) was applied, which has a frequency, wavelength, and duration. The selection of a sine wave as an input for seismic wave simulation facilitates the comparison of velocity histories with the seismic source. Its simplicity of generation, fixed shape, and adaptability make it a good choice for understanding the changes that take place for the different conditions in the numerical models in this study and, consequently, for evaluating the model's performance and stability. Stable numerical simulations necessitate the utilisation of a seismic wave source that is designed in accordance with the mechanical parameters of the model. The behaviour of seismic waves in the simulated environment is influenced by various mechanical parameters, including material stiffness, density, and boundary conditions.

$$y = A \sin(\omega)$$

*Eq 3.16*

where:

- $y$  is the value of the wave at a given point in time or space.
- $A$  is the amplitude of the wave, which represents its maximum displacement from the equilibrium position (the peak value).
- $\omega$  is the angular frequency of the wave, which determines how quickly the wave oscillates.

The sine function,  $\sin(\omega)$ , produces a wave that oscillates between -1 and 1. The amplitude  $A$  scales this oscillation to reach a maximum value of  $A$  and a minimum value of  $-A$ .

The angular frequency  $\omega$  is related to the regular frequency  $f$  (the number of oscillations per unit of time).

$$\omega = 2\pi f$$

Eq 3.17

So,  $\omega$  represents how fast the wave oscillates in radians per unit of time.

One of the following options is available for applying dynamic input in FLAC<sup>3D</sup>: A **force history**, an **acceleration history**, a **velocity history**, a **stress (or pressure) history**, or another type of history. The figure 3.9 shows where the seismic source is located on the surface of the models and shows where the waves are managed to start travelling. This helps us correctly understand modelling results and how the subsurface moves and changes in different situations.

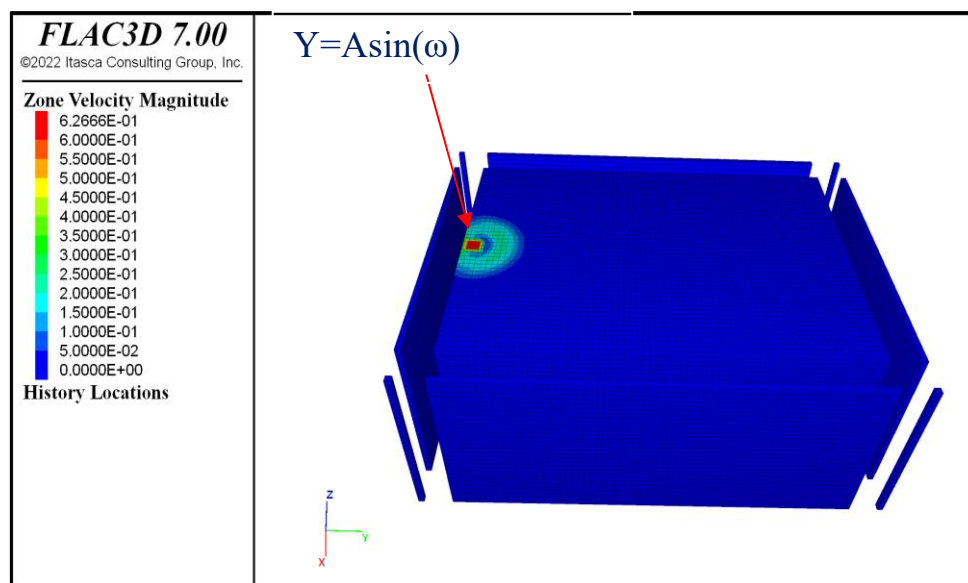


**Figure 3.9:** Dynamic input direction (applied on second, third, and four model).

### 3.3.7 Element size

In the realm of dynamic analysis, potential distortions in the numerical transmission of seismic waves can arise due to various modelling conditions. The interplay of both the input seismic wave frequency and the wave velocity characteristics intrinsic to the medium significantly impact the numerical simulation of wave propagation. For achieving an exact representation of wave transmission through a medium the element size (size of the small volume components that comprise the total volume of the model, in this study, these are little cubes), must be smaller

than roughly one-tenth to one-eighth of the wavelength related with the maximum frequency component of the incident seismic wave (Sebaaly, 2013). Figure 3.10 explain the model element shape and size.

$$\Delta l \leq \frac{\lambda}{10}$$

Eq 3.18

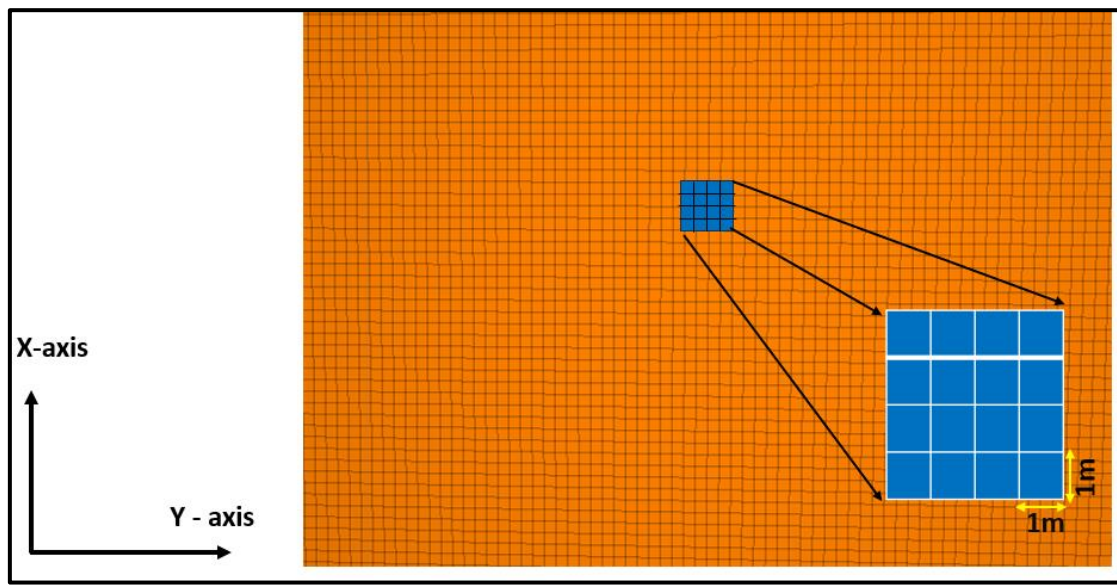


**Figure 3.10:** A cross section in 2D, the shape of the element, which is a square, and the size of the element, which is 1m in all axes, this shape and size of the element is applied to all models.

However, a small element size requires a larger number of elements and a smaller time step, increasing the model simulation run time. Thus, when selecting the element size, one should also take the computation time into consideration.

### 3.4 Numerical modelling of the propagation of a sine wave

Four models were developed, the first model is considered preliminary, and the seismic wave source was applied to the entire bottom face of the model. Its main purpose was to test and validate the boundary conditions.

The remaining three models deviate from the initial model in various aspects, primarily in terms of their mechanical properties and the seismic wave source location. Additionally, an expanded array of control points has been incorporated. Notably, a crucial development in these subsequent models involves the introduction of volumes with different properties (objects) from the model within the modelled space as detailed in table 3.2.

**3.4.1 Generation and analysis of synthetic data (Step2 & Step3):**

The object chosen for the numerical model is steel, selected due to its prevalence in brownfield sites. Steel's properties are well-documented in the table below, making it a reliable material for simulations. This choice helps in understanding how steel materials in brownfield sites respond to seismic waves.

Concrete and PVC plastic are also common in brownfield areas, but the study was more detailed on steel. This is due to some reasons, the most important of which is that the results were close, as concrete was tested at a depth of 1 m.

**Table 3.1:** Summarize the main characteristics of the models and the object.

Model No,	Model Dimensions (X, Y, Z)	Element Dimensions	Mechanical Properties			Seismic Source frequency and location	purpose
			Density (kg/m <sup>3</sup> )	Shear modulus (Pa)	Bulk modulus (Pa)		
1	100m × 80m×40m	1m × 1m×1m	2000	7 x 10 <sup>9</sup>	26 x 10 <sup>9</sup>	70 Hz, Applied at the whole model base ( sine wave with half cycle)	To validate the choice of boundary conditions
2	50m × 70m×30m	1m × 1m×1m	2000	2x 10 <sup>8</sup>	4.4 x 10 <sup>8</sup>	20 Hz, Applied as point on the model top surface (sine wave with two cycles and half)	Simulate the low Seismic Velocity Soil of Brownfield Site
3	50m × 70m×30m	1m × 1m×1m	2100	1.42x 10 <sup>9</sup>	2.5 x 10 <sup>9</sup>	50 Hz, Applied as point on the model top surface (sine wave with two cycles and half)	Simulate the medium Seismic Velocity Soil of Brownfield Site
4	50m × 70m×30m	1m × 1m×1m	2000	7 x 10 <sup>9</sup>	20.8 x 10 <sup>9</sup>	70 Hz, Applied as point on the model top surface (sine wave with sixteen cycles and half)	Simulate the high Seismic Velocity Soil of Brownfield Site
Object (steel)	1m × 1m×1m	-----	7700	25 x 10 <sup>10</sup>	40 x 10 <sup>10</sup>	-----	-----

The mechanical properties and frequency differ to allow for a range of seismic waves velocities to be used in detecting objects in different brownfield sites

### 3.4.2 Model 1

The main goal of building this preliminary model is to ensure that the seismic waves pass through the model without interference or distortion, as the source of the seismic waves was applied to the entire bottom face of the model. The mechanical properties were chosen as in table 3.1. As a testing ground for the implementation and validation of the quiet boundary condition, it also makes sure that the model's boundaries allow seismic waves to propagate without creating any unintended disturbances.

The origin of the coordinate axes for the FLAC<sup>3D</sup> model is at the bottom left corner as shown in figure 3.11.

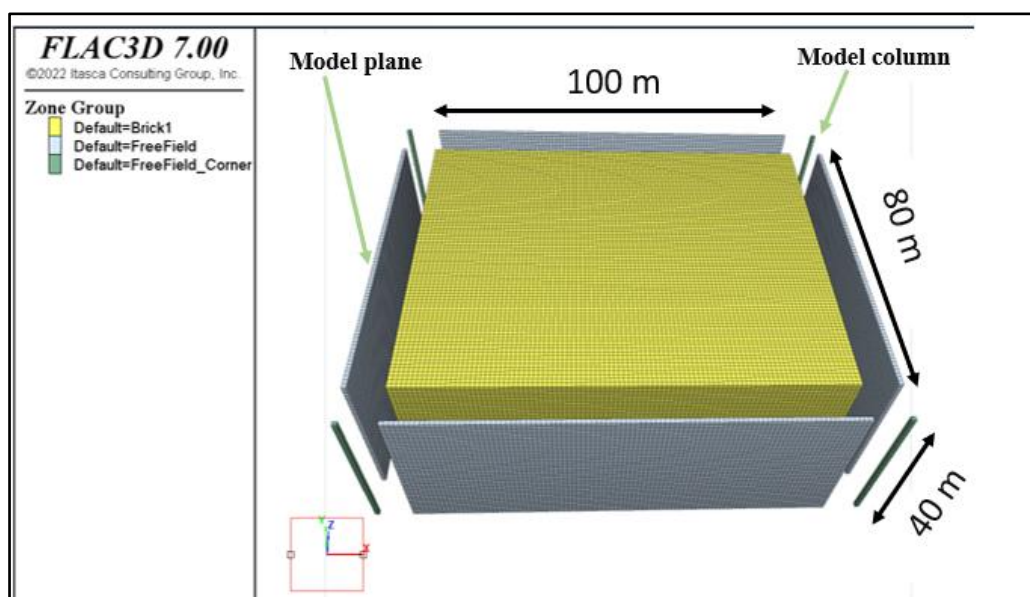


**Figure 3.11:** The origin of the coordinate system and a homogeneous model's geometry. The conditions at the free-field boundary are represented by the "extended walls".

On the model's surface, three control points ( $v_1$ ,  $v_2$ ,  $v_3$ ) were chosen and set with equal distances between them. Figure 3.13 shows the monitoring points distribution on the model surface.

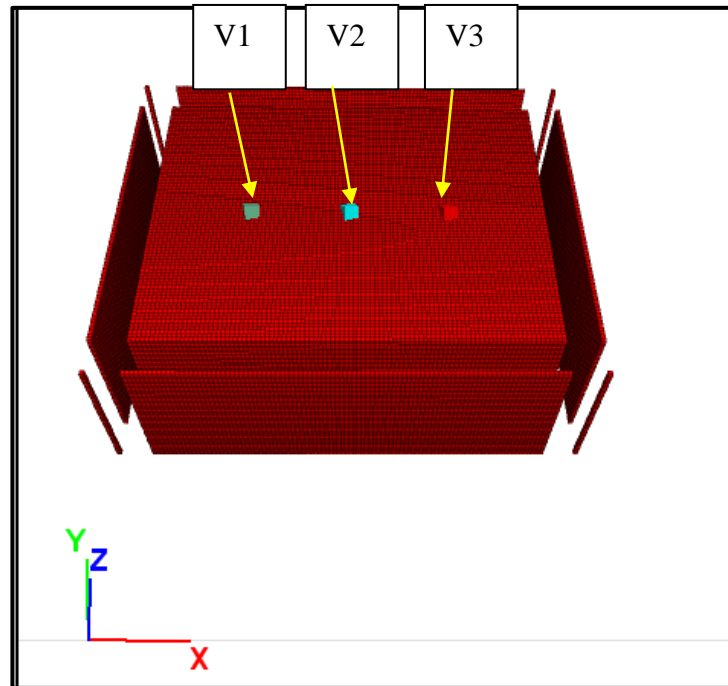


**Figure 3.12:** Monitoring points deployed at the surface of the model 1.

The dynamic source is a sinusoidal wave with a single cycle as the seismic wave source. It is a sinusoidal wave with an amplitude of 0.001m, frequency of 70 Hz, and 0.00144 seconds in duration. Choosing a frequency for the seismic wave source wave is based mainly on the mechanical properties of the model and the element size of the model. The application of the wave across the entire lower face of the model and in an upward direction provided the basis for this decision. Making the decision to use a single wave cycle is consistent with the goal of minimizing any potential wave interference that could result from using multiple waves, particularly in relation to reflections from the free surface.

The mechanical properties of this model were chosen as hard soil. Based on these values, the shear and primary velocity and wavelength were calculated, and it was also verified that the wavelength of the seismic waves fulfils the equation of numerical models and allows the passage of seismic waves inside the model without any problems as described below.

Based on the Equation 3.7 and Equation 3.8, the shear and primary velocity is equal to:

$$V_s = \sqrt{\frac{7 \times 10^9}{2200}}$$

$$V_s = 1870.828 \text{ m/sec}$$

$$V_P = \sqrt{\frac{(26 \times 10^9 + \frac{4}{3} \times 7 \times 10^9)}{2200}}$$

$$V_P = 4250.490 \text{ m/sec}$$

the wavelength can be calculated from the equation below:

$$\lambda = \frac{V_s}{f} = \frac{1870.828}{70}$$

$$\lambda \approx 27 \text{ m}$$

To pass seismic waves without interference or distortion through this model, the size of the element must meet the conditions (Abbasi et al., 2013):

$$\Delta l \leq 2.7 \text{ m} \quad (\text{element size of the model } 1 \text{ m in X Y Z direction})$$

$$\sigma_s = 2(\rho C_s) v_s$$

Eq 3.19

Where:

$\sigma_s$  = applied stress.

$\rho$  = density.

$C_s$  = speed of wave propagation through the medium

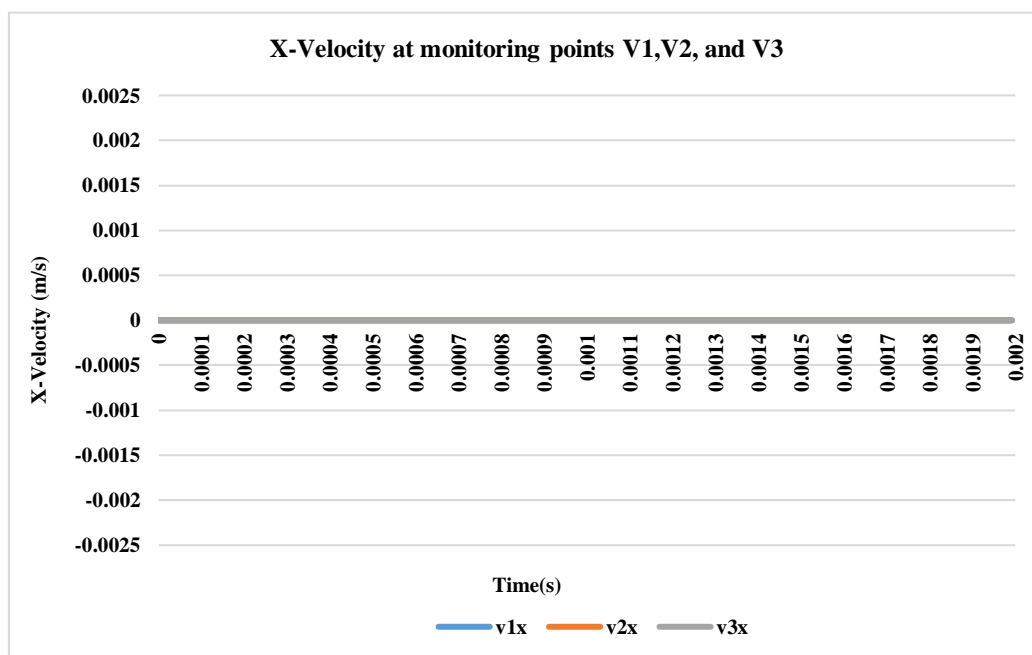
$v_s$  = input particle velocity.

This equation indicates that the applied stress in a material due to a wave is directly proportional to the density of the material, the speed of the wave, and the particle velocity.

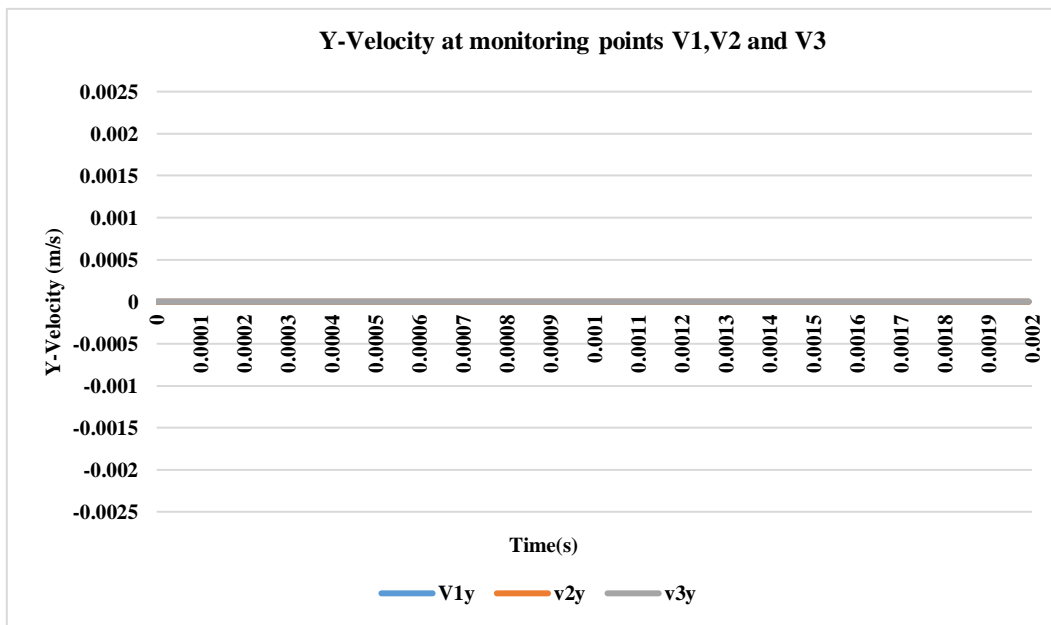
#### 3.4.2.1 Velocity history for homogenous model (model 1)

Figure 3.13, Figure 3.14, and Figure 3.15 show the velocity history at all three monitoring points along the X, Y, and Z directions, respectively. All three stations recorded identical velocities along the Z direction, as was expected of a homogeneous media (Figure 3.15). The maximum amplitude of the velocities recorded in the Z direction is double (0.002 m/s) the input maximum amplitude (0.001 m/s). This was expected and reflects the free surface effect (on the surface, both up going and the down going reflected waves are exactly in phase and the resultant amplitude is doubled). Because I had applied a quiet (viscous) boundary at the bottom of the model, no reflections from the free surface that reach the bottom are reflected and as such, the velocity at the monitoring points returns to zero, following the input waveform of the source.

Along the X and Y directions, no velocities were recorded at monitoring point V1 (the very small amplitudes of the order of  $10^{-18}$  m/sec shown in Figure 3.13 and Figure 3.14 are due to numerical effects). The absence of significant velocities in the X and Y directions is the result of destructive interference between waves due to the signal being emitted from the full bottom surface of the model, creating what could be explained as multiple sources of the same frequency that create concentric waves. This simple model verified the choice of boundary conditions, which are then adopted for the subsequent models.



**Figure 3.13:** Velocity history in X-direction at monitoring stations V1, V2 and V3



**Figure 3.14:** Velocity history in Y-direction at monitoring stations V1, V2 and V3

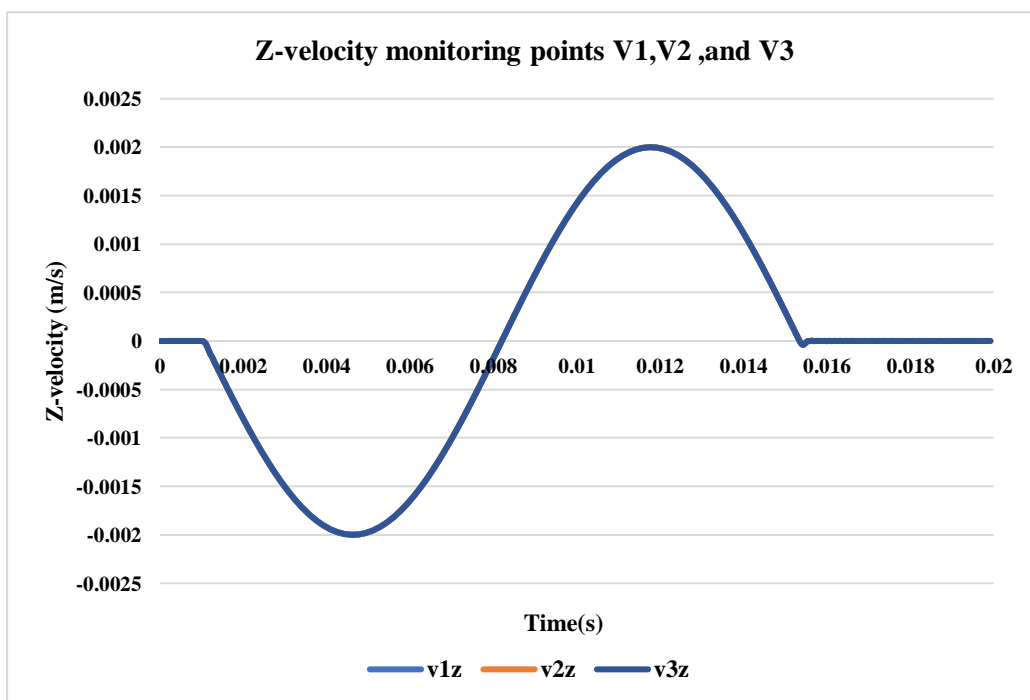


**Figure 3.15:** Velocity history in Z-direction at monitoring stations V1, V2 and V3.

### 3.4.3 Model 2 – Brownfield soil (lower threshold for seismic velocity range)

This model was built differently from the model 1 in terms of dimensions and mechanical properties. In this model, 25 monitoring stations were deployed on the surface of the model, with the distance between them was 2m in all directions. It was designed in this way to record the reflected seismic waves at different locations on the surface of the model, so that the paths and reflections of the seismic waves could be tracked and to understand the impact of objects on the properties of seismic waves. Figure 3.16 below shows the monitoring points on the model surface. Two sites were designed A and B with the monitoring points at site A are positioned within less than 30m from the seismic source, whereas at site B, the monitoring points are situated more than 30m away from the seismic source (this discussed in more detail in chapter 4). In this figure, only site A is shown.

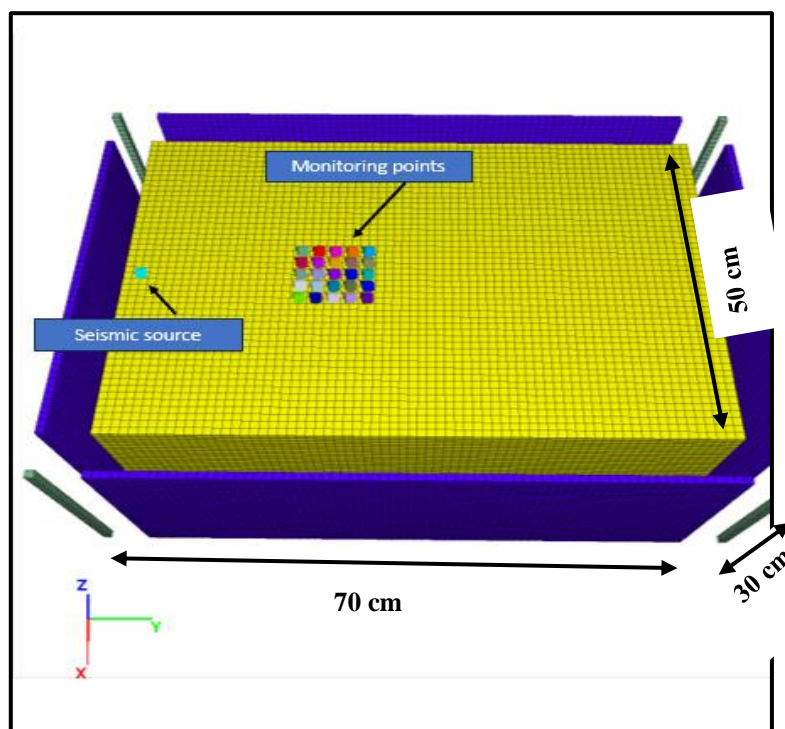


**Figure 3.16:** model dimensions and monitoring stations on the model surface

The calculations made during the passage of the seismic waves into the model were based on the values of mechanical properties in the table 3.1. These values are comparable to values in brownfields soil (Volpini, Douglas and Nielsen, 2021). Based on the following equations, the shear and primary velocity is equal to:

$$V_s = \sqrt{\frac{2 \times 10^8}{2000}}$$

$$V_S = 316 \text{ m/sec}$$

$$V_P = \sqrt{\frac{(4.4 \times 10^8 + \frac{4}{3} \times 2 \times 10^8)}{2000}}$$

$$V_P = 594 \text{ m/sec}$$

the wavelength can be calculated from the equation below:

$$\lambda = \frac{V_s}{f} = \frac{316}{20} \approx 16 \text{ m}$$

To pass seismic waves without interference or distortion through this model, the size of the element must verify the numerical model equation 3.18 (Abbasi et al., 2013):

$$\Delta l \leq \frac{\lambda}{10}$$

$$\Delta l \leq 1.58 \text{ (element size for model 1 m in X Y Z direction)}$$

#### 3.4.4 Model 3– Brownfield soil (upper threshold for seismic velocity range)

This model was built with the same dimensions as Model 2, with a difference in the mechanical properties of the model and the properties of the seismic wave source. Because the mechanical properties of the soil found in brownfields change from one site to another. For this reason, I changed these mechanical properties to cover possible changes in the soil, which led to an increase in the velocity of the seismic waves, and a source of seismic waves with a higher frequency than the second model. The geometry and monitoring points of the current model are identical to those of the preceding one, maintaining structural and spatial consistency.

Based on the mechanical property values in the table 3.1, calculations were done as seismic waves propagate within the model. These values are comparable to those found in soil from brownfields. Based on the following equations, the shear and primary velocity is equal to:

$$V_S = \sqrt{\frac{1.42 \times 10^9}{2100}}, V_S = 822.31 \text{ m/sec}$$

$$V_P = \sqrt{\frac{(2.5 \times 10^9 + \frac{4}{3} \times 1.42 \times 10^9)}{2100}}, V_P = 1446.4 \text{ m/sec}$$

the wavelength can be calculated from the equation below:

$$\lambda = \frac{V_s}{f} = \frac{822.3}{50} \approx 17 \text{ m}$$

To pass seismic waves without interference or distortion through this model, the size of the element must verify the numerical model equation (Abbasi et al., 2013):

$$\Delta l \leq \frac{\lambda}{10}$$

$\Delta l \leq 1.65 \text{ m}$  ( element size for model 3 1m in X Y Z direction)

### 3.4.5 Model 4 – Brownfield soil (end threshold for seismic velocity range)

This model's mechanical characteristics closely resemble those of sandstone, which is unusual in brownfield settings. However, this model's development was done primarily to address scenarios in which brownfields have very compacted soil compositions. The mechanical characteristics of this model and the origin of the seismic waves that were applied to it are different from the previous model. The geometry of the model remains the same. I consider it the worst scenario in simulating seismic waves in brownfield sites because most brownfields have mechanical properties of soil that is not solid.

Calculations were made based on the mechanical property values listed in the table 3.1 to simulate the propagation of seismic waves. The mechanical properties listed in the same table are comparable to the soil of strong rock and have a higher hardness than the properties of the soil that were simulated in the previous two models. In accordance with the equations provided, the values for shear velocity and primary velocity are equivalent to:

$$V_s = \sqrt{\frac{7 \times 10^9}{2000}}, V_s = 1738 \text{ m/sec}$$

$$V_p = \sqrt{\frac{(20.8 \times 10^9 + \frac{4}{3} \times 7 \times 10^9)}{2000}} \quad V_p = 3881 \text{ m/sec}$$

the wavelength can be calculated from the equation below:

$$\lambda = \frac{V_s}{f} = \frac{1738}{70} \approx 24.8 \text{ m}$$

The size of the element must validate the numerical model equation for seismic waves to travel through this model without interference or distortion (Abbasi et al., 2013)

$$\Delta l \leq \frac{\lambda}{10}$$

$\Delta l \leq 2.48\text{m}$  ( element size for model 4 1m in x y z)

### 3.5 Analysis of seismic velocity data

I tackled this research from two separate angles: the frequency domain and the time domain.

#### 3.5.1 Time-Domain Seismic Analysis: Understanding Wave Interactions and Attenuation

Understanding seismic wave behaviour and energy distribution in time-domain analysis of seismic waves depends on the study of wave properties changed by the presence of objects or geological features (Cui *et al.*, 2021). The amplitude of seismic waves, which directly reflects the seismic energy recorded by seismometers, was analysed. The amplitude offers understanding the energy of the seismic waves (Poppeliers and Mallinson, 2015).

Seismic wave amplitude is influenced by several factors:

**Medium Properties:** Depending on the density, elasticity, and other physical characteristics of the geological materials, seismic waves' amplitude could increase or decrease as they pass through them (Lu and Wang, 2010).

**Attenuation:** A process known as attenuation occurs when seismic waves are absorbed by the Earth's medium and lose energy as a result. The amplitude gradually decreases with increasing distance from the source as a consequence of this energy loss. The characteristics of the materials that waves pass through affect the rate of attenuation (Liu *et al.*, 2022).

**Scattering:** When seismic waves contact heterogeneities such as cracks, cavities, or variable material qualities inside the Earth, they disperse in various directions. Scattering redistributes wave energy, usually diminishing the amplitude of the direct wave (Yomogida and Benites, 2002).

#### 3.5.2 Spectral Analysis of Seismic Waves

Spectral analysis refers to analysis in the frequency domain (Pesaran, 2008). One approach to achieve this objective is the conversion of data from the time domain to the frequency domain is using either the Fourier transform or Welch's method. For seismic wave analysis, where signals are often noisy and non-stationary, Welch's method is preferred due to its robustness

and capability to provide a more stable spectral estimate (Szymko *et al.*, 2021). The Power Spectral Density (PSD) estimation method, particularly when applied to Welch's method. PSD estimation helps to understand the distribution of power or energy within a signal across various frequency components, uncovering patterns and trends within time series data and identifying dominant frequencies that may hold critical information (Solomon, 1991).

Utilizing the Welch method, the "welch" equation can be used to calculate a signal's power spectral density (PSD). To get a more accurate estimation of the signal's frequency content using this method, the signal is divided into overlapping segments, the periodograms of each segment are calculated, and the resulting periodograms are then averaged (N. Robertson, 2019). the best representation of seismic waves spectrum by using PSD which illustrates the power measurements contact vs frequency (Same *et al.*, 2021).

Mathematically, the PSD  $S_{xx}(f)$  can be expressed as:

$$S_{xx}(f) = \frac{1}{L} \sum_{m=0}^{L-1} \frac{1}{U} \left| \sum_{n=0}^{N-1} w(n) x_m(n) e^{-j2\pi f n/N} \right|^2 \quad \text{Eq 3.20}$$

$x(n)$  is the  $m$ -th segment of the signal  $x(n)$

$w(n)$  is the window function applied to each segment.

$N$  is the length of each segment.

$L$  is the number of segments.

$U$  is a normalization factor, typically the sum of the squares of the window function  $w(n)$ , i.e.,

$$U = \sum_{n=0}^{N-1} w^2(n). \quad \text{Eq 3.21}$$

The signal  $x(n)$  is divided into  $L$  overlapping segments.

Each segment  $x_m(n)$  is windowed with the window function  $w(n)$ .

The Discrete Fourier Transform (DFT) is computed for each windowed segment.

The magnitude squared of each DFT is computed to obtain the periodogram.

The periodograms are then averaged to produce the final PSD estimate.

In MATLAB, this process has an in-built function, Pwelch.

$$[P_{xx}, f] = \text{pwelch}(x, \text{window}, \text{overlap}, \text{nfft}, \text{fs}). \quad \text{Eq 3.22}$$

The input arguments are:

**x:** Input signal vector

**window:** Window vector of length

**overlap:** Number of overlapped samples (used for DFT averaging)

**nfft:** Number of points in DFT

**fs:** Sample frequency in Hz (N. Robertson, 2019).

**The window length** refers to the number of data points or samples evaluated in each signal segment during transformation. It effectively specifies the length of each section. A small window collects finer details but has lower frequency resolution, whereas a longer window captures broader characteristics with higher frequency resolution (Saini & Mehra, 2015). In this research study, the selection of the window length was determined by the specific characteristics of the seismic signals. Given that seismic signals are known for their rapid changes, I opted for a smaller number of windows. These windows were then applied to all velocities histories of seismic data that recorded from mode2, model 3, and model 4.

**Overlap:** Overlap is the number of data points shared by each window segment with the neighbouring segments. It is commonly represented as a percentage of the length of the window. Overlapping windows help to prevent information loss at segment edges. In this study, an overlap value of 50% was used, which may increase or decrease slightly. It was applied to the data obtained from Models 2,3,and 4 (Kisohara *et al.*, 2020).

**Nfft (Number of Points in the Fast Fourier Transform):** It's often set equal to or greater than the window length N. Increasing nfft can provide finer frequency resolution in the output, but it also increases computational complexity (Schmischke, 2010). Common practice is to set nfft equal to N when using the Discrete Fourier Transform (DFT) or its fast implementation. In this study the nfft value is bigger than window length. Using a larger nfft compared to the

window length will result in better frequency resolution in the resulting power spectral density (PSD) estimate. (Cerna & Harvey, 2000). This means I can distinguish between closely spaced frequency components more accurately.

**Sampling frequency:** Sampling frequency, measured in (Hz), represents the number of samples taken per second from the continuous analogue signal. Sampling frequency in all MATLAB analysis was calculated from each velocity history based on number samples (Mutagi, 2014).

### 3.6 Validation and verification of numerical models (Step 4)

For several convincing reasons, conducting a field study is an essential component of my research. For starters, a field study enables for direct observation and data collecting in real-world settings. Going into the field allows me to immerse myself in the exact conditions I want to research. The major goal of the series of experiments undertaken in the Stepps area is to validate and corroborate the results gained from prior seismic wave models. Extensive investigations were carried out throughout these simulations to determine the fundamental features of seismic waves in the objects. Furthermore, the simulations sought to investigate how the existence of buried objects alters these properties.

Field studies are essential for validating theoretical models and hypotheses generated in controlled environments. When I obtained the results from the process of simulating seismic waves using FLAC<sup>3D</sup> software, it was necessary to go to the field and conduct some experiments for some reasons:

**Validation:** Field experiments provide an opportunity to validate the results obtained from simulations. Simulations are based on mathematical models that may have simplifications and assumptions. Field data allow me to confirm the accuracy of these models and adjust any parameters if needed.

**Confirmation of Experiment:** Field experiments offer a means to confirm whether the characteristics of seismic waves observed in simulations aligns with field experiment results. It's crucial to ensure that the simulation results accurately represent what occurs in the field.

**Data Verification:** Field experiments provide independent data that can be used to verify the accuracy of the simulated data. This verification is essential for building confidence in the simulation results and ensuring that they are reliable for further analysis.

More detailed on the field study are provided in chapter 5.

## Chapter 4 : Numerical simulation of seismic waves propagation through media

### 4.1 Introduction

The objective of this chapter is to investigate the changes in the characteristics of seismic waves when encountering buried objects in the ground and determine if these changes can be utilized to identify the characteristics of such objects. Three numerical models are presented. The models are referred to as model 2, model 3, and model 4, each having distinct mechanical properties. The knowledge obtained from these simulations would inform survey strategy.

### 4.2 Models set up

Three homogenous models the same dimensions and same element size were built (see Table 3.1). The only difference between them is only in the mechanical properties. The mechanical properties of these models were chosen to match the mechanical properties of soils in brown field areas (as shown in Table 3.1). Later on, an object, i.e., grid elements with different mechanical properties assigned compared to the rest elements of the models, was added. The dimensions of this object were 1 m long in the X– direction, 1 m wide in the Y-direction, and 1 m high in the Z – direction, with its mechanical properties shown in table 4.1.

**Table 4.1** Mechanical properties of steel material which represents the buried object .

Steel	Shear modulus Pa	Bulk modulus Pa	Density kg/m <sup>3</sup>
	$25 \times 10^{10}$	$40 \times 10^{10}$	7700

All three models were subjected to a seismic wave simulated by a sine wave. The sine wave had a different frequency for each model, chosen to ensure stability in the numerical simulation and be compatible to the chosen wave velocity. The wave was applied as a single seismic source, using two elements along the X direction and two elements along the Y direction on the model surface. The sinusoidal waves had the same amplitude of 1m and were sampled at a rate of 1000 Hz for all three models.

A total of 25 monitoring stations were deployed across each of the three models' surface. They were placed at a 2m spacing in both horizontal directions in a grid geometry of 5 stations over 5 rows. This spacing ensures that the stations are close enough to accurately detect variations in seismic wave behaviour, while also covering a large enough area for comprehensive data collection.

Two specific locations on the model surface, referred to as Site A and Site B (figure 4.1), were

**Site A** encompasses an area where all 25 monitoring stations are deployed within a 30-meter radius of the seismic source. This means that the monitoring stations at Site A are relatively close to the seismic source.

**Site B**, is an area where all 25 monitoring stations are positioned at distances greater than 30 meters from the seismic source. These monitoring stations at Site B are comparatively farther away from the source of seismic waves. Increasing the distance to more than 30 meters was to track the path of propagation and reflection of seismic waves.

The choice of the two sites was based on expectations that there would be a change in the paths of the seismic waves, but the change was also related to the depth of the object, the frequency of the source of the seismic waves, and the mechanical properties of the medium.

Out of the total 25 monitoring stations deployed on the model surface, I have selected 15 monitoring stations for analysis. The monitoring stations are symmetrical with regards to the source of the seismic waves, that's why only one side was considered for further analysis.

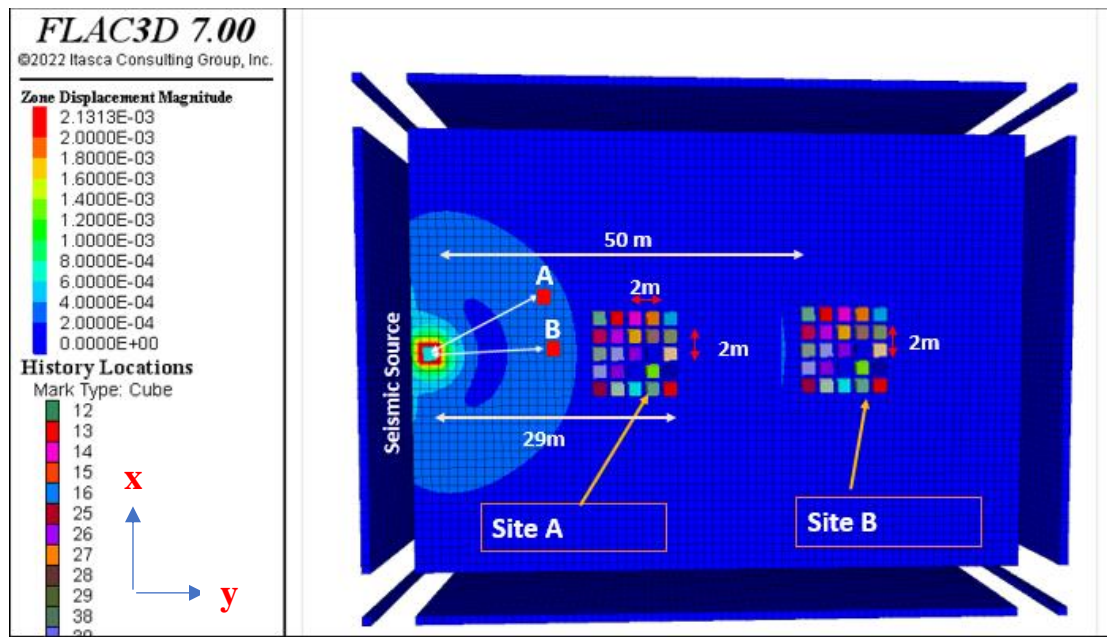


**Figure 4.1:** Site A and B locations on the model. The distances between the monitoring stations are 2m s in both horizontal directions with the monitoring points placed on the surface.

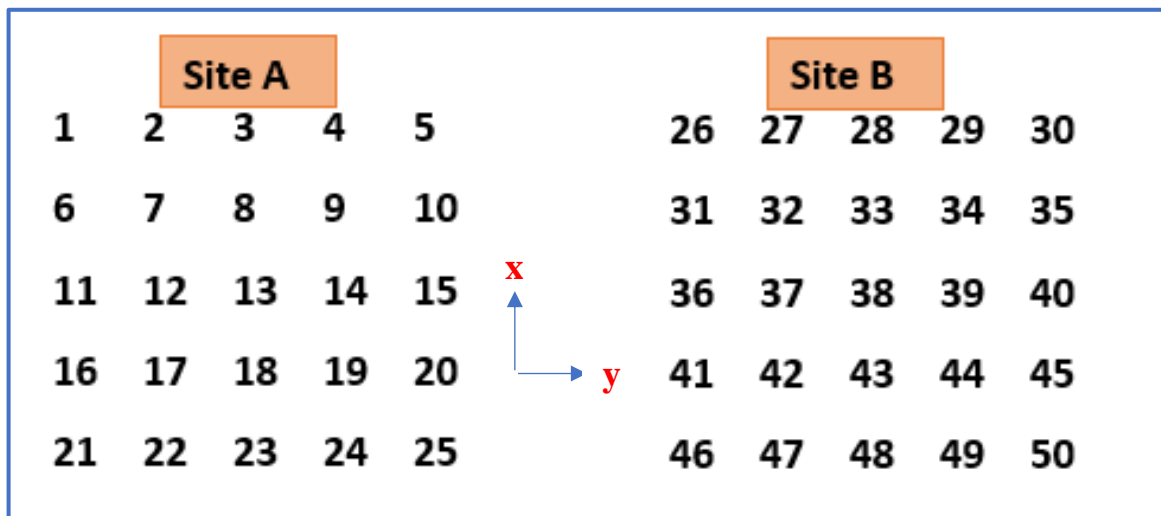


**Figure 4.2:** Numbering of the monitoring stations at site A and site B on the model’s surface.

### 4.3 Model 2

#### 4.3.1 Material properties

The table below shows the material properties of the homogenous model (no buried object).

Table 4.2 : Input material properties for model 2.

Soil 1	Shear modulus	Bulk modulus	Density	Shear velocity (m/s)	Primary velocity (m/s)
	$2 \times 10^8$ Pa	$4.4 \times 10^8$ Pa	$2000 \text{ kg/m}^3$	316	594

4.3.2 Dynamic input:

Figure 4.3 shows the seismic source input for model 2. A sine wave with a frequency of 20 Hz and an amplitude of 1 m/s, applied on the surface of the model along the Z direction. The sinusoidal wave was sampled at 1000 Hz.

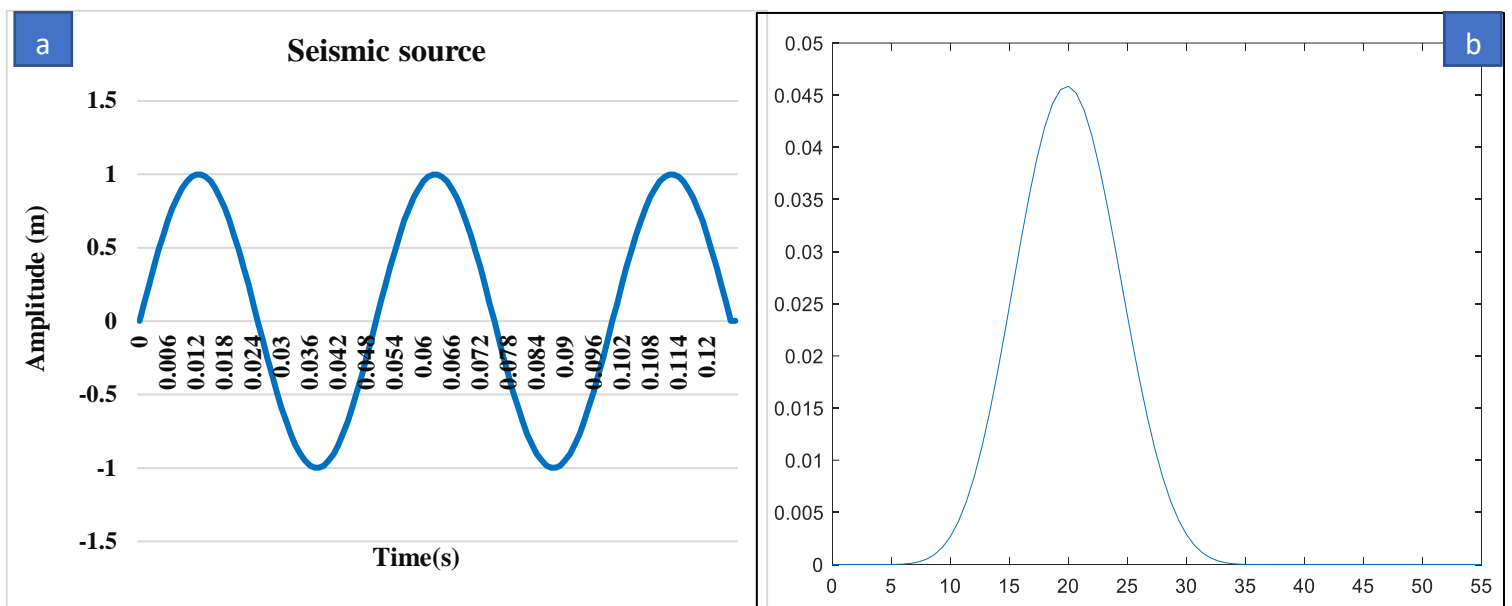


Figure 4.3: a) The sinusoidal wave dynamic source applied to model 2 in along Z-direction, b) PSD of seismic source.

Figure 4.3a shows a 20 Hz seismic source, while 4.3b shows the PSD, indicating no frequency change between recordings in homogeneous model and the model with the object.

Table 4.3: Shows the parameters used for eq 3.22 for model 2.

	Window length	Overlap %	Nfft	fs
Homogenous model	30	20	1500	208

---

<b>Model with buried object</b>	300	100	1500	3918.6
---------------------------------	-----	-----	------	--------

---

In this case the surface of the object is at 1m depth from the surface. The mechanical properties of the object were given in table 3.1. All other setup is exactly the same as for the homogenous model.

#### **4.3.3 Results for site A.**

Homogenous model: The power spectral density (PSD) of these waves and frequencies was analysed as described in chapter 3. Results show that the amplitude of the seismic wave is higher at stations closer to the source. As the distance from the seismic source increases, the amplitude of seismic waves decreases, demonstrating attenuation (figure 4.4 and 4.5). This reduction is observed both in the time and frequency domains. This overall attenuation reflects the spectral properties of seismic waves at site A. For the full velocity histories and PSD plots for all 15 points (see figure 4.4,4.5 ,4.6).

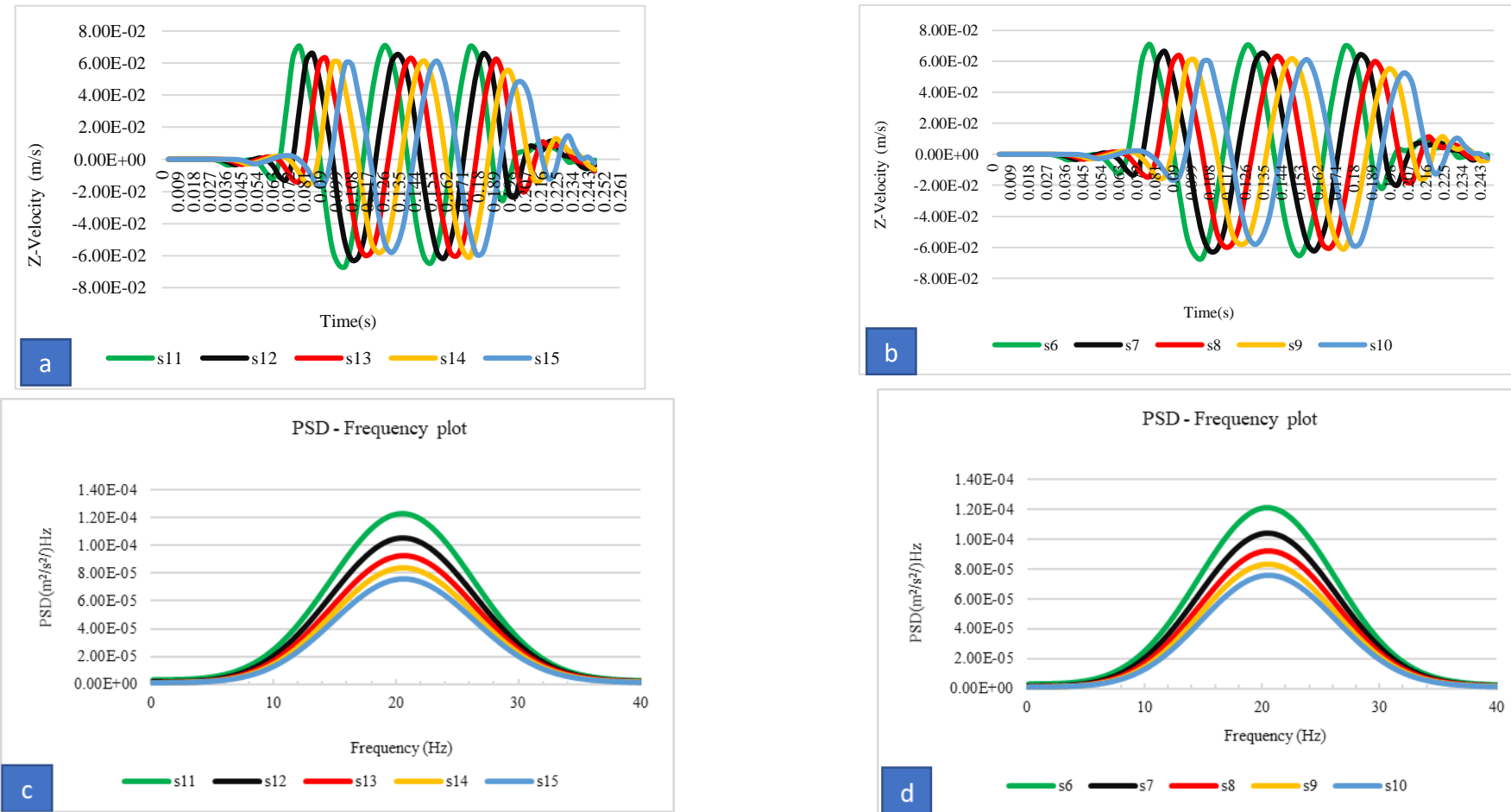


**Figure 4.4:** Homogenous model: Velocity history at stations: 11–15, 11, (b) 6 – 10. The stations closest to the source, has the largest wave amplitudes. Also shown are the PSDs for stations (c) 11 – 15 and (d) 6 – 10 .

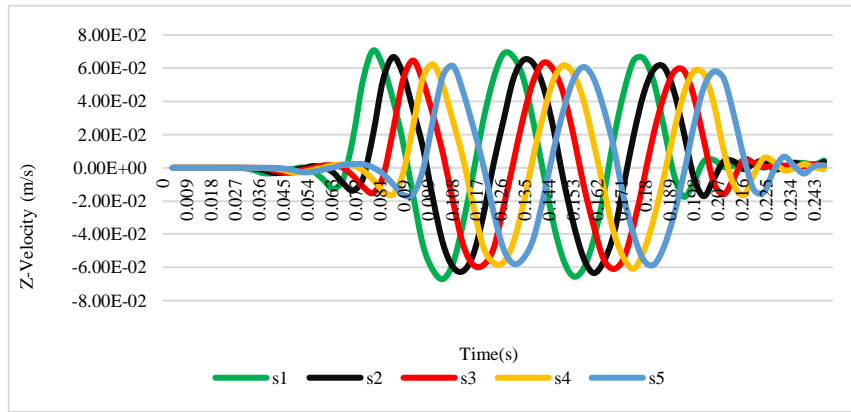


**Figure 4.5:** Velocity history recorded at monitoring stations s1, s2, s3, s4, and s5 from the homogenous model.

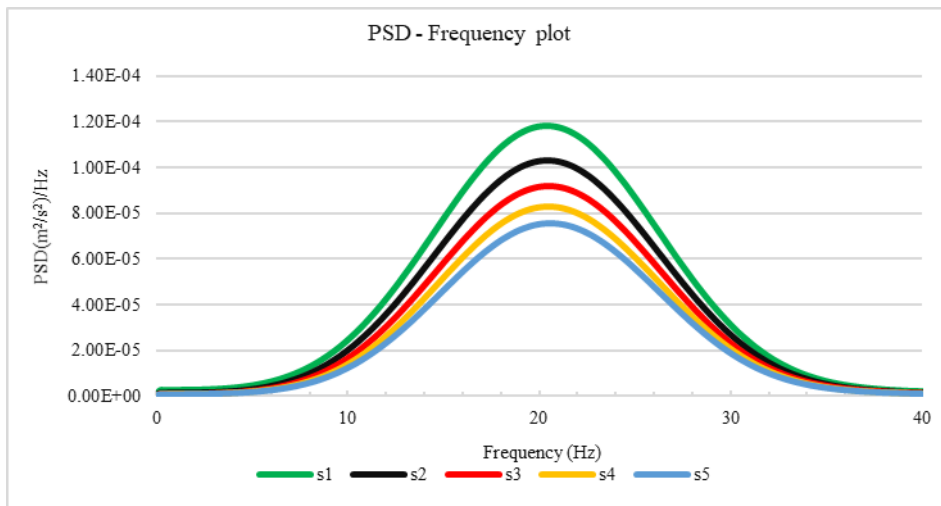


**Figure 4.6:** PSD of the velocity history recorded at monitoring stations s1, s2, s3, s4, and s5 in the homogeneous model.

#### 4.3.4 Model 2 with buried object

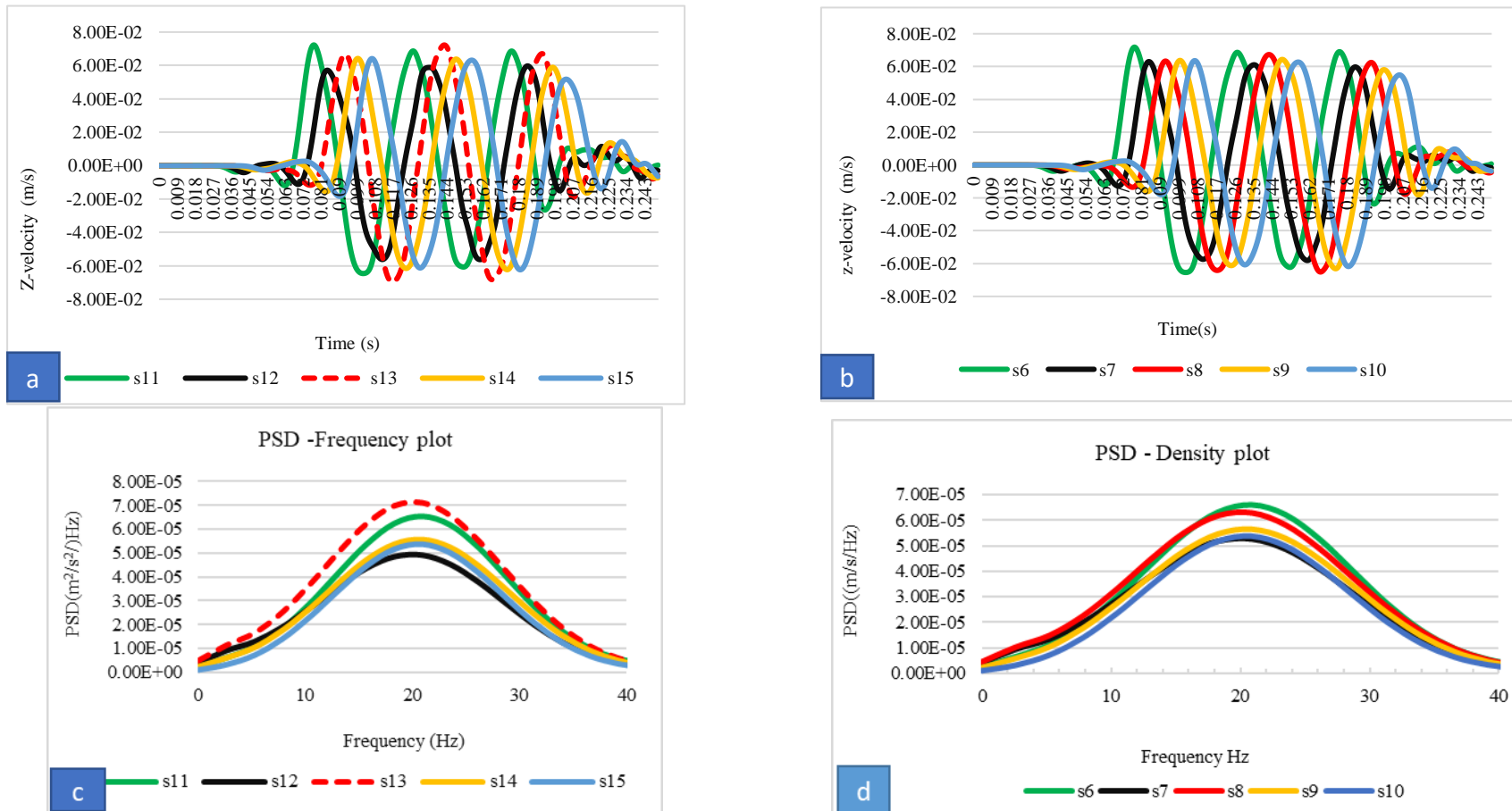
##### I. First scenario: The object at 1m depth

Figure 4.7 – 4.9 show the results of the analysis for model 2 with a buried object at depth of 1m. As for the homogenous model, stations 1, 6 and 11 exhibit the highest amplitude (fig 4.7 a, b and 4.8) which is expected as they are the closest to the source. In contrast to the homogenous model, in the present case the station with the second highest amplitude is station 13, located directly above the object (fig 4.7 a) is interpreting to note that the amplitude of troughs is higher (in absolute terms) to that of station 11. This indicates that the largest amount of seismic energy was detected at this location. The primary reason for this high amplitude is the small angle of incidence and reflection at this station, which results in most of the seismic energy being reflected back to s13. Consequently, this station recorded not only the highest amplitude but also the highest power spectral density (PSD) of the seismic waves, this is evident in the frequency vs. PSD plot. further confirming the presence of the object directly underneath (see figure 4.7c).

In the analysis of the velocity history of seismic waves recorded at the monitoring stations s1, s6, and s11 recorded the highest because they are closest to the source of the seismic waves. Regards to monitoring stations s6, s7, s8, s9, and s10, station 8, located next to object, recorded a higher wave amplitude among its line of stations (figure 4.7 b). This suggests that a significant amount of seismic energy was detected at station s8. The presence of the nearby object influenced the behaviour of the seismic waves, causing an increase in wave amplitude (in time domain) (detailed in chapter 3, section 3.1.3). This is also reflected in the higher PSD values recorded at station s8, indicating that the object had impact on the propagation and energy distribution of the seismic waves in its vicinity.

For monitoring stations s1, s2, s3, s4, and s5, located approximately 4 m or more away from station 13, the influence of the object was less pronounced, if not insignificant. However, the seismic waves that recorded at s3 showed some alterations in wave propagation characteristics, indicating a minor yet detectable impact of the object compared to s1, s2, s4, and s5.

The maximum power spectral density amplitude recorded at station 13 which located above the steel object is  $7.12E-05$  ( $m^2/s^2$ ) /Hz (see fig 4.7).



**Figure 4.7:** a) Model 2 with buried object at 1m depth. Velocity histories at stations 11–15 show Station 13 with the largest wave amplitude, indicating higher seismic energy due to the buried object b) Station 8, influenced by the nearby object, had the highest wave amplitude among stations 7–10. c) Station 13, directly above the object exhibits the highest PSD value. d) Station 8 had a higher PSD peak value than the other three stations (s7, s9, s10) due to the nearby object. S6 has a high PSD because it's the closest station to source amongst all stations along the line s6 – s10.

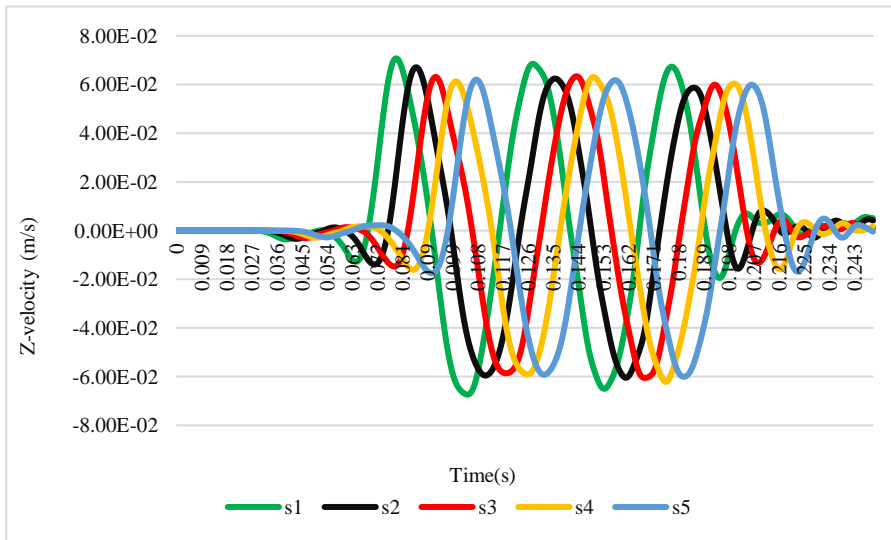


**Figure 4.8:** Model 2 with buried object at 1m depth. Velocity history recorded at monitoring stations s1, s2, s3, s4, and s5.

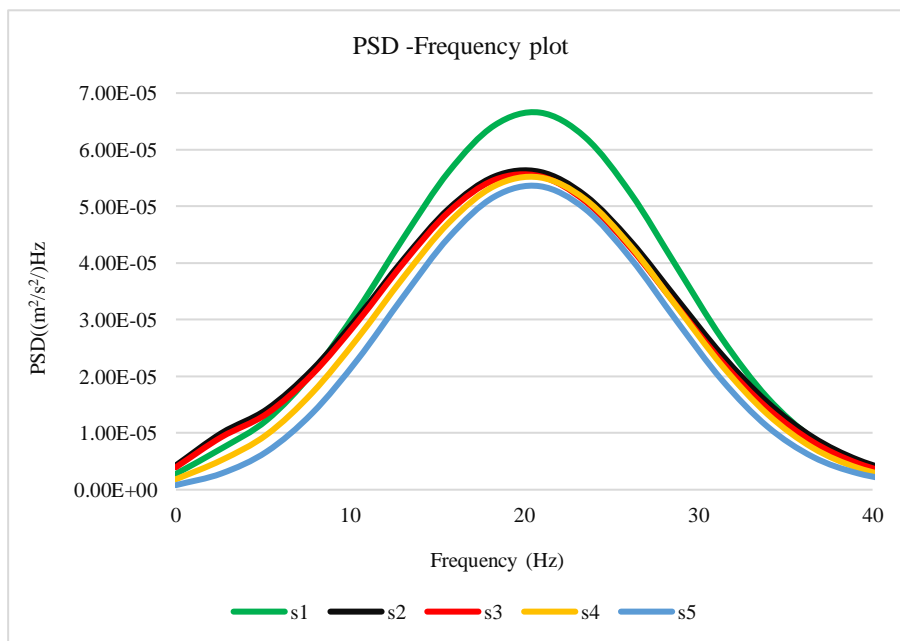


**Figure 4.9:** Model 2 with buried object at 1m depth .PSD of the velocity history at monitoring stations s1, s2, s3, s4, and s5

**II. Second scenario: The object at 2m depth**

The depth of the object increased to 2m from the model surface to the top of the object. Monitoring station No. s13, directly above the object, exhibits the highest amplitude, whether in the time or frequency domain.

Similarly, monitoring station No. s8, located 2m away from the source, showed a higher wave amplitude than nearby stations, suggesting stronger energy reflection at this point.

The power spectral density (PSD) at station No. s13 was the highest among the monitored stations, confirming that the object at 2m depth still influenced seismic wave characteristics. This observation was consistent at other stations, like s8, showing higher amplitudes and PSD values, indicating that objects at this depth impact seismic wave properties at nearby stations. The maximum PSD amplitude recorded at station 13 decreased from  $7.12\text{E-}05$  ( $\text{m}^2/\text{s}^2$ )/ Hz when the object was at a depth of 1m to  $6.82\text{E-}05$  ( $\text{m}^2/\text{s}^2$ )/ Hz when the object depth increased to 2m, representing a decrease of approximately 4.21%. (see figure 4.10).

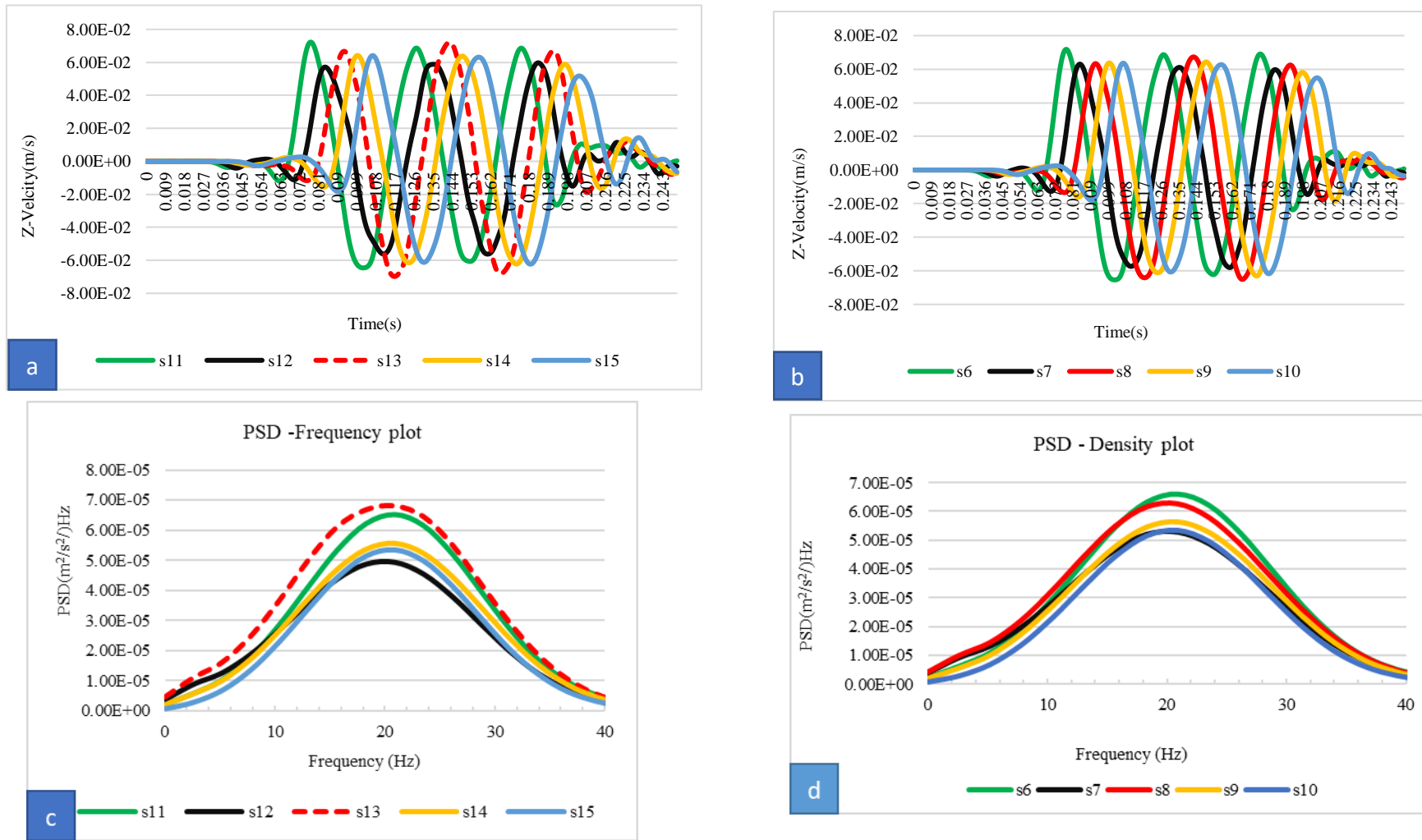


**Figure 4.10:** a) Model 2 with buried object at 2m depth. Velocity history comparison at stations 11–15 shows Station 13, directly above the object, with the highest wave amplitude b) Station 8, 2 meters away, has a higher wave amplitude than stations 7, 9, and 10, reflecting the largest energy amount c) The highest PSD value was recorded at Station 13 d) Station 8 recorded a higher PSD than stations 7, 9, and 10 due to the nearby object.

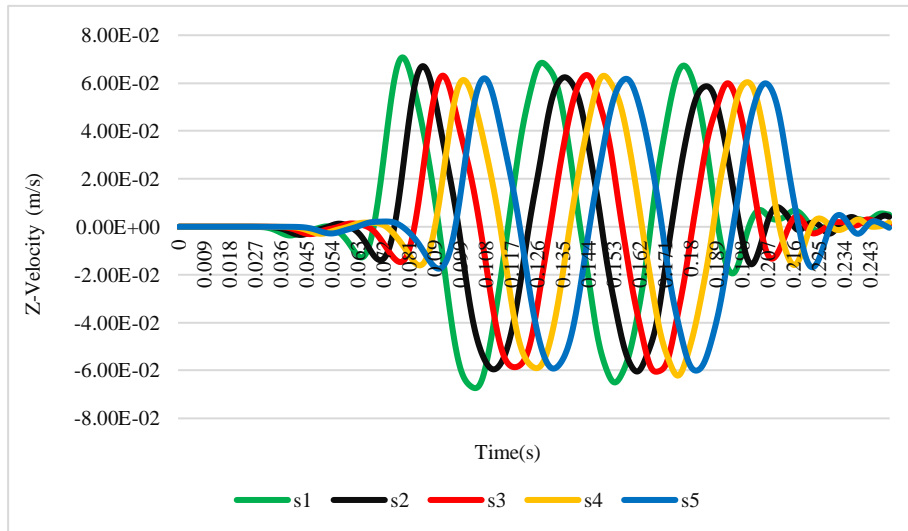


**Figure 4.11:** Model 2 with buried object at 2m depth. Velocity history recorded at monitoring stations s1, s2, s3, s4, and s5 from the homogenous model.

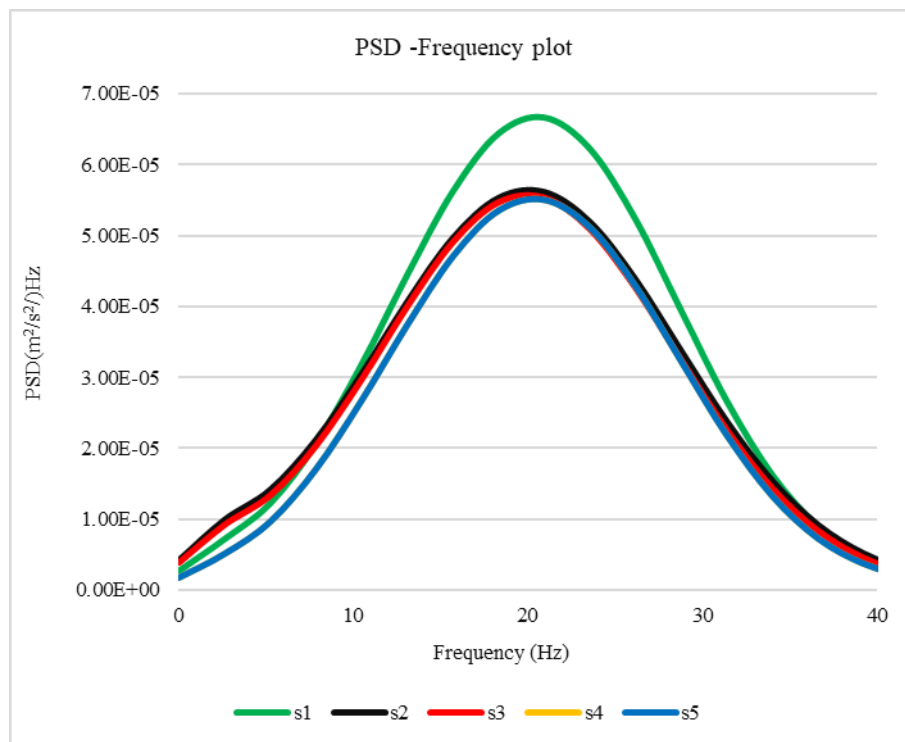


**Figure 4.12:** Model 2 with buried object at 2m depth .PSD of the velocity history recorded at monitoring stations s1, s2, s3, s4, and s5

**III. Third scenario: The object at 3m at depth**

To investigate the impact on seismic wave propagation, the depth of the object was increased to 3 m. Monitoring stations s11, s12, s13, s14, and s15 recorded velocities, with station No. s13, directly above the object, showing distinct seismic wave characteristics due to reflection alterations. Similarly, station No. s8, near the object, experienced significant changes in wave behaviour compared to other stations (figure 4.13).

At station No. s3, located 4m from the object, there were minor variations in recorded velocities and power spectral density (PSD), indicating a subtle influence from the object. Overall, the object's presence at a depth of 3m continues to affect seismic wave propagation and energy distribution.

The power spectral density amplitude of seismic waves recorded at station No. s13, directly above the object, decreased from  $7.12E-05$  to  $5.79E-05(m^2/s^2)/Hz$ , representing a decrease of approximately 18.69%. This means that the seismic energy recorded at the surface of the model decreased as the depth of the object increased. (see figure 4.13).

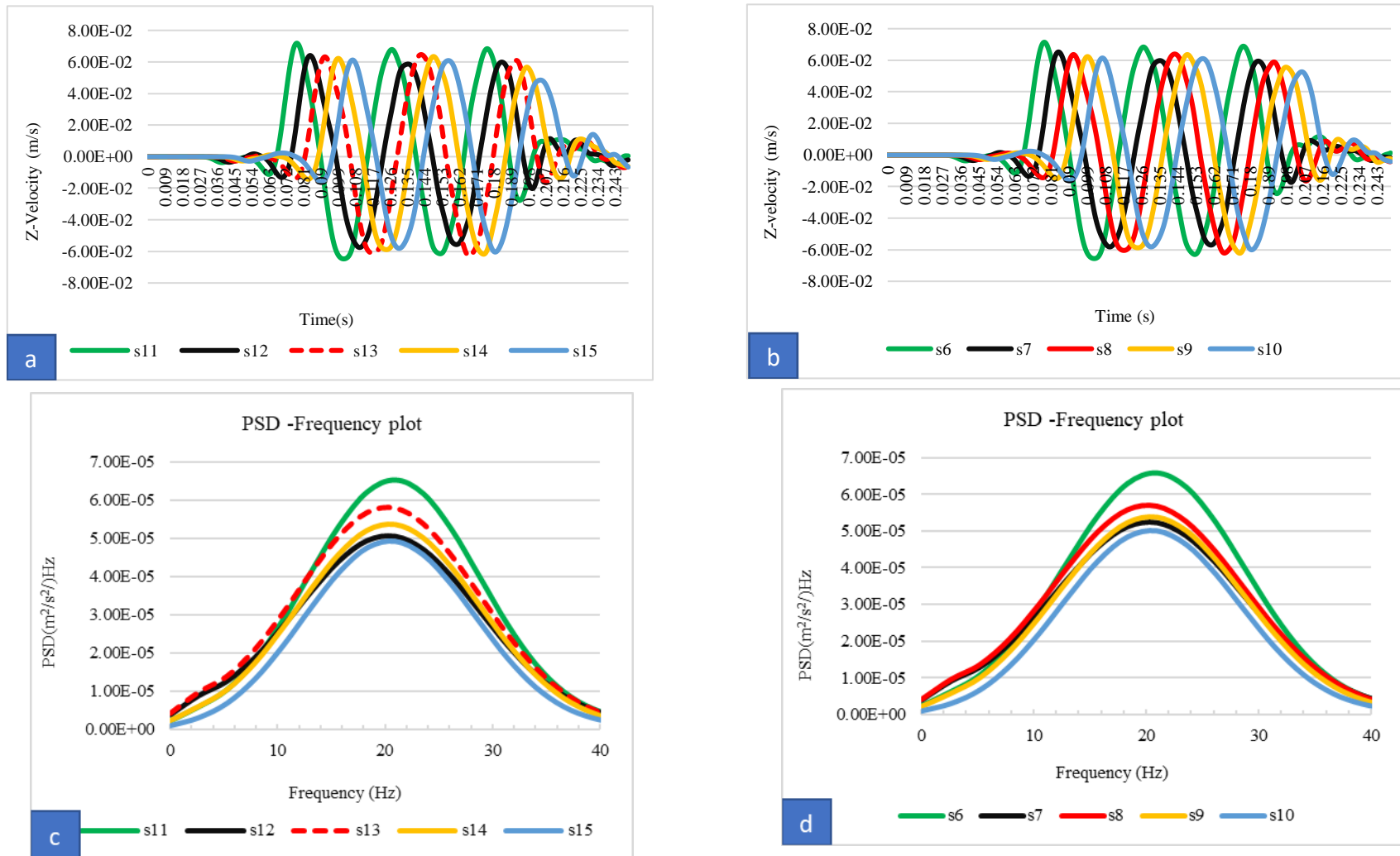


**Figure 4.13:** a) Model 2 with buried object at 3m depth .Velocity histories at stations 11–15 show Station 13, directly above the object, still affected by its presence b) Station 8, 2 meters away, has a larger wave amplitude than stations 7, 9, and 10, detecting the object at this distance c) The highest PSD value was recorded at Station 13.d) Station 8 recorded a higher PSD than other stations due to the nearby object.

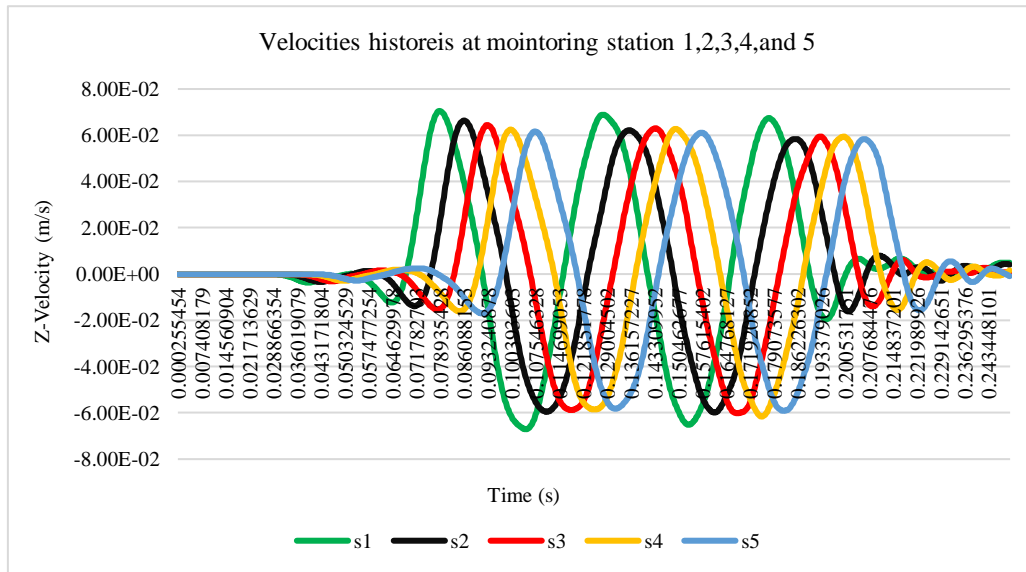


**Figure 4.14:** Velocity history recorded at monitoring stations s1, s2, s3, s4, and s5 from the homogenous model.

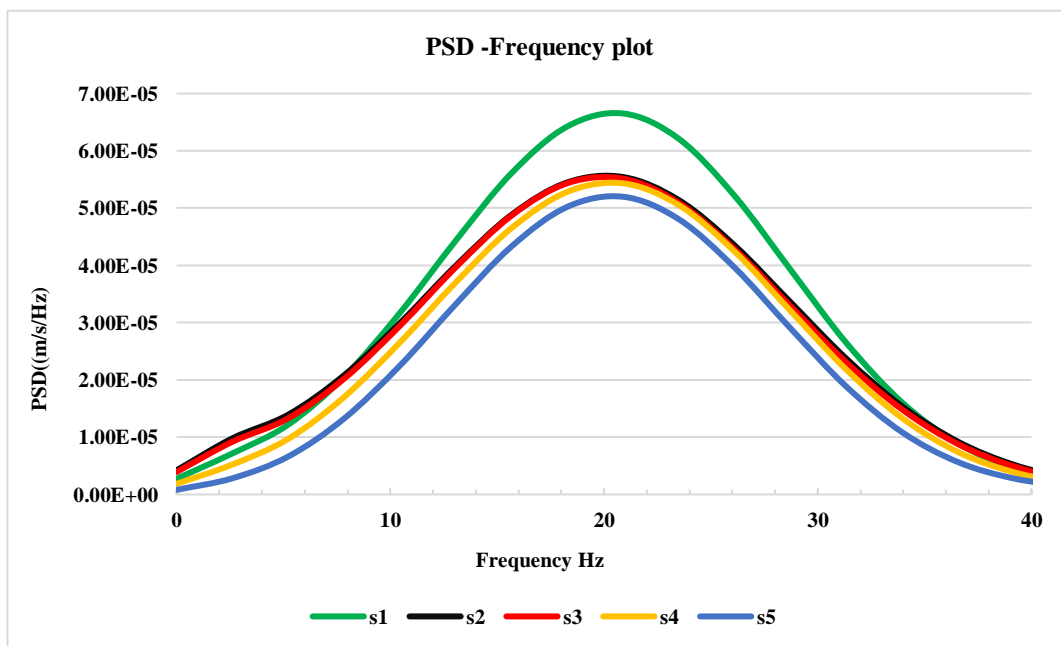


**Figure 4.15:** PSD of the velocity history recorded at monitoring stations s1, s2, s3, s4, and s5

#### 4.3.5 Wave Propagation in Homogeneous and Heterogeneous Media: Travel Time, Amplitude, and Frequency Alterations

The results of the homogeneous model demonstrated that seismic waves propagated uniformly through the subsurface, with monitoring stations recording consistent velocity histories and predictable attenuation of amplitudes as distance from the source increased. Power Spectral Density (PSD) analysis confirmed uniform energy distribution, indicating the absence of subsurface anomalies. When a buried object was introduced into the model, significant changes in wave propagation were observed; amplified seismic wave amplitudes and concentrated energy at the monitoring stations positioned directly above or within 2-4 meters of the object.

For the homogeneous model, this time is consistent across all stations and reflects the uniformity of the medium. When an object is introduced, the reflected wave behaves differently based on the material properties, depth of the object. Upon reaching the buried object, part of the seismic wave reflects back toward the surface while the rest continues to propagate. The reflected wave manifests itself as an increased amplitude of the recorded seismic wave at the surface at monitoring stations positioned directly above or near the object due to the acoustic impedance contrast between the object and the surrounding material.

**Figure 4.16** This figure shows the seismic wave travel path in a homogeneous medium. The seismic waves are depicted traveling directly from the source to station No. s13, arriving at approximately 0.089 seconds. The time it takes for the waves to travel through the homogeneous medium is represented by the straight-line path, indicating the faster arrival.

**Figure 4.17** illustrates the seismic wave travel path in a model with the target. The waves travel towards the object, reflect off it, and then continue to station No. s13, resulting in a longer arrival time of 0.095 seconds. The extra travel distance and the time spent reflecting at the object are shown in this figure, indicating the delayed arrival time compared to the homogeneous model.

The frequencies did not change in this simulation process because both the model and the object were small and each was homogeneous. This is in contrast to fieldwork scenarios where the soil is often heterogeneous, leading to more complex and variable wave propagation.

However, the amplitude of the seismic waves was noticeably higher when the object was present. This increase in amplitude occurred because the waves, after interacting with the object, were reflected and focused towards the monitoring station located directly above it.

The seismic waves observed in this study were shear waves, rather than compressional waves. Shear waves are characterized by the direction of particle movement being perpendicular to the direction of wave propagation. The specific behaviour of shear waves, particularly in their interaction with the object, plays a crucial role in how seismic energy is transmitted through the medium and how it is detected by monitoring stations. This interaction highlights the importance of understanding the type of seismic waves in play, as their properties dictate how energy is reflected, focused, and ultimately measured.

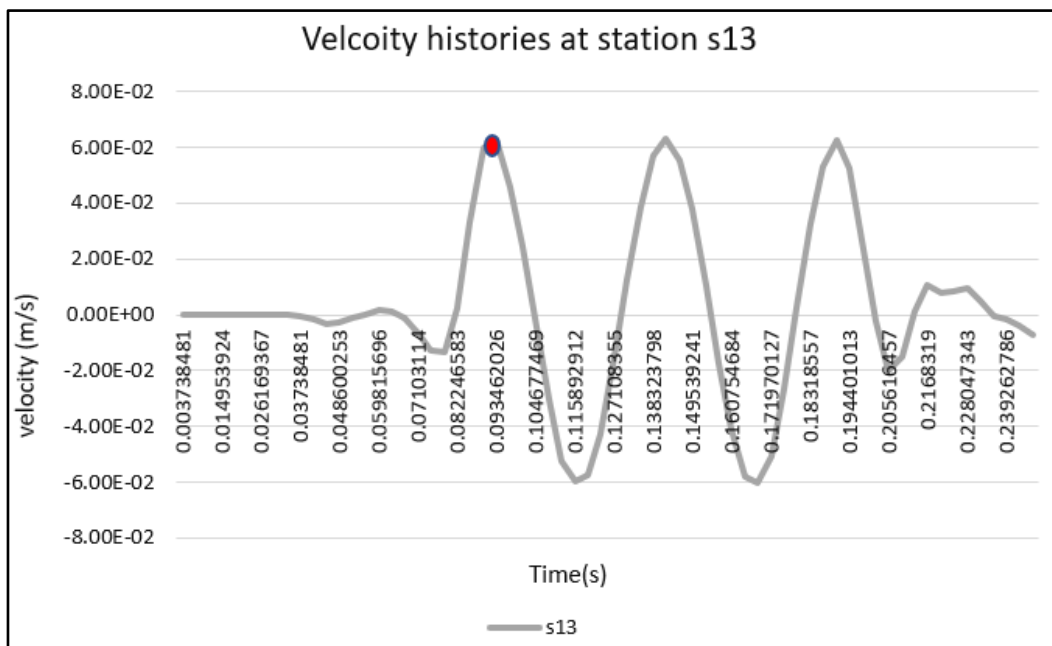


**Figure 4.16:** Model 2: The velocity history results at station 13 recorded from the homogenous model (The red dot on the graph marks the maximum peak velocity observed at station s13, occurring at approximately 0.089 seconds)

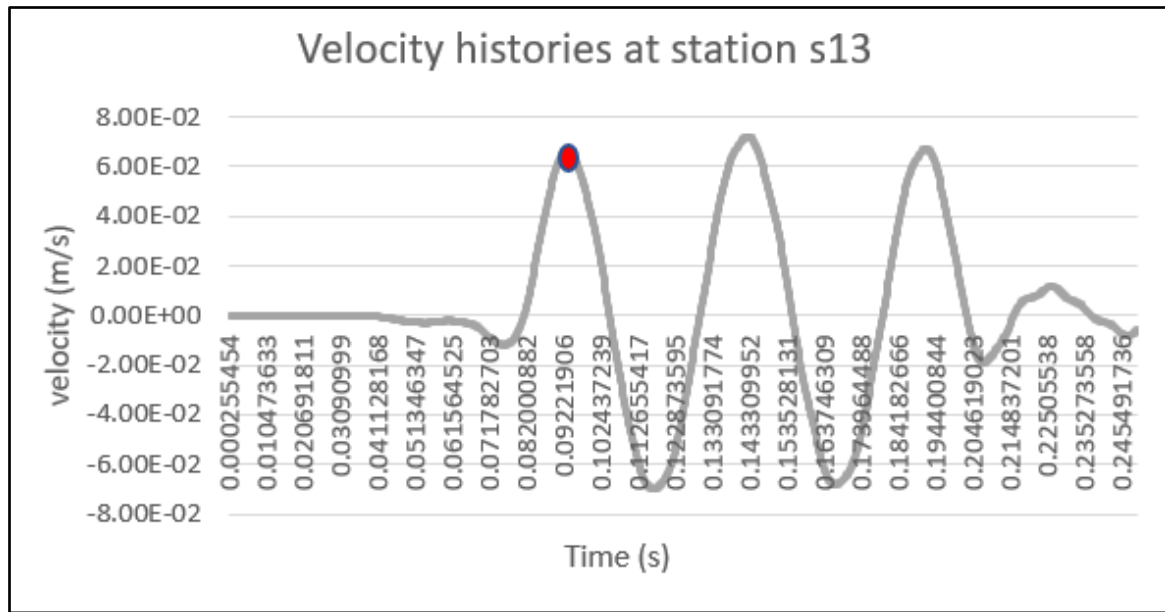


**Figure 4.17:** Model 2 with a buried object: The velocity history results at station 13 recorded from the homogenous model with the object at 1 m depth (The red dot on the graph marks the maximum peak velocity observed at station s13, occurring at approximately 0.095 seconds)

The following section uses the results from Model 2 to explain the principle of the reflected wave and support vertical incidence angle. For the calculations, the times of the maximum peak particle velocity are used instead of the arrival times, as the latter are difficult to pick with accuracy because of the absence of impulsive arrivals. In the Homogeneous model 2, the time it takes for the max peak to appear at Station s13 is 0.089 sec. The same time for the Model with the object at 1m depth is 0.095 sec. The difference between these two times is 0.006 sec. Here, the hypothesis is that this time difference is due to the time it takes for the wave to travel from s13 to the top of the object and reflect back to s13 (two-way time  $\Delta t$ ). If this hypothesis is correct then this time should be consistent with the depth of the object for the given wave speed. The time that the wave takes to travel from the surface at s13 to the top of the object is  $\Delta t/2 = 0.006/2 = 0.003$  sec. Using this time and the velocity of the seismic wave we can calculate the distance travelled:

$$d = (\Delta t / 2) * v \tag{Equation 4. 1}$$

$$d = 0.003 * 316 = 0.948 \text{ m}$$

This distance of 0.948m is consistent with the actual object depth of 1m in this Model and supports the hypothesis of the two-way time and reflected wave path.

**Table 4.4:** Shows the values for  $\Delta t$ ,  $v$ , and the depth estimation (d)

Scenario	First arrival time	Velocity (v)	$\Delta t_1$ ( $\Delta t$ object 1m- $\Delta t$ homo model)	$\Delta t_1 / 2$ (one-way travel time)	Estimated depth (d)
Homogeneous Model	0.089723545	316	0.005560969	0.002780485	$\approx 0.9$ m
Object Present (1 m)	0.095284514				

**4.3.6 Results for site B.**

At this location, the distance between the source of the seismic waves and the monitoring stations has been increased to more than 30m. The main purpose is to understand and track the path of reflection and propagation of the seismic waves at longer distances.

Homogenous model: Results are the same as for the homogenous model for site A but now the peak particle velocity is smaller compared to the values at site A , as expected , due to the longer distance away from the source ( see plot in Appendix A.1) .In the time domain of seismic waves, it was observed that the seismic waves take longer to reach the monitoring stations, indicating a delay in time (see Appendix A.1).

**4.3.7 Site B: Model 2 with buried object**

**I.First scenario: The object at 1m depth**

At this location, monitoring stations are positioned more than 30m from the seismic wave source, with an object situated over 50m away.

Among the monitoring stations (s36, s37, s38, s39, and s40), station s38, located directly above the object, recorded the highest wave amplitude. This indicates a pronounced reflection of seismic energy from the object at station s38. Similarly, at side monitoring stations (s26, s27, s28, s29, and s30), station s28 recorded a higher wave amplitude, showing the object's influence on seismic wave characteristics.

The power spectral density (PSD) analysis further supports these observations. Station s38's PSD curve, showing a higher peak or maximum value compared to other stations, suggests a concentration of seismic energy due to the object's presence.

Stations positioned 4m or slightly more away show no noticeable effect from the object, indicating its limited impact at that distance. The maximum PSD amplitude recorded at station s38, above the steel object, is  $3.37 \times 10^{-5}$  ( $\text{m}^2/\text{s}^2$ ) /Hz (see Appendix A.2).

### **II. Second scenario: The object at 2m depth**

In this scenario, the depth of the object is increased by an additional meter from the surface of the model to the top of the object. Based on the theory of seismic wave propagation, it was observed that as the object depth increases, the angles of incidence and reflection decrease, causing the waves to scatter and reflect in different directions.

Seismic waves recorded at various monitoring stations were analysed both in the time and frequency domains to study their frequency properties, which represent the amount of reflected seismic energy. Among the monitoring stations s36, s37, s38, s39, and s40, station s38 recorded the maximum wave amplitude, indicating significant reflection from the object.

Further comparisons were made for stations s31, s32, s33, s34, and s35, where station s33 showed a higher wave amplitude, suggesting an impact on the wave path at this location. The power spectral density (PSD) analysis revealed that station s38, directly above the object, recorded the highest PSD value, while station s33 also showed a significant amount of reflected seismic energy.

For stations s26, s27, s28, s29, and s30, no noticeable effect from the object was observed. The wave amplitudes gradually decreased as the distance from the source increased. The PSD analysis for these stations confirmed that seismic energy was greater at stations closer to the source and decreased progressively, indicating minimal influence from the object as these stations were more than four meters away from it. The power spectral density amplitude s38, above the steel object decreased from  $3.37 \times 10^{-5}$ . to  $2.89 \text{E-}05$  ( $\text{m}^2/\text{s}^2$ ) /Hz, representing a decrease of approximately 14.24%: (see Appendix A.3).

### **III. Third scenario: The object at 3m depth**

Monitoring stations s36, s37, s38, s39, and s40 recorded varying wave amplitudes. Station s38, located over the object, recorded a higher amplitude compared to others, except for station s36, which, being closest to the source, recorded the highest amplitude due to receiving the strongest

waves. Similarly, side monitoring station s31, 2m away from the object, recorded the highest amplitude among its group, with station s33 also showing significant amplitudes.

The power spectral density (PSD) analysis shows that station s38 recorded a higher PSD compared to others, except station s36. Similarly, station s33, a side monitoring station, recorded higher PSD values compared to others, except station s31. Monitoring stations s26, s27, s28, s29, and s30, positioned laterally and more than 4m away from the object, showed minimal influence from the object, indicating that its impact on seismic waves is negligible at those locations. The power spectral density amplitude decreased s38, above the steel object from  $3.37 \times 10^{-5}$  to  $2.69 \times 10^{-5} (\text{m}^2/\text{s}^2) / \text{Hz}$ , representing a decrease of approximately 20.18% (see Appendix A.4).

#### **4.3.8 Seismic power variation**

In this research, all power spectral density values are obtained from the history of seismic velocities after converting them to the frequency domain, and the PSD directly represents the amount of seismic power of the signal. The PSD curves that have a high amplitude represent the highest amount of recorded seismic energy. In the previous sections, identifying the station that exhibits the higher seismic energy was straightforward because the input seismic wave was a simple sine wave with a single frequency. As such, the PSD has a single peak. This is not the case for real seismic signals which are noisy and contain a range of frequencies. To identify the location of highest energy in this case, requires a more robust approach, other than the usually observed maximum peak. Calculating the power of the signal of the seismic would be a suitable way. This can be achieved by calculating the area under PSD curves. The area under the curves was calculated using MATLAB and shown in the tables below.

*Note: the cells have been coloured based on the max PSD value for each case (red) and moving towards green as the values reduced compared to max value*

Site A

Table 4.5: Site A, Homogeneous model.

S21	0.0098	S16	0.0101	S11	0.0102	S6	0.0101	S1	0.0098
S22	0.0084	S17	0.0084	S12	0.0087	S7	0.0084	S2	0.0084
S23	0.0074	S18	0.0075	S13	0.0076	S8	0.0075	S3	0.0074
S24	0.0066	S19	0.0067	S14	0.0067	S9	0.0067	S4	0.0066
S25	0.006	S20	0.0061	S15	0.0061	S10	0.0061	S5	0.006

Table 4.6: Site A - Model 2 with object at 1m depth

S21	0.000524	S16	0.000516	S11	0.000511	S6	0.000516	S1	0.000524
S22	0.000472	S17	0.00044	S12	0.000412	S7	0.00044	S2	0.000472
S23	0.000458	S18	0.000514	S13	0.00058	S8	0.000514	S3	0.000458
S24	0.000432	S19	0.000449	S14	0.000448	S9	0.000449	S4	0.000432
S25	0.000394	S20	0.000399	S15	0.000401	S10	0.000399	S5	0.000394

Arranging the tables to reflect the deployment geometry at site A and B, the tables practically represent a "heat" map indicating the location of the object. They also serve as visual representation of the propagation of the wave (from top to bottom in each row) away from the source (source assumed to be at top of the table). They also serve as visual representation of the propagation of the wave (from top to bottom in each row) away from the source (source assumed to be at top of the table) as shown in Figure 4.3 (b) which is consistent with the colour changes as shown in Table 4.5 for the homogeneous model (spherical spreading away from source).

Table 4.7: Site A - Model 2 with buried object at 2m depth

S21	0.000524	S16	0.000516	S11	0.000511	S6	0.000516	S1	0.000524
S22	0.000472	S17	0.00044	S12	0.000411	S7	0.00044	S2	0.000472
S23	0.000458	S18	0.000513	S13	0.000535	S8	0.000513	S3	0.000458
S24	0.000432	S19	0.000449	S14	0.000447	S9	0.000449	S4	0.000432
S25	0.000431	S20	0.000399	S15	0.000401	S10	0.000399	S5	0.000431

**Table 4.8:** Site A - Model 2 with buried object at 3m depth

S21	0.000522	S16	0.000513	S11	0.000509	S6	0.000513	S1	0.000522
S22	0.000466	S17	0.00044	S12	0.000428	S7	0.00044	S2	0.000466
S23	0.000458	S18	0.000469	S13	0.000488	S8	0.000469	S3	0.000458
S24	0.000428	S19	0.000428	S14	0.000428	S9	0.000428	S4	0.000428
S25	0.000383	S20	0.000372	S15	0.000368	S10	0.000372	S5	0.000383

In a homogeneous medium, seismic wave radiate outward from the source in a spherical pattern, distributing energy across the surface of an expanding sphere. As the wave front moves farther from the source, its surface area increases significantly, causing the energy per unit area (intensity) to decrease. This trend is evident in the recorded energy values presented in Table 4.5.

Stations in the first row (s1, s6, s11, s16, and s21), located approximately 19 meters from the source (site A), recorded the highest energy values, ranging from 0.0098 to 0.0102. At this short distance, the wave front remains relatively small, concentrating energy over a limited spherical surface. As the wave propagates outward, the recorded energy decreases progressively. In the second row (s2, s7, s12, s17, and s22), energy values range from 0.0084 to 0.0087, while in the third row (s3, s8, s13, s18, and s23), values fall between 0.0074 and 0.0076. By the fifth row (s5, s10, s15, s20, and s25), the energy drops to approximately 0.006. This steady reduction illustrates how spherical spreading disperses energy over an expanding surface area, leading to a consistent attenuation of intensity. For instance, at 19 meters (first row), station s1 records an energy value of 0.0098, whereas at a greater distance (fifth row), station s5 records 0.006.

This pattern aligns with the inverse square law governing spherical wave propagation. As the radius of the wave front doubles, the energy is spread over four times the area, resulting in a significant decrease in intensity. This relationship holds as long as no additional energy loss mechanisms, such as absorption, are present. The observed trend confirms that seismic energy is most concentrated near the source and predictably diminishes with distance. The same explanation applies across all tables, as the pattern of energy attenuation due to spherical spreading remains consistent across varying distances and datasets.

In the case of the model with the object, the propagation mechanism of seismic waves remains constant and does not change, just as in the homogeneous model. Table 4.7 shows a noticeable change in recorded seismic energy when waves collide with the target. The highest energy values are observed at the monitoring stations placed directly above the target, indicating that a significant portion of the seismic energy is concentrated in this region upon interaction. This suggests that the target alters the energy distribution, leading to localized amplification at specific stations. This pattern can be applied to all scenarios, as the interaction between seismic waves and a target consistently results in energy concentration at specific locations.

**Site B**

**Table 4.9:** Site B, Homogeneous model.

S46	0.003	S41	0.00352	S36	0.00375	S31	0.00352	S26	0.003
S47	0.00277	S42	0.00331	S37	0.00355	S32	0.00331	S27	0.00277
S48	0.00246	S43	0.00297	S38	0.00319	S33	0.00297	S28	0.00246
S49	0.00205	S44	0.00245	S39	0.00263	S34	0.00245	S29	0.00205
S50	0.00192	S45	0.00223	S40	0.00238	S35	0.00223	S30	0.00192

**Table 4.10:** Site B- Model 2 with buried object at 1m depth

S46	0.000179	S41	0.000204	S36	0.000213	S31	0.000204	S26	0.000179
S47	0.000162	S42	0.000184	S37	0.000189	S32	0.000184	S27	0.000162
S48	0.000155	S43	0.000212	S38	0.000254	S33	0.000212	S28	0.000155
S49	0.000134	S44	0.000173	S39	0.000188	S34	0.000173	S29	0.000134
S50	0.000135	S45	0.000161	S40	0.000173	S35	0.000161	S30	0.000135

**Table 4.11:** Site B- Model 2 with buried object at 2m depth

S46	0.000179	S41	0.000204	S36	0.000213	S31	0.000204	S26	0.000179
S47	0.000161	S42	0.000181	S37	0.000186	S32	0.000181	S27	0.000161
S48	0.000155	S43	0.000198	S38	0.000219	S33	0.000198	S28	0.000155
S49	0.000133	S44	0.000166	S39	0.000178	S34	0.000166	S29	0.000133
S50	0.000132	S45	0.000154	S40	0.000164	S35	0.000154	S30	0.000132

**Table 4.12:** Site B- Model 2 with buried object at 3m depth

S46	0.000179	S41	0.000205	S36	0.000213	S31	0.000205	S26	0.000179
S47	0.000163	S42	0.000175	S37	0.000186	S32	0.000175	S27	0.000163
S48	0.000154	S43	0.00019	S38	0.000215	S33	0.00019	S28	0.000154
S49	0.000132	S44	0.000161	S39	0.000178	S34	0.000161	S29	0.000132
S50	0.00013	S45	0.00015	S40	0.000164	S35	0.00015	S30	0.00013

**4.3.9 Discussion of results (model 2)**

At site (A), Table 4.5 shows that the area under the PSD curves for seismic waves recorded from the homogeneous model is highest at monitoring stations close to the source and gradually decreases due to spherical spreading. Adding an object (steel) at a depth of 1 m, as shown in Table 4.6, station No. s13, located directly above the object, recorded the highest PSD area value (0.00058 m<sup>2</sup>/s<sup>2</sup>/Hz) compared to all other stations. Stations s8 and s18, 2m away from the object, also recorded high values affected by the object's presence.

In Table 4.7, with the object at a depth of 2m, the PSD area at station s13 decreased by approximately 8.62%, from 0.00058 to 0.000535 m<sup>2</sup>/s<sup>2</sup>/Hz. The value also decreased at the side monitoring stations as well. At a 3 m depth (Table 4.8), the PSD area at station s13 further decreased by approximately 7.92%, from 0.00053 to 0.000488 m<sup>2</sup>/s<sup>2</sup>/Hz. From 1 m to 3 m depth, the total decrease in the PSD area is approximately 15.86%. The object can be easily detected at a depth of 3 m and also at side monitoring stations up to 2m away.

When the distance between the seismic wave source and the monitoring stations exceeded 30 m (Site B), monitoring stations close to the source (s26, s31, s38, and s41) recorded the highest PSD values, as shown in Table 4.9. Compared to location A, the stations at location B recorded lower seismic energy due to the spherical spreading of wave propagation. With an object 1 m deep, station s38 recorded the highest PSD value ( $0.000254 \text{ m}^2/\text{s}^2/\text{Hz}$ ), confirming the object's impact on the seismic waves (Table 4.10). At 2m depth, station s38's PSD value decreased by approximately 13.78% to  $0.000219 \text{ m}^2/\text{s}^2/\text{Hz}$  (Table 4.11). At 3 m depth, the PSD value at station s38 further decreased by approximately 1.83% to  $0.000215 \text{ m}^2/\text{s}^2/\text{Hz}$  (Table 4.12). Despite these decreases, the object can still be detected at a depth of 3 m and at a side monitoring station 2 m away.

When the seismic wave source distance exceeded 30m, some seismic energy dissipated. Comparing stations s38, s33, and s28 showed an increase in energy from s38 to s28, attributed to the increased reflection angle.

#### **4.4 Model 3**

##### **4.4.1 Material properties**

In simulating seismic waves using this model, the mechanical properties of the model were increased. By increasing these mechanical properties, I aimed to create a more accurate representation of the actual soil conditions found in brownfields. These changes in mechanical properties could involve various factors such as increased density and shear modulus of the materials used in the model. These adjustments are essential because soil properties can vary significantly from one location to another, and the brownfields may have distinctive characteristics that affect how seismic waves propagate through them.

By matching the model's mechanical properties to those found in the brown fields, the simulation becomes more representative of the real-world conditions. This allows for a more accurate assessment of how seismic waves interact with the objects and soil properties present in the brown fields, which is crucial for the reliability and validity of the seismic wave simulation results. The choice of mechanical properties for the model depends on the specific application and the characteristics of the subsurface being simulated. To ensure that seismic waves propagate without distortion in numerical modelling, the mechanical properties should be selected in a way that aligns with the governing equations and accurately represents the behaviour of the subsurface materials. When modelling seismic waves with various speeds and frequencies, it is crucial to take into consideration any difference in the mechanical

characteristics of the soil at the brownfield sites. The mechanical properties are shown in the table below (Volpini, Douglas and Nielsen, 2021).

**Table 4.13:** Input material properties for model 3.

Soil 2	Shear modulus	Bulk modulus	Density	Shear velocity (m/s)	Primary velocity (m/s)
	1.42x 10 <sup>9</sup> Pa	2.5 x 10 <sup>9</sup> Pa	2100 kg/m <sup>3</sup>	822.31	1446.4

#### 4.4.2 Dynamic input

Based on the provided information, Figure 4.18 represents a dynamic input for the numerical model. It shows a sine wave with a frequency of 50 Hz and an amplitude of 1 m/s. This sine wave is used as a single seismic source applied to the surface of the model. The sampling frequency for this sinusoidal wave is given as 1000 Hz.

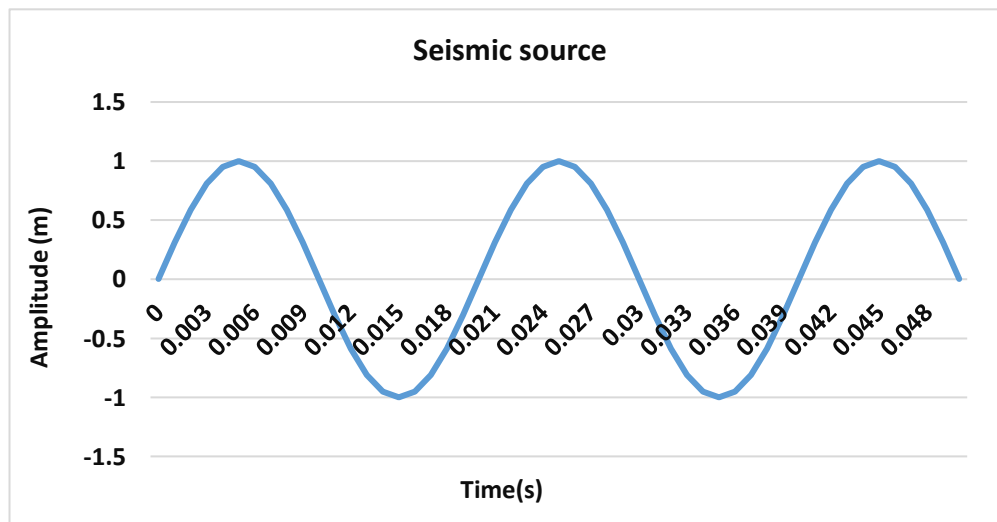


**Figure 4.18:** The sinusoidal wave dynamic source applied to model 3 in the Z-direction.

#### 4.4.3 Results

The results for this model shown here are limited to those obtained from spectral analysis as these are the most important ones for detection of a buried object. The analysis steps are exactly the same as model 2. All time – domain plots are presented in Appendix B. The value for the parameters used for the calculation of the PSD are shown in Table 4.14.

**Table 4.14:** Shows the parameters used for this case

	Window length	Overlap %	Nfft	fs
Homogenous model	55	30	3500	660.9
Model with buried object	150	100	3500	3914.3

#### 4.4.4 Results for site A.

homogenous model: Results are similar to those for homogenous of model 2 but the actual values are different due to different mechanical properties.

For the complete velocity histories and PSD plots see (Appendix B.1).

#### 4.4.5 Model with buried object

##### I. First scenario: Object at 1m depth

In this model, the same object with unchanged dimensions and mechanical properties was added, while the speed and frequencies of seismic waves were increased. The goal was to understand the seismic wave paths, reflections, and spectral changes. The results show again that seismic waves recorded at monitoring station s13, directly above the object, exhibited higher amplitudes, indicating the object's influence. Monitoring station s11, closest to the seismic source, recorded the maximum wave amplitude and power spectral density (PSD). Side monitoring stations, about 2 m from the object, were also affected, with station s8 recording a higher wave amplitude. The frequency domain analysis revealed that station s13 had a high PSD value, reflecting greater seismic energy, while station s11, near the source, had the highest PSD value, indicating peak seismic energy due to proximity to the source. The highest PSD amplitude value recorded at the monitoring station s13 was  $5.01\text{E-}05$  ( $\text{m}^2/\text{s}^2$ ) /Hz (see Appendix B.2).

##### II. Second Scenario: Object at 2m Depth

In this scenario, the object's depth is increased to 2 m to observe its influence on seismic waves at site A. Monitoring station s13, directly above the object, recorded the highest wave amplitude, second only to station s11 near the seismic source. Side monitoring station s8, about two meters from the object, also exhibited greater amplitude, indicating the object's continued influence.

In the frequency domain, station s13 recorded the highest power spectral density (PSD), suggesting significant seismic energy, while station s8 showed a slightly higher PSD compared to other side stations. The absence of noticeable differences in seismic waveforms among the stations in the time domain suggests that the object does not significantly impact wave amplitudes. Similarly, no discernible differences in frequency content or PSD across the stations indicate that the object is not causing substantial modifications to the seismic wave frequencies. Overall, the object is still detected and influences the seismic waves, even at a depth of 2m. The maximum PSD amplitude recorded at station s13 decreased from  $5.01E-05$   $m^2/s^2/Hz$  when the object was at a depth of 1 meter to  $3.70E-05$   $m^2/s^2/Hz$  when the object depth increased to 2m, representing a decrease of approximately 26.15% (see Appendix B.3).

### III. Third Scenario: Object at 3m Depth

In this scenario, the object's depth is increased to 3m to determine if it can still be detected. Monitoring station s13, located directly above the object, recorded a higher wave amplitude, indicating the object still influences seismic wave propagation even at this depth. Similarly, station s8, near the object, showed a slight increase in wave amplitude compared to other stations.

The frequency domain analysis revealed that the power spectral density (PSD) of seismic waves decreases as the object's depth increases, indicating a reduction in energy content. Notably, the PSD curves for stations s12 and s13 are similar, suggesting similar energy distributions and impacts from the object at these locations.

In the time domain, there are no significant differences in seismic wave amplitudes among the monitoring stations, suggesting that the object does not significantly impact wave amplitudes. Similarly, the frequency domain comparison shows no discernible differences or anomalies in the frequency content or PSD across the stations, indicating that the object does not cause noticeable modifications or reflections of seismic wave frequencies. The maximum PSD amplitude recorded at station s13 decreased from  $5.01E-05$   $m^2/s^2/Hz$  when the object was at a depth of 1m to  $3.47E-05$   $m^2/s^2/Hz$  when the object depth increased to 3m, representing a decrease of approximately 30.94% (see Appendix B.4).

#### 4.4.6 Result for site B.

Homogenous model: As the distance between the source and the monitoring stations increases, the seismic waves travel a longer path, resulting in a longer travel time. This can be observed in the recorded arrival times of seismic waves at different stations. The time lag between the

arrival of the seismic waves at the source and the monitoring stations increases with distance (see Appendix B.5).

#### 4.4.7 Model with buried object

##### **I. First scenario: Object at 1m depth**

In the time domain, monitoring point s38, positioned over the object, shows seismic waves with the highest amplitude, indicating the object's significant influence on the reflected waves at this location. Similarly, monitoring station No. s33 records a notable increase in wave amplitude, suggesting a noticeable effect of the object on the recorded seismic waves at this station.

In the frequency domain, the power spectral density (PSD) analysis reveals that monitoring station s38 records a high PSD value, indicating significant energy content in the seismic waves at this location. Monitoring station No. s33 also shows a higher PSD value compared to other stations, reinforcing the observation that the object impacts the energy distribution across frequencies. The maximum PSD amplitude was recorded at station s38 is  $1.61E-05 \text{ m}^2/\text{s}^2/\text{Hz}$  (see Appendix B.6).

##### **II. Second scenario: Object at 2m depth**

In the time domain, seismic waves at station s36, closer to the seismic source, show higher amplitudes due to less attenuation and geometric spreading. Monitoring station s38, positioned directly above the object, records the highest wave amplitude among the stations, indicating the object's significant impact. For side monitoring stations, the seismic waves at station s33 exhibit a higher amplitude compared to other stations, suggesting that the object affects wave reflection even at a distance of about two meters.

In the frequency domain, monitoring station s36 shows a higher energy content in the PSD, likely due to its proximity to the seismic source. Station s38 also records a higher PSD value, reflecting the object's clear impact on energy distribution. Monitoring station s33 receives more seismic energy compared to other stations.

However, in the additional comparisons, there is no discernible effect of the object on side stations located approximately 4 meters or more away from the object, indicating that the object's influence diminishes with distance. The maximum power spectral density (PSD) amplitude at station 38, located directly above the object, decreased from  $1.61E-05 \text{ m}^2/\text{s}^2/\text{Hz}$  when the object was at a depth of 1m to  $1.42E-05 \text{ m}^2/\text{s}^2/\text{Hz}$  when the object was at a depth of 2m, representing a decrease of approximately 11.80%. (see Appendix B.7).

**III.Third scenario: Object at 3m depth**

In the time domain, seismic waves at monitoring station s38 show a decrease in amplitude with the increased depth of the object to 3m. This decrease suggests that the object's depth influences the amplitude of seismic waves at this station. Similarly, the decrease in wave amplitude at monitoring station s33 is due to wave attenuation, scattering, energy absorption, or dispersion caused by the object's deeper position.

In the frequency domain, the power spectral density (PSD) shows a drop-in amplitude at monitoring station s38, indicating that the object's deeper location affects the energy level of the seismic waves detected at this station. The deeper object has a slight impact on the spectral characteristics of seismic waves, suggesting minimal alteration in the frequency content or distribution of the waves.

Additionally, no discernible effect from the object is noted on the seismic waves recorded at the side stations located approximately four meters or more from the object. These side stations do not exhibit significant changes in their recorded seismic wave characteristics he maximum power spectral density (PSD) at station 38, located directly above the object, decreased from 1.61E-05 m<sup>2</sup>/s<sup>2</sup>/Hz when the object was at a depth of 1m to 1.32E-05 m<sup>2</sup>/s<sup>2</sup>/Hz when the object was at a depth of 2 m, representing a decrease of approximately 18.01% (see Appendix B.8).

**4.4.8 Seismic power variation**

*Note: the cells have been coloured based on the max PSD value for each case (red) and moving towards green as the values reduced compared to max value.*

**Site A**

**Table 4.15:** Site A - homogeneous model.

S21	0.0114444	S16	0.011737	S11	0.011844	S6	0.011737	S1	0.011444
S22	0.0098736	S17	0.010067	S12	0.010136	S7	0.010067	S2	0.009874
S23	0.0085535	S18	0.008698	S13	0.008747	S8	0.008698	S3	0.008553
S24	0.0074093	S19	0.007533	S14	0.007574	S9	0.007533	S4	0.007409
S25	0.0063933	S20	0.006506	S15	0.006543	S10	0.006506	S5	0.006393

**Table 4.16:** Site A - Model 3 with buried object at 1m depth

S21	0.001564	S16	0.001561	S11	0.00155	S6	0.001561	S1	0.001564
S22	0.0012333	S17	0.001185	S12	0.001113	S7	0.001185	S2	0.001233
S23	0.001079	S18	0.001222	S13	0.0015	S8	0.001222	S3	0.001079
S24	0.0009635	S19	0.001019	S14	0.001017	S9	0.001019	S4	0.000964
S25	0.0008601	S20	0.000899	S15	0.000911	S10	0.000899	S5	0.00086

**Table 4.17:** Site A - Model 3 with buried object at 2m depth

S21	0.0015511	S16	0.001535	S11	0.001524	S6	0.001535	S1	0.001551
S22	0.001282	S17	0.001219	S12	0.00117	S7	0.001219	S2	0.001282
S23	0.0012121	S18	0.001288	S13	0.001342	S8	0.001288	S3	0.001212
S24	0.0011258	S19	0.001143	S14	0.001137	S9	0.001143	S4	0.001126
S25	0.0010228	S20	0.001024	S15	0.001019	S10	0.001024	S5	0.001023

**Table 4.18:** Site A - Model 3 with buried object at 3m depth.

S21	0.0015511	S16	0.001535	S11	0.001537	S6	0.001543	S1	0.001554
S22	0.001282	S17	0.001219	S12	0.001199	S7	0.001229	S2	0.001282
S23	0.0012121	S18	0.001288	S13	0.001287	S8	0.00124	S3	0.001205
S24	0.0011258	S19	0.001143	S14	0.001128	S9	0.001127	S4	0.001117
S25	0.0010228	S20	0.001024	S15	9.91E-04	S10	9.99E-04	S5	0.00101

**Site B**

**Table 4.19:** Site B - homogeneous model.

S46	0.0029983	S41	0.003283	S36	0.003397	S31	0.003283	S26	0.002998
S47	0.0026277	S42	0.002884	S37	0.002989	S32	0.002884	S27	0.002628
S48	0.0022937	S43	0.002511	S38	0.002603	S33	0.002511	S28	0.002294
S49	0.0019467	S44	0.002118	S39	0.002192	S34	0.002118	S29	0.001947
S50	0.00166	S45	0.001789	S40	0.001845	S35	0.001789	S30	0.00166

**Table 4.20:** Site B - Model 3 with buried object at 1m depth.

S46	0.0007017	S41	0.000779	S36	0.000806	S31	0.000779	S26	0.000702
S47	0.0005958	S42	0.000659	S37	0.000668	S32	0.000659	S27	0.000596
S48	0.0005433	S43	0.000701	S38	0.000812	S33	0.000701	S28	0.000543
S49	0.0004855	S44	0.000583	S39	0.000617	S34	0.000583	S29	0.000485
S50	0.0004627	S45	0.000529	S40	0.000561	S35	0.000529	S30	0.000463

**Table 4.21:** Site B - Model 3 with buried object at 2m depth.

S46	0.0007054	S41	0.00078	S36	0.000564	S31	0.00078	S26	0.000705
S47	0.0005905	S42	0.000646	S37	0.00046	S32	0.000646	S27	0.00059
S48	0.0005421	S43	0.000659	S38	0.0005	S33	0.000659	S28	0.000542
S49	0.0004829	S44	0.000565	S39	0.000417	S34	0.000565	S29	0.000483
S50	0.0004562	S45	0.000511	S40	0.000375	S35	0.000511	S30	0.000456

**Table 4.22:** Site B - Model 3 with buried object at 3m depth.

S46	0.1820326	S41	0.000786	S36	0.000571	S31	0.000786	S26	0.182033
S47	0.1203673	S42	0.000655	S37	0.000472	S32	0.000655	S27	0.120367
S48	0.0661582	S43	0.000631	S38	0.000474	S33	0.000631	S28	0.066158
S49	0.0004829	S44	0.00055	S39	0.000406	S34	0.00055	S29	0.000483
S50	0.0445942	S45	0.000498	S40	0.000364	S35	0.000498	S30	0.044594

**4.4.9 Discussion of results (model 3)**

At site A, represented in Table 4.15, the area under the PSD curves from the homogeneous model shows that monitoring stations (s1, s6, s11, s16, and s21) closest to the wave emission source recorded the largest average value of 0.01164128 m<sup>2</sup>/s<sup>2</sup>/Hz, while farther stations recorded an average of 0.00646826 m<sup>2</sup>/s<sup>2</sup>/Hz. Table 4.16 shows the PSD area for the homogeneous model with a steel object 1m below the surface. Station s13, directly above the object, recorded 0.0015 m<sup>2</sup>/s<sup>2</sup>/Hz, indicating the object's significant impact on seismic wave

characteristics. Symmetrical stations s8 and s18, approximately 2m away, recorded 0.001222 m<sup>2</sup>/s<sup>2</sup>/Hz, confirming object detection at side stations. When the object's depth increased to 2m, the PSD area at station No. 13 decreased by 10.53% to 0.001342 m<sup>2</sup>/s<sup>2</sup>/Hz, and further to 0.001287 m<sup>2</sup>/s<sup>2</sup>/Hz at 3m, a total decrease of 14.20%. Despite these decreases, object detection remains clear.

**4.5 Model 4**

**4.5.1 Material properties**

In this model, there have been specific changes made to the mechanical properties and the source of seismic waves while keeping the dimensions and element size consistent with the previous models. The adjustments include increasing the velocities of the shear waves to 1783 m/s and increasing the frequency of the sine wave applied to the surface of the model (70 Hz). By increasing the velocities of the shear waves, the seismic waves in the model will propagate at a faster rate compared to the previous models. This can have implications for the overall characteristics of the seismic waves, including their amplitude, frequency content, and energy distribution. The mechanical properties of the homogenous model are shown in Table 4.23.

**Table 4.23:** Input material properties for model 4.

	<b>Shear modulus</b>	<b>Bulk modulus</b>	<b>Density</b>	<b>Shear velocity (m/s)</b>	<b>Primary velocity (m/s)</b>
<b>Soil 3</b>	7 x 10 <sup>9</sup> Pa	20.8 x 10 <sup>9</sup> Pa	2000 kg/m <sup>3</sup>	1783	3881

**4.5.2 Dynamic input:**

The seismic source is represented by a basic waveform mode, specifically a sine wave. Figure 4.19 illustrates a sine wave with an amplitude of 1 m and a frequency of 70 Hz. The sine wave is applied to the surface of the model as a single seismic source. The sine wave is sampled at a rate of 1000 Hz, meaning that 1000 samples per second are taken to record the waveform. To implement the sine wave input on the model surface, two elements are used along the X direction and two elements along the Y direction. This arrangement helps ensure that the seismic wave is properly distributed and propagated throughout the model . In this model, a seismic wave source using a sine wave with more cycles was applied, unlike in the previous

models. This was done to observe any changes in the results due to the increased number of sine wave cycles.

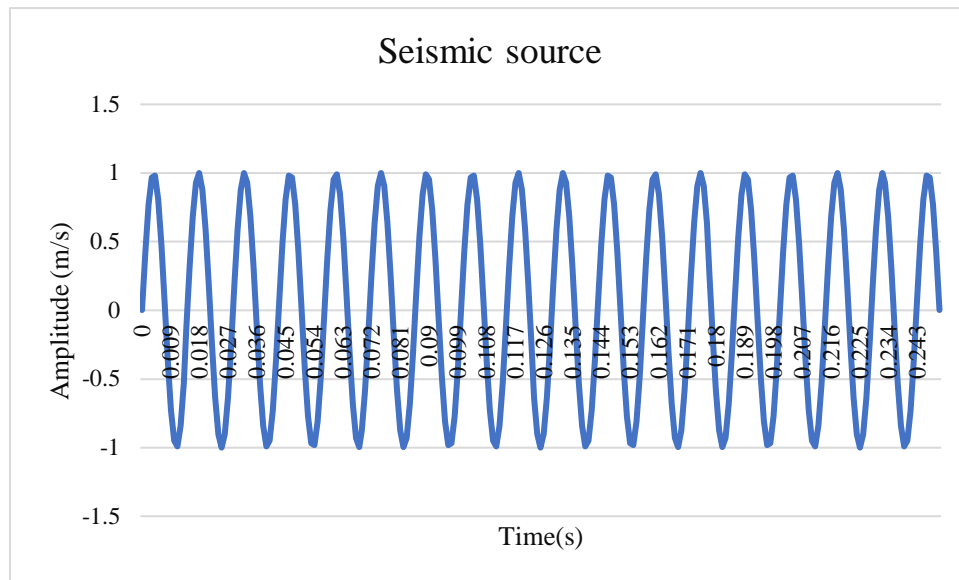


**Figure 4.19:** The sinusoidal wave dynamic source applied to the model in the Z-direction.

### 4.5.3 Results

The results for this model shown here are limited to those obtained from spectral analysis as these are the most important ones for detection of a buried object. The analysis steps are exactly the same as model 2. All time – domain plots are presented in Appendix. The value for the parameters used for the calculation of the PSD are shown in Table 4.24.

**Table 4.24:** Shows the parameters used in this case

	Window length	Overlap %	Nfft	fs
<b>Homogenous model</b>	200	100	1000	1750
<b>Model with buried object</b>	200	100	1000	3993

### 4.5.4 Results site A.

Homogenous model: Results are similar to those for homogenous of model 3 but the actual values are different due to different mechanical properties.

For the complete velocity histories and PSD plots see (Appendix C.1).

#### 4.5.5 Model with buried object

##### **I. First scenario: Object at 1m depth**

Monitoring station s11, being closest to the source, recorded the highest amplitude of seismic waves, followed sequentially by stations s12 and s13. Notably, station s13 recorded the highest wave amplitude compared to stations s12, s14, and s15, indicating greater energy at this station.

The effect of the object on seismic waves is further highlighted by the recordings at station s8, which showed a higher wave amplitude. Station s11, close to the wave source, recorded the highest PSD value, indicating a higher concentration of energy across the frequency range. The presence of the object beneath station s13 resulted in a higher PSD amplitude compared to stations s12, s14, and s15, demonstrating the object's influence on energy distribution.

In summary, the addition of the steel object significantly affected the seismic wave properties, particularly at station s13. In contrast, side stations located approximately 4m from the object showed no significant impact on the recorded seismic waves (see Appendix C.2).

##### **II. Second scenario Object at 2m depth**

Increasing the object's depth to 2m from the surface aims to investigate how depth affects the spectral characteristics, trajectories, and reflections of seismic waves. This modification provides insights into how the object's depth influences seismic wave behaviour in the surrounding medium.

The comparison of seismic waves in the time domain reveals that the wave amplitude recorded at monitoring station s13 decreases with the object at a 2m depth. Additionally, the PSD amplitude at station s13, located directly above the object, also decreases, indicating reduced seismic energy in that frequency range. Despite this decrease, objects at a 2m depth can still be detected due to changes in seismic wave characteristics and interactions, such as attenuation and scattering.

For side monitoring stations located approximately 2m or slightly more from the object, no significant effects on seismic wave properties are observed in both the time and frequency domains. Similarly, the farthest side monitoring stations (s1, s2, s3, s4, and s5) show no discernible impact from the object on seismic waves. As the distance from the source increases, seismic energy gradually decreases.

In the study, it is noted that at a depth of 2m, the object can still be detected at the monitoring station directly above it and nearby side stations. However, beyond this depth, the effects on seismic waves may not be significant enough for detection (see Appendix C.3).

#### **4.5.6 Results for site B.**

#### **4.5.7 Model with buried object**

##### **I.First scenario: Object at 1m depth**

Based on the recorded seismic data at monitoring sites s36, s37, s38, s39, and s40, several key observations can be made. Firstly, monitoring station s36, being closest to the seismic source, records the shortest arrival time for seismic waves due to its proximity. Secondly, station s38, which is directly above the object, records a high wave amplitude, indicating significant seismic energy interaction with the object. The power spectral density (PSD) analysis further reveals a higher PSD value at station s38, suggesting increased energy content due to reflection or scattering by the object. Additionally, when comparing seismic waves at monitoring stations s31, s32, s33, s34, and s35, which are side stations located 2m or more from the object, station s33, adjacent to the object, records the highest wave amplitude among these stations. The PSD comparison shows that station s33 has the highest PSD amplitude, indicating detectable seismic signals originating from the object and a significant impact on this station. Notably, the effect of the object on the seismic waves is observable even at the farthest monitoring stations, located more than 4m away, in both the time and frequency domains (see Appendix C.4).

##### **II.Second scenario: Object at 2m depth**

In this scenario, the object is still 50m from the seismic source, but its depth has been increased to 2m. This adjustment aims to study the effect of depth on the spectral properties and trajectories of seismic waves. Monitoring station s36, being closer to the seismic source, records a higher wave amplitude compared to station s40, which is further away. Station s38, directly above the object, also shows a high wave amplitude, indicating significant seismic energy at this location. The power spectral density analysis shows that s38 recorded the highest seismic energy among the five stations, suggesting a stronger impact due to the object's proximity 2m below. A comparison of seismic waves at stations s31 to s35 reveals that the object still influences the recordings at a 2m depth, with s33 showing a notably high amplitude. This indicates the object's presence or activity can be detected by side stations. Even at the farthest monitoring stations, more than 4m from the object, the effect is noticeable both in time and frequency domains. Station s28, the farthest, recorded higher seismic energy than the

others, demonstrating that waves reflected from the object retain detectable energy over significant distances (see Appendix C.5).

**4.5.8 Seismic power variation**

*Note: the cells have been coloured based on the max PSD value for each case (red) and moving towards green as the values reduced compared to max value*

**Site A**

**Table 4.25:** Site A - Model 4 with buried object at 1m depth

S21	0.0012546	S16	0.001393	S11	0.001448	S6	0.001393	S1	0.001255
S22	0.0011019	S17	0.001204	S12	0.001259	S7	0.001204	S2	0.001102
S23	0.001	S18	0.001151	S13	0.001466	S8	0.001151	S3	0.001
S24	0.0008307	S19	0.000889	S14	0.000922	S9	0.000889	S4	0.000831
S25	0.0006099	S20	0.00063	S15	0.000639	S10	0.00063	S5	0.00061

**Table 4.26:** Site A - Model 4 with buried object at 2m depth

S21	0.0012422	S16	0.001376	S11	0.001428	S6	0.001376	S1	0.001242
S22	0.0010893	S17	0.001192	S12	0.001239	S7	0.001192	S2	0.001089
S23	0.0009977	S18	0.001125	S13	0.001217	S8	0.001125	S3	0.000998
S24	0.0008335	S19	0.000906	S14	0.000948	S9	0.000906	S4	0.000834
S25	0.0006099	S20	0.00063	S15	0.000638	S10	0.00063	S5	0.00061

**Site B**

**Table 4.27:** Site B - Model 4 with buried object at 1m depth

S46	0.0006178	S41	0.000615	S36	0.000613	S31	0.000615	S26	0.000618
S47	0.0005978	S42	0.000602	S37	0.000604	S32	0.000602	S27	0.000598
S48	0.0006699	S43	0.000697	S38	0.000739	S33	0.000697	S28	0.00067
S49	0.0004965	S44	0.000497	S39	0.000499	S34	0.000497	S29	0.000496
S50	0.0004782	S45	0.000484	S40	0.000486	S35	0.000484	S30	0.000478

**Table 4.28:** Site B - Model 4 with buried object at 2m depth

S46	0.0006162	S41	0.000612	S36	0.000611	S31	0.000612	S26	0.000616
S47	0.0005962	S42	0.000598	S37	0.000599	S32	0.000598	S27	0.000596
S48	0.0006679	S43	0.000685	S38	0.000694	S33	0.000685	S28	0.000668
S49	0.0004951	S44	0.000495	S39	0.000617	S34	0.000495	S29	0.000495
S50	0.0004771	S45	0.000482	S40	0.000561	S35	0.000482	S30	0.000477

**4.5.9 Discussion of results (model 4)**

At site A, closer to the seismic wave source, objects were detectable only directly above the monitoring stations up to a depth of 1m, with no noticeable impact on the side stations located 2m away. In contrast, at site B, which is further from the source, the decreased velocity and spherical spreading of the waves allowed for object detection at a depth of 2m and at distances exceeding 4m from the side monitoring stations.

**4.6 Summary of Seismic Wave Simulation**

**Table 4.29:** Results of numerical simulations and the effect of seismic wave source locations on the wave characteristics with changing speeds and frequencies. Green colour signifies the potential to detect objects, red colour indicates the incapacity to identify objects. Black colour indicates that the object is not simulated at this depth. The orange colour indicates that the methodology followed in this chapter.

Site A (< 30 m distance from the source)							
Model name	Seismic source frequency (Hz)	Shear velocity (m/s)	Potential for detecting objects at monitoring station located directly above the objects			Possibility of detecting objects at side monitoring stations (lateral distance)	
			@ 1m depth	@ 2m depth	@ 3m depth	@ 2m From object	@ 4m From object
Model 2	20	316	Green	Green	Green	Green	Red
Model 3	50	822	Green	Green	Green	Green	Red
Model 4	70	1783	Green	Orange	Black	Red	Red
Site B (> 50 m distance from the source)							
Model 2	20	316	Green	Green	Green	Green	Red
Model 3	50	822	Green	Orange	Orange	Green	Red
Model 4	70	1783	Green	Green	Black	Green	Green

#### 4.7 Further investigations based on numerical simulations (model 2)

To account for the variability in soils and their mechanical properties within brownfields, three distinct models were created to simulate objects buried in the subsurface. Each model was designed with different mechanical properties to represent the diverse soil conditions found across various locations within brownfields. To assess the characteristics of seismic waves in these different scenarios, sources of seismic waves with varying velocities were applied to each model.

Out of the three models, the model 2 most closely matched the soil characteristics seen in brownfield areas. It was purposefully chosen to be the focal point the investigations presented below because of this similarity. Site A was selected since the distance between the source and the observation points is less than 30m. Using the second model as a framework. The simulation process aimed to understand the influence of the mechanical characteristics of the soil on seismic wave propagation, reflection, and scattering. Important inquiries about the behaviour of seismic waves in this model were responded to throughout this extended investigation. The detectability and detect of objects buried at different depths were explored, along with the influence of object size on seismic energy distribution and the impact of varying seismic velocities on wave propagation. By incorporating steel and concrete objects, observations were made regarding how the properties of these materials interacted with seismic waves, affecting wave propagation, reflection, and scattering within the subsurface.

##### 4.7.1 How does the size of an object impact the reflection and transmission of seismic energy?

To answer this question, I have used a steel object of varying size. The steel object had a cube shape. The size of the cube was the only aspect that changed in the model; everything else remained the same.

**Table 4.30:** Shows the steel object dimensions.

	<b>Dimension (in x, y, z)</b>
Object 1	80 cm
Object 2	1 m
Object 3	1.5 m

Observation station No. s13 has been selected as it is directly located above the object. Figure 4.20 illustrates the effects of three different sizes of the object located at a depth of 1m on seismic wave energies. Notably, the PSD amplitude recorded in the case of the 80 cm size appears significantly larger compared to the PSD amplitude recorded for the 1m and 1.5m sizes of the object.

The analysis shows that subsurface object size and depth significantly affect seismic wave characteristics, as seen in Power Spectral Density (PSD) amplitude values. The PSD amplitude values for the 80 cm and 1.5 m objects show a consistent pattern across all depths. At 1 m depth, the PSD for the 80 cm object is approximately  $0.00008889 \text{ m}^2/\text{s}^3/\text{Hz}$ , while for the 1.5 m object, it is around  $0.0000692 \text{ m}^2/\text{s}^3/\text{Hz}$ . At 2 m depth, the PSD amplitude for the 80 cm object is  $0.00008268 \text{ m}^2/\text{s}^3/\text{Hz}$ , compared to  $0.0000580 \text{ m}^2/\text{s}^3/\text{Hz}$  for the 1.5 m object. At 3 m depth, the 80 cm object records a PSD of  $0.00008067 \text{ m}^2/\text{s}^3/\text{Hz}$ , while the 1.5 m object has a lower value of  $0.00005318 \text{ m}^2/\text{s}^3/\text{Hz}$ . Across all depths, the 80 cm object consistently produces higher PSD amplitude values, and both objects show a decrease in PSD amplitude as depth increases (see figure 4.20). This indicates that larger objects scatter and absorb more seismic energy, reducing the energy reflected back to the surface. Additionally, maximum PSD amplitude values decrease slightly with increasing depth, meaning that shallower objects have a more pronounced effect on seismic wave reflections. Therefore, smaller and shallower objects are more detectable due to their higher PSD impact, while larger and deeper objects require more sensitive detection techniques. This highlights the importance of considering both size and depth in seismic detection applications.

The discrepancy in energy can be explained by two possible scenarios. Firstly, for smaller objects, seismic waves may have been minimally affected, allowing a larger portion of seismic energy to pass through the model. Alternatively, significant reflection of seismic waves near the monitoring station could have resulted in a higher proportion of reflected energy being detected in the recordings.

In contrast, for larger objects, the recorded seismic energy is relatively lower. This can be attributed to two factors. Firstly, seismic waves may have encountered the edge of the object, causing a significant portion to be reflected before reaching observation station No. s13, thereby diverting energy away from the station. Secondly, the larger object size leads to the dispersion of seismic energy in multiple directions, causing the energy to be spread over a wider area and resulting in decreased energy levels at the observation station.

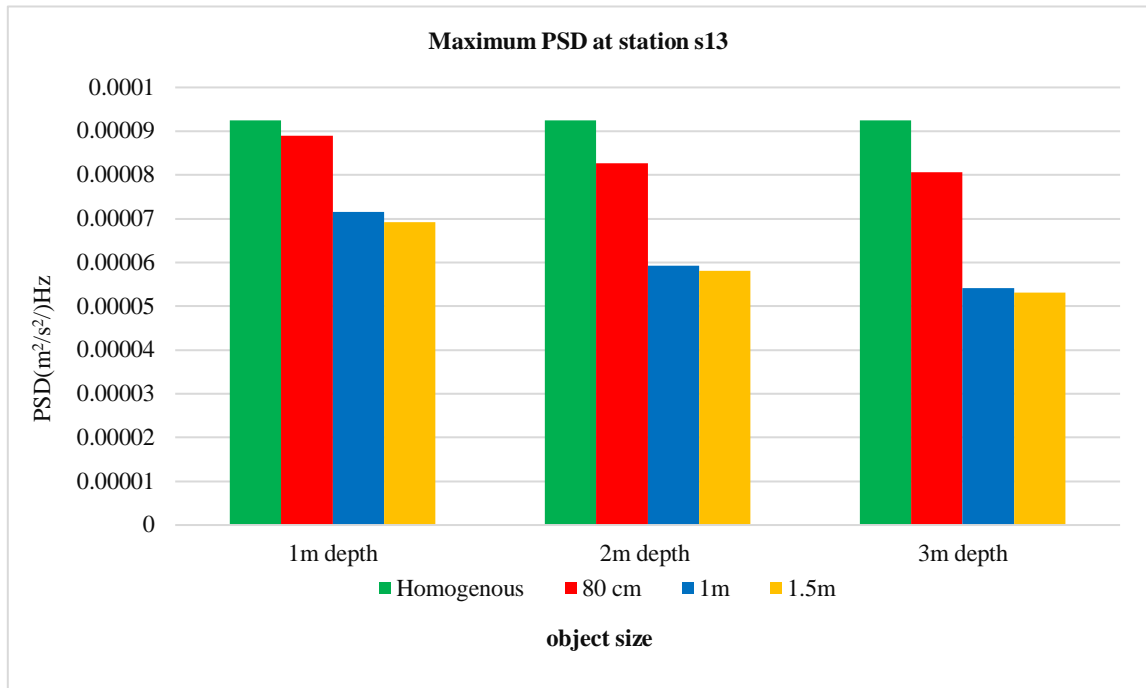


**Figure 4.20:** Maximum of PSD amplitude at monitoring station s13.

#### 4.7.2 What is the maximum depth at which objects can be identified or captured through the study of seismic wave properties?

##### 4.7.2.1 In case the object size (steel properties) is 80 cm × 80 cm × 80 cm

To address this question, some analyses conducted which is focusing on monitoring station No. s13, which is situated directly above the object. It should be noted that the ability to detect objects at specific depths is contingent upon the size of the object itself. To illustrate this relationship, I examined a figure where the object size was set at 80 cm and positioned at a depth of 1m.

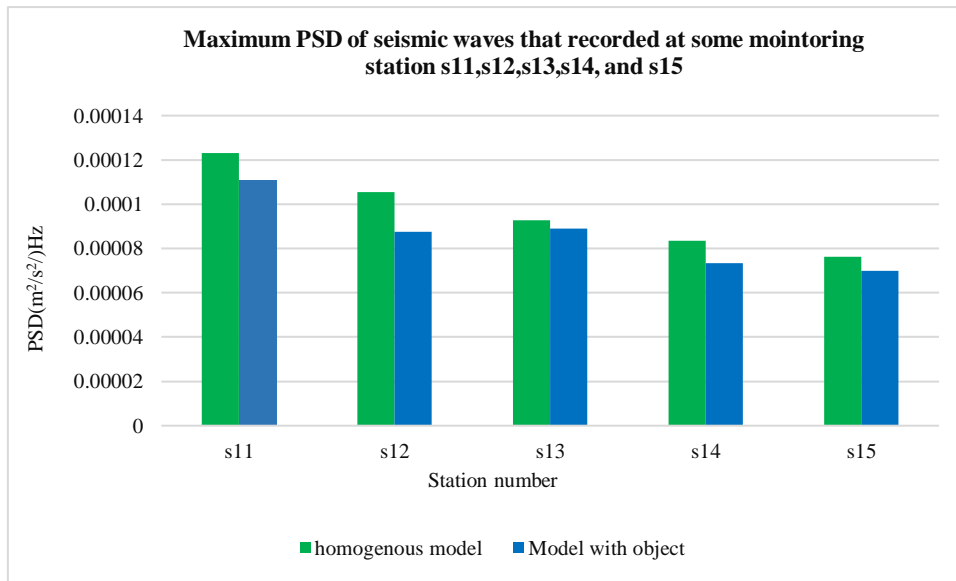


**Figure 4.21:** Maximum PSD value at station s11 – s15. Station s13, positioned directly above the object, displays the highest values among most stations. However, station s11 records the highest overall value due to its closer proximity to the seismic source. (The object is 1m depth).

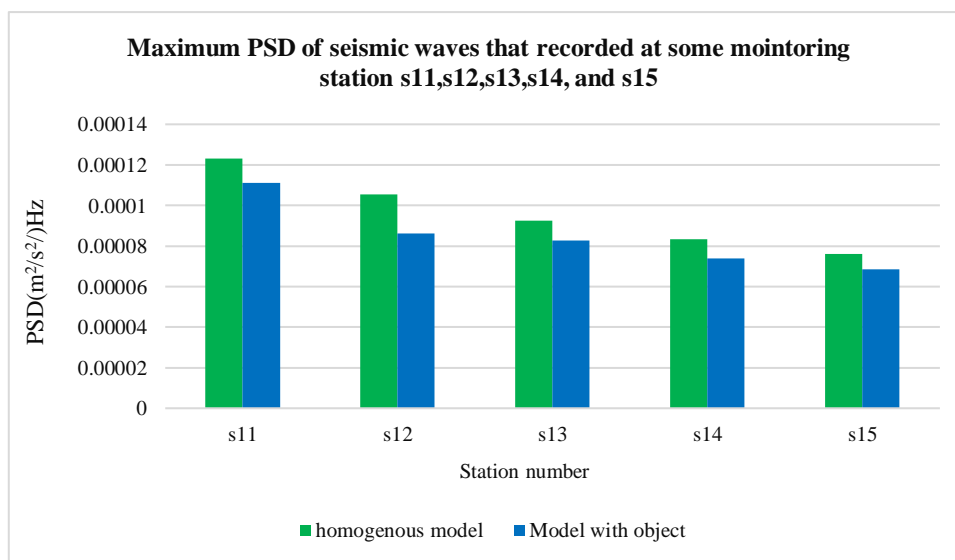


**Figure 4.22:** Maximum PSD value at station s11 – s15. Station s13, positioned directly above the object, displays a decrease in PSD value. (object at 2m depth).

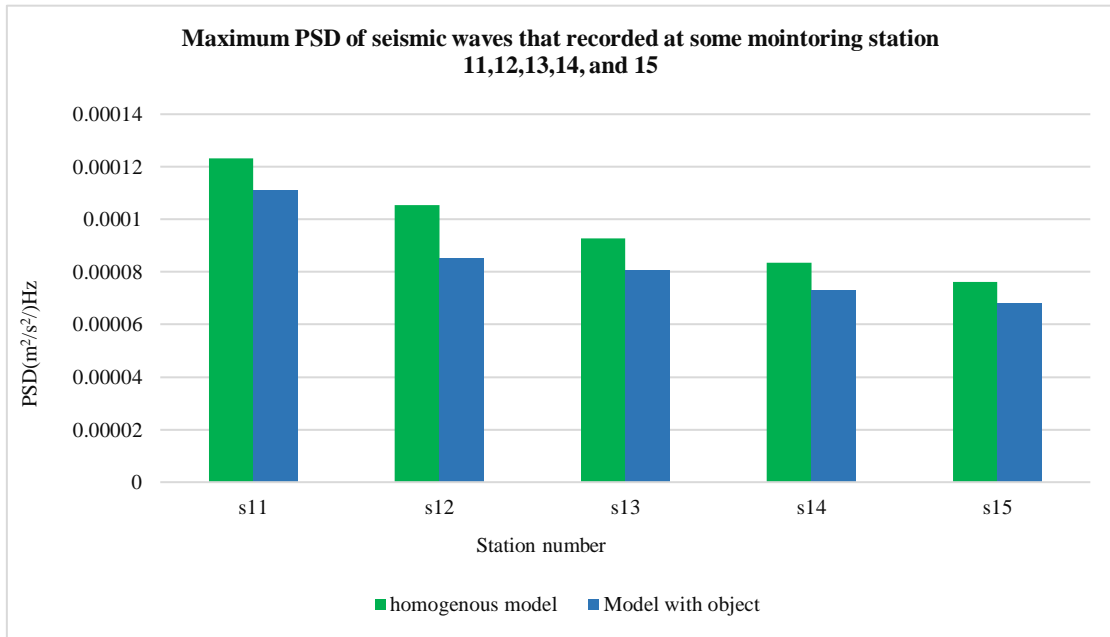


**Figure 4.23:** Maximum PSD value at station s11 – s15. Station s13, positioned directly above the object, displays a decrease in PSD value. (object at 3m depth).

The analysis of the figures shows a substantial decrease in the detectability of objects smaller than 1m, with PSD values dropping significantly for these smaller objects. This reduction indicates that smaller objects have a diminished impact on seismic wave reflections, making their detection challenging. The figures demonstrate that such objects can only be reliably detected within a maximum depth of 1m. Beyond this depth, the PSD values are too low to distinguish these objects from background noise, complicating their identification.

4.7.2.2 In the case of the object (steel properties) size 1 m × 1 m × 1 m

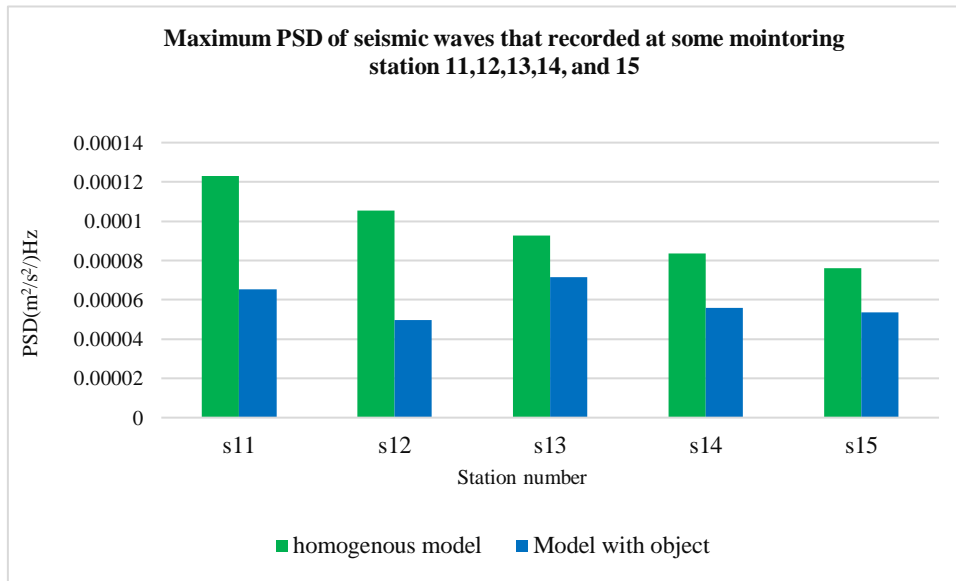


**Figure 4.24:** Maximum PSD value at station s11 – s15. Station s13, positioned directly above the object, displays a decrease in PSD value. (object at 1m depth).

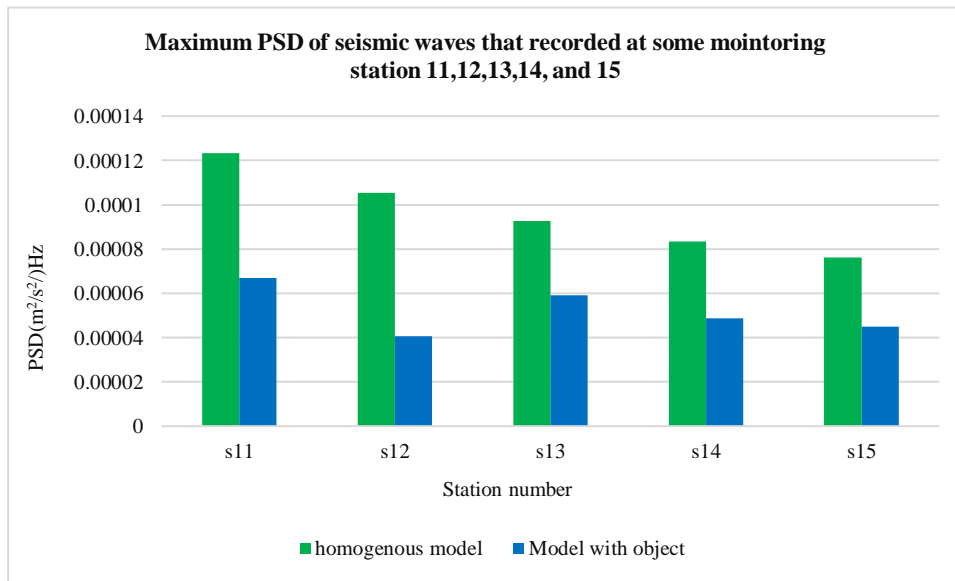


**Figure 4.25:** Maximum PSD value at station s11 – s15. Station s13, positioned directly above the object, displays a decrease in PSD value. (object at 2m depth).

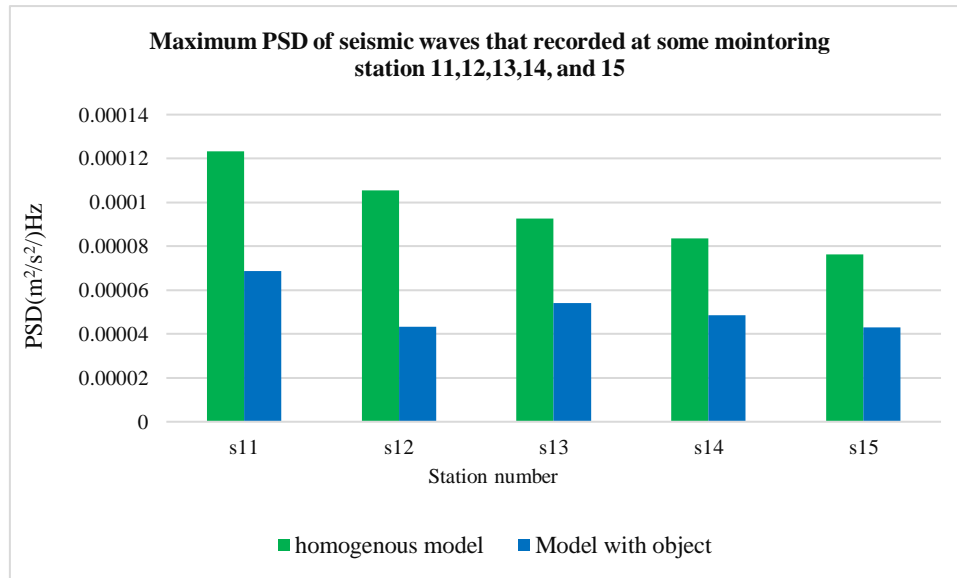


**Figure 4.26:** Maximum PSD value at station s11 – s15. Station s13, positioned directly above the object, displays a decrease in PSD value. (object at 3m depth).

The analysis conducted with an object size of 1m in the X, Y, and Z directions reveals compelling findings regarding its detectability. It has been observed that the objects can be successfully detected at depths of up to 3m when utilizing a monitoring station directly positioned above the object, specifically represented by monitoring station s13.

The results show that the object's presence can still be reliably detected at significant depths, as seismic waves propagate through the subsurface to the monitoring station. Data from station s13 consistently reveals clear indicators of the object, even as depth increases.

When the object size was 80 cm × 80 cm × 80 cm, the highest power spectral density (PSD) amplitude recorded was  $8.89 \times 10^{-5}$  m<sup>2</sup>/s<sup>2</sup>/Hz at station s13 (figure 4.26). In comparison, for objects sized 1m × 1 m × 1 m, the PSD values were  $7.15 \times 10^{-5}$  m<sup>2</sup>/s<sup>2</sup>/Hz. Despite these higher PSD values for small object, the 80 cm × 80 cm × 80 cm object could only be reliably detected at a depth of 1m, whereas objects ranging from 1m × 1 m × 1 m could be detected at depths up to 3m. When the object size was 1.5m × 1.5m × 1.5m, it was observed minimal difference compared to the 1m × 1 m × 1 m object. These results are presented in the appendix D.

#### 4.7.3 Can objects be detected at lateral monitoring stations, and what is the maximum distance at which they can be detected?

Based on the simulation results of seismic waves using the three models, I can assert that detecting objects at lateral monitoring stations is indeed possible. However, the feasibility of

detection depends on several factors that directly impact seismic wave propagation and interaction with the subsurface. One significant factor to consider is the size of the object itself. Smaller objects may present challenges in terms of detection at lateral monitoring stations due to the diminishing energy levels reaching those locations. Larger objects, on the other hand, tend to generate more pronounced seismic responses, increasing the likelihood of detection even at lateral monitoring stations.

The mechanical properties of the brownfield soil model, including composition, density, and elasticity, significantly impact seismic wave behaviour. High attenuation or low elasticity in the soil can impede wave propagation, reducing object detectability at lateral monitoring stations. Seismic wave velocity and source characteristics, such as frequency content and amplitude, also influence detection. Wave velocity affects the travel time to monitoring stations, while source characteristics determine wave strength and detectability at varying distances.

**4.7.3.1 In the case of the object (steel properties) size of 80cm**

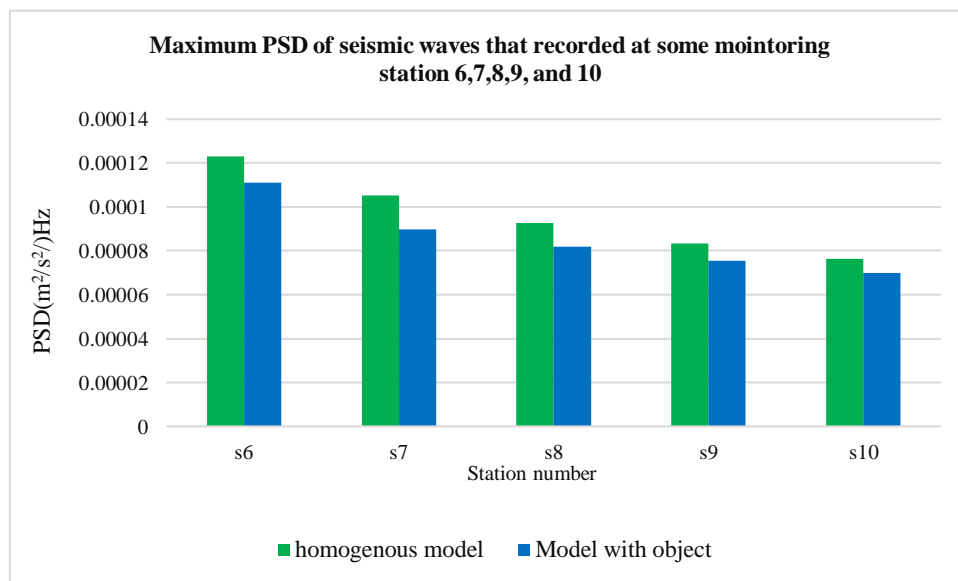


**Figure 4.27:** Maximum PSD value at station s6 – s10.

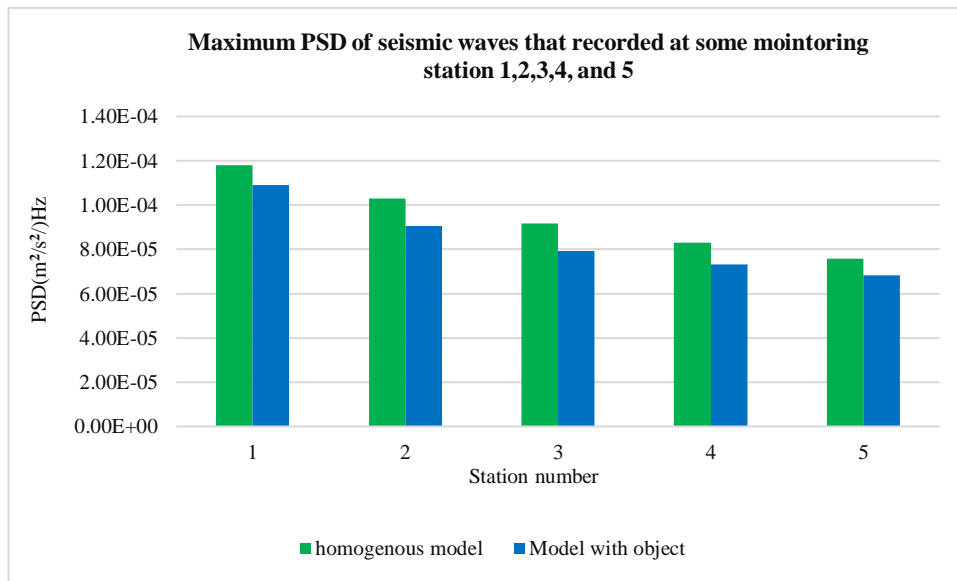


Figure 4.28: Maximum PSD value at station s1 – s5

4.7.3.2 In the case of the object (steel properties) size of 1m

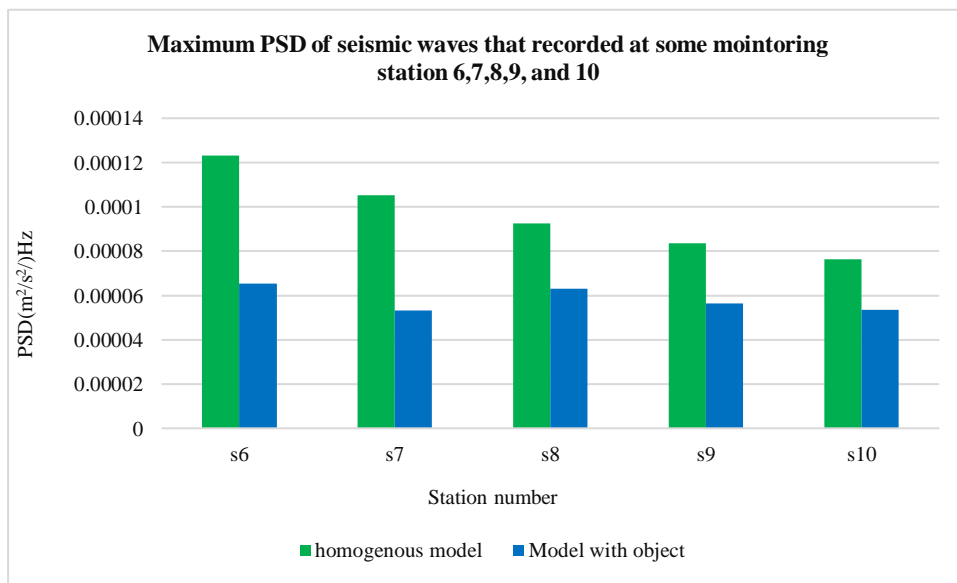
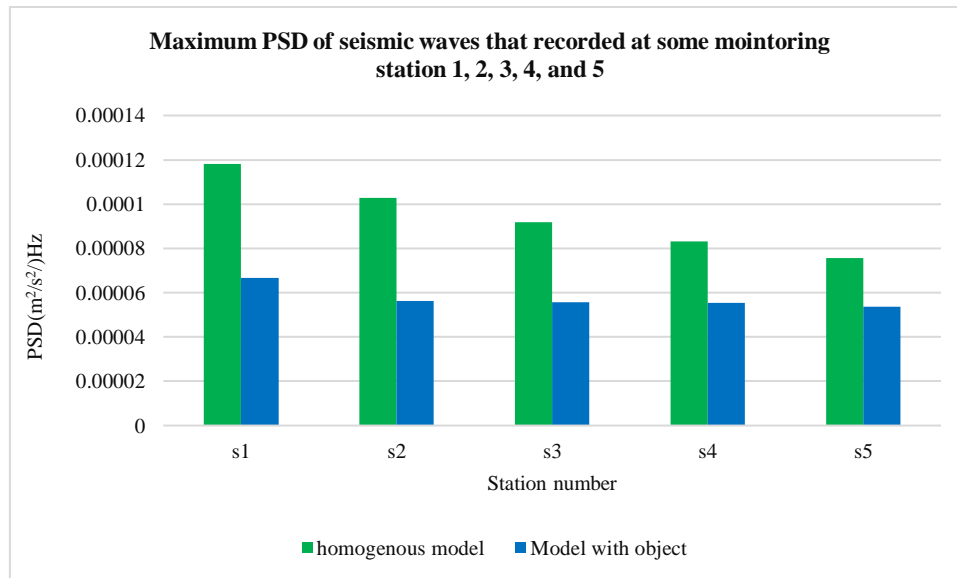


Figure 4.29: This figure compares maximum PSD amplitude values at side stations (s6-s10) for homogeneous and object models. Station s8 shows the greatest PSD reduction, indicating the object's strong effect on wave propagation (1m depth).



**Figure 4.30:** The monitoring stations, located 4 m or more from the object, show a reduction in seismic energy as the distance from the source increases. Consequently, the object's presence at a depth of 1 m has no noticeable impact at these lateral stations.

When considering objects with a size of 1m, my analysis reveals that they can indeed be successfully detected at lateral monitoring stations located at 2m or slightly more from the object. This notable finding underscores the reliability of detection capabilities even at laterally positioned stations.

As seismic waves interact with the subsurface and encounter the object, they exhibit complex behaviour that influences their propagation, reflection, and scattering. Despite the lateral distance between the monitoring stations and the object, the seismic waves still manage to carry valuable information about the presence of the object.

Based on ray path theory of the seismic waves which discussed in detail in chapter 3, as the object's depth increases, the incident and reflected angles become smaller, leading to reduced seismic energy and increased wave scattering. At depths of around 3m, seismic waves reflect almost vertically, with the angles becoming less steep at greater depths. As a result, the highest seismic energy is recorded by monitoring stations directly above the object, making it difficult to detect seismic signals at more distant lateral monitoring stations.

4.7.3.3 In the case of the object (steel properties) size of 1.5m

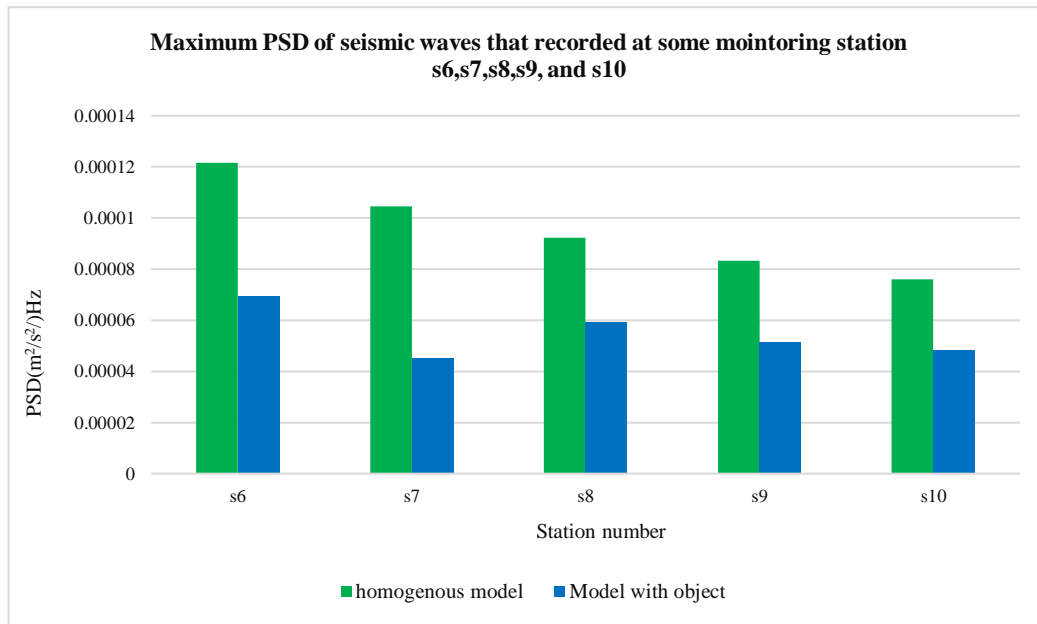


**Figure 4.31:** The monitoring stations are positioned about 2m or a little bit farther away from the object. Notably, Station s8 had the greatest PSD (Power Spectral Density) amplitude measurements that had ever been made. The important finding strongly implies that the object, which is located at a depth 1m, can be seen at a lateral distance of two metres from its position.

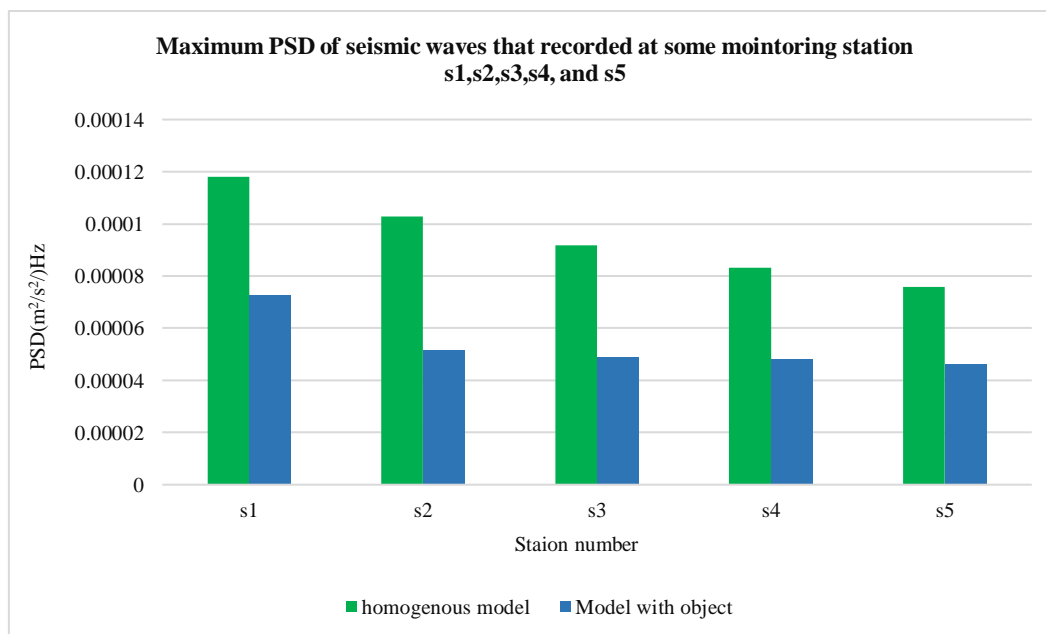


**Figure 4.32:** The monitoring stations are positioned 4m or somewhat farther away from object. As we go further away from the seismic source, the energy of the seismic waves decreases. As a result, the object's presence at these lateral monitoring stations, which is at a depth of 1m, has no obvious effect.

**4.7.4 Can concrete objects be detected in brownfield areas, and how does concrete affect the properties of seismic waves?**

To comprehend the variations in seismic wave properties resulting from differences in object mechanical properties, a comparison was conducted between steel and concrete objects. To achieve this, a concrete object was introduced to model 2 at site A to simulate its characteristics when seismic waves pass through or reflect from it. Choosing site, A only because the results at site B are expected the same as site A results. and also, to avoid exaggerating the thesis.

The concrete block has dimensions of 1 m × 1 m × 1 m in all direction. The table below presents the mechanical characteristics of the concrete object.

**Table 4.31:** Shows the mechanical properties of concrete.

	<b>Shear modulus</b>	<b>Bulk modulus</b>	<b>Density</b>
Concrete	70 <sup>9</sup> Pa	60 <sup>9</sup> Pa	2800

**4.7.4.1 Can the properties of reflecting seismic waves be used to detect the concrete object buried at depths ranging from 1 to 3m below the surface of the earth?**

Based on the simulation results on the concrete object, it is evident that a concrete object buried at close depths to the surface of the earth can be successfully detected. The simulations conducted on the second model, with the concrete object positioned at site A directly beneath Station No. s13, provided compelling evidence of its detectability.

The recorded data at Station No. s13 demonstrated clear indications of the concrete object's presence. Seismic waves interacting with the concrete material exhibited distinct responses, enabling reliable identification of the buried object.

In Figure 4.33, a comparison is presented between seismic waves recorded at monitoring stations s11, s12, s13, s14, and s15, all positioned along the Y-axis. An intriguing observation emerges from the analysis: the seismic waves recorded at monitoring station s13, which lies directly above the object's location, exhibit the highest amplitude among all the recorded waves. This notable discrepancy in amplitude strongly indicates the presence of the object beneath monitoring station s13. The distinct high amplitude recorded at this specific station reaffirms the object's detectability based on the information derived from the time domain of the seismic waves.

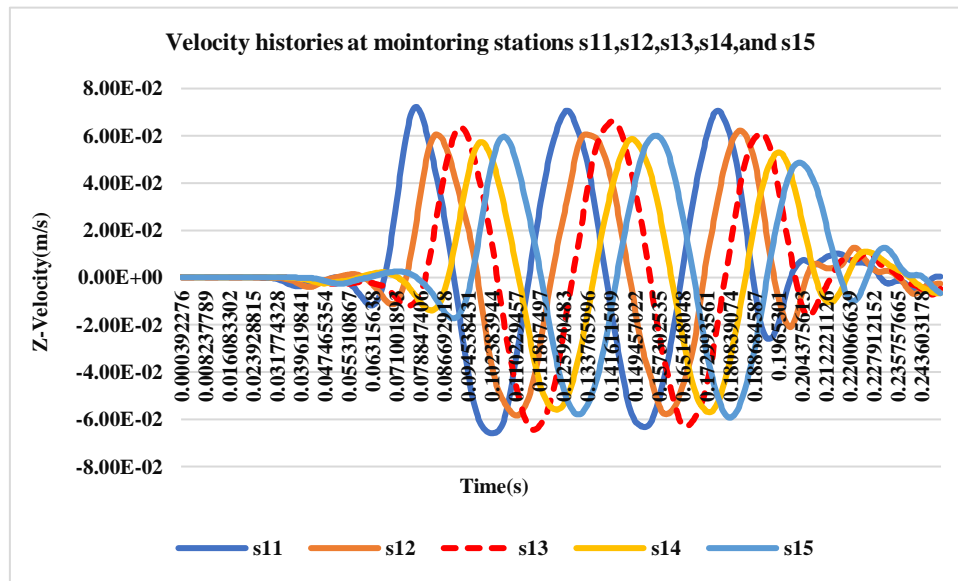


**Figure 4.33:**The time domain comparison where we can see the monitoring station s13 which deployed over the object reflected with high amplitude.

The amount of reflected energy detected at each station can be determined by comparing the PSD of seismic waves recorded from monitoring stations s11, s12, s13, s14, and s15. A measure of the energy distribution in the seismic waves that were recorded is the power spectral density. Notably, the findings show that monitoring station No. s13, which was directly above the object—recorded the highest energy levels across the PSD. The possibility of capturing detection with concrete qualities is strongly supported by this remarkable observation.

The increased energy levels at monitoring station No. s13 show that the seismic waves and the concrete object have had significant interaction. The distinct characteristics of concrete have a noticeable effect on wave propagation, which causes a noticeable response in the seismic data that was acquired. This demonstrates the capability of seismic techniques to successfully locate concrete objects buried below the surface.

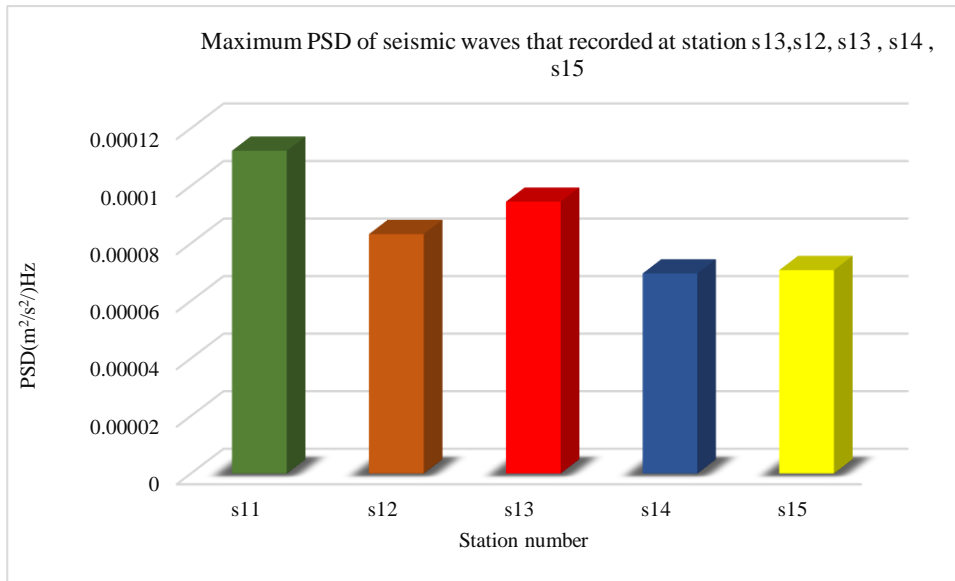


**Figure 4.34:** The PSD (Power Spectral Density) maximum values are shown in the figure, which highlights an interesting finding. Station 13's PSD has the highest PSD values.

The investigation into the characteristics of concrete objects provides important knowledge on their detection. It was discovered that side observation stations placed 2m or slightly away from the object's location can detect concrete objects. Because seismic waves and concrete react differently, it is possible to reliably identify and record the presence of the object figure 4.35. However, attenuation makes the task more difficult for observation stations that are 4m or more away, leading to lower energy levels and less certain identification (as shown the figure below).

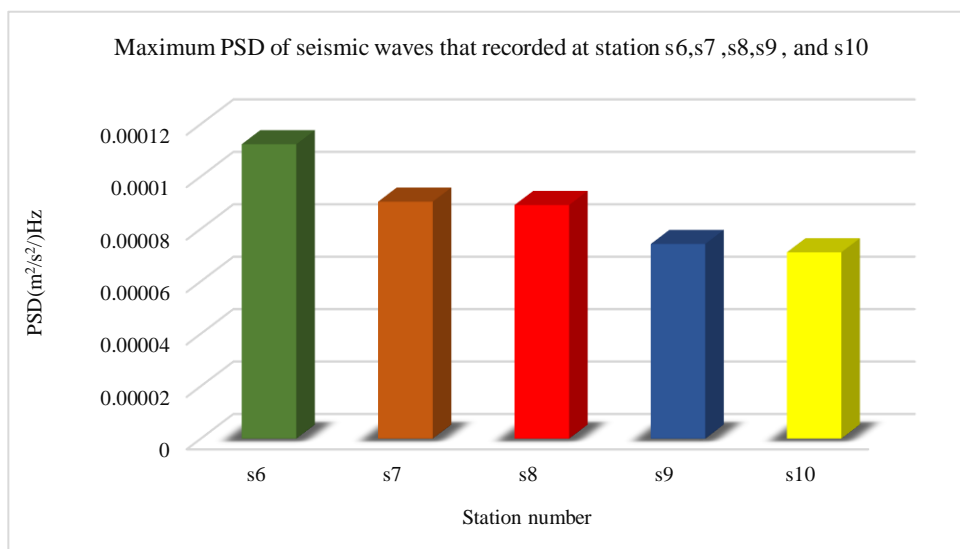


**Figure 4.35:** The PSD (Power Spectral Density) amplitude values displayed reveal an intriguing finding: the greatest PSD amplitudes are found at Station s8.

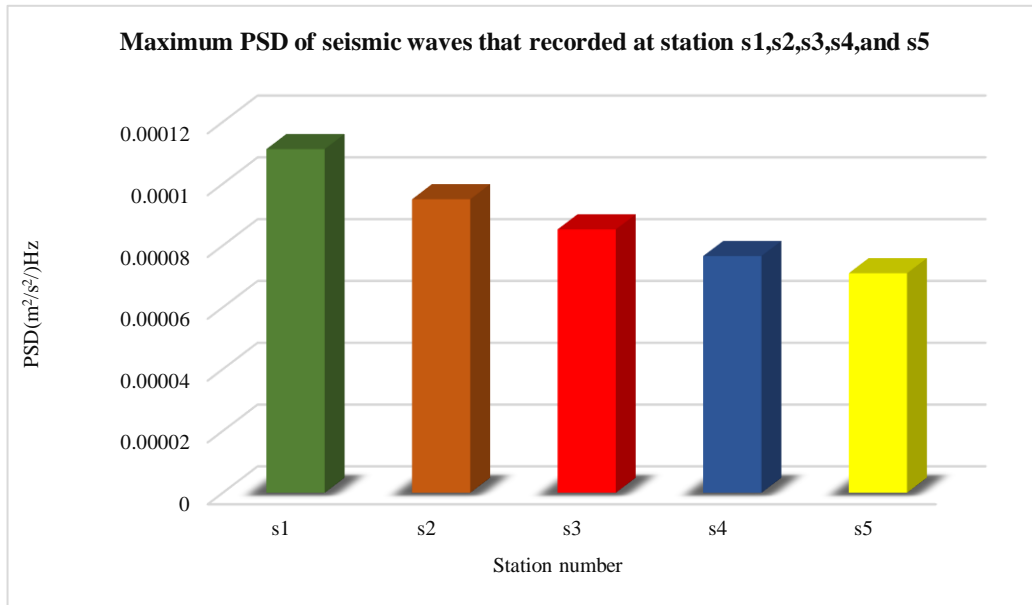


**Figure 4.36:** The monitoring stations are positioned 4m or somewhat farther away from the object. As we go further away from the seismic source, the energy of the seismic waves decreases. As a result, the object's presence at these lateral monitoring stations, which is at a depth of 1m, has no observable influence.

#### 4.7.5 The relationship between object depth and the quantity of reflected energy

Figure 4.37 shows the comparison of seismic energy represented by the Power Spectral Density (PSD) recorded at monitoring station s13. In this scenario, the object placed directly beneath station s13 is composed of steel material. The aim is to investigate the effect of object depth on the seismic energy recorded. Through careful analysis, I observed a clear trend in the PSD as the object depth increased from the model's surface toward the top of the model. Specifically, as the object depth increases, the PSD experiences a gradual decrease. This decline in PSD indicates a reduction in the amount of reflected energy recorded at monitoring station s13.

The observed trend can be attributed to the varying distances the seismic waves have to travel from the source to the object and then to the monitoring station. As the object is placed deeper into the model, the seismic waves encounter a larger volume of the surrounding medium, leading to energy dispersion and attenuation. Consequently, less energy reaches the monitoring station, resulting in lower PSD values.

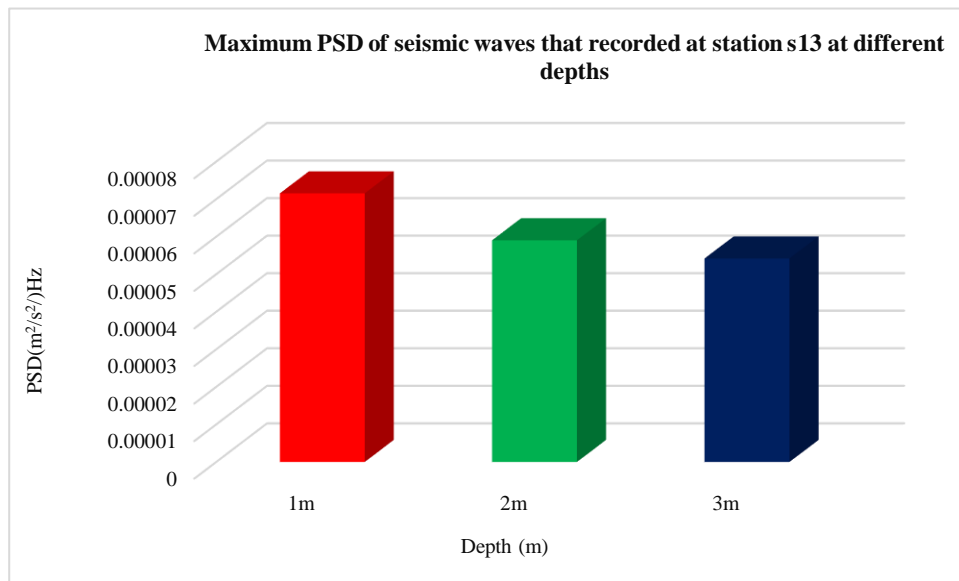


**Figure 4.37:** Monitoring station s13 shows a trend in Power Spectral Density (PSD) amplitude as the object depth increases. This decrease in PSD that seismic energy captured diminishes as the object is deeper (the object is steel).

#### 4.7.6 How do the mechanical properties of objects (concrete and steel) influence the amount of seismic energy reflected from them?

Based on the simulation results of seismic waves interacting with different objects, including concrete and steel, a clear distinction emerges between their respective characteristics in brownfields. While both objects can be successfully detected in this environment, their mechanical properties influence the amount of seismic energy reflected.

Steel, known for its high hardness and greater density compared to concrete, leads to a dispersal of seismic energy upon collision. Consequently, the amount of seismic energy reflected from steel objects is relatively small. On the other hand, concrete, with its distinct properties, exhibits a different response. Seismic waves interacting with concrete objects experience less dispersion, resulting in a higher amount of seismic energy recorded (Tang *et al.*, 2022).

The contrasting energy reflection patterns between concrete and steel have significant implications for shallow subsurface investigations and object identification.

In Figure 4.38, a comparison between steel and concrete objects is depicted. The seismic waves' interactions with these two distinct materials are highlighted, showcasing their contrasting effects on the recorded seismic energy.

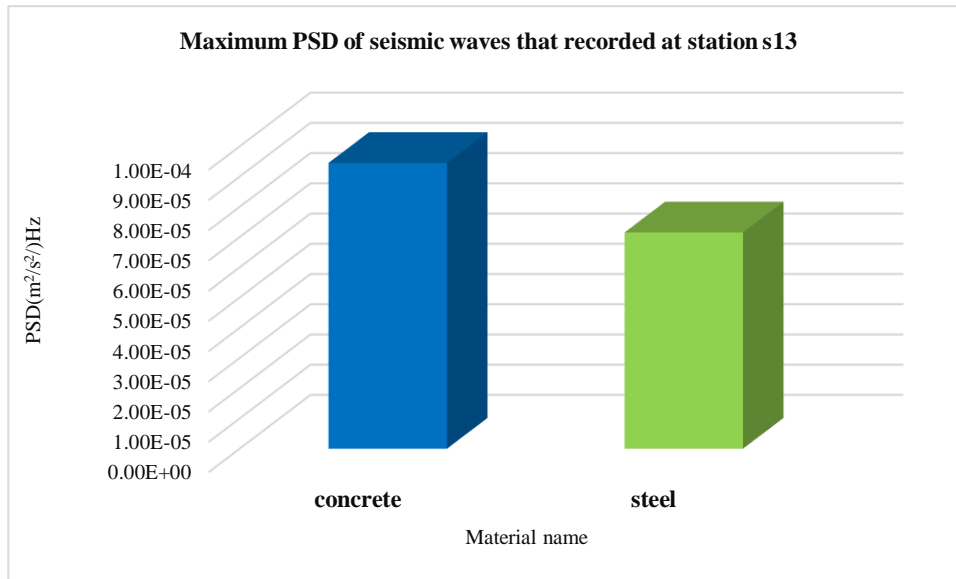


**Figure 4.38:** Monitoring station s13 recorded the highest frequency spectrum density for both steel and concrete objects, with the PSD for the concrete object being higher than that of the steel object.

#### 4.7.7 What is the most suitable source of seismic waves to be utilized for shallow subsurface investigations in brownfields?

The comprehensive study of simulated seismic waves involved the application of three distinct sources, each represented by a sinusoidal wave with frequencies of 20 Hz, 50 Hz, and 70 Hz. These seismic waves were applied to three separate models, specifically the model 2, model3, and model 4, respectively. The selection of frequencies, 20 Hz, 50 Hz, and 70 Hz, was a meticulous process that considered the mechanical properties of the homogeneous model and the shear velocity of the seismic waves. The primary objective was to ensure that the passage of seismic waves through the model was smooth and undisturbed. The variation in shear velocity, specifically 316, 822, and 1783 m/s, was important in addressing the heterogeneity of soil and brownfields, where mechanical properties can vary significantly. By incorporating these distinct shear velocities, I was able to emulate real-world scenarios more accurately and replicate the diverse conditions encountered in subsurface environments.

The model 2 used seismic wave simulations with a shear velocity of 316 m/s and 20 Hz. The waves spread horizontally and vertically, causing significant energy reflections at depths of 1, 2, and 3m. Monitoring stations above the object detected a significant increase in reflected energy, indicating a strong interaction between the waves and the object. Additionally, side monitoring stations 2m away from the object recorded a considerable amount of reflected seismic energy, confirming the object's significant influence on seismic wave behaviour, resulting in energy reflections at lateral distances. In the model 3, the shear velocity increased

to 822 m/s, and the frequencies of the seismic wave source were raised to 50 Hz. As a result, we observed that the objects buried in Site A and Site B could be detected at both the monitoring stations positioned directly above the objects and the side monitoring stations located 2m away. This successful detection validates the accuracy and effectiveness of identifying the objects at these specific locations.

In the model 4, characterized by an increased shear velocity of 1738 m/s and frequencies of seismic waves set at 70 Hz, it was observed distinct effects on object detection at different locations. At site A, closer to the seismic wave source, objects were only detectable directly above the monitoring stations up to a depth of 1m. There was no noticeable impact on the side stations located at 2m. Conversely, at site B, further away from the source, the decreased velocity and spherical spreading of the waves allowed for object detection not only at a depth of 2m but also at a distance exceeding 4m from the side monitoring stations. According to the findings from this chapter, the ideal seismic wave source for brownfields should possess a frequency range between 20 to 70 Hz and maintain a velocity of seismic waves below 1800 m/s. These specific characteristics enable seismic waves to propagate extensively both horizontally and vertically.

With such a seismic wave source, objects located in proximity, within less than 30m, can be accurately detected. Furthermore, this setup allows for the successful detection of distant objects situated beyond 30m. The object can be detected at both the monitoring station located directly above it and the side monitoring station positioned 4m away from the object, at depths of up to 3m.

## Chapter 5 : Validation of numerical modelling results

### 5.1 Introduction

Chapter 5 is dedicated to validating the outcomes of the seismic wave simulation from numerical modelling discussed in Chapter 4. For this purpose, I made use of experimental data collected during a previous field experiment carried out at Heriot-Watt University campus (unpublished data), where a passive seismic survey was designed and conducted aiming to identify two buried objects a PVC pipe and a JCB bucket.

I used my numerical model to try and interpret the results from the analysis of the field data as presented in Yfantis and Pytharouli (2015), an internal Strathclyde report, made available to me by Dr Pytharouli.

### 5.2 Field experiment

#### 5.2.1 Instrumentation

A passive micro seismic array comprising three single - component short period seismometers and two 3 – components seismometers short period seismometers with a flat response between 1Hz and 100Hz was utilised. Seismometers were linked to two data-loggers (130 RefTek) that utilised a 200Hz sampling rate. Separately connected to GPS antennas for the purpose of time synchronisation, both data loggers were fuelled by 40Ah, 12V car batteries. Every sensor was affixed directly to the surface of the soil.

#### 5.2.2 Experiment BP: Buried PVC Pipe

A trench was dug to a depth of 1.5m, as depicted in figure 5.1 a, and subsequently a PVC pipe measuring 6.21 m in length with a 0.5 m diameter was placed within it.

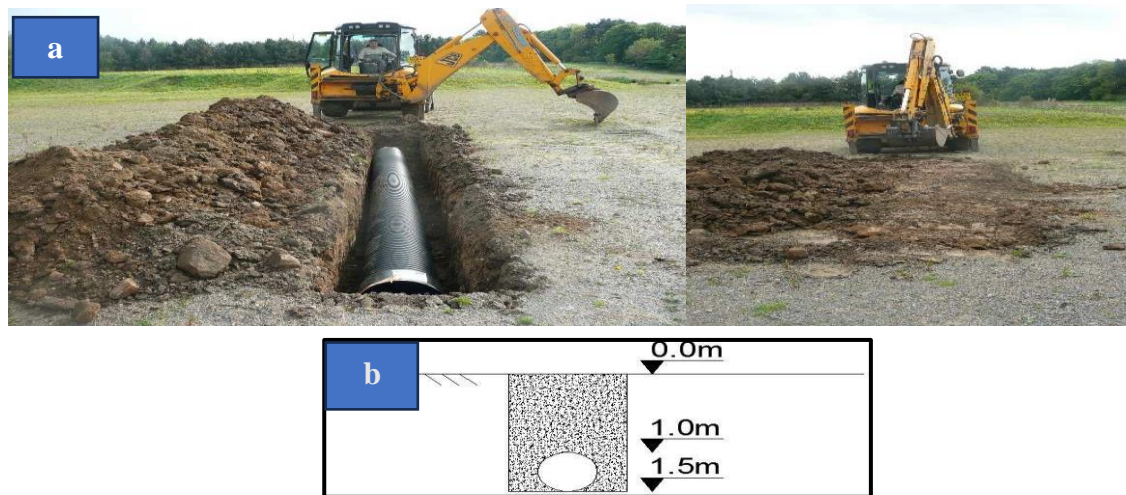


**figure 5.1:** a) Images illustrating the PVC pipe's condition, one when it was initially positioned in the trench (on the left), and the other after it had been buried (on the right), are provided. b) A visual representation is included, illustrating the different depths involved in Experiment BP (after Yfantis and Pytharouli 2015).

### 5.2.2.1 Seismic array geometry (Experiment BP)

This geometry is shown in Figure 5.2. Two of 3D sensors placed directly above the pipe. One of the 1D sensor was placed to the north, between the seismic wave source and the object, and the other 1D sensor was placed to the west. Two sensors were placed close to each other, one 1D and the other in 3D on the southern side of the object.

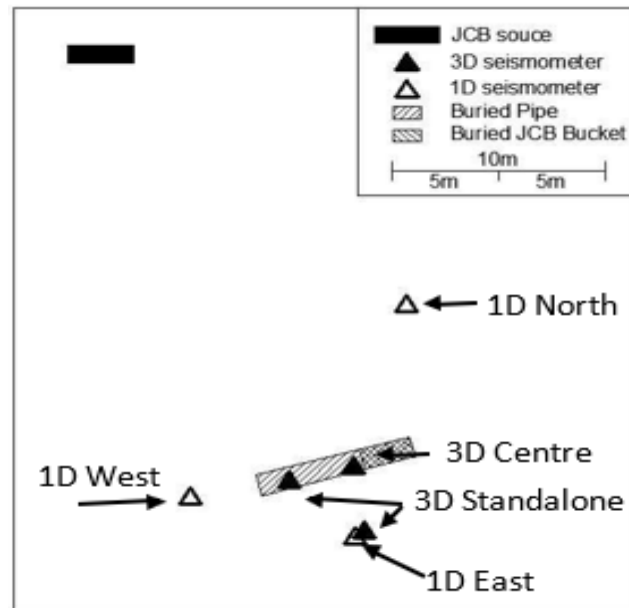


**Figure 5.2:** Deployment geometry of the seismometers, the area where the PVC pipe was buried as well as the location of the JCB (after Yfantis and Pytharouli 2015).

### 5.2.3 Experiment BB: Buried bucket

In this experiment, the object buried in the trench was a JCB bucket, as depicted in Figure 5.3a. The bucket occupied a relatively smaller portion of the excavated trench, as shown in Figure 5.3b, with dimensions measuring 1.52m in length, 0.6m in width, and 0.5m in height.

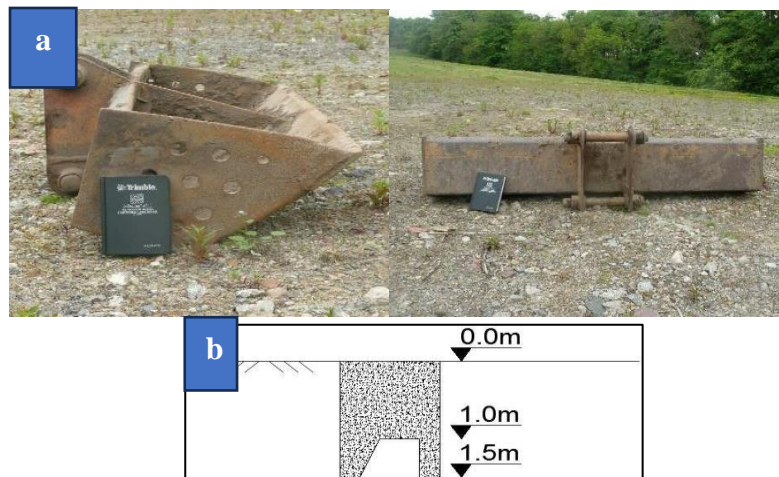


**Figure 5.3:** a) JCB bucket used for this experiment. b) Cross section of buried bucket with elevation marks shown (after Yfantis and Pytharouli 2015).

#### 5.2.3.1 Nanoseismic geometry (Experiment BB)

This geometry is shown in Figure 5.4: The description of the seismometer placement, the area where the JCB bucket was buried, and the positioning of the JCB vehicle (after Yfantis and

Pytharouli 2015), and only one 3D sensor directly above the buried JCB bucket. One of the 1D sensor was placed to the north, between the seismic wave source and the object, and the other 1D sensor was placed to the west. Two sensors were placed close to each other, one 1D and the other in 3D on the southern side of the object.

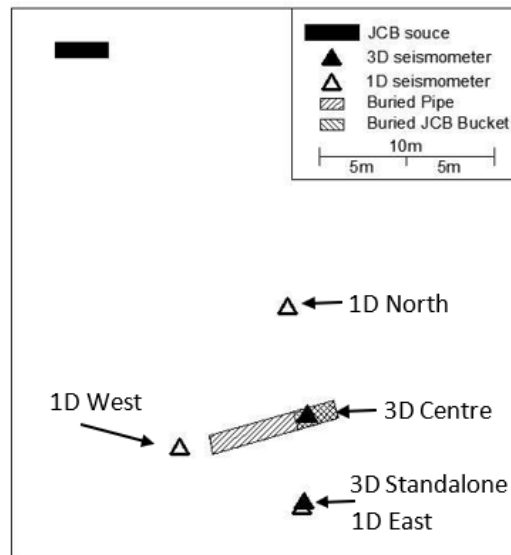


**Figure 5.4:** The description of the seismometer placement, the area where the JCB bucket was buried, and the positioning of the JCB vehicle (after Yfantis and Pytharouli 2015).

#### 5.2.4 Spectral analysis of seismic waves

Analysis of seismic data showed that the sensors deployed directly above the objects recorded a high amount of seismic energy compared to the seismic energy recorded by sensors placed several meters away from these objects. This is the best evidence that objects buried in brownfields can be detected using micro seismic technology.

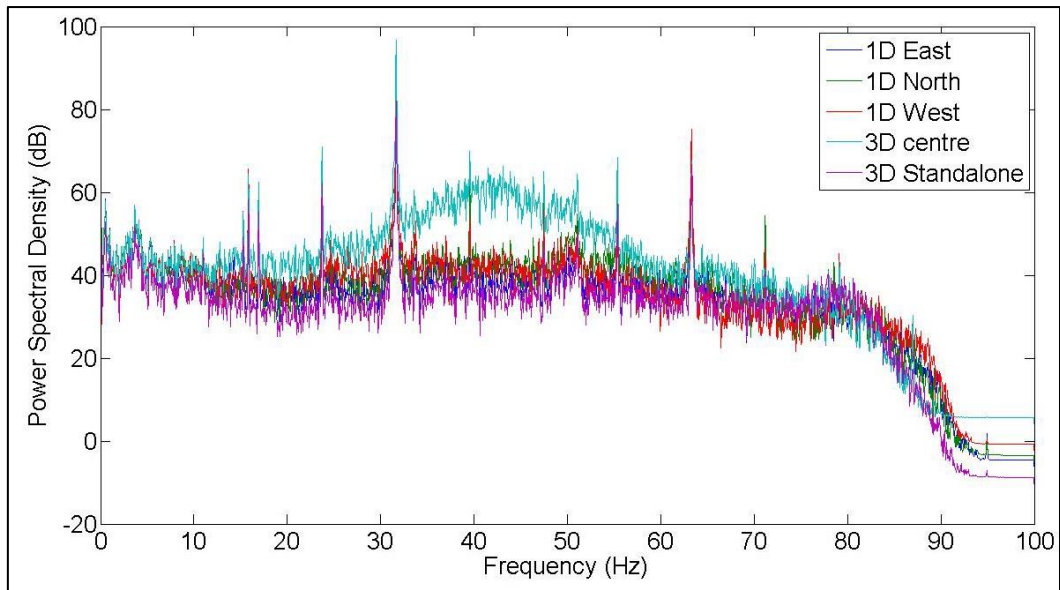


**Figure 5.5:** PSD curves of all vertical traces of all sensors. All curves are almost identical except the curve corresponding to the 3D sensor Centre (for the frequencies between 30Hz and 55Hz) which is placed upon the buried PVC pipe (after Pytharouli 2015).

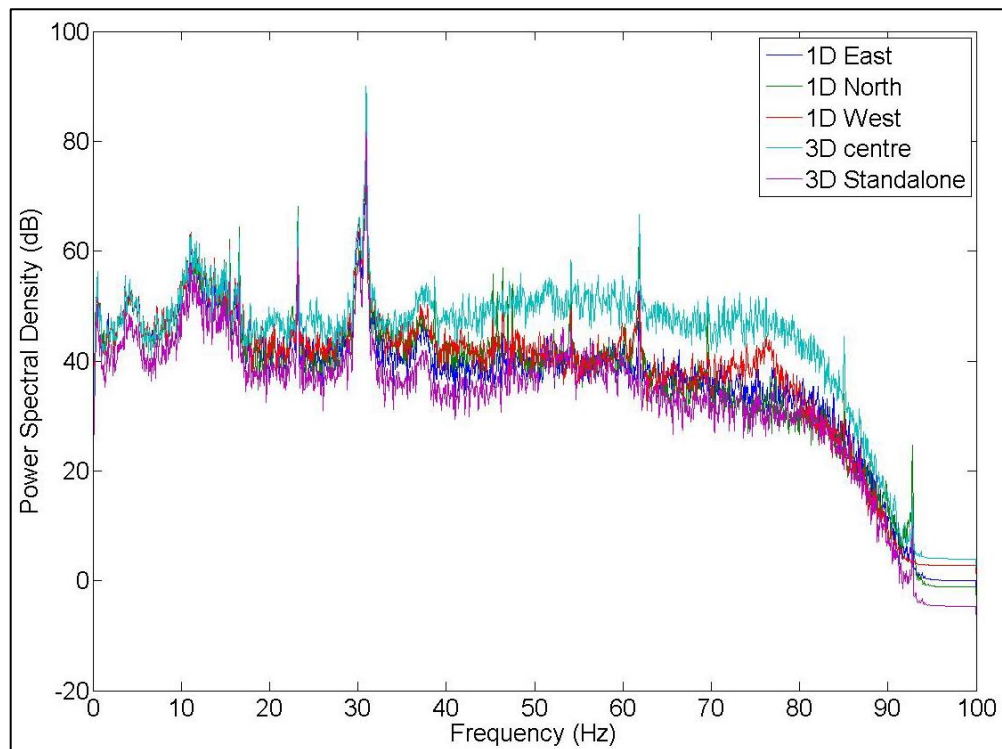


**Figure 5.6:** PSD curves of all vertical traces for the time window analysed when the JCB bucket was buried. All traces are identical except the vertical trace of the 3D central seismometer, which is placed upon the buried JCB bucket. Its spectral amplitude is higher between frequencies 20Hz to 85Hz, with the differences more evident after 35Hz (after Pytharouli 2015).

### 5.3 Simulation of the objects (PVC pipe and a JCB bucket) that used in Heriot Watt experiment study.

In this study, numerical modelling was used to simulate seismic waves passing through or reflecting from a PVC pipe and a JCB bucket. The model was designed to replicate the mechanical properties of the gravelly clay soil at the experimental site. The dimensions of the model—50 m long in the x-direction, 70 m wide in the y-direction, and 30 m high in the z-direction—matched those of previous models (2, 3, and 4) to ensure consistency in the results. The model mesh had an element size of 1 m × 1 m × 1 m in 3D. Additionally, a PVC pipe and a JCB bucket, with the same dimensions as those used in the field experiment, were included in the model to simulate real-world conditions accurately.

#### 5.3.1 Simulation of PVC pipe

##### 5.3.1.1 Dimensions and mechanical properties of PVC pipe

The PVC pipe is about 6.2m long and 0.6m in diameter. It was placed at a depth of 1m from the surface of the model to the top of the pipe. The following table shows the virtual mechanical properties of PVC pipe.

**Table 5.1:** Mechanical properties of PVC pipe (De Martins, Freire and Hemadipour, 2009).

	Shear modulus Pa	Bulk modulus Pa	Density (kg/m <sup>3</sup> )
PVC pipe	0.5 x 10 <sup>9</sup>	5 x 10 <sup>9</sup>	1200

##### 5.3.1.2 dynamic input

The same seismic source used in Model 4 (Chapter 4) was applied. A sine wave with an amplitude of 1 m and a frequency of 70 Hz. This is applied on the model surface as a single seismic source.

##### 5.3.1.3 monitoring stations and source array

Figure 5.7 below shows the locations of the monitoring stations and the distance between them, as well as the location of the source of the seismic waves.

**Note:** Stations A, B, C, D, and E from the simulation (figure 5.7) correspond to the following stations in the field experiment: A is 1D North, B is 3D Centre, C is 3D Standalone, E is 1D East, and D is 1D West.

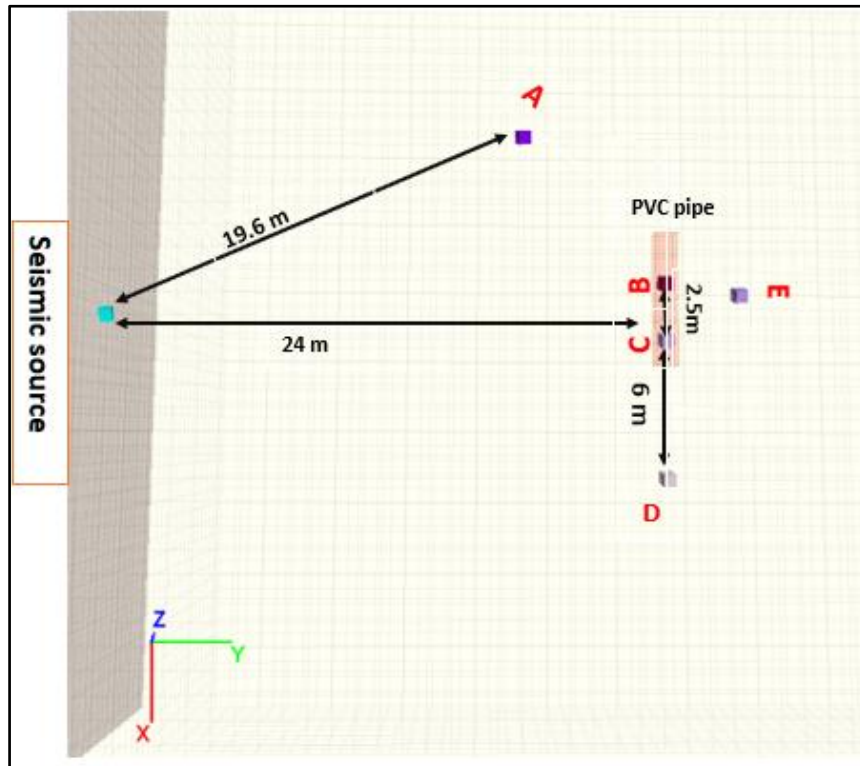


**Figure 5.7:** The figure illustrates the locations of the monitoring stations (A, B, C, D, and E) on the model surface, including the distances between them and from the seismic source. It also indicates the position of the object (PVC pipe), which is situated beneath stations B and C.

#### 5.3.1.4 Velocity history results of the PVC pipe simulation

In this simulation of seismic waves, the history velocities were recorded in the z component at all monitoring stations A, B, C, D, and E. Figure 5.8 shows the comparison between the history of velocities in the time domain of seismic waves at all monitoring stations. The two monitoring stations B and C recorded the highest amplitude of seismic waves compared to the other stations.

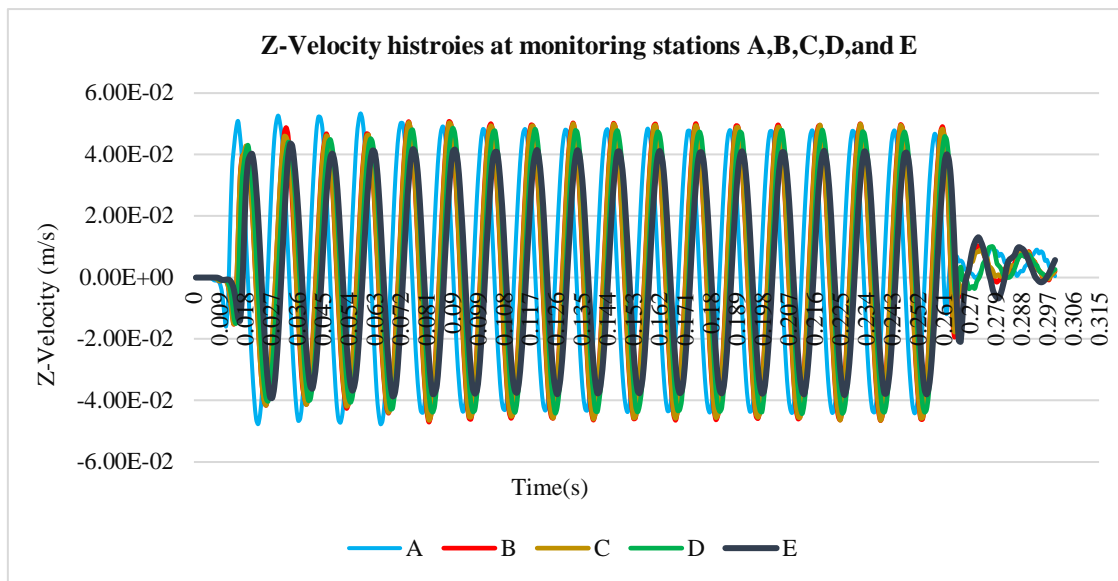


**Figure 5.8:** A comparison of velocity histories recorded at monitoring stations A, B, C, D, and E showed that stations B and C had the highest wave amplitudes, indicating that these two stations received the largest amount of seismic energy.

### 5.3.1.5 Spectral properties of the seismic waves

The seismic waves recorded at monitoring stations B and C showed high PSD values, indicating they received a greater amount of seismic energy reflected from the PVC pipe.

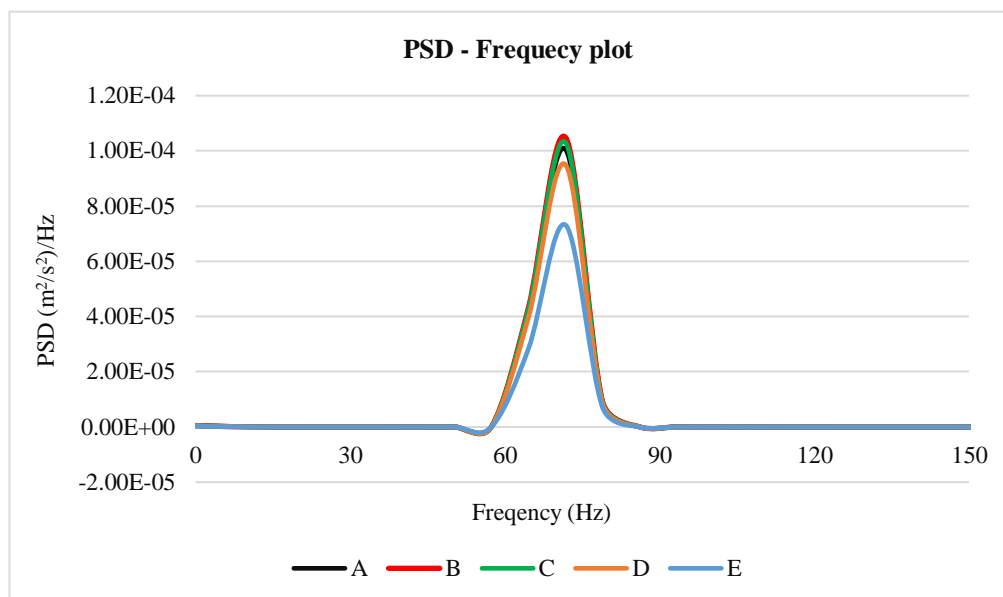


**Figure 5.9:** The PSD of seismic waves recorded at monitoring stations A, B, C, D, and E. Stations B and C, located directly above the PVC pipe, exhibit the highest power spectral density values, indicating they recorded the largest amount of reflected seismic energy.

### 5.3.1.6 Calculating the area under PSD curves

**Table 5.2:** The calculated area under the density curves is represented in Figure 5.9, High seismic energy is indicated by red, while low energy is represented by green.

A	0.000153
B	0.000158
C	0.000157
D	0.000144
E	0.000109

From the table above, it is clear that stations B and C, located directly above the object, recorded the highest value of reflected seismic energy.

### 5.3.2 Simulation of JCB bucket

#### 5.3.2.1 Geometry and mechanical properties of the model

The same previous model that was used in the simulation of the PVC pipe with the same dimensions and properties, as well as the same source of seismic waves, and the only change is to replace the PVC pipe with a JCB bucket. JCB bucket has mechanical properties and is made of alloy steel material, and it differs from the PVC pipe as in table 5.3. The JCB bucket is about 1.5m long and 0.6m in diameter. It was placed at a depth of 1 m from the surface of the model to the top of the bucket under monitoring station B.

**Table 5.3:** Mechanical properties of JCB bucket.

JCB bucket (Alloy steel)	Shear modulus Pa	Bulk modulus Pa	Density kg/m <sup>3</sup>
	$60 \times 10^{10}$	$120 \times 10^{10}$	8000

#### 5.3.2.2 monitoring stations and source array

Figure 5.10 below shows the monitoring stations' locations and the distance between them, as well as the location of the source of the seismic waves.

**Note:** Stations A, B, C, D, and E from the simulation (figure 5.10) correspond to the following stations in the field experiment: A is 1D North, B is 3D Centre, C is 1D west, D is 1D East, and E is 3D standalone.

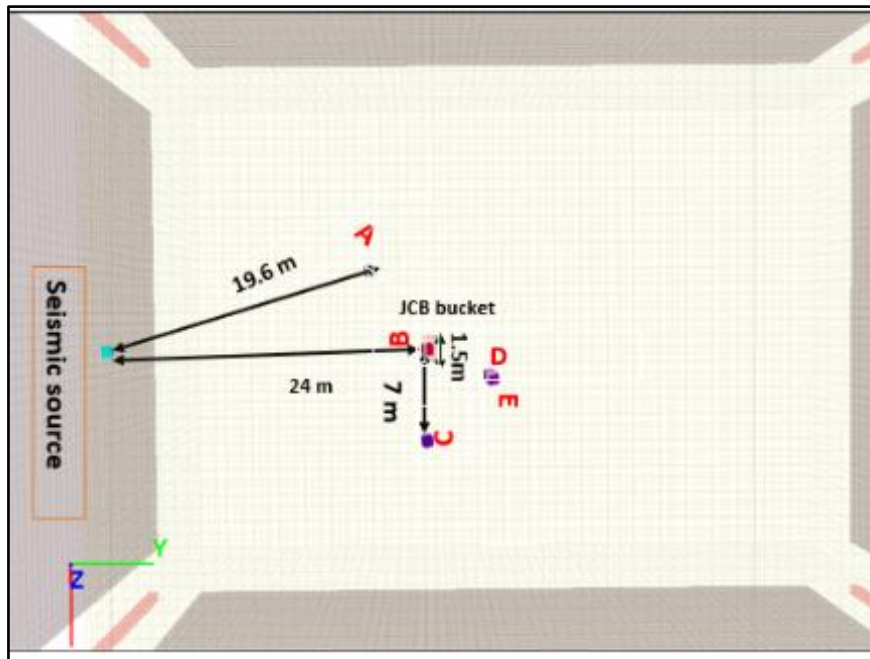


**Figure 5.10:** The figure displays the locations of monitoring stations A, B, C, D, and E, along with the distances between them and from the seismic source. It also clearly identifies the position of the JCB bucket, which is situated beneath monitoring station B.

### 5.3.2.3 Velocity history and PSD results of the JCB bucket simulation

The velocity histories at monitoring stations A, B, C, D, and E were recorded for the z component during this seismic wave simulation. Figure 5.11 shows the time-domain history of seismic wave velocities at all monitoring stations. The maximum amount of seismic wave energy was recorded at monitoring station B, which was positioned above the JCB bucket.

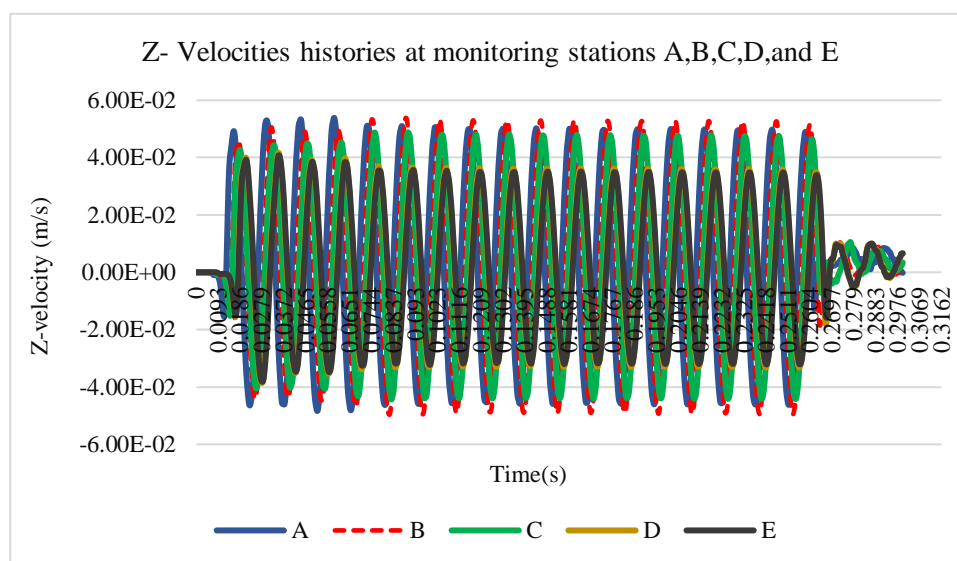


**Figure 5.11:** A comparison of the velocity histories recorded at monitoring stations A, B, C, D, and E revealed that the highest wave amplitude was noted at station B.

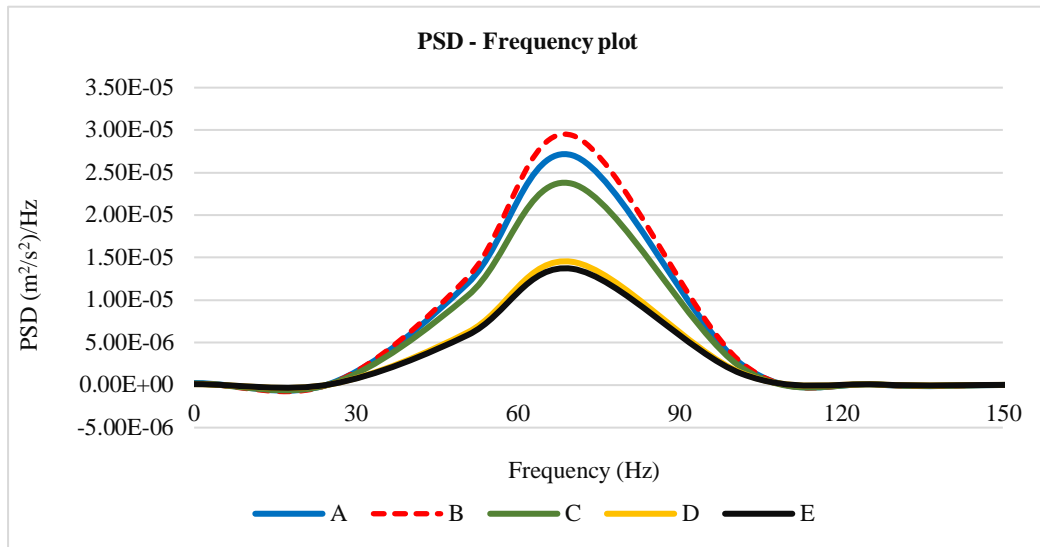


**Figure 5.12:** The PSD of seismic waves recorded at monitoring stations A, B, C, D, and E showed that station B, situated directly above the JCB bucket, exhibited the highest power spectral density values. This indicates that station B recorded the largest amount of reflected seismic energy.

**5.3.2.4 Calculating the area under PSD curves**

**Table 5.4:** The calculated area under the density curves is represented in Figure 5.12, High seismic energy is indicated by red, while low energy is represented by green

A	4.19844E-05
B	4.51239E-05
C	3.66801E-05
D	2.24786E-05
E	2.12468E-05

From the table above, it is evident that stations B, situated directly above the bucket, recorded the highest values of reflected seismic energy. This suggests a strong reflection signal from the object, indicating its presence and confirming the effectiveness of the monitoring setup in detecting subsurface features. The elevated readings at these stations highlight the localized increase in seismic energy, which is a direct result of the seismic waves interacting with the buried object.

#### **5.4 Comparative Study of Simulation Versus Field Data Results**

Although the PSD curves in the seismic simulation were presented on a linear scale and the field experiment data were presented on a logarithmic scale, the results are similar and serve the same purpose. The simulation results align closely with the field data findings. Both sets of results demonstrate that monitoring stations directly above buried objects (PVC pipe and JCB bucket) record higher PSD values, indicating increased reflected seismic energy. In the simulations, stations B and C recorded the highest PSD values above the PVC pipe, and station B did the same above the JCB bucket. This mirrors the field data, where the central sensors over the PVC pipe and JCB bucket displayed distinct PSD curves with higher amplitudes in specific frequency ranges.

The consistent observation across both simulation and field data is the significant increase in spectral amplitude in the presence of buried objects, particularly within specific frequency bands. For the PVC pipe, the field data highlighted differences between 30 Hz and 55 Hz, while the JCB bucket showed increased amplitudes from 20 Hz to 85 Hz, especially post-35 Hz. The simulations similarly noted the highest PSD values at stations directly above these objects, reinforcing the reliability of the simulated model in replicating real-world conditions.

The results illustrate the effectiveness of spectral analysis in detecting and characterizing shallow buried objects. Both the simulation and field experiment confirm that buried objects affect the characteristics of seismic waves, leading to noticeable variations in PSD values. The agreement between simulation and field results enhances confidence in the use of simulation models for predicting seismic wave interactions and improves the understanding of subsurface object identification.

## **Chapter 6 : Brownfield site investigation: Pilot study**

### **6.1 Introduction**

The main purpose of this chapter (Chapter 6) is to conduct further field studies to verify numerical results. Accordingly, a series of controlled experiments were held in the Stepps area, Glasgow.

Three objects were chosen for the field study: A steel drum, a concrete block, and a PVC drum.

### **6.2 Field site**

The area for the field experiments was chosen for several reasons. The topography of the chosen location is flat. Easy accessibility and authorization for excavation and burial of objects below ground surface were important considerations in selecting this location. The land was owned by the University of Strathclyde, making it easier to obtain permission and access. Figure 6.1 depicts the location of the field area. The experiment site was located approximately half a mile from the main road. A football field was situated nearby, though no sporting activities were observed on the day of the experiment. The soil at the site was saturated with water, and the weather conditions were notably cold.

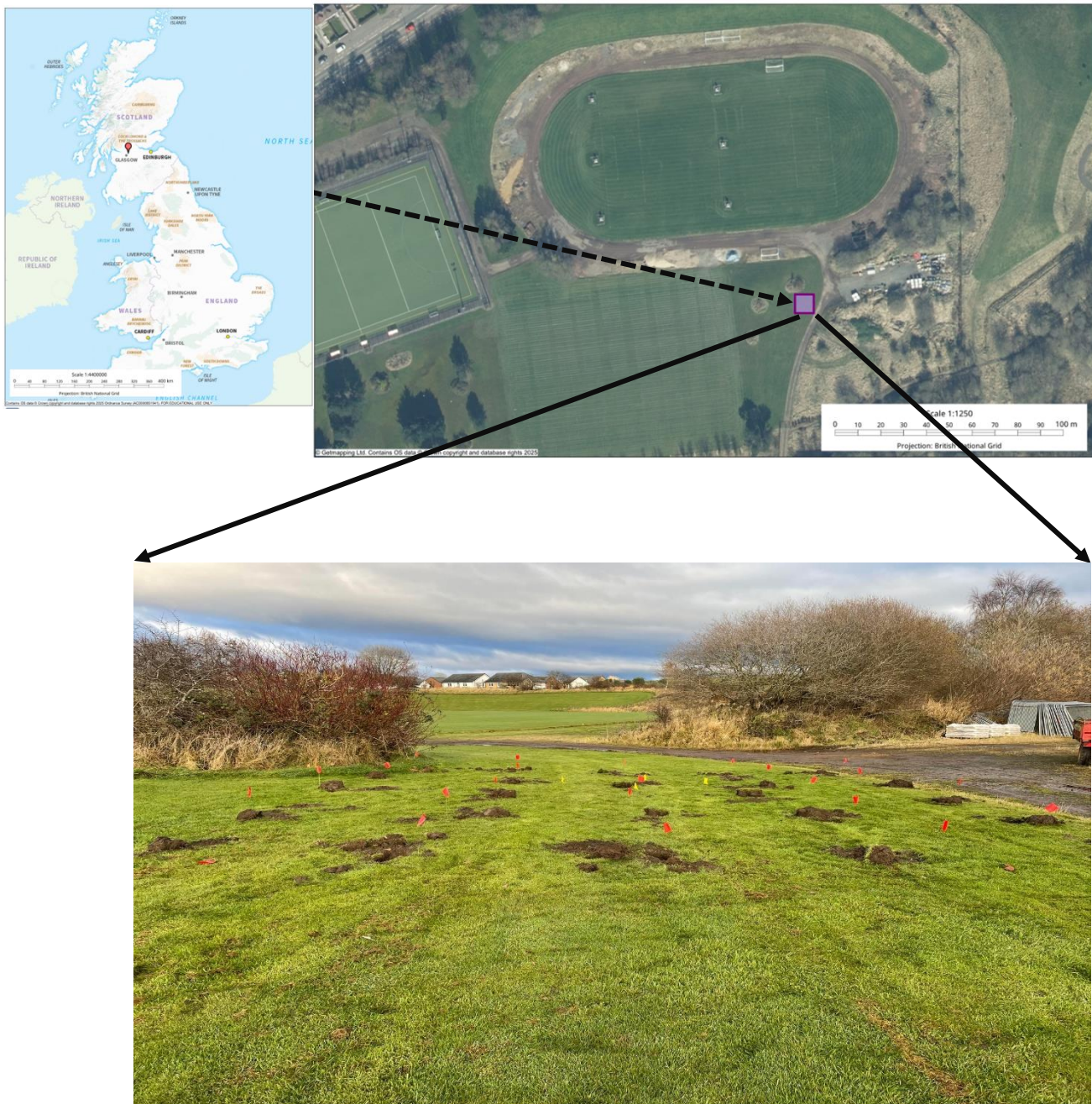


**Figure 6.1:** Field experiment Site: Top left - Location map of the field site (created using Digimap, © Crown copyright and database rights “2025” Ordnance Survey (AC0000851941)). The field site is in Stepps, Glasgow. Top right - Aerial map of the site with the actual site indicated by a purple rectangle, created using Digimap (© Getmapping Ltd). Bottom - Panoramic View of the Experimental area with the locations of seismic nodes indicated by red flags (author's own photo).

### 6.3 Seismic Source

In these experiments, seismic waves are generated using a JCB digger (figure 6.2), producing seismic waves with a frequency range of 10 to 50 Hz. The JCB digger was placed at two distances, 20m and 40m, from the buried objects.



**Figure 6.2:** JCB used as seismic source.

### 6.4 Seismic nodes

In these experiments, 27 the Smart Solo IGU-16HR 3C seismic nodes were used. (Zeckra, 2022). The Smart Solo IGU-16HR 3C, record ground motion in vertical, and 2 two orthogonal horizontal directions using its three-component geophone technology. The sensors are compact, and are commonly utilised for environmental geophysics, and seismic surveys. Its lightweight and portable design facilitates transport and deployment. Their technical characteristics are shown in table 6.1. Smart Solo sensors were chosen for this study due to their numerous advantages. As wireless, low-power seismic devices with an integrated geophone and recorder, they were ideal for capturing the low frequencies expected in this study, ranging from 10 to 20 Hz. Their high sensitivity, combined with GPS synchronization, onboard data storage, and easy deployment, made them suitable for scalable seismic surveys across various field conditions.

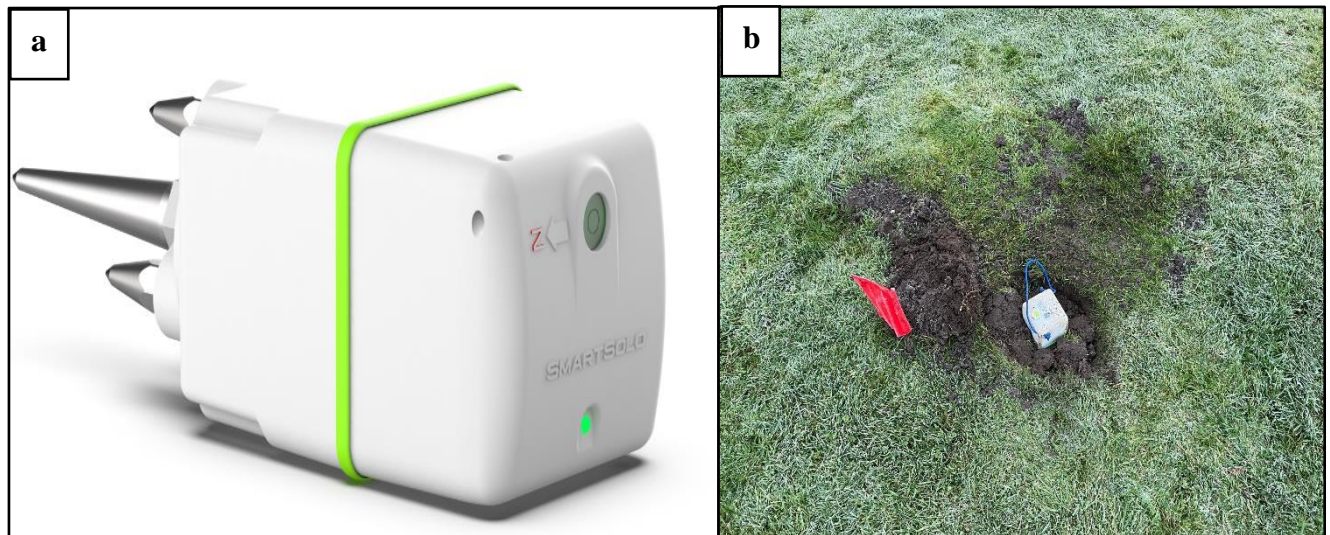


**Figure 6.3:** a) Smart Solo Seismic sensor (Zeckra, 2022): b) Seismic sensor deployed on site

**Table 6.1:** Smart Solo IGU-16HR 3C technical specification (<https://smartsolo.com>).

Smart Solo IGU-16HR 3C	
Seismic data channel(s)	3
Operating temperature	-40°C ~ +70°C
Natural Frequency	5- 10 Hz
Sensitivity	76.7 – 78.7 V/m/s (1.95 V/in/s)
Damping	0.7
Weight	2.4kg (Including internal battery and spike)
Re charging time	<6 hours
Data Storage	64 GB
Frequency Response	0 ~ 1652Hz

### 6.5 Experimental Set-Up:

Three separate field experiments were carried out in the Stepps area; each experiment was given a unique name that corresponded to the main emphasis of the study. The Concrete Experiment, the PVC Drum Experiment, and the Steel Drum Experiment with the buried object being a concrete block, a PVC drum, and a steel drum. The aim is to see whether these objects alter the seismic energy of the seismic waves as these are recorded by the deployed sensors.

### 6.6 Sensors' geometry

The plan for the field experiments was to set up the monitoring stations in the shape of a square, with 25 sensors to match the geometry of the sensors in seismic wave simulations. The distance between sensors was 2m in both directions.

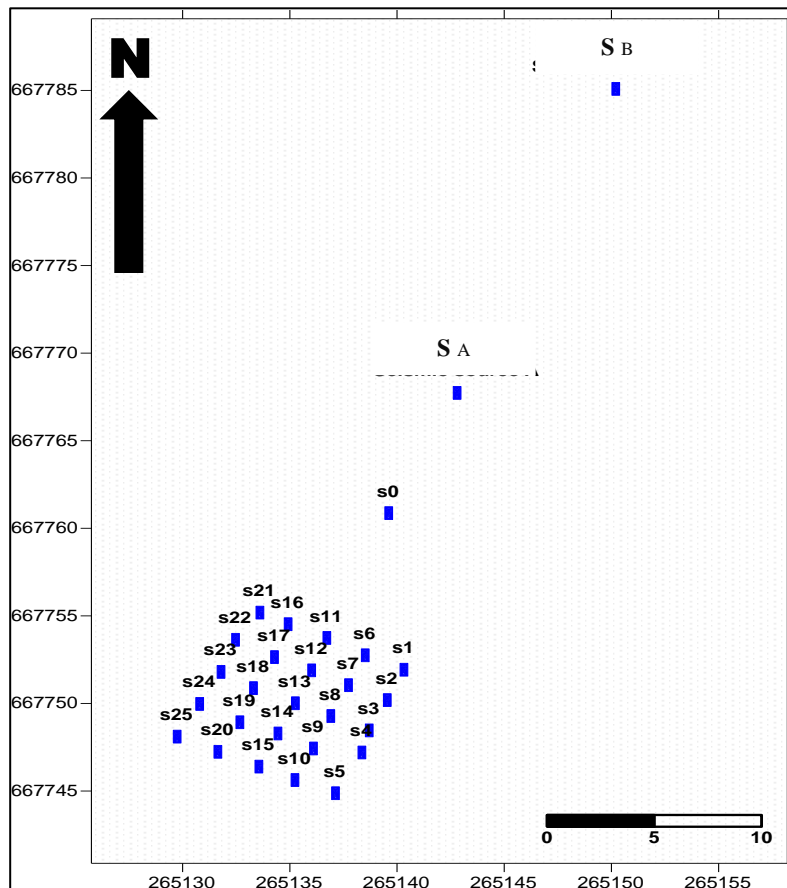


**Figure 6.4:** Array of seismic sensors and locations of seismic sources. s0 to s25 indicate locations of the seismic sensors. S<sub>A</sub> and S<sub>B</sub> are the locations of seismic source (JCB digger).

### 6.7 Geometrical characteristics of buried objects.

A steel drum, a PVC drum, and a concrete block on the characteristics of seismic waves, was studied, as they were buried at a depth of 1m from the ground surface figure 6.5 shows the three objects and their dimensions.

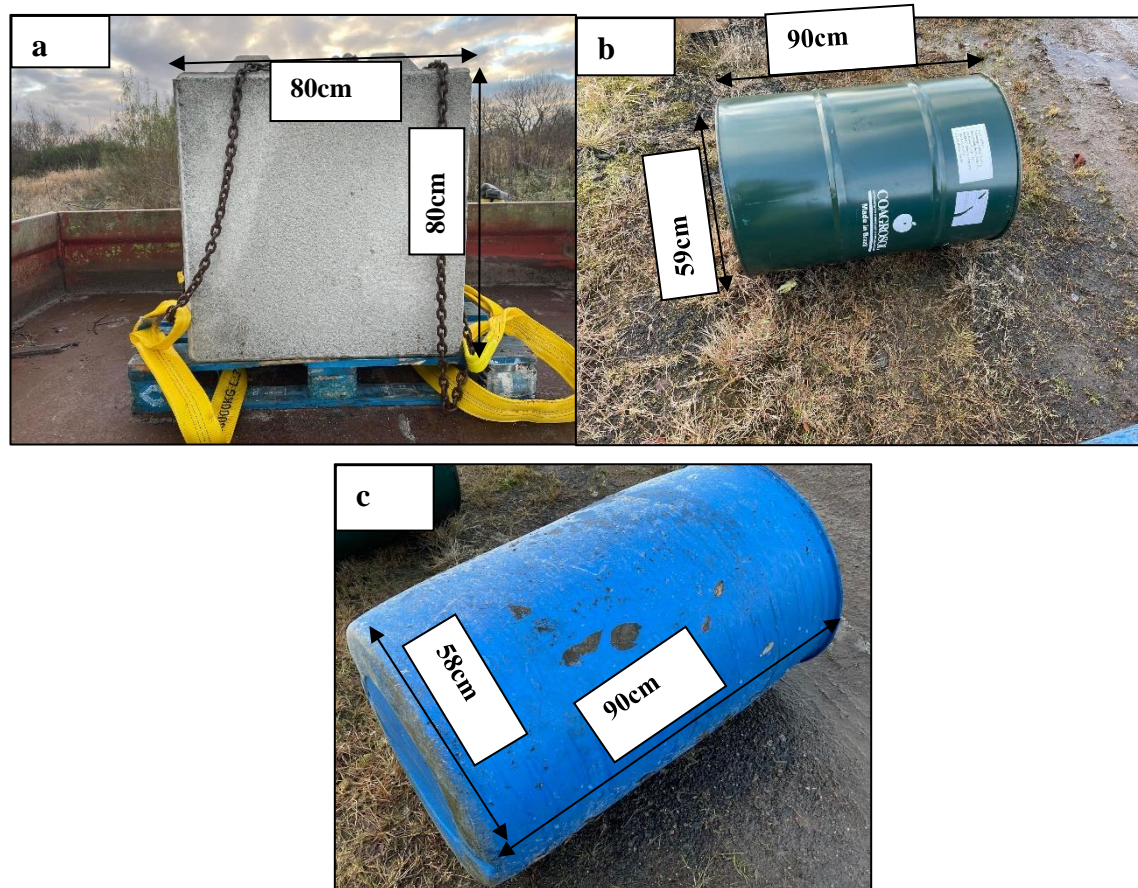


**Figure 6.5 :** Objects that were buried as part of the field experiments. **a)** Concrete block. **b)** Steel drum  
**c)** PVC drum.

## 6.8 Experimental Procedure

Conducting the experiment includes some important steps:

1. **Sensor Deployment:** A 20 cm by 20 cm hole was excavated for each sensor. A total of 25 sensors were deployed across the study area in the shape of a 2m  $\times$  2m grid (figure 6.4). Additionally, two additional stations were established: one near the seismic wave source and another positioned between the source and the monitoring stations. These sensors aimed to record the seismic signal at the source location but served no other purpose. The sensors were placed in such direction so that one horizontal component was oriented North – South, and the other East – West.
2. **Sensor location:** Using GNSS (Global Navigation Satellite System) receiver, the coordinates for the seismic source, sensors, and object locations were determined (Figure 6.6). The coordinates were in the British National Grid (OSGB36).

3. **Data acquisition:** data acquisition started at 09:00 am



**Figure 6.6:** Determination of sensor locations using GNSS receivers.

4. **Initial Recording:** At 10:15 am, prior to any excavation, seismic data recorded for 20 minutes at each source location (SA and SB). these data were then used as baseline data.
5. **Excavation:** Excavation began at 11:06 am and continued until 12:30 pm at the location of monitoring station No. s13, centrally located within the sensor array. The excavated hole measured approximately 1m in length and width, with a depth of 1.90 m, as depicted in Figure 6.7. Soils with bricks, roots, and small irregular objects are highly heterogeneous, with hard brick fragments, irregular root networks.



**Figure 6.7:** Excavation for buried objects.

6. **Object Placement and Recording:** Following the completion of excavation, the first object (concrete) block placed in the excavation, and soil backfilled and compacted. Data were recorded twice: once with the JCB at location SA and once at location SB (figure 6.4). This procedure was repeated for all subsequent objects. All sensors recording continuously apart from s13 which was turned on and off for the buried of each object.



**Figure 6.8:** a) placement of concrete block inside the hole. b) Steel drum inside the hole. c) PVC drum inside the hole. d) Demonstrating the process of backfilling the hole and planting the sensor s13 on top of it. The vertical distance from the surface of these objects to the surface of the ground is about 1m.

7. **Noise Minimization:** During the activation of the JCB engine as seismic source, all personnel ceased movement to prevent the recording of any random noise. This protocol was maintained throughout the entire recording period, which lasted approximately 6 hours.

### 6.9 Data collection

In the seismic data collection process involving 25 monitoring stations, each station recorded seismic waves in three directions: vertical, north-south, and east-west, recording seismic activity over a 20-minute source activation period. The experiment initiates with the start of the digger's engine, which emits seismic waves that propagate through the Earth's ground. Before burying any objects ("homogeneous" case), the seismic waves were recorded twice, with a digger at the 2 source locations. After that, twice again for each object, with a difference in the location of the source of the seismic waves. In each experiment, it was conducted two recordings at different wave source locations, recording 26 sets of seismic data each time. In each experiment, two recordings were conducted at different wave source locations. Two sensors were placed—one near the seismic source for  $S_A$  waves and the other near the source for  $S_B$  waves. Unfortunately, it was found that the sensor close to source location  $S_B$  was not recording, leading to a total of 208 sets of recorded seismic data. Total length of the

experiments was 6 hours. Figure 6.9 shows representative recordings from station No. s12 for a period of 6 hours, which contain some random noise and include recording during the drilling digging operation.

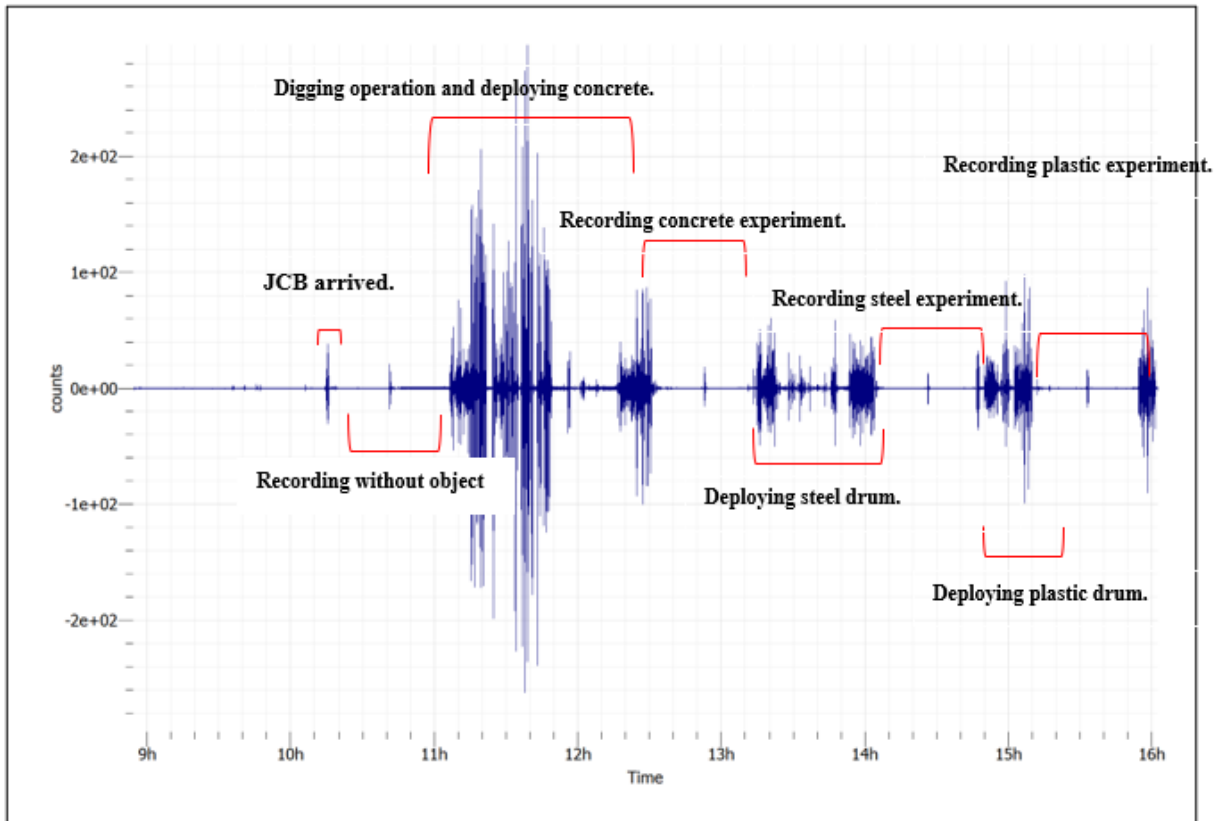


**Figure 6.9:** The entire duration of the micro seismic recording period.

### 6.10 Data Pre - processing

The first step in the data was to download the data from the Smart Solo sensors. The Geopsy software was then utilized to verify the data and convert the data to ASCII format so that they can be imported in Matlab. A preliminary review of the data was conducted, and the portions of the time recordings that corresponded to the duration of each experiment were isolated as separate files, as shown in Figure 6.9. Subsequently, each data segment was imported into Matlab software, where the spectral analysis was carried out.

### 6.11 Methodology

Using Geopsy software, time segments containing local noise were identified. Local noise is defined as any significant spikes in seismogram recordings (Li, 2008). Random noise in the seismic data was successfully recognized and classified. During the field experiment, I

documented instances of random seismic sources, which helped identify and exclude noise during data processing. The real seismic data is what was used in the analysis, and random noise was removed as much as possible.

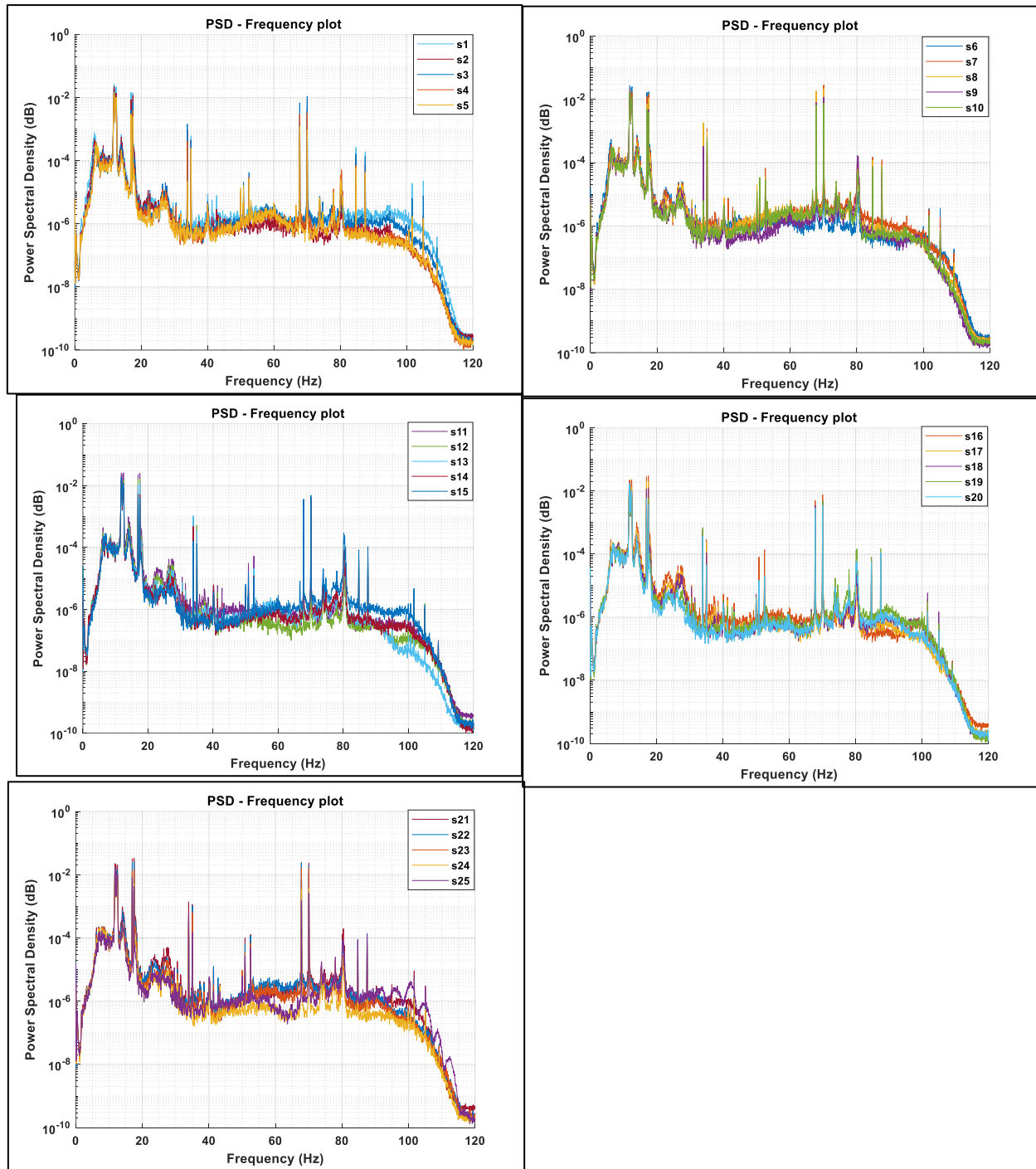
### 6.12 Baseline data

Figure 6.10 represents the amount of seismic energy calculated from the PSD curves of seismic waves recorded at each monitoring station. The area under each curve was calculated and represented in columns. These data were recorded before digging and before burying any object underground. From the results, it can be observed that the general trend of the amount of seismic energy gradually decreases as the seismic waves move away from their source. This is a result of the spherical spread of the seismic waves, which leads to a loss of seismic energy. Part of the seismic energy may be lost as a result of local heterogeneity of the soil. It is also clear that a random increase in seismic energy was recorded at some of the monitored stations as a result of the non-homogeneity of the soil or the presence of some previously buried objects.

Due to the overlapping and lack of clarity in the power spectral density (PSD) curves shown in Figure 6.10, it was necessary to calculate the area under each PSD curve to accurately represent the seismic energy. The area under the curve provides a quantitative measure of the amount of seismic energy recorded at each station. As indicated in Table 6.2, the seismic energy generally decreases with increasing distance from the source, which is expected due to the natural attenuation of seismic waves as they travel through the ground. However, an exception was observed at several distant stations—specifically s20, s15, and s10—where an unexpected increase in seismic energy was recorded.

This anomaly could be attributed to local soil heterogeneity, where variations in soil composition, moisture content, or other subsurface conditions may have caused certain areas to either amplify or transmit seismic waves more efficiently. Such factors can create localized amplification effects, which would explain the higher-than-expected energy levels at these stations, despite their greater distance from the seismic source. Further investigation into the soil properties at these locations would be necessary to fully understand the cause of this irregularity. Recording the seismic data when JCB was at location SB showed that the recorded seismic energy (Table 6.3), was higher than the seismic energy recorded when the wave source was at location SA. This was a result of the fact that the soil characteristics at site B were solid soil and harder than the soil at site A.

6.12.1 Seismic source (JCB) at SA



**Figure 6.10: No object:** PSD of 5 mins segments of data recorded at all monitoring stations when the seismic source (JCB) was at location SA.

**Table 6.2 :** The calculated area under the PSD curves in figure 6.10 of seismic waves for all monitoring stations when JCB was at SA. No buried objects buried present.

S21	0.471687	S16	0.418897	S11	0.436234	S6	0.420621	S1	0.401077
S22	0.362204	S17	0.269964	S12	0.260387	S7	0.371329	S2	0.301322
S23	0.333	S18	0.209785	S13	0.198102	S8	0.259632	S3	0.223987
S24	0.198737	S19	0.194999	S14	0.188195	S9	0.209824	S4	0.186268
S25	0.167	S20	0.21895	S15	0.244659	S10	0.230546	S5	0.183131

### 6.12.2 Seismic source (JCB) located at SB

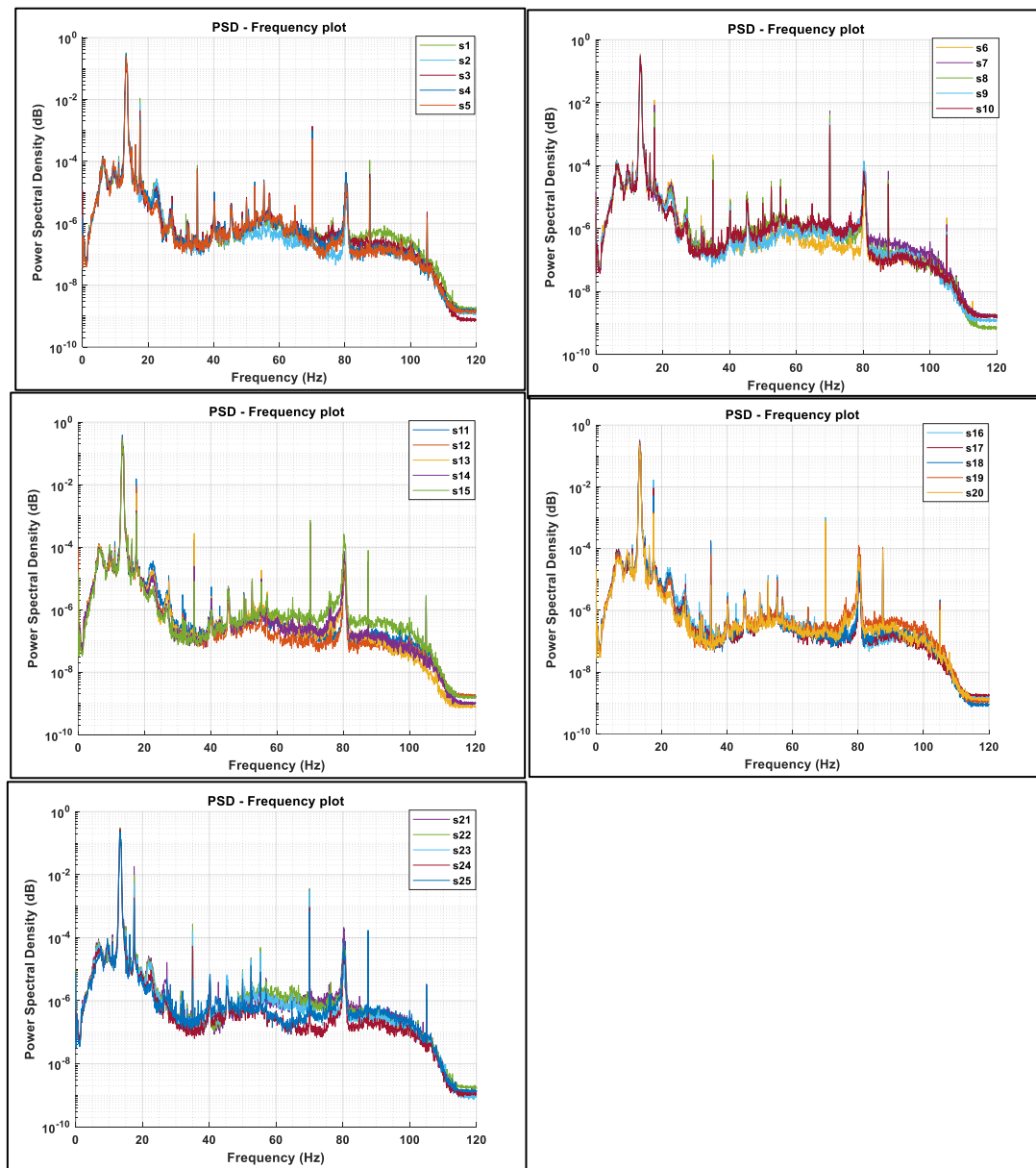


**Figure 6.11:** Power spectral density curves of seismic waves recorded at all monitoring stations with the seismic source (JCB) positioned at location SB.

**Table 6.3:** Calculated area under the PSD curves of seismic waves for all monitoring stations when JCB was at SB (figure 6.11).

S21	2.226055	S16	2.49987	S11	2.799393	S6	2.601943	S1	2.377471
S22	2.178452	S17	2.215213	S12	2.261324	S7	2.357392	S2	1.815494
S23	1.72825	S18	1.870614	S13	1.793337	S8	1.797384	S3	1.694104
S24	1.875332	S19	1.930717	S14	1.78602	S9	1.953083	S4	2.191628
S25	1.643756	S20	1.550467	S15	2.004737	S10	1.956848	S5	1.800035

## 6.13 Vertical component (Seismic Source located at SA)

### 6.13.1 Concrete block experiment.

In a time-domain analysis, the amplitude-time plot of the Z-component seismic waves across stations s1 to s25 will reveal the impact of a subsurface concrete object located 1m beneath station s13. Seismic waves will reflect and scatter off the concrete object, resulting in high-energy waves with significantly amplified amplitudes at station s13 (see appendix E1).

In terms of frequency domain analysis, a comparison of the Power Spectral Density (PSD) of vertically recorded seismic waves reveals that the PSD at Station 13, located directly above the concrete object, shows distinct differences from the other stations within a specific frequency range (see Figure 6.12). This variation in frequency response is due to the interaction between the seismic waves and the subsurface concrete block, causing altered spectral characteristics at Station 13 compared to the surrounding stations.

The Power Spectral Density (PSD) curves for seismic waves at all monitoring stations reveal notable variations in energy distribution across frequencies. Station s13 (red dashed line) consistently exhibits higher PSD values between 20 Hz and 100 Hz, likely due to the concrete block beneath it. While some noise-related spikes appear, the overall trend reflects genuine seismic data. In the low-frequency range (below 20 Hz), all stations show a gradual increase in PSD, capturing ambient seismic energy. In the mid-frequency range (20–40 Hz), s13 displays elevated energy levels, highlighting the influence of the underlying concrete. Although the higher-frequency range (40–100 Hz) shows a decline in energy across most stations, s13 maintains higher PSD values, indicating a stronger seismic response due to the concrete block (see figure 6.13). This is further supported by Table 6.3, which shows the calculated area under the curves, revealing that s13 has the highest energy value.

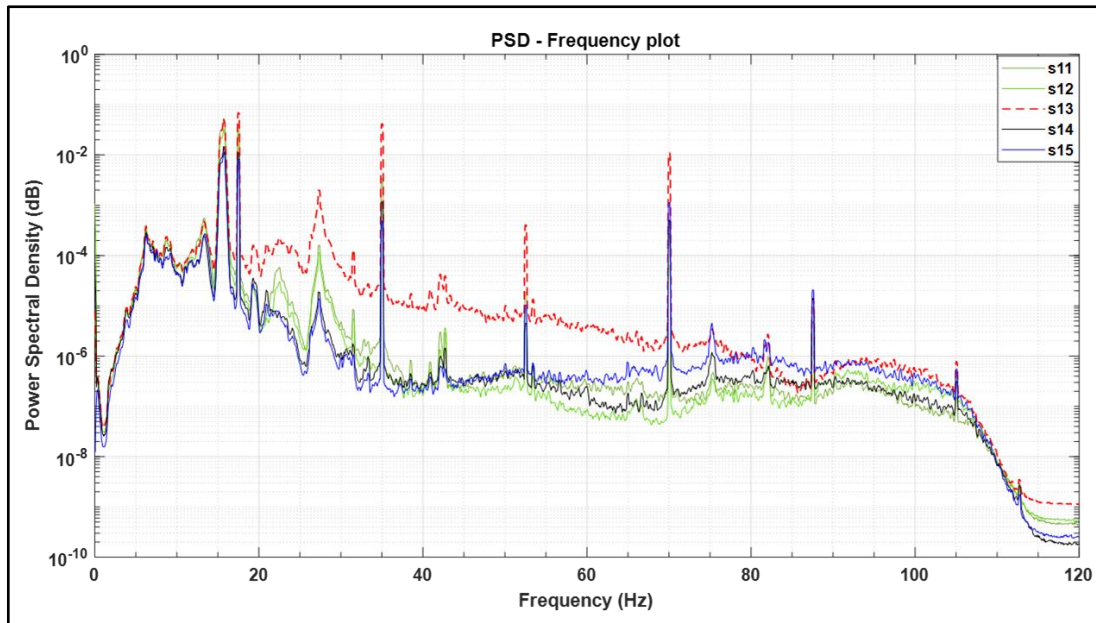


**Figure 6.12:** A comparison of the PSD of seismic waves recorded vertically. The PSD at station No. s13 located above the object (concrete) differs from the others in the frequency range from 18 to 80 Hz.

**Table 6.4:** The area under the curves of the PSD of seismic waves recorded at stations s11 to s15 in figure 6.12.

S11	0.86
S12	0.554
S13	1.29
S14	0.253
S15	0.202

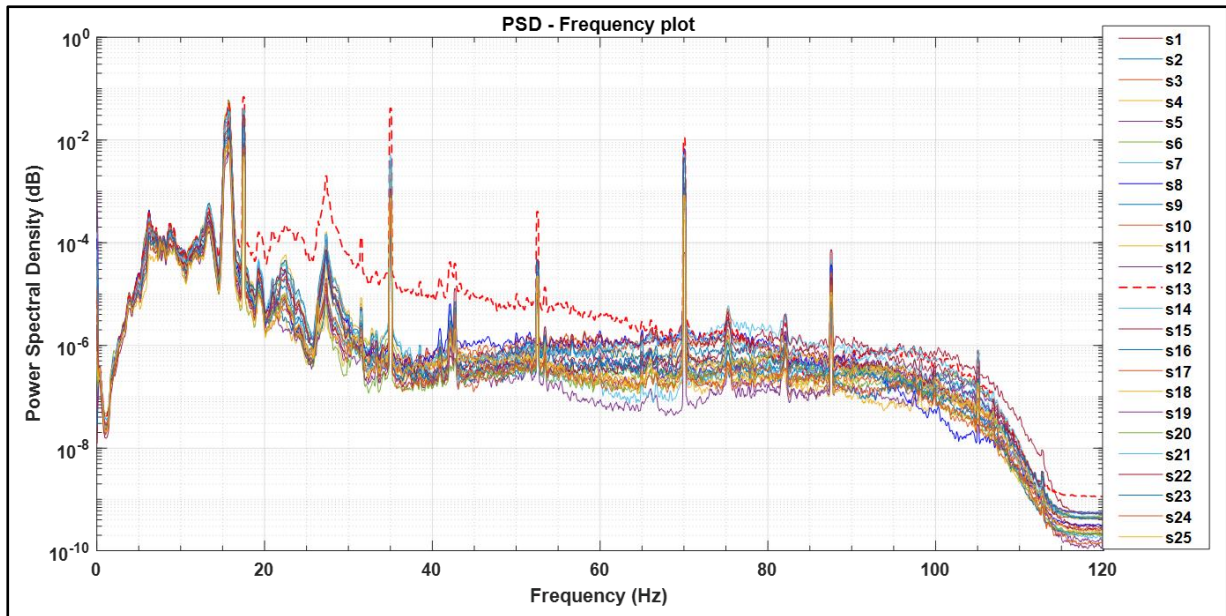


**Figure 6.13:** Station 13's PSD curve (red dashed line) shows significant peaks of frequency range from 20 Hz to 80 Hz, indicating strong reflections and resonances caused by the concrete object beneath it. In contrast, other stations (s1 to s25) exhibit lower and more uniform PSD peaks. These variations highlight the impact of the steel object on seismic wave propagation and energy distribution

**Table 6.5:** The calculated area beneath each Power Spectral Density (PSD) curve in figure 6.13, for all recorded seismic waves at every monitoring station (concrete block).

S21	0.703	S16	0.727	S11	0.86	S6	0.869	S1	0.837
S22	0.478	S17	0.516	S12	0.554	S7	0.526	S2	0.401
S23	0.333	S18	0.331	S13	1.29	S8	0.29	S3	0.228
S24	0.151	S19	0.131	S14	0.253	S9	0.238	S4	0.176
S25	0.167	S20	0.152	S15	0.202	S10	0.223	S5	0.138

### 6.13.2 Steel drum experiment

In the context of time domain analysis, the figure displays seismic waves recorded at all monitoring stations. While station s13 shows notably higher amplitudes, it remains difficult to distinguish these waves from those at other stations, as their distinct features are not easily discernible within the overall waveform pattern in the time domain (see appendix E 2).

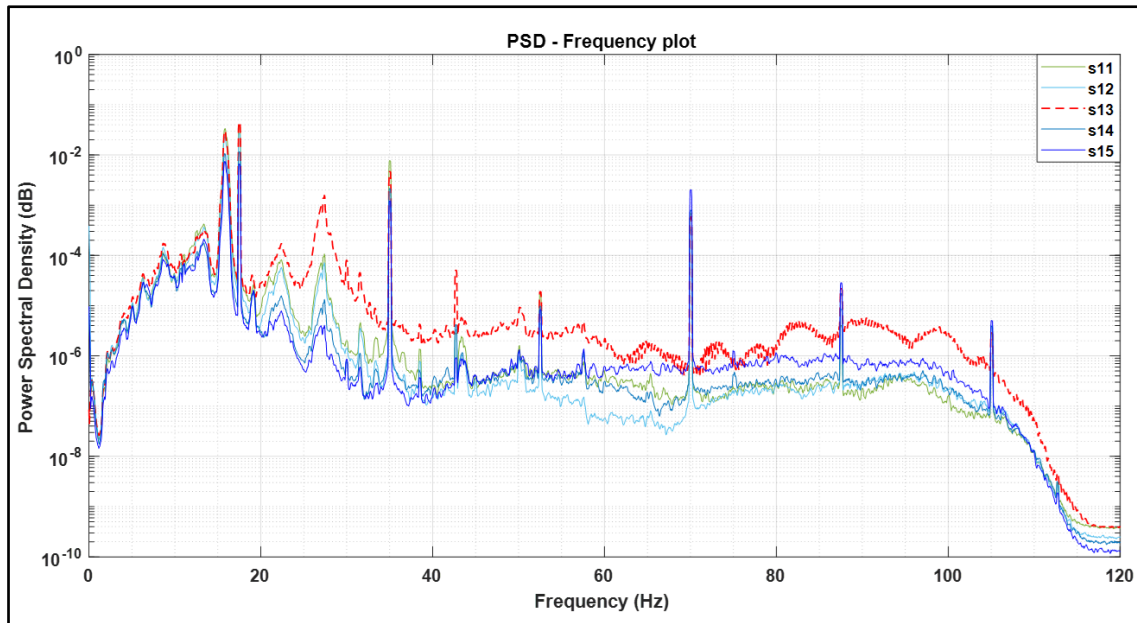


**Figure 6.14:** The Power Spectral Density (PSD) of seismic waves recorded at monitoring stations (s11, s12, s13, s14, s15) illustrates varying levels of seismic energy. Notably, monitoring station s13, deployed directly above the steel drum, recorded the highest seismic energy. This peak corresponds to a frequency range from 20 to 120 Hz on the PSD - Frequency plot.

**Table 6.6:** In the table summarizing the calculated areas under the PSD curves in Figure 6.14, the highest value is attributed to station No. s13. This station, situated directly above the steel drum, recorded the largest amount of seismic energy, indicating a notable concentration of seismic energy in that specific frequency range (steel object).

S11	0.598
S12	0.391
S13	0.606
S14	0.185
S15	0.131

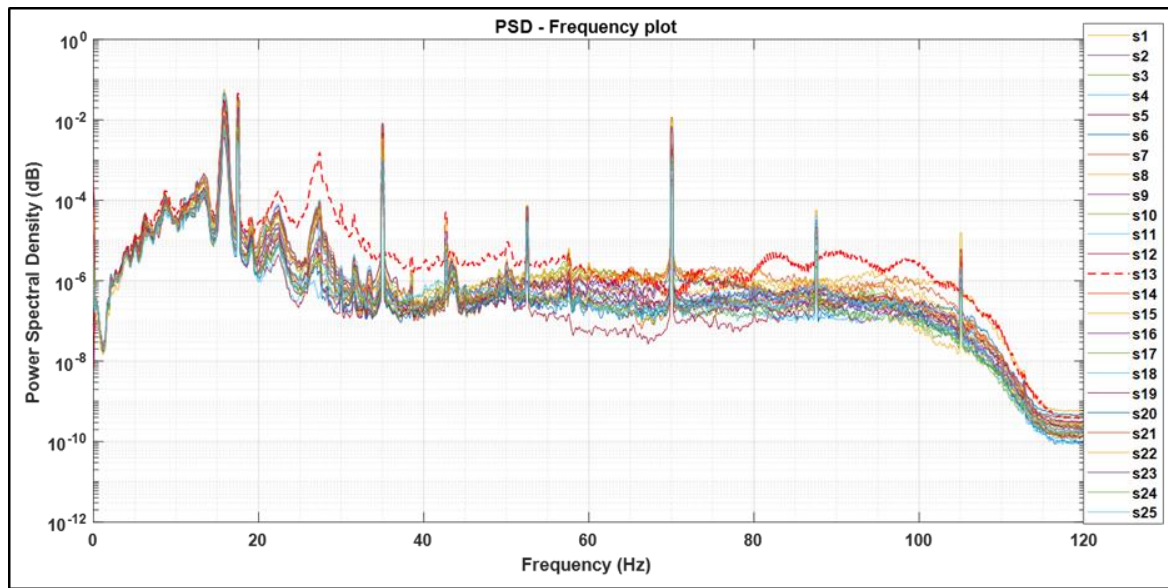


**Figure 6.15:** The PSD curves depicting seismic waves recorded at all monitoring stations. It is clear that the PSD curve at s13 has the highest value. This notable peak occurs within two frequency ranges: approximately 20 to 70 Hz and 80 to 120 Hz, emphasizing that the largest amount of seismic energy detected at the s13, which is positioned above the steel drum.

**Table 6.7:** The computed area under the Power Spectral Density (PSD) curves in Figure 6.15. Monitoring station s13 exhibits a significant value. However, some other monitoring stations recorded seismic energy levels exceeding those observed at s13. This is due to the local heterogeneity present in the soil.

S21	0.475	S16	0.482	S11	0.598	S6	0.689	S1	0.8
S22	0.35	S17	0.339	S12	0.391	S7	0.512	S2	0.469
S23	0.273	S18	0.233	S13	0.606	S8	0.261	S3	0.254
S24	0.112	S19	0.098	S14	0.185	S9	0.161	S4	0.132
S25	0.09	S20	0.089	S15	0.131	S10	0.146	S5	0.089

In the conducted steel drum experiment, where the drum was buried approximately 1 m beneath the earth's surface, the analysis of the results was performed. This analysis included an examination of the seismic data in time domain, PSD curves representing the recorded seismic energy, along with corresponding tables quantifying the values under these curves.

The outcome of this investigation has provided important evidence that the steel drum can be effectively detected when the seismic wave source is located 20m away from the steel. The main observation is that the monitoring station s13 which is deployed directly above the steel drum recorded the highest amplitude of the seismic wave. This phenomenon was evident not

only in the time domain, where the waveform characteristics were assessed, but also in the frequency domain, where the distribution of energy across different frequencies was examined. This peak corresponds to a frequency range that extends from 20 to 120 Hz on the PSD - Frequency plot, and it is the one that has detected the highest amount of seismic energy.

### 6.13.3 Plastic drum experiment

Seismic waves from the vertical component were detected at several monitoring stations, with the seismic wave source positioned away from the subsurface object (plastic drum). Notably, station s13, located directly above the object, exhibited significantly greater amplitudes in the recorded waves compared to all other monitoring stations (see appendix E3).

In the PSD-frequency plot for all monitoring stations, the PSD curves are largely similar, with the exception of the curve at station s13, which is positioned directly above the plastic drum. This station recorded the highest PSD values, particularly in the frequency interval between 18 and 50 Hz, highlighting a specific concentration of seismic energy.

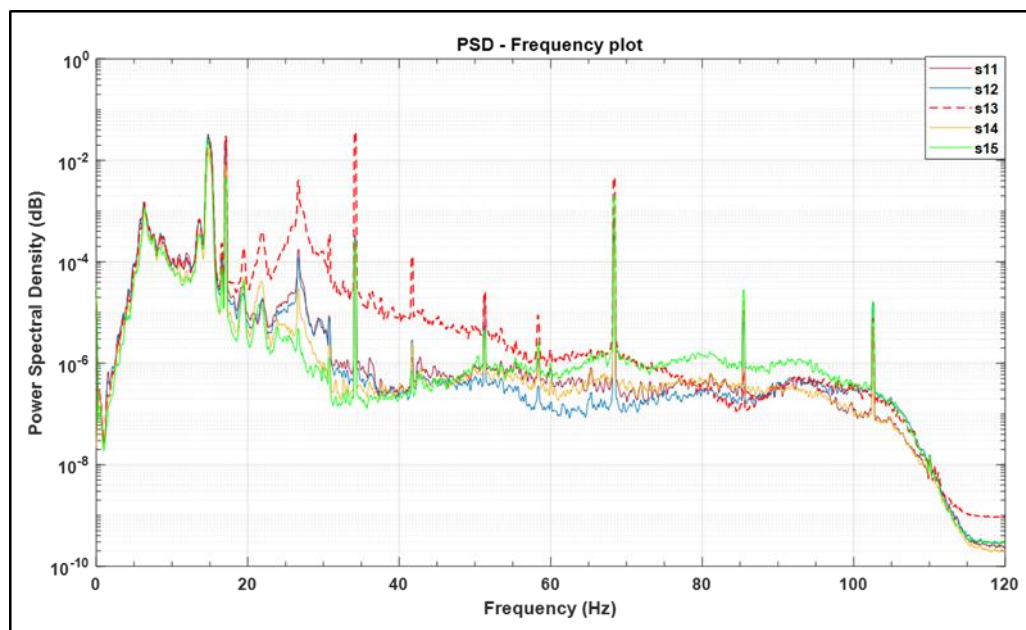


**Figure 6.16:** Within the Power Spectral Density (PSD) - Frequency plot, which includes some monitoring stations, station s13 shows the peak PSD of seismic waves, with the maximum value recorded between 18 and 70 Hz. This indicates a high concentration of seismic energy in this specific frequency range throughout the monitoring sites.

**Table 6.8:**The table presents the Power Spectral Density (PSD) values calculated from the areas under the PSD curves shown in Figure 6.16. It indicates that monitoring station No. s13 captured the highest amount of seismic energy compared to other stations (plastic drum).

S11	0.589
S12	0.505
S13	0.795
S14	0.249
S15	0.343

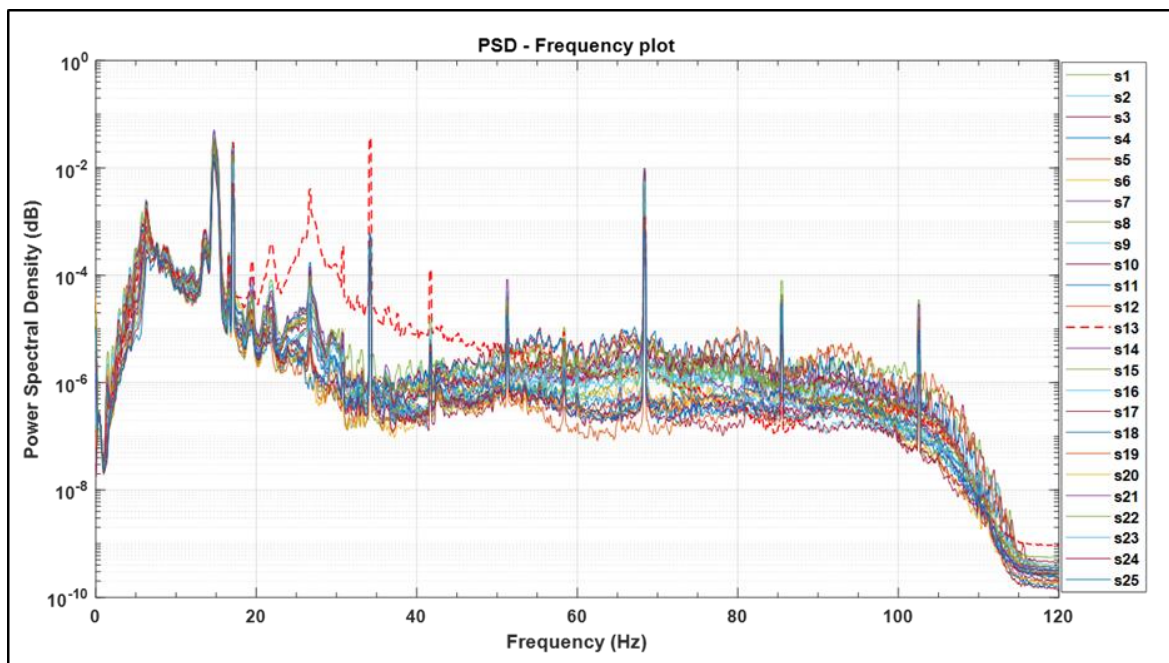


**Figure 6.17:** In the PSD - Frequency plot showing all monitoring stations, The PSD curves are almost identical, except for the PSD curve at monitoring station s13, located directly above the plastic, which showed a difference that recorded the highest value of the PSD which correspond to frequency interval between 18 and 50 Hz., highlighting a specific concentration of seismic energy.

**Table 6.9:**The table provides the calculated area beneath the PSD curves depicted in Figure 6.17. Evidently, the highest value was recorded at monitoring station No. s13 (plastic drum).

S21	0.72	S16	0.687	S11	0.589	S6	0.437	S1	0.497
S22	0.533	S17	0.495	S12	0.505	S7	0.458	S2	0.419
S23	0.273	S18	0.27	S13	0.795	S8	0.346	S3	0.372
S24	0.191	S19	0.208	S14	0.249	S9	0.287	S4	0.29
S25	0.227	S20	0.223	S15	0.343	S10	0.347	S5	0.239

Based on the experiment findings, it is possible to conclude that a plastic drum buried at a depth of 1 m from the earth surface in brownfields can be identified using seismic wave analysis of the vertical component. The study supports this result by finding that monitoring station No. s13, which was located precisely above the object (plastic drum), recorded the greatest quantity of seismic energy. This data emphasizes the efficacy of studying the vertical seismic wave properties in identifying and collecting beneath objects, as shown by the increased seismic energy concentration at station No. s13.

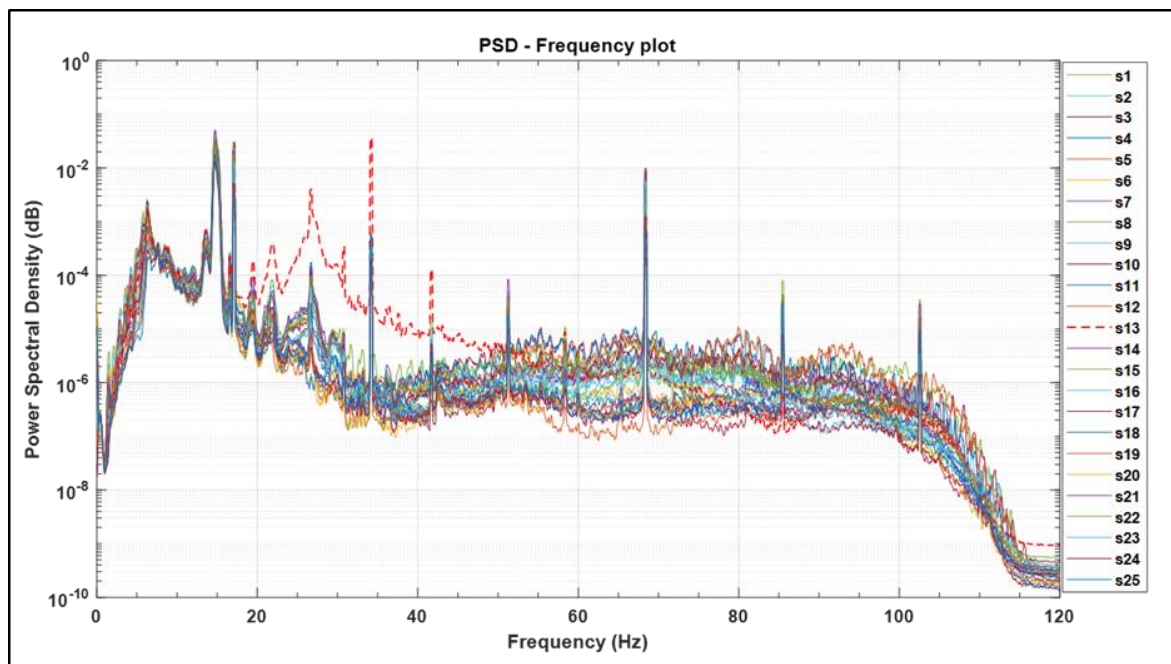


**Figure 6.18:** In the PSD - Frequency plot showing all monitoring stations, The PSD curves are almost identical, except for the PSD curve at monitoring station s13, located directly above the plastic, which showed a difference that recorded the highest value of the PSD which correspond to frequency interval between 18 and 50 Hz., highlighting a specific concentration of seismic energy.

**Table 6.10:** The table provides the calculated area beneath the PSD curves depicted in Figure 6.18. Evidently, the highest value was recorded at monitoring station No. s13.

S21	0.72	S16	0.687	S11	0.589	S6	0.437	S1	0.497
S22	0.533	S17	0.495	S12	0.505	S7	0.458	S2	0.419
S23	0.273	S18	0.27	S13	0.795	S8	0.346	S3	0.372
S24	0.191	S19	0.208	S14	0.249	S9	0.287	S4	0.29
S25	0.227	S20	0.223	S15	0.343	S10	0.347	S5	0.239

Based on the experiment findings, it is possible to conclude that a plastic drum buried at a depth of 1 m from the earth surface in brownfields can be identified using seismic wave analysis of the vertical component. The study supports this result by finding that monitoring station No. s13, which was located precisely above the object (plastic drum), recorded the greatest quantity of seismic energy. This data emphasizes the efficacy of studying the vertical seismic wave properties in identifying and collecting beneath objects, as shown by the increased seismic energy concentration at station No. s13.

## 6.14 Vertical component (Seismic Source located at SB)

### 6.14.1 Concrete experiment

In time domain analysis, the seismic waves that were recorded at monitoring stations s1 to s25 reveal an important observation: monitoring station No. s13 which deployed over the concrete detected the greatest wave amplitude, which was greater than the amplitudes of the other seismic waves (see appendix F1).

The PSD curves of the vertical traces from all 25 sensors reveal that most of the curves are nearly identical, indicating similar seismic responses across the monitoring stations. However, a notable exception is the curve associated with Station s13, which is positioned directly above the buried concrete. This specific curve stands out, especially in the frequency range between 18 Hz and 75 Hz, where it exhibits significantly higher values. This difference suggests that the interaction between the seismic waves and the buried concrete has led to a unique concentration of seismic energy at Station 13, highlighting its distinct response compared to the other monitoring stations (see figure 6.19 and figure 6.20).

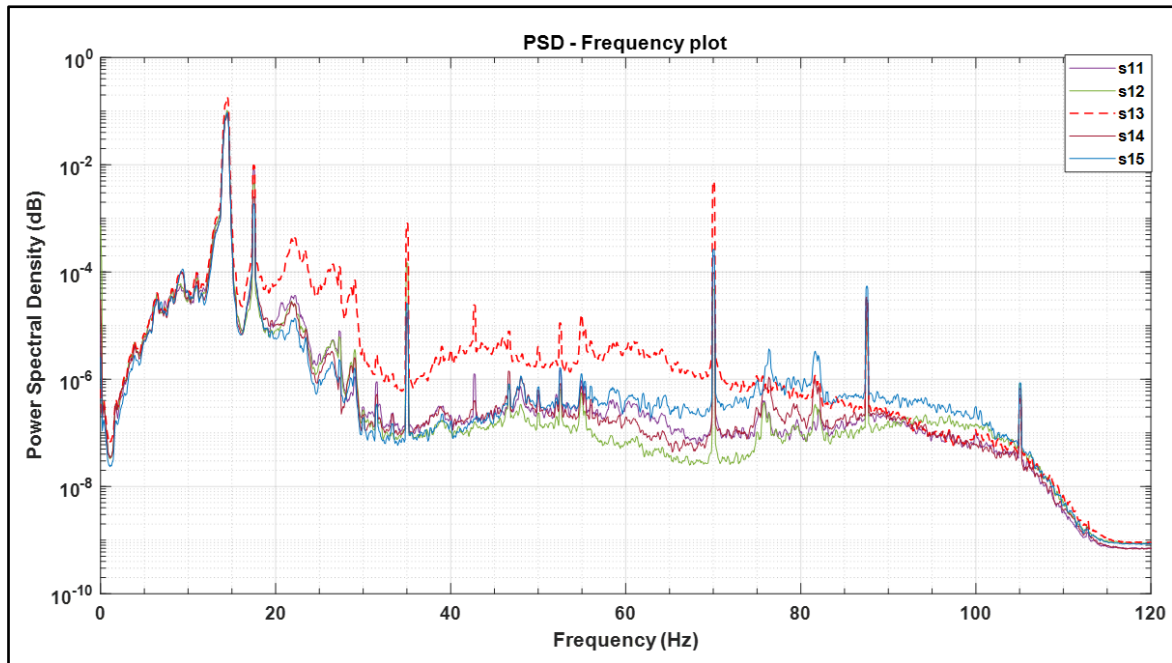


**Figure 6.19:** An examination of the Power Spectral Density (PSD) of vertically recorded seismic waves reveals distinct variations. Notably, at Station No. s13, situated directly above the object (concrete), the PSD diverges from the others within the frequency range spanning from 18 to 80 Hz.

**Table 6.11:** The area beneath each curve in figure 6.19, ranging from monitoring station No. s1 to Monitoring Station No. s25 (concrete block).

S11	1.049
S12	1.139
S13	2.04
S14	0.962
S15	1.011

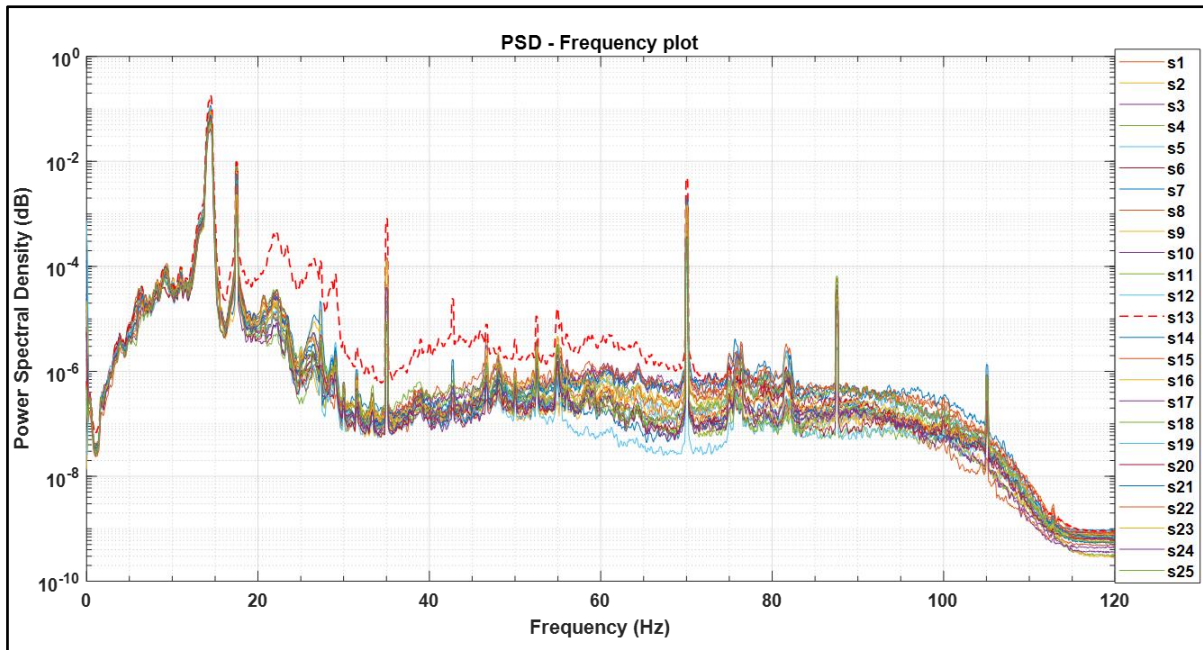


**Figure 6.20:** PSD curves of all vertical traces of all 25 sensors. most of the curves are almost identical except the curve corresponding to the monitoring station s13 (for the frequencies between 18Hz and 75Hz) which is placed upon the buried concrete.

**Table 6.12:** The table presents the area under the Power Spectral Density (PSD) curves for all monitoring stations, as depicted in Figure 6.20. Monitoring station s13 exhibited the highest Power Spectral Density (PSD) value among all stations (concrete block).

S21	0.843	S16	0.983	S11	1.049	S6	0.983	S1	1.01
S22	0.721	S17	0.821	S12	1.139	S7	1.29	S2	1.083
S23	0.515	S18	0.614	S13	2.04	S8	1.084	S3	0.887
S24	0.483	S19	0.67	S14	0.962	S9	0.984	S4	0.919
S25	0.629	S20	0.703	S15	1.011	S10	0.995	S5	0.877

### 6.14.2 Steel drum experiment

The seismic waves were recorded at all monitoring stations when the seismic wave source was positioned 40m away from the object (steel drum). Station No. s13 (deployed directly above the steel) exhibited a higher amplitude in the recorded waves compared to all the other monitoring stations (see appendix F2).

Figure 6.21 and figure 6.22 presents the PSD curves of seismic waves detected at all monitoring stations. In the frequency range of 15 to 60 Hz, Station 13, located directly above the object, recorded the highest PSD values. In contrast, the other curves show mostly similar patterns without significant differences. Above the 60 Hz threshold, the distinction between the PSD curves becomes less clear and more difficult to discern.

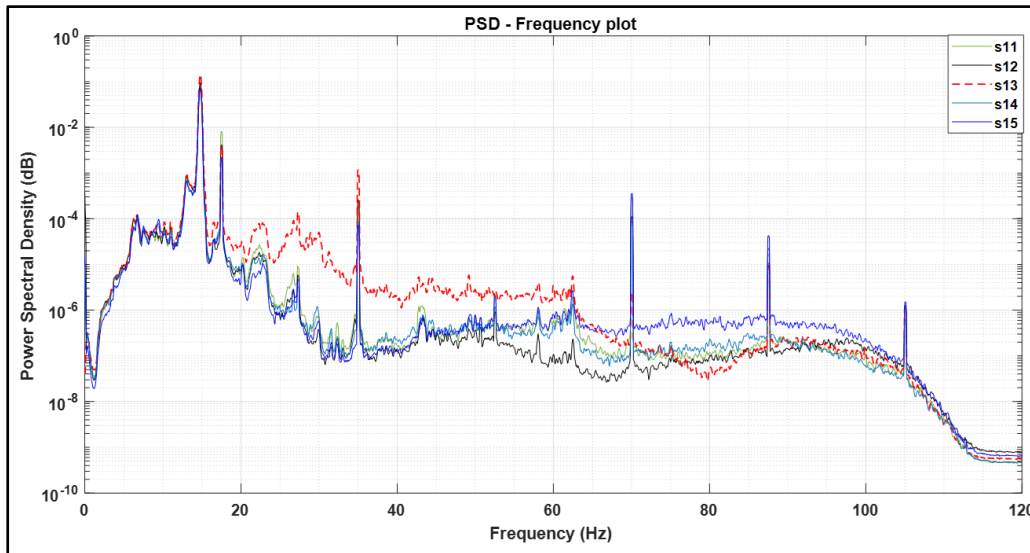


**Figure 6.21:** The Power Spectral Density (PSD) of seismic waves recorded at monitoring stations s11, s12, s13, s14, and s15 indicates nearly identical PSD curves. However, there is an exception: the curve associated with monitoring station s13 (placed upon the steel drum), specifically in the frequency range between 18Hz and 65Hz, exhibits a distinct deviation.

**Table 6.13:** The area beneath each curve in figure 6.21, ranging from monitoring station No. s11 to Monitoring Station No. s15 (Steel drum).

S11	0.666
S12	0.741
S13	1.122
S14	0.55
S15	0.555

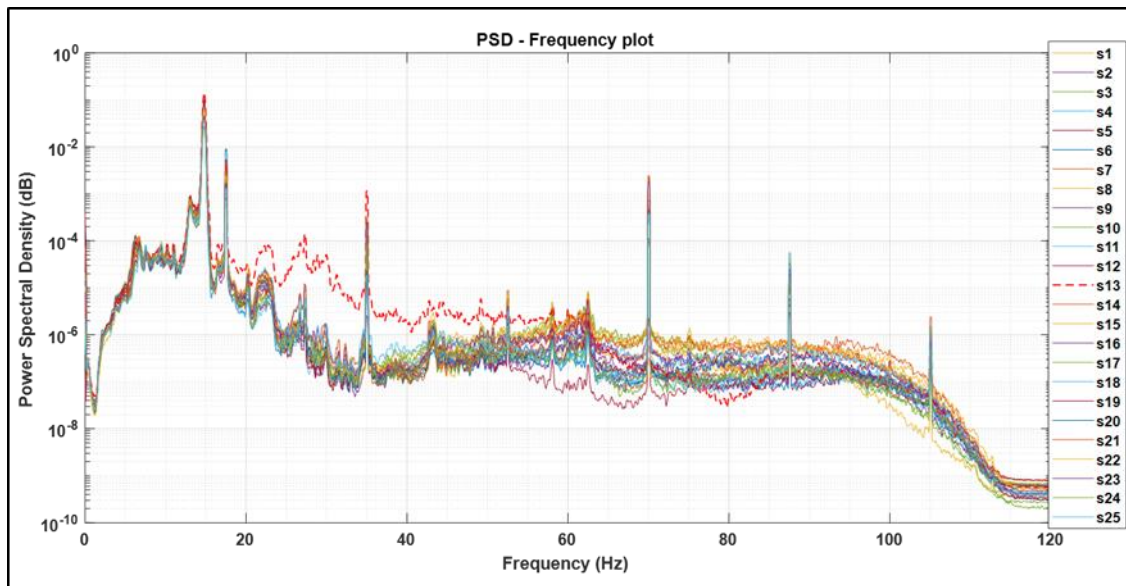


**Figure 6.22:** This figure illustrates the PSD curves of seismic waves detected across all monitoring stations. Within the frequency range of 15 to 60 Hz, monitoring station s13, situated directly above the object, recorded the highest PSD, while the remaining curves exhibit mostly similar patterns with no noticeable distinctions. Beyond the 60 Hz threshold, differentiation between the PSD curves becomes less apparent and more challenging (steel drum).

**Table 6.14:** The numbers in the table correspond to the values beneath the power spectral density curves in the figure 6.22. Station No. s13 registered the maximum seismic energy among all the stations (steel drum).

S21	0.601	S16	0.687	S11	0.666	S6	0.588	S1	0.611
S22	0.525	S17	0.582	S12	0.741	S7	0.834	S2	0.707
S23	0.367	S18	0.397	S13	1.122	S8	0.708	S3	0.582
S24	0.225	S19	0.31	S14	0.55	S9	0.608	S4	0.57
S25	0.308	S20	0.354	S15	0.555	S10	0.609	S5	0.568

### 6.14.3 Plastic drum experiment

In the time domain analysis of seismic waves recorded across all monitoring stations, Station 13, positioned directly above the object and marked by the red dashed line, consistently exhibits the highest wave amplitude. This increased amplitude indicates a significant interaction between the seismic waves and the underlying object, highlighting Station 13's crucial role in capturing the effects of the subsurface object and distinguishing it from the other stations (appendix F 3).

PSD of seismic waves recorded at all monitoring stations, the dashed line representing Station 13, located directly above the object, reveals the highest values within the frequency range of 18 to 55 Hz (see Figures 23 and 24). This suggests that the interaction between the seismic waves and the object significantly enhances the recorded energy at this station. In contrast, the PSD curves of all other stations exhibit nearly identical patterns, indicating a uniform response across those locations. This distinction underscores the unique impact of the subsurface object on the seismic data collected at Station 13.

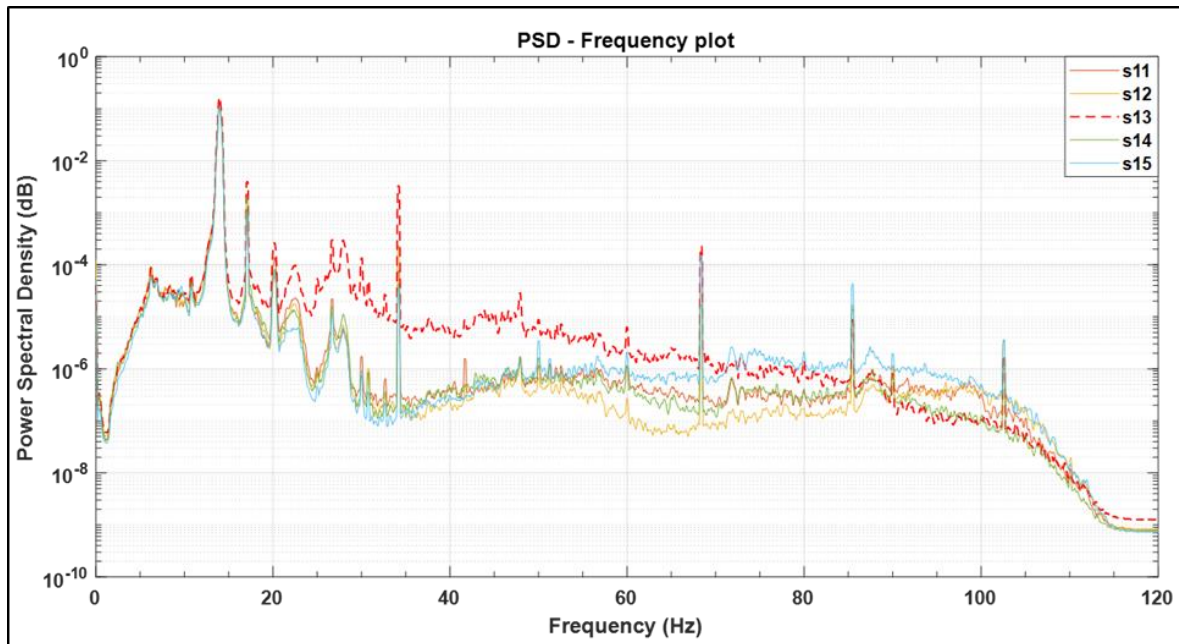


**Figure 6.23:** The PSD of some seismic waves recorded in the vertical component. All PSDs curves are identical except for the curve, which represents the PSD recorded at monitoring station s13, which is located directly above the plastic. The largest amount of seismic energy was recorded at monitoring station s13, which corresponds to a frequency of 18 to 70 Hz. And this indicates the presence of the object.

**Table 6.15:** The calculated area under the PSD curves in the figure 6.23. It is clear that the monitoring station recorded the highest value compared to the other stations (plastic drum).

S11	1.025
S12	1.161
S13	1.498
S14	0.953
S15	0.968

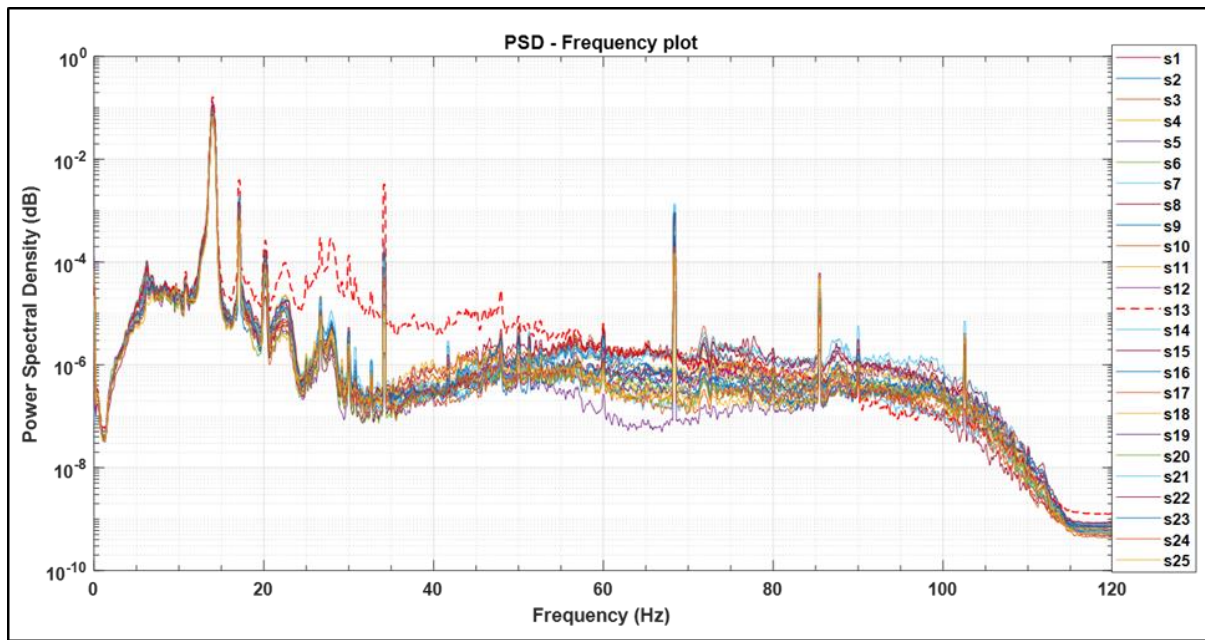


**Figure 6.24:** Comparing the PSD of seismic waves recorded at all monitoring stations, the dashed line representing the monitoring station No. s13, which is situated above the object, showed the highest value within the frequency range of 18 to 55 Hz. All other PSD curves exhibit nearly identical patterns.

**Table 6.16:** The calculated PSD value is shown under each curve in Figure 6.24. Comparison to all values at other stations, the station s13 showed the highest value (plastic drum).

S21	0.736	S16	0.868	S11	1.025	S6	0.955	S1	0.95
S22	0.692	S17	0.848	S12	1.161	S7	1.205	S2	0.905
S23	0.535	S18	0.69	S13	1.498	S8	0.934	S3	0.72
S24	0.552	S19	0.739	S14	0.953	S9	0.892	S4	0.785
S25	0.613	S20	0.698	S15	0.968	S10	0.914	S5	0.752

### 6.15 Summary of Vertical Component Results

**In concrete experiment,** when seismic source located at SA, The Power Spectral Density (PSD) analysis of seismic waves recorded in the Z-component at all monitoring stations reveals a distinctive anomaly at station s13 in the frequency range of 20 to 70 Hz, as shown in Figure 6.13. Table 6.5, which accompanies the PSD plots, numerically represents the area under each curve. Larger areas under the PSD curves indicate higher seismic energy, and station s13 displays a significant response above the concrete object. Similar results were obtained when the wave source was located at position SB.

This distinct pattern confirms the presence of the concrete structure, as observed when the seismic source is positioned at both locations SA and SB. The heightened wave amplitude at monitoring station s13 suggests that the concrete structure significantly influences the seismic waves recorded at this location. The distinctiveness of the amplitude patterns, in comparison to other stations, indicates the specific response of the concrete to seismic activity.

**In the steel drum experiment**, where the drum was buried approximately 1 m beneath the earth surface, the analysis of seismic data in both the time and frequency domains provided good results. Monitoring station s13, directly above the steel drum, recorded the highest amplitude of the seismic waves (appendix E2). This phenomenon was evident not only in the time domain, where the waveform characteristics were assessed, but also in the frequency domain, where the distribution of energy across different frequencies was examined. The peak values occur at approximately 20 to 70 Hz and 80 to 120 Hz, with s13 recording the highest seismic energy above the steel drum (figure 6.15). Even when the seismic source was at SB, located farther away, the steel drum's location was still identifiable by analysing the vertical component of the seismic waves. Figures 6.22 illustrate the seismic wave characteristics influenced by the steel drum, confirming its detectability and demonstrating its effect on the recorded seismic waves.

**The plastic drum experiment** demonstrated that a plastic drum buried at a depth of 1 m in brownfields could be identified using seismic wave analysis of the vertical component. The study supports this conclusion by showing that monitoring station s13, located directly above the plastic drum, recorded the greatest quantity of seismic energy. This data emphasizes the efficacy of studying vertical seismic wave properties in identifying and detecting buried objects, as indicated by the increased seismic energy concentration at station s13. By comparing the seismic waves in the time domain, it became clear that the waves reflected from the plastic drum had greater amplitudes than those recorded at other monitoring stations, as shown in appendix E 3. Calculating the PSD of the seismic waves, which represents the amount of seismic energy, also confirmed that station s13 recorded a larger seismic energy value, as depicted in Figure 6.23. Despite some overlapping curves, calculating the area under each curve for the PSD revealed that the largest value was at station s13, as shown in Table 6.15.

These findings collectively highlight that vertical component seismic wave analysis is a reliable method for detecting buried objects, such as concrete structures, steel drums, and plastic drums.

## 6.16 East – West component (Seismic Source located at SA)

### 6.16.1 Concrete experiment

In the time domain analysis of seismic wave recordings for the East-West component across all monitoring stations, station s13, marked by the dashed red line and positioned directly above the concrete, consistently exhibited the highest energy levels. This heightened energy response at station s13 highlights a significant interaction between the seismic waves and the underlying concrete structure, setting it apart from the other stations. The increased energy levels suggest that the concrete's presence amplifies or alters the wave propagation, making station 13's recordings distinct in comparison to the relatively uniform signals from the other monitoring stations ( see appendix G 1).

The Power Spectral Density (PSD) analysis of seismic waves detected across all monitoring stations shows that Station 13, positioned above a subsurface concrete object, recorded the highest spectral density in the 15 to 27 Hz range. This peak indicates a significant concentration of seismic energy at Station 13, likely due to the interaction between the waves and the concrete. In contrast, the other stations show more uniform PSD patterns, emphasizing the distinct seismic response at Station 13 caused by the subsurface object (see figure 6.25 and figure 6.26).

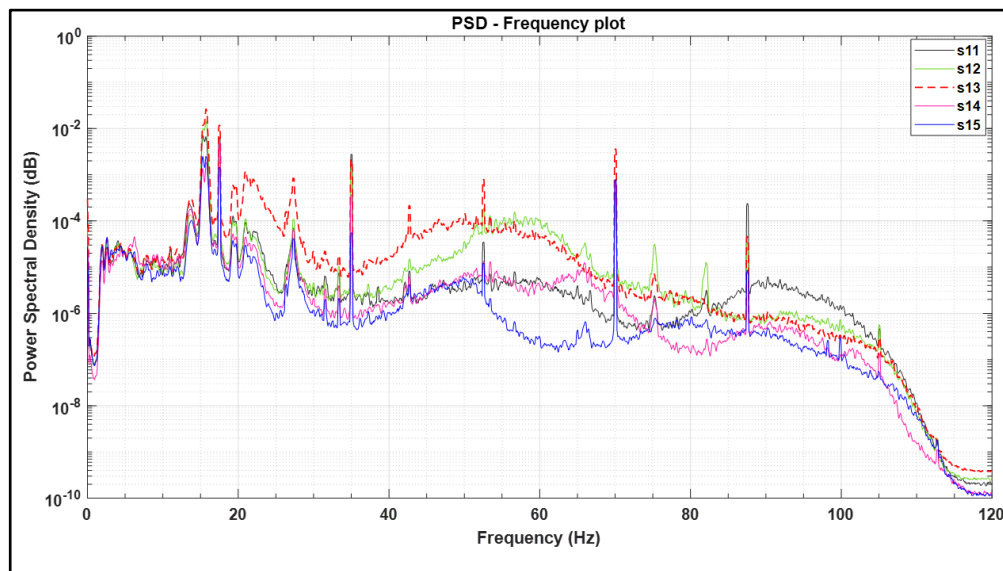


**Figure 6.25:** The PSD plot for seismic waves at monitoring stations s11-s15 displays different patterns, where station s13 stands out with high seismic energy across a wide frequency range (18 to 50 Hz). This signifies a more prominent influence from the underlying concrete.

**Table 6.17:** The calculated area under the PSD curves in Figure 6.25.

S11	0.167
S12	0.239
S13	0.491
S14	0.069
S15	0.058

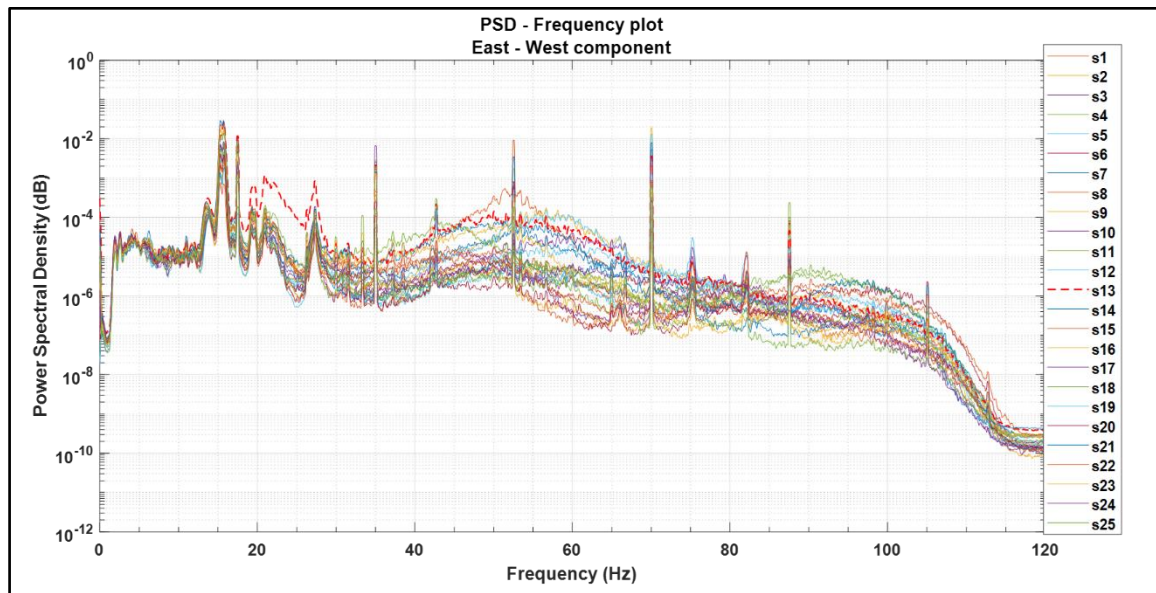


**Figure 6.26:** The PSD of all seismic waves detected by all monitoring stations. The maximum value of the spectral density curve was measured at monitoring station s13 over a frequency range of 15 to 27 Hz.

**Table 6.18:** This table represents the estimated area under the curves for the PSD of all seismic waves at all monitoring stations in figure 6.26. The calculated area under the PSD curve at monitoring station s13 recorded a high value compared to all other stations except for station No., which recorded the highest value (concrete object).

S21	0.499	S16	0.292	S11	0.167	S6	0.115	S1	0.194
S22	0.365	S17	0.215	S12	0.239	S7	0.201	S2	0.203
S23	0.31	S18	0.281	S13	0.491	S8	0.096	S3	0.1
S24	0.137	S19	0.118	S14	0.069	S9	0.054	S4	0.073
S25	0.112	S20	0.082	S15	0.058	S10	0.067	S5	0.131

### **6.16.2 Steel drum experiment**

A comparison of seismic waves in the time domain reveals that the red dashed curve, representing the seismic waves recorded at Station s13, exhibits the highest wave amplitude compared to all other monitoring stations. Station s13 is positioned directly above steel drum. The increased amplitude suggests that the object beneath the station influences wave propagation. In contrast, the other monitoring stations, which are not directly above the object, display waveforms with lower amplitudes, reflecting a more uniform seismic response. This comparison highlights the impact of steel drum on seismic wave behaviour, with Station s13 showing a clear distinction due to its proximity to the object (see appendix G2).

The Power Spectral Density (PSD) analysis of seismic waves recorded at monitoring stations s11, s12, s13, s14, and s15 reveals that Station s13 exhibits the highest PSD values in the frequency range of 18 to 40 Hz (see Figure 6.27). This suggests a significant concentration of seismic energy at Station s13 compared to the other stations within this frequency band. Station 13 is positioned above a subsurface object, which likely contributes to this unique frequency response due to wave interactions with the buried material.

Further, when examining the PSD of seismic waves across all monitoring stations, the curve for Station s13 again stands out, recording the highest values within the narrower frequency range of 20 to 25 Hz (see Figure 6.28). This consistent pattern of elevated PSD values highlights the impact of the subsurface object on seismic wave behaviour, particularly in specific frequency intervals. The comparison underscores the distinct seismic response at Station s13, driven by the interaction between the waves and the underlying structure. In contrast, the PSD curves from other stations remain relatively uniform, indicating less significant local influences.

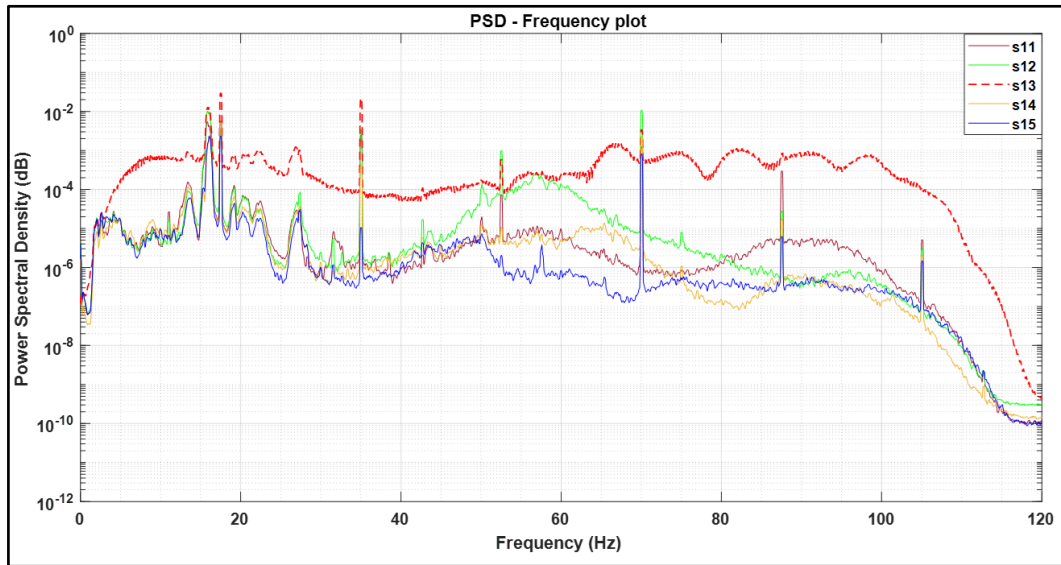


**Figure 6.27:** This figure depicts the Power Spectral Density (PSD) curves of seismic waves recorded at monitoring station s11, s12, s13, s14, s15. The PSD of seismic waves recorded at monitoring station No. s13 is the highest compared to other stations. This indicates that the largest amount of seismic energy was reflected from the steel drum and recorded at station No. s13, which is located directly above the steel drum

**Table 6.19:** The table outlines the areas under the Power Spectral Density (PSD) curves that were previously illustrated in Figure 6.27. Each entry in the table corresponds to a different monitoring station. It is noted that monitoring station No. s13 recorded the highest PSD value among all stations listed.

S11	0.126
S12	0.258
S13	1.284
S14	0.075
S15	0.047

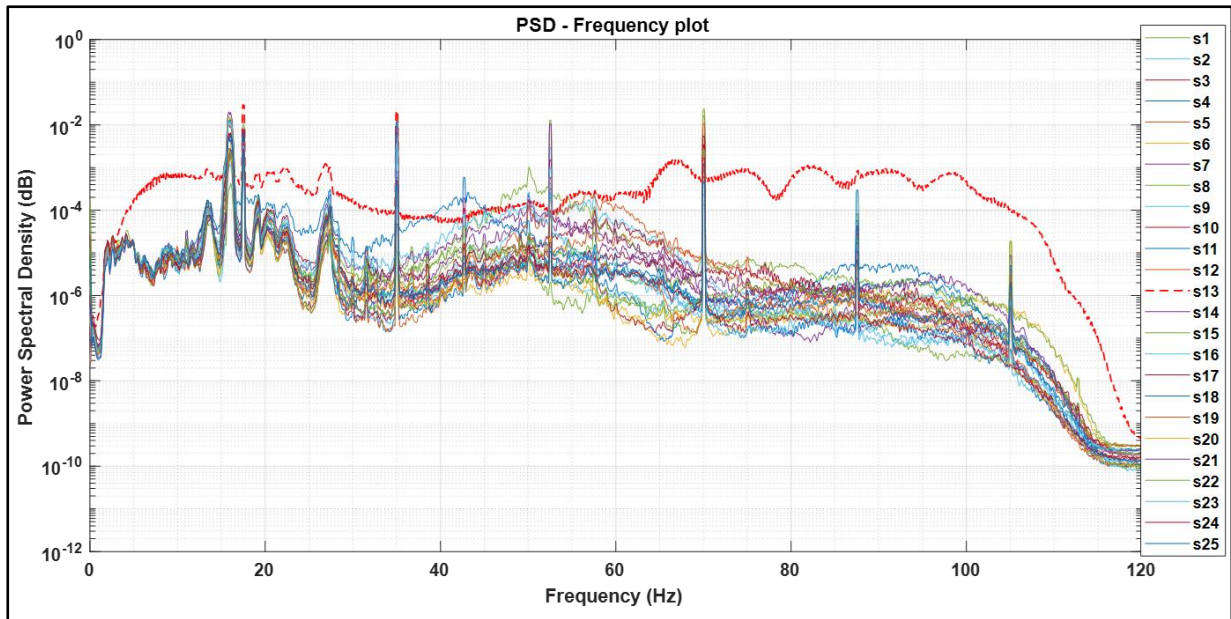


**Figure 6.28:** This figure displays the Power Spectral Density (PSD) curves of seismic waves recorded at all monitoring stations, with station No. s13 recording the highest PSD values for seismic waves.

**Table 6.20:** The values in the table correspond to the area beneath the Power Spectral Density (PSD) curves presented in Figure 6.28. Station No. s13 recorded the highest seismic energy among all the stations.

S21	0.366	S16	0.187	S11	0.126	S6	0.107	S1	0.256
S22	0.229	S17	0.191	S12	0.258	S7	0.173	S2	0.15
S23	0.23	S18	0.322	S13	1.284	S8	0.211	S3	0.076
S24	0.112	S19	0.106	S14	0.075	S9	0.051	S4	0.064
S25	0.088	S20	0.061	S15	0.047	S10	0.058	S5	0.125

### 6.16.3 Plastic drum experiment

A comparison of seismic waves recorded at all monitoring stations shows that Station s13, represented by the red dashed curve, exhibits the highest wave amplitude. Positioned above a plastic drum object, Station 13's amplified response is likely due to wave interactions with the material beneath it, such as reflections or scattering. In contrast, other stations display more uniform and moderate amplitudes, highlighting the unique impact of the subsurface object on wave propagation at Station s13.

The Power Spectral Density (PSD) analysis of seismic waves recorded at monitoring stations s11, s12, s13, s14, and s15 shows that Station s13 has the highest PSD values in the frequency range of 18 to 40 Hz (see Figure 6.29). Additionally, when examining the PSD across all monitoring stations, Station s13 again stands out, recording the peak values specifically within the frequency range of 20 to 25 Hz (see Figure 6.30).

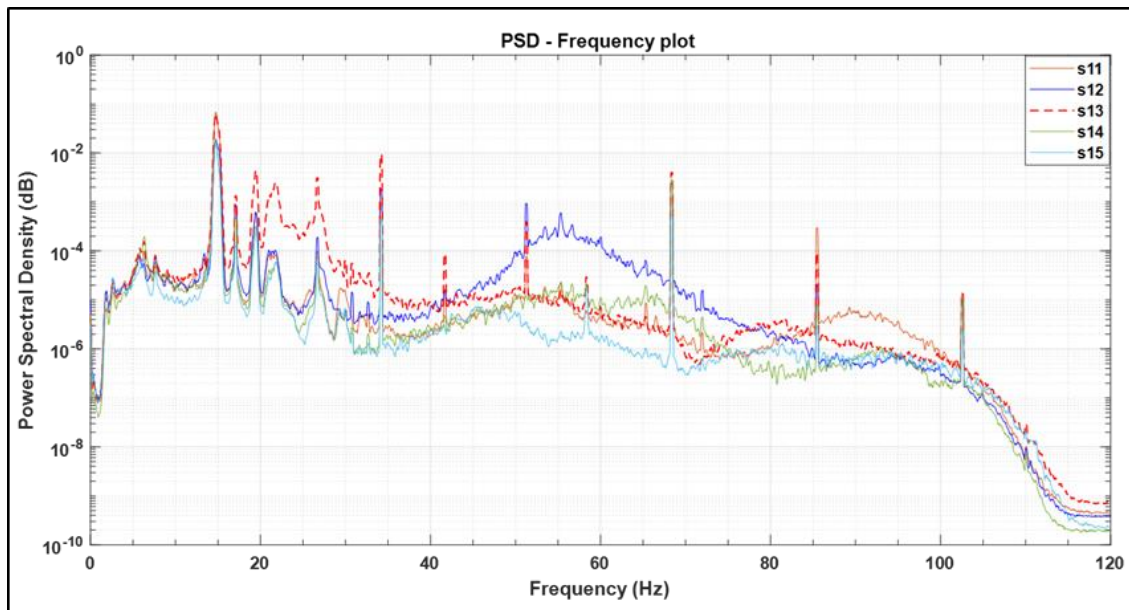


**Figure 6.29:** The PSD of the seismic waves recorded at monitoring stations s11, s12, s13, s14 and s15. I notice that the curve representing the PSD of the seismic waves recorded at monitoring station s13 records the highest value corresponding to the frequency period from 18 to 40 Hz.

**Table 6.21:**The calculated Power Spectral Density (PSD) values are depicted beneath each curve in Figure 6.29. Upon comparison with values from other stations, it is evident that station s13 exhibited the highest PSD value.

S11	0.764
S12	0.33
S13	0.933
S14	0.216
S15	0.175

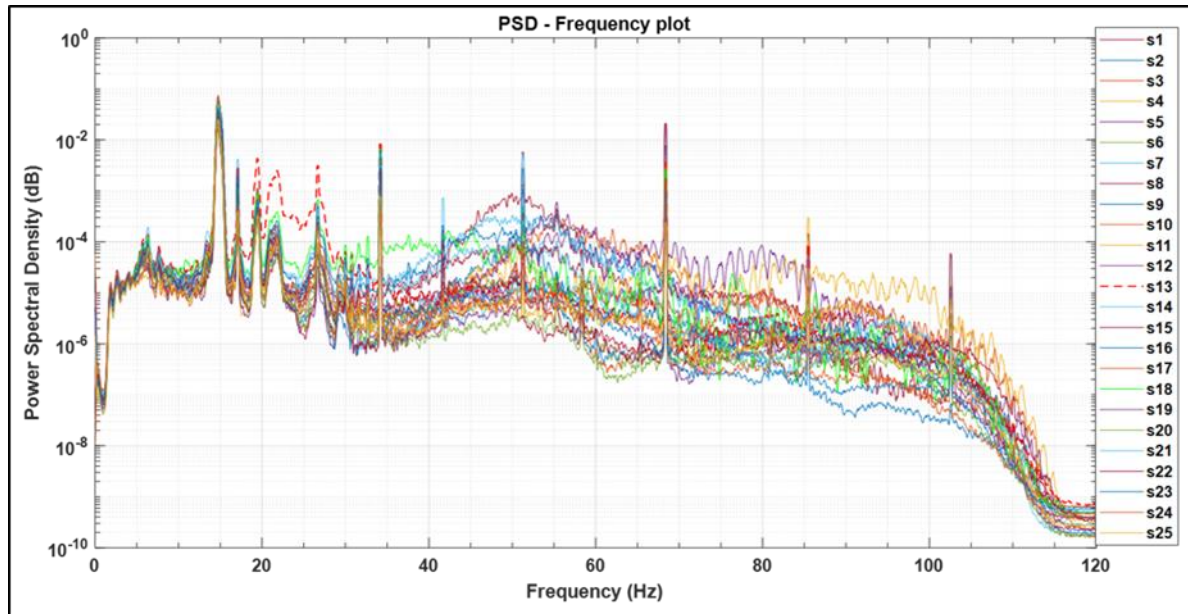


**Figure 6.30:** Power Spectral Density (PSD) of seismic waves recorded at all monitoring stations. The curve depicting the PSD of seismic waves at monitoring station s13 recorded the highest value within the frequency range spanning from 20 to 25 Hz.

**Table 6.22:** The computed PSD value is shown under each curve in Figure 6.30. In comparison to all other stations, Station s13 has the greatest value.

S21	0.68	S16	0.803	S11	0.764	S6	0.554	S1	0.62
S22	0.484	S17	0.829	S12	0.33	S7	0.461	S2	0.422
S23	0.577	S18	0.71	S13	0.933	S8	0.472	S3	0.324
S24	0.28	S19	0.205	S14	0.216	S9	0.21	S4	0.277
S25	0.277	S20	0.194	S15	0.175	S10	0.22	S5	0.362

### 6.17 East – West component (Seismic Source located at SB)

#### 6.17.1 Concrete experiment

A comparison of seismic waves in the east-west component recorded at monitoring stations s11 to s15 reveals that Station s13, located directly above the concrete and indicated by the red dashed line, has the largest peak wave amplitude. This indicates stronger seismic activity at Station 13, likely due to the interaction between the seismic waves and the underlying concrete, which enhances the recorded signal. In contrast, the other stations show lower peak amplitudes, reflecting a more typical seismic response without the influence of a significant subsurface

feature. This emphasizes the impact of geological conditions on wave propagation and local seismic activity (see appendix H1).

Power Spectral Density (PSD) Curves for Seismic Waves at Monitoring Stations s11 to s15 Show Notable Increase at Station s13. Analysis of PSD curves for seismic waves recorded at stations s11 to s15 indicates a significant increase in PSD values at Station s13, which is located on buried concrete. This increase is particularly pronounced within the 18 Hz to 55 Hz frequency range, especially between 20 Hz and 35 Hz, as shown in Figure 6.31. The Power Spectral Densities (PSDs) of the seismic waves recorded at all monitoring stations indicate that Station S13, situated on buried concrete, exhibits a higher spectral amplitude in the frequency range of 20 Hz to 35 Hz (figure 6.32).

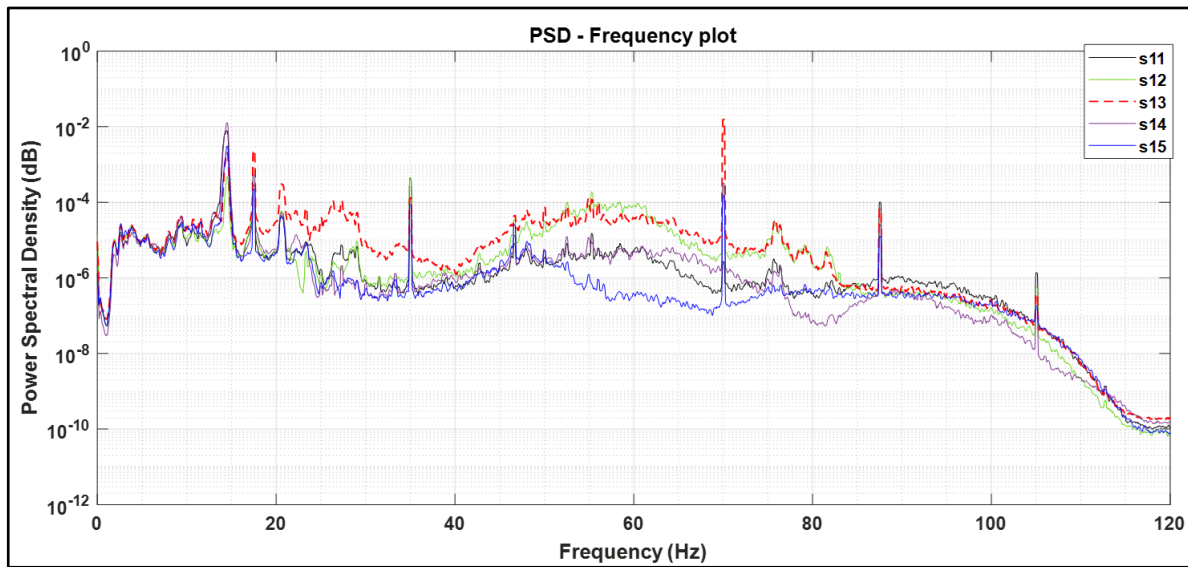


**Figure 6.31:** Power Spectral Density (PSD) Curves for Seismic Waves at Monitoring stations s11 to s15: Notable Increase in PSD Values at Station 13 Over Concrete in the 18Hz to 55Hz Range.

**Table 6.23:** Estimated area under PSDs curves (figure 6.31), the area value under PSD curve which recorded at monitoring station s13 is higher than the others.

S11	0.098
S12	0.037
S13	0.145
S14	0.126
S15	0.033

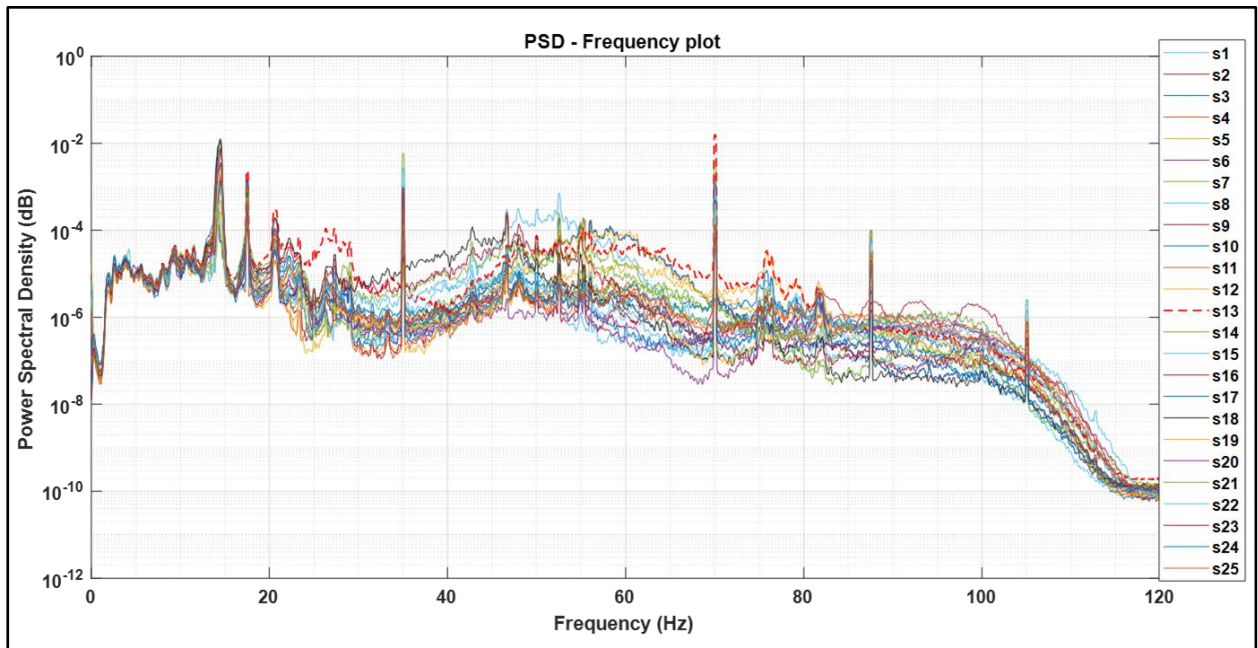


**Figure 6.32:** PSDs of the seismic waves that recorded at all monitoring stations, s13, which is placed upon the buried concrete. Its spectral amplitude is higher between frequencies 20Hz to 35Hz.

**Table 6.24:** This table shows the estimated PSD area under the curves for the seismic waves at all monitoring stations in figure 6.32. Concrete's had a little effect on seismic waves that recorded at monitoring station No. 13's which located above the concrete.

S21	0.062	S16	0.05	S11	0.098	S6	0.045	S1	0.074
S22	0.037	S17	0.139	S12	0.037	S7	0.047	S2	0.046
S23	0.099	S18	0.148	S13	0.145	S8	0.029	S3	0.046
S24	0.076	S19	0.032	S14	0.126	S9	0.021	S4	0.022
S25	0.073	S20	0.064	S15	0.033	S10	0.021	S5	0.026

### 6.17.2 Steel experiment

A comparison of the seismic waves recorded at monitoring stations s11, s12, s13, s14, and s15 reveals that Station s13 recorded the highest wave amplitude. This increased amplitude can be attributed to the influence of the nearby steel drum. The seismic waves were captured at all monitoring stations with the source located at SB. Notably, Station s13, which is positioned directly above the steel drum, displayed significantly greater amplitude in the recorded waves compared to the other monitoring stations (see appendix H2).

The Power Spectral Density (PSD) curves for seismic waves recorded at monitoring stations s11, s12, s13, s14, and s15 show that station s13 reached its peak PSD within the frequency range of 18 to 40 Hz. This indicates that seismic activity in this frequency band had the highest energy concentration, as illustrated in Figure 6.33. Furthermore, within the narrower frequency range of 18 to 30 Hz, station s13 exhibited its maximum PSD value. This finding underscore that the concentration of seismic energy was particularly strong in this specific range, as shown in Figure 6.34.

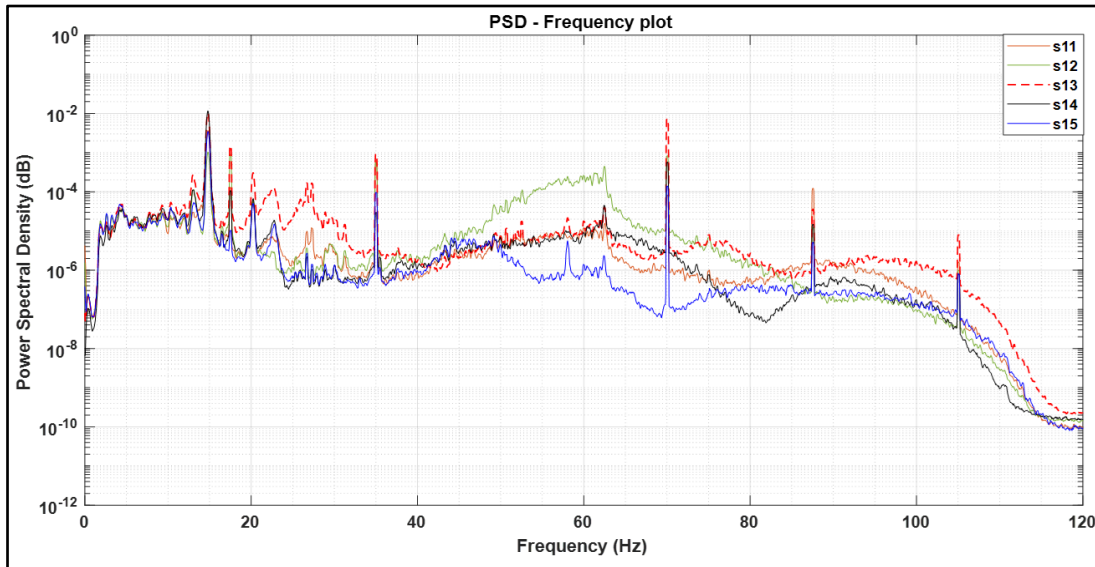


**Figure 6.33:** Power Spectral Density (PSD) curves of seismic waves recorded at monitoring stations s11, s12, s13, s14, and s15. The PSD of seismic waves at s13 reached its peak within the frequency range of 18 to 40 Hz. This indicates that seismic activity exhibited the highest energy concentration in this specific frequency band.

**Table 6.25:** This table provides a quantitative analysis of the areas under the Power Spectral Density (PSD) curves as showed in Figure 6.33. It lists each monitoring station alongside the corresponding area values, calculated from their PSD curves. Notably, monitoring station No. s13 is highlighted for recording the highest PSD value, indicating a greater concentration of seismic energy across the frequency spectrum compared to other stations.

S11	0.042
S12	0.071
S13	0.151
S14	0.099
S15	0.034

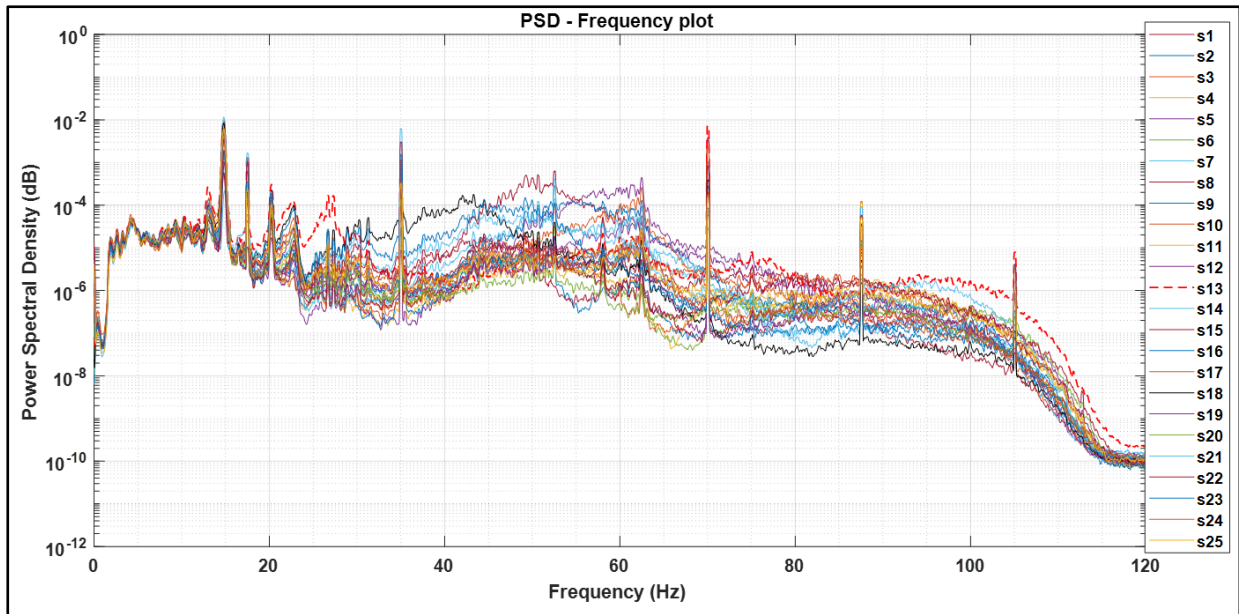


**Figure 6.34:** The Power Spectral Density (PSD) curves depict seismic waves recorded at all monitoring stations. Within the frequency range of 18 to 30 Hz, the PSD of seismic waves at station s13 attains its maximum value. This observation signifies that the concentration of seismic energy was highest within this particular frequency band.

**Table 6.26:** The calculated values are under the curves of the PSD curves in Figure 6.34. Since the PSD represents the amount of recording seismic energy, the highest value of the seismic energy was recorded at monitoring station No. s13. This is evidence of the presence of the object’s influence on the characteristics of the seismic waves.

S21	0.084	S16	0.031	S11	0.042	S6	0.022	S1	0.088
S22	0.052	S17	0.068	S12	0.071	S7	0.034	S2	0.052
S23	0.086	S18	0.103	S13	0.151	S8	0.04	S3	0.042
S24	0.061	S19	0.049	S14	0.099	S9	0.023	S4	0.039
S25	0.061	S20	0.053	S15	0.034	S10	0.035	S5	0.047

### 6.17.3 Plastic drum experiment

A comparison of the seismic waves recorded by various monitoring stations highlights the challenges in distinguishing the differences and characteristics of the waves based on amplitude. Notably, the seismic waves recorded at monitoring station s13 show a slightly higher amplitude than those at the other stations. The plot further illustrates the fluctuations in amplitude over the observed time period across the different monitoring stations (see appendix H3).

The Power Spectral Density (PSD) of seismic waves recorded at various monitoring stations provides valuable insights into energy distribution across different frequencies. Monitoring station s13 recorded the highest energy concentration in the frequency range of 18 to 35 Hz, as shown in Figure 6.35. Notably, this peak is particularly pronounced within the narrower band of 25 to 27 Hz.

Despite station s13's higher energy levels, distinguishing between the monitoring stations remains challenging. The overlapping energy levels and similar amplitude patterns complicate the ability to differentiate their seismic responses, as illustrated in Figure 6.36. This highlights the need for further analysis to better understand the variations in seismic wave behaviour across the stations.

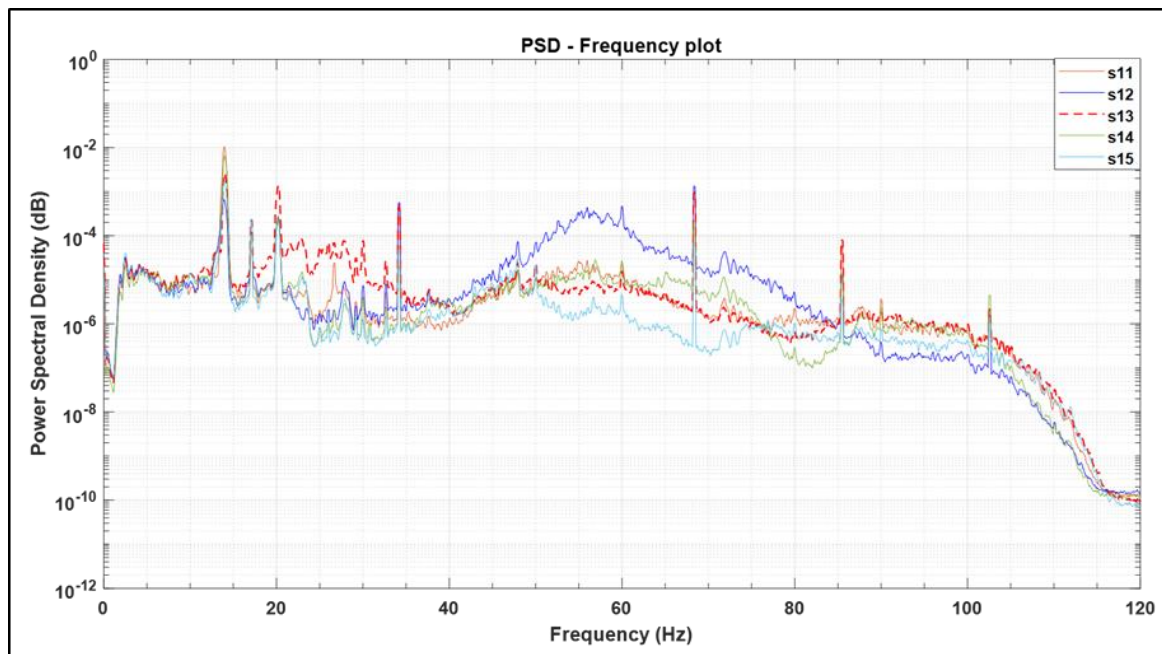


**Figure 6.35:** The PSD of seismic waves at some monitoring stations. Monitoring station s13 recorded the highest amount of energy corresponding to a frequency period from 18 to 35 Hz.

**Table 6.27:** The calculated Power Spectral Density (PSD) values are depicted beneath each curve in Figure 6.35. it is difficult to identify the object based on the area under the PSDs curves.

S11	0.099
S12	0.084
S13	0.06
S14	0.069
S15	0.025

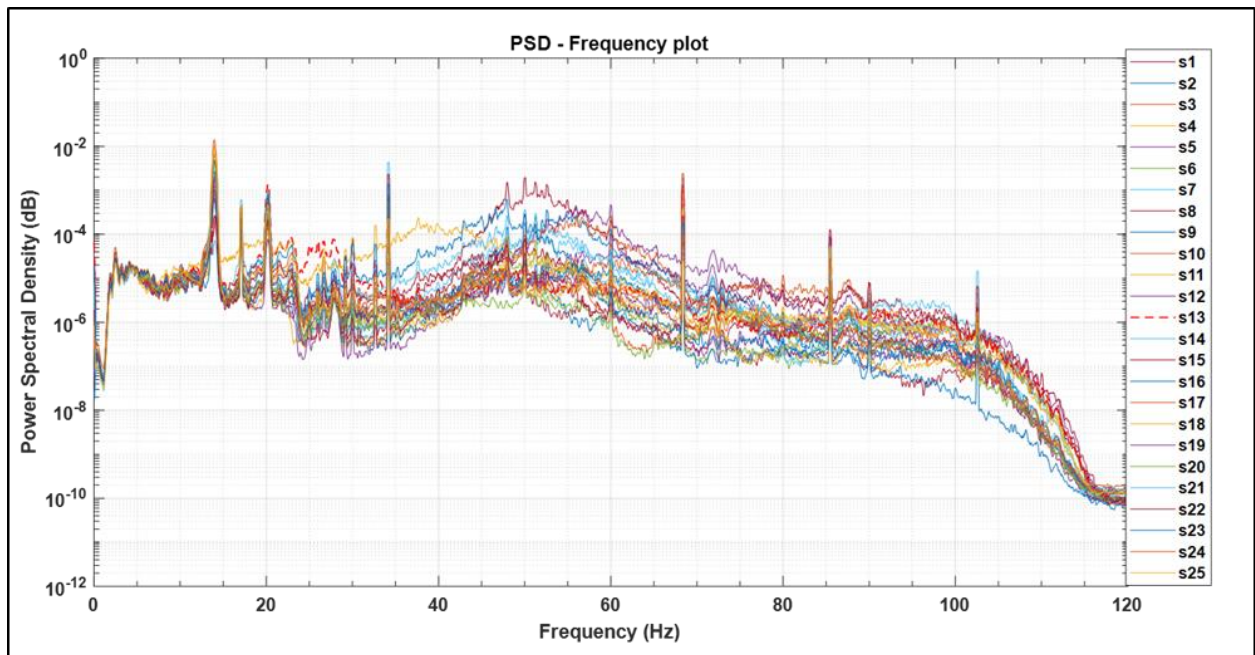


**Figure 6.36:** The PSDs curves depict the seismic waves recorded at all monitoring stations. Despite the monitoring station s13 with the highest energy being identified within a narrow frequency range of 25 to 27 Hz, distinguishing between the monitored stations remains challenging.

**Table 6.28:** The calculated Power Spectral Density (PSD) values are depicted beneath each curve in Figure 6.36. When comparing with all other stations, it is apparent that the plastic drum cannot be detected through the East-West component.

S21	0.096	S16	0.041	S11	0.099	S6	0.045	S1	0.18
S22	0.036	S17	0.15	S12	0.084	S7	0.049	S2	0.06
S23	0.11	S18	0.139	S13	0.06	S8	0.033	S3	0.054
S24	0.07	S19	0.033	S14	0.069	S9	0.015	S4	0.033
S25	0.078	S20	0.047	S15	0.025	S10	0.03	S5	0.038

### 6.18 Summary of E - W Component Results

**Objects (concrete)** can be detected in brownfield areas by analysing the characteristics of seismic waves recorded from the horizontal component (E-W) when the seismic wave source is at SA (20 m away). This detection capability is evident in appendix G1, which shows the time domain, and Figure 6.26, which shows the frequency domain. The Power Spectral Density (PSD) of seismic waves detected by all monitoring stations indicates that the maximum value of the spectral density curve was measured at monitoring station s13 over a frequency range of 15 to 27 Hz. This finding is further confirmed by calculating the area under the curves, as

represented in Table 6.18, where the highest value was recorded for the curve corresponding to station s13. By examining the seismic wave characteristics recorded from the horizontal component (E-W) at seismic source location SB (40m from the concrete), the presence of objects, including concrete, in brownfield areas can also be detected. Appendix G2 illustrate this capability, demonstrating that even at greater distances, the seismic signature of buried concrete remains discernible. This extended detection range highlights the robustness of using seismic wave analysis for subsurface exploration and monitoring in various field conditions.

The results show the successful detection of the **steel drum** when the seismic wave source is at SA. Figure 6.27 displays the Power Spectral Density (PSD) curves, with station s13 recording the highest PSD, indicating the largest seismic energy reflected from the drum. Figure 6.28 and Table 6.20 further confirm that station s13 recorded the highest seismic energy.

When the seismic source is at SB, Figure 6.34 shows the PSD curves, with station s13 peaking within the 18 to 30 Hz range, indicating the highest energy concentration. Table 6.25 confirms that station s13 recorded the highest PSD value, showing greater seismic energy concentration compared to other stations.

**In the plastic experiment**, when the seismic source was at SA, the Power Spectral Density (PSD) of seismic waves recorded at all monitoring stations indicated that station s13 had the highest value within the 20 to 25 Hz range (Figure 6.30). Table 6.21 confirms that station s13 recorded the greatest PSD value.

At SB, Figure 6.36 shows the PSD curves for all stations, with station s13 showing the highest energy in a narrow 25 to 27 Hz range, making it difficult to distinguish between stations. Table 6.28 indicates that the plastic drum cannot be detected through the East-West component.

## **6.19 North – South component (Seismic Source located at SA)**

### **6.19.1 Concrete experiment**

A comparison of seismic waves recorded from the North-South component at all monitoring stations s11 – s25 reveals notable differences in wave characteristics, particularly at station s13. Station s13, which is positioned directly above a concrete block, exhibits a slightly higher wavelength in the seismic waves compared to the other monitoring stations.

This higher wavelength at station s13 suggests that the presence of the concrete beneath the station may be influencing the propagation of the seismic waves. Concrete, due to its density

and stiffness, could be affecting the wave speed and wavelength, potentially leading to this observed increase (see appendix I 1).

. The Power Spectral Densities (PSDs) of seismic waves recorded at monitoring stations s11, s12, s13, s14, and s15 reveal that station s13, positioned directly above the concrete block, recorded the highest PSD values within the frequency range of 20 Hz to approximately 55 Hz, as shown in Figure 6.37. This confirms that the presence of the concrete continues to influence the seismic wave behaviour, which is evident from the recordings in the North-South component. Similarly, PSD measurements taken at all monitoring stations demonstrate that station s13, located above the concrete block, recorded the maximum PSD values within the 20 Hz to 55 Hz frequency range, as illustrated in Figure 6.38.

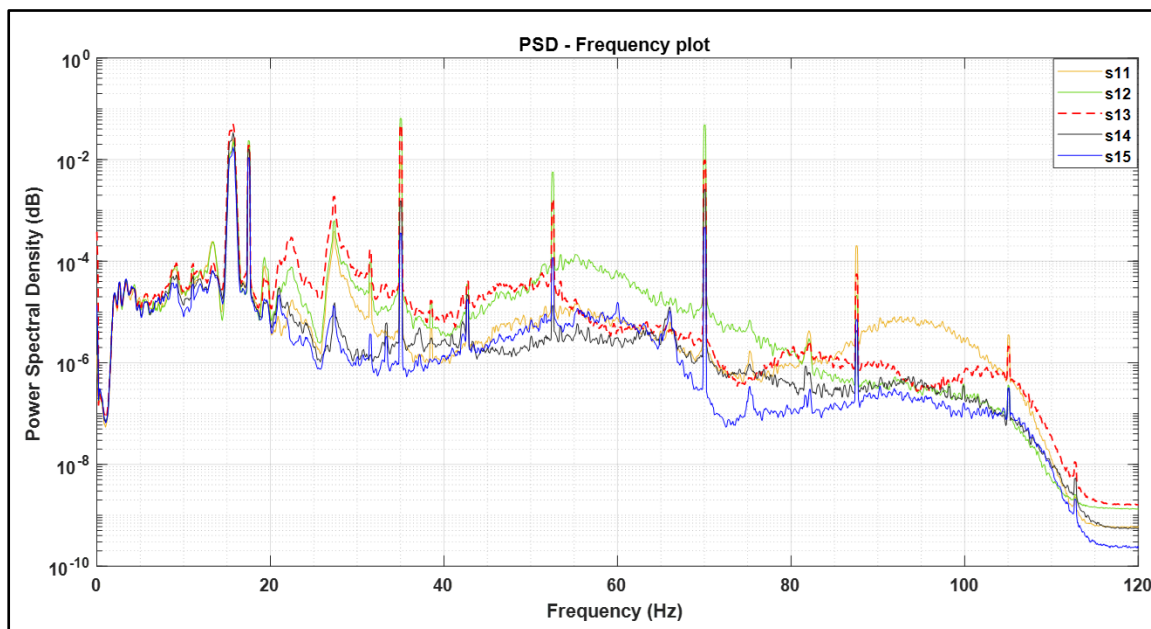


**Figure 6.37:** PSDs of seismic waves recorded at monitoring stations s11, s12, s13, s14, and s15. It is clear that station No. s13, located directly above the concrete, recorded the highest value of the PSD corresponding to the frequency from 20 Hz to approximately 55 Hz. This confirms that the concrete still has an effect and can be detected from recording the seismic waves in the north-south component.

**Table 6.29:** This table represents the calculated area under the curves in the figure 6.37 for the PSD. It is clear that station No. s13 received the largest amount of seismic energy (concrete block).

S11	0.482
S12	1.023
S13	1.08
S14	0.516
S15	0.272

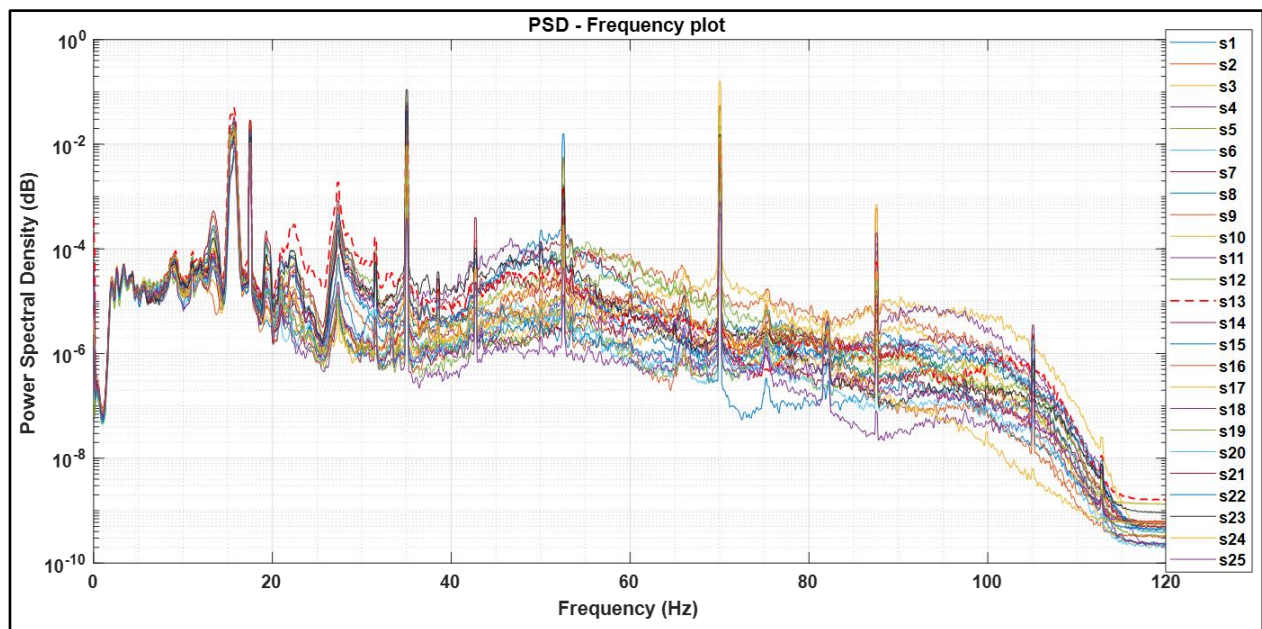


**Figure 6.38:** PSDs of seismic waves were measured at all monitoring stations. It is obvious that station No. s13, placed directly above the concrete, recorded the maximum PSD value corresponding to the frequency range of 20 Hz to about 55 Hz. This demonstrates that the concrete still has an effect, which may be observed by measuring seismic waves in the north-south component (concrete block).

**Table 6.30:** This table represents the calculated area under the curves in the figure 6.38 for the PSD. It is clear that station No. s13 received the largest amount of seismic energy compared to the majority of other stations, but it was noted that station No. s17 received the largest amount of seismic energy, and this may be the result of the local heterogeneity of the soil (concrete block).

S21	0.453	S16	0.534	S11	0.482	S6	0.341	S1	0.562
S22	0.425	S17	1.293	S12	1.023	S7	0.642	S2	0.621
S23	0.928	S18	0.671	S13	1.08	S8	0.453	S3	0.312
S24	0.408	S19	0.383	S14	0.516	S9	0.298	S4	0.192
S25	0.215	S20	0.244	S15	0.272	S10	0.25	S5	0.24

### 6.19.2 Steel drum experiment

Seismic waves were recorded at all monitoring stations with the source located 20 meters from a steel drum. Station s13, positioned directly above the steel drum, displayed a significantly greater wave amplitude compared to other stations. This suggests that the steel drum amplified the seismic waves at s13 due to its material properties, such as density and stiffness, which likely influenced wave transmission and reflection (appendix I 2).

The Power Spectral Density (PSD) of seismic waves recorded from the North-South component reveals a significant finding: station s13 distinctly recorded the highest PSD value among all the monitoring stations. This observation, as depicted in Figure 6.39, indicates that the greatest concentration of seismic energy was detected at this particular station. The elevated PSD values suggest that station s13 experienced the most pronounced response to seismic activity in this direction. Further analysis of the PSD across all monitoring stations highlights that station s13, positioned directly above a steel drum, consistently recorded the highest PSD value, as shown in Figure 6.39. This serves as evidence that the presence of the steel drum had a substantial impact on the characteristics of the seismic waves. The steel drum likely altered the behaviour of the seismic waves, amplifying the energy recorded at s13 in comparison to other stations.

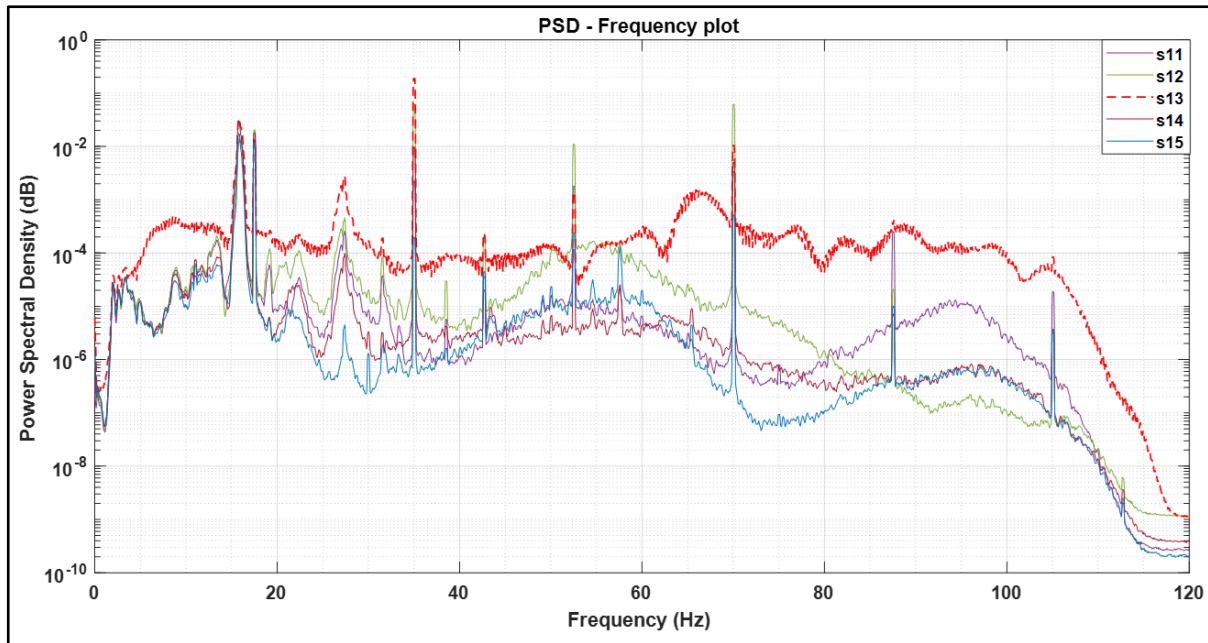


**Figure 6.39:** PSD of seismic waves recorded from the North-South Component distinctly reveals that station No. s13 recorded the highest PSD value. This observation signifies that the greatest amount of energy was detected at this particular station.

**Table 6.31:** The table describes the areas under the Power Spectral Density (PSD) curves from Figure 6.39, showing that monitoring station No. s13 recorded the highest PSD value. This high value is linked to the station's location above a buried steel drum, suggesting significant alterations in seismic wave characteristics due to the steel drum's presence. This comparison highlights the influence of steel material on seismic data.

S11	0.286
S12	1
S13	1.883
S14	0.465
S15	0.235

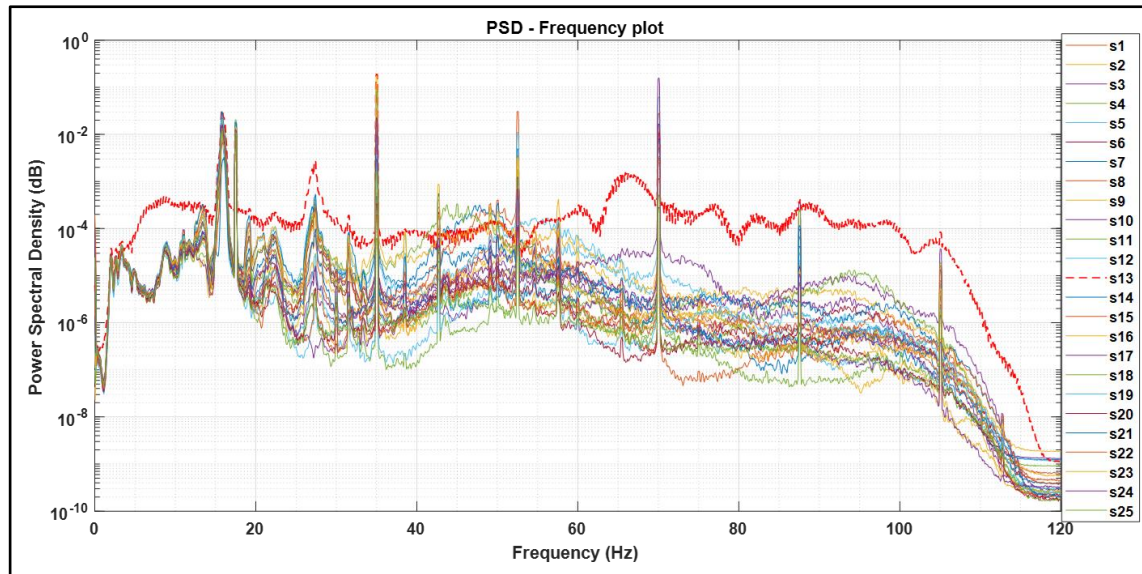


**Figure 6.40:** The PSD of the seismic waves recorded from the North-South Component at all monitoring stations. It was noted that the highest value of the PSD was recorded at monitoring station No. s13. This is important evidence that the steel drum had an impact on the characteristics of the seismic waves.

**Table 6.32:** The values derived from calculations are depicted beneath the PSD curves in Figure 6.40. The table highlights the highest calculated area under the curves, corresponding to the PSD recorded at station No. 13. This indicates that station No. s13 exhibited the most significant seismic energy among all the stations, as represented in the table.

S21	0.224	S16	0.294	S11	0.286	S6	0.203	S1	0.514
S22	0.297	S17	1.166	S12	1	S7	0.797	S2	0.445
S23	1.235	S18	0.83	S13	1.883	S8	0.507	S3	0.348
S24	0.438	S19	0.319	S14	0.465	S9	0.269	S4	0.236
S25	0.189	S20	0.204	S15	0.235	S10	0.246	S5	0.203

### 6.19.3 Plastic drum experiment

A comparison of seismic waves recorded at several monitoring stations highlights the difficulty of detecting an object (plastic drum) based solely on seismic wave amplitude. Variations in amplitude across stations may be too subtle to clearly identify the object, especially when factors like material type, depth, and distance from the wave source affect the readings (Appendix I 3).

The Power Spectral Density (PSD) curves for monitoring stations s11, s12, s13, s14, and s15 reveal the impact of a plastic drum on seismic wave behavior. Station s13 (red dashed line) shows prominent peaks between 20 Hz and 100 Hz, especially at 20 Hz, 40 Hz, and 80 Hz, indicating strong reflections and resonances from the steel object directly beneath it. In contrast, stations s11, s12, s14, and s15 display lower, more uniform peaks, showing less influence from the steel object (Figure 6.41).

Figure 6.42 highlights that station s13 also recorded the highest PSD values in the 20 Hz to 30 Hz range, directly correlating with the presence of a plastic drum beneath it. This demonstrates station s13's significance in detecting seismic energy influenced by subsurface objects in specific frequency bands. Both figures underscore the importance of station s13 in seismic monitoring, showing how buried objects can affect wave propagation.

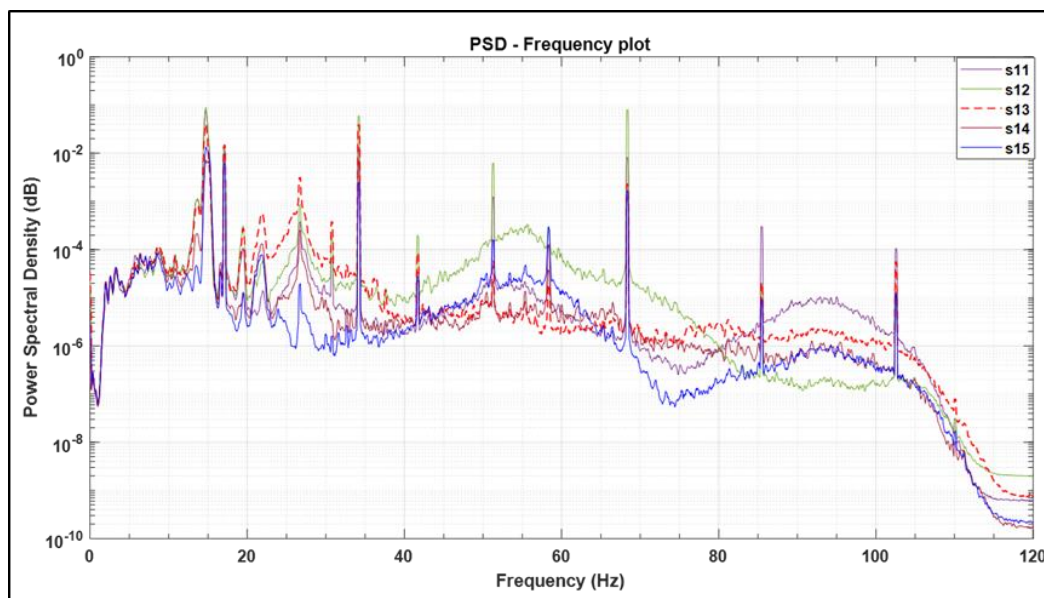


**Figure 6.41:** The Power Spectral Density (PSD) curves for monitoring stations s11, s12, s13, s14, and s15 show how seismic waves are affected by a plastic drum. Station 13 (red dashed line) exhibits prominent peaks between 20 Hz and 100 Hz, particularly around 20 Hz, 40 Hz, and 80 Hz, indicating strong reflections and resonances caused by the plastic drum directly below it. In contrast, the PSD curves for stations s11, s12, s14, and s15 display lower and more uniform peaks, suggesting less influence from the plastic drum object.

**Table 6.33:** This table represents the calculated areas under the PSD curves for seismic waves at monitoring stations s11 to s15 as shown in Figure 6.41.

S11	0.916
S12	1.69
S13	0.747
S14	0.219
S15	0.239

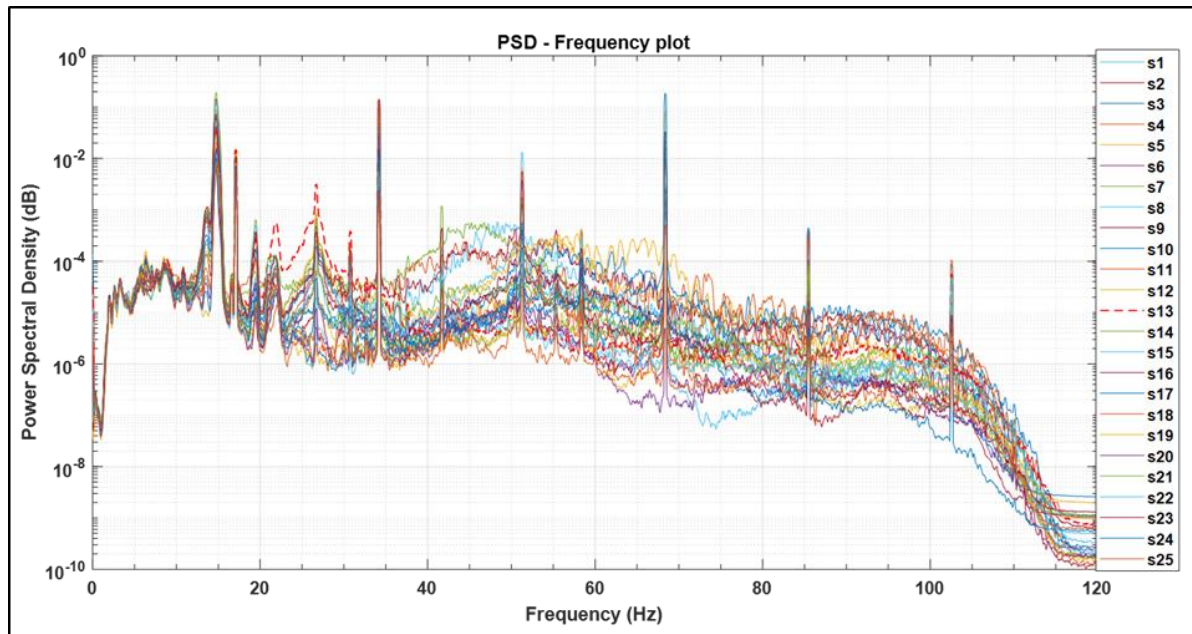


**Figure 6.42:** This figure illustrates the Power Spectral Density (PSD) of select recorded seismic waves. It is noteworthy that the maximum PSD value was observed at monitoring station s13, precisely positioned directly above the plastic drum. This peak PSD value corresponds to a frequency period ranging from 20 to 30 Hz. The results emphasize the significance of monitoring station s13 in capturing seismic energy within this specific frequency range and its direct correlation with the presence of the plastic drum.

**Table 6.34:** Figure 6.42 shows that station s13 did not record the highest PSD values compared to other stations, complicating the identification of the underlying object.

S21	2.2	S16	1.78	S11	0.916	S6	0.537	S1	0.521
S22	1.38	S17	1.7	S12	1.69	S7	1.056	S2	0.341
S23	1.56	S18	1.6	S13	0.747	S8	0.332	S3	0.252
S24	0.384	S19	0.199	S14	0.219	S9	0.168	S4	0.236
S25	0.137	S20	0.227	S15	0.239	S10	0.305	S5	0.49

## 6.20 North – South component (Seismic Source located at SB)

### 6.20.1 Concrete experiment

A comparison of seismic waves in the time domain recorded at all monitoring stations highlights the difficulty in distinguishing amplitudes due to the influence of the underlying concrete block. This effect can obscure subtle variations, making it challenging to differentiate between the stations (Appendix J 1). The Power Spectral Density (PSD) curves for seismic waves recorded at all monitoring stations indicate that station s13 achieved the highest PSD value in the frequency range of approximately 20 to 35 Hz (Figure 6.43). However, the PSD of seismic waves across these stations does not display a consistent trend among the PSD-frequency curves. Notably, the peak PSD at station s13, which is situated above the steel drum, occurs within the frequency ranges of 25 to 35 Hz and 70 to 85 Hz (Figure 6.44).

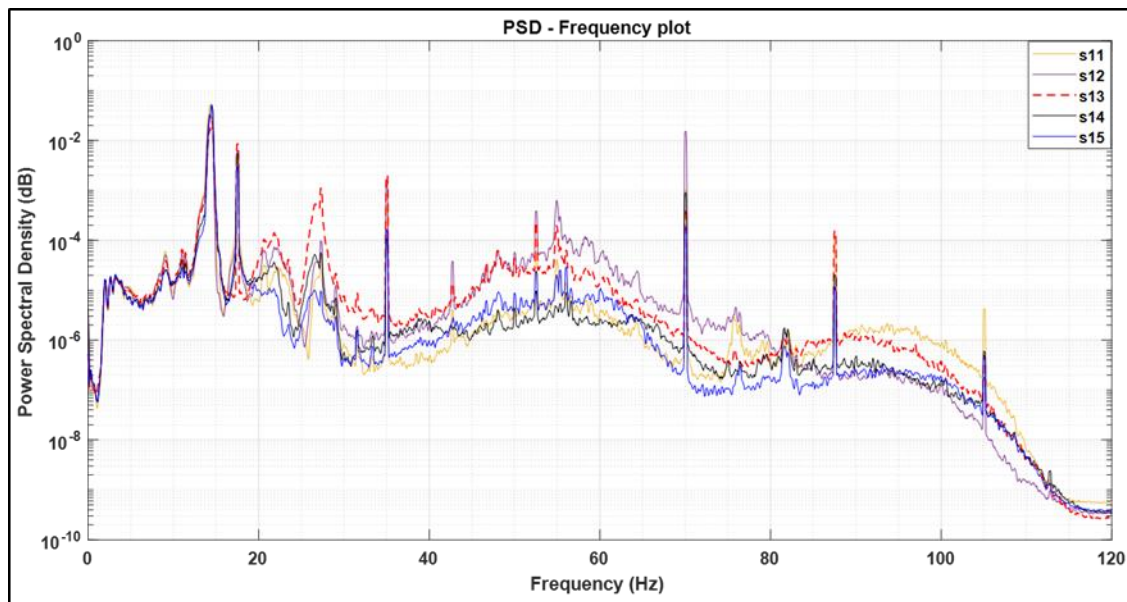


**Figure 6.43:** PSDs curves for seismic waves recorded at monitoring stations s11, s12, s13, s14, and s15. The PSD of the seismic waves recorded at monitoring station s13, which is located above the concrete, recorded the highest value corresponding to the frequency from 20 to 40 Hz.

**Table 6.35:** The estimated area under the PSDs curves in the figure. 6.43 As there is no effect of concrete on the monitoring station planted above the object according to this table.

S11	0.69
S12	0.539
S13	0.356
S14	0.488
S15	0.501

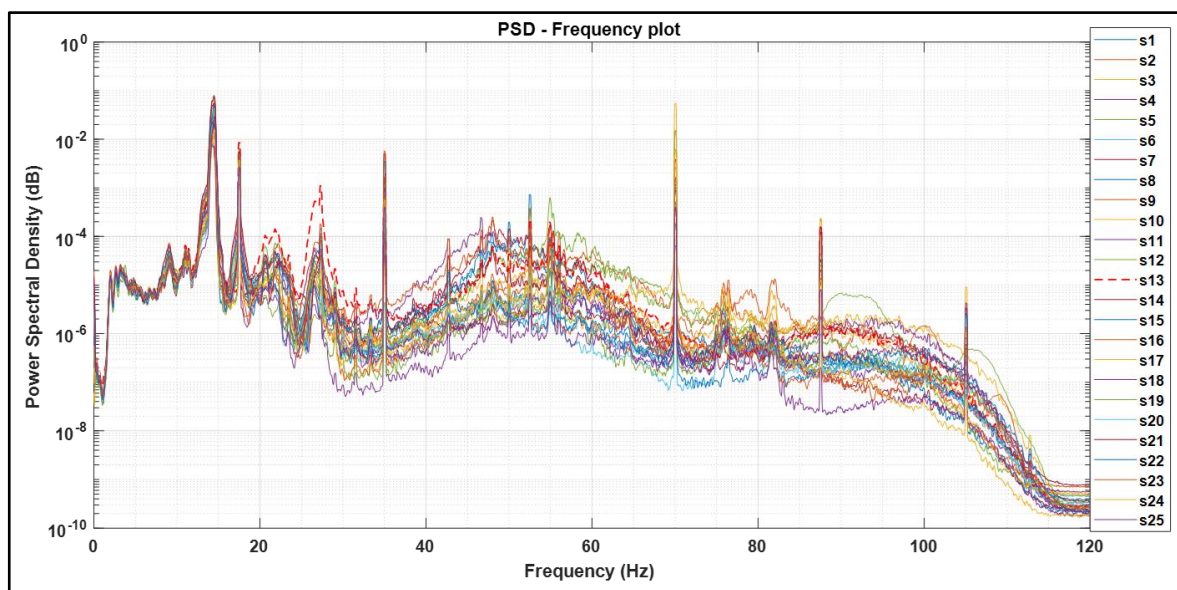


**Figure 6.44:** The Power Spectral Density (PSD) curves for seismic waves across all monitoring stations reveal that monitoring station No. s13 recorded the peak PSD value within the frequency range of approximately 20 to 35 Hz.

**Table 6.36:** The estimated area beneath the Power Spectral Density (PSD) curves in Figure 6.44 indicates that, according to the table, it is not possible to differentiate concrete based on the quantity of seismic energy recorded.

S21	0.95	S16	0.887	S11	0.69	S6	0.589	S1	0.466
S22	0.339	S17	0.527	S12	0.539	S7	0.272	S2	0.206
S23	0.232	S18	0.168	S13	0.356	S8	0.265	S3	0.188
S24	0.203	S19	0.338	S14	0.488	S9	0.401	S4	0.346
S25	0.271	S20	0.417	S15	0.501	S10	0.611	S5	0.589

### 6.20.2 Steel experiment

Comparing seismic waves recorded at all monitoring stations, the difficulty in detecting the object becomes apparent when considering the amplitude of seismic waves (Appendix J 2).

This figure presents the Power Spectral Density (PSD) of several recorded seismic waves. Notably, monitoring station s13, located directly above the plastic drum, displayed the highest PSD value, with this peak occurring in the frequency range of 20 to 35 Hz (Figure 6.45). While the PSD of seismic waves recorded at all monitoring stations generally does not facilitate determining the object's location, there was a significant increase in the spectral density curve at station s13, particularly for frequencies between 20 and 45 Hz (Figure 6.46).

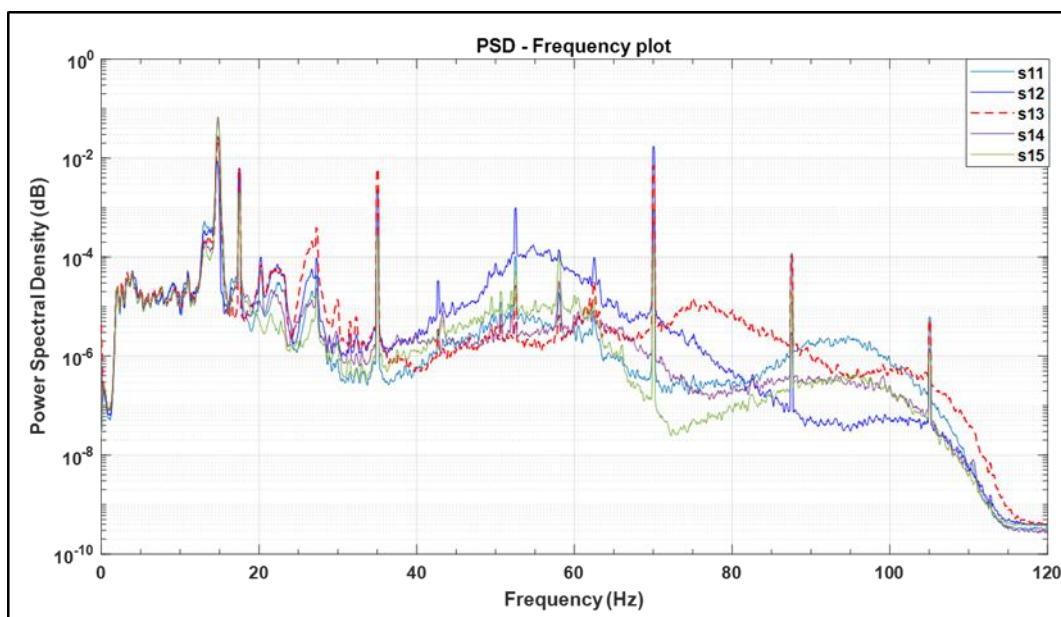


**Figure 6.45:** PSD of seismic waves recorded at these monitoring stations does not exhibit a consistent trend across all PSD - Frequency curves. It was observed that the PSD reached its peak at the monitored station s13 (deployed above the steel drum) within the frequency range of 25 to 35 Hz and from 70 to 85 Hz.

**Table 6.37:** The calculated area under each curve in the figure 6.45.

S11	0.264
S12	0.242
S13	0.315
S14	0.53
S15	0.475

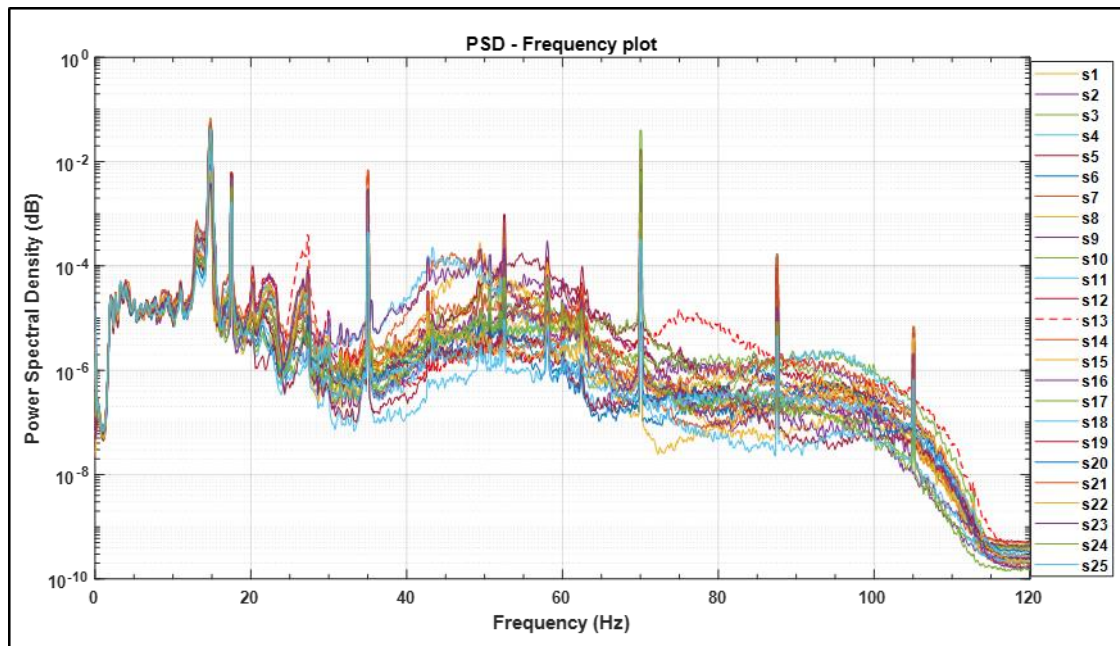


**Figure 6.46:** In the Power Spectral Density (PSD) - Frequency plot encompassing all monitoring stations, the PSD of seismic waves at station s13 reaches its peak, recording the highest value within the frequency period of 25 to 33 Hz. This indicates a notable concentration of seismic energy in that specific frequency range across the monitoring stations.

**Table 6.38:** shows the power spectral density value which calculated under the PSD curves in figure 6.46.

S21	0.543	S16	0.41	S11	0.264	S6	0.198	S1	0.167
S22	0.119	S17	0.28	S12	0.242	S7	0.143	S2	0.127
S23	0.138	S18	0.181	S13	0.315	S8	0.307	S3	0.262
S24	0.28	S19	0.408	S14	0.53	S9	0.438	S4	0.354
S25	0.339	S20	0.422	S15	0.475	S10	0.53	S5	0.466

### 6.20.3 Plastic drum experiment

A comparison of seismic waves recorded at all monitoring stations highlights the challenges in detecting the object, particularly when examining the amplitude of the seismic waves (Appendix J 3).

Power Spectral Density (PSD) of various recorded seismic waves. Notably, monitoring station s13, located directly above the plastic drum, recorded the highest PSD value, with this peak occurring in the frequency range of 20 to 35 Hz (Figure 6.47). While the PSD of seismic waves across all monitoring stations typically does not provide sufficient information to determine

the object's location, a significant increase in the spectral density curve at station s13 was observed, particularly for frequencies between 20 and 45 Hz (Figure 6.48).

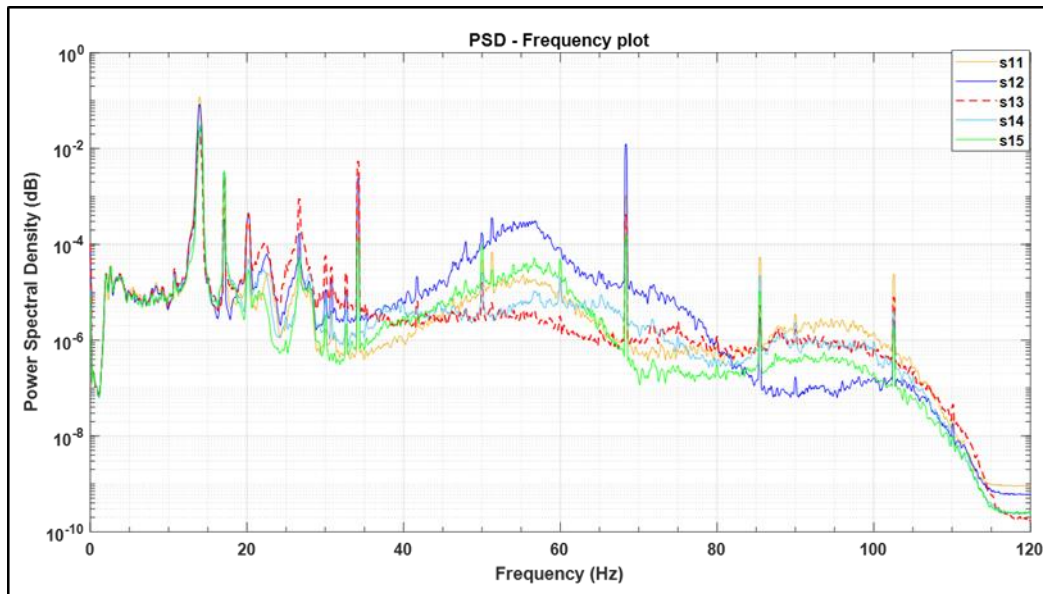


**Figure 6.47:** In this figure, the Power Spectral Density (PSD) of some recorded seismic waves is presented. Notably, monitoring station s13, situated directly above the plastic drum, exhibited the highest PSD value. This peak PSD value aligns with a frequency period ranging from 20 to 35 Hz.

**Table 6.39:** The Power Spectral Density (PSD) values are depicted below each curve in Figure 6.47.

S11	0.916
S12	1.69
S13	0.747
S14	0.219
S15	0.239

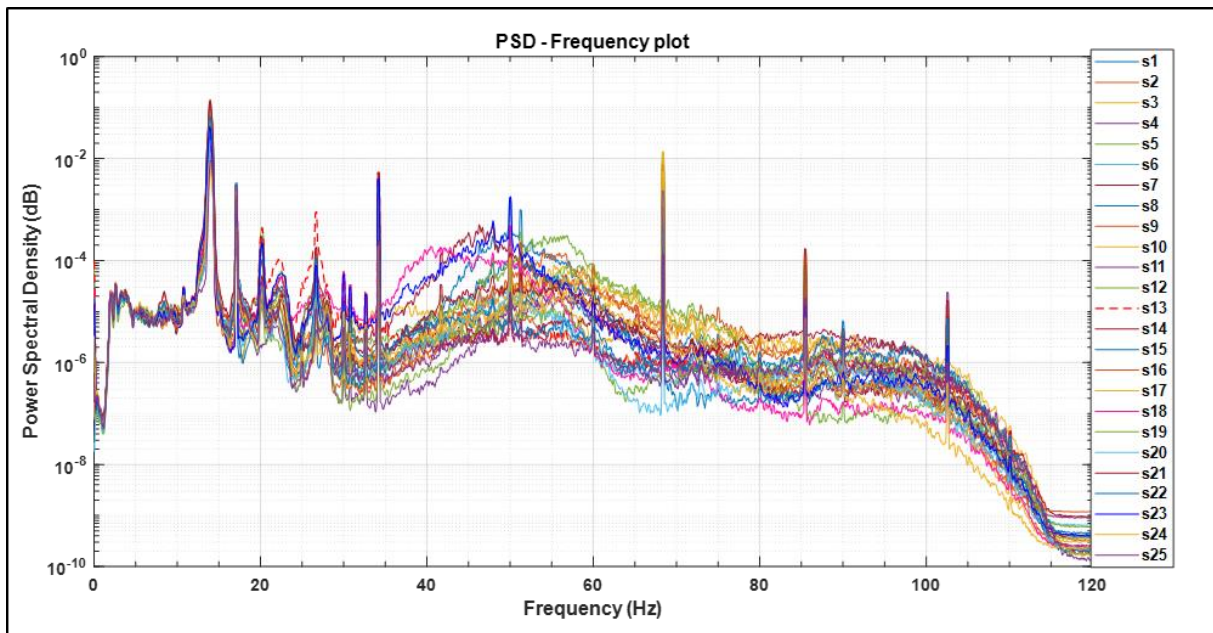


**Figure 6.48:** The PSD of seismic waves detected across all monitoring stations generally does not allow for the determination of the object's location. However, there was a noticeable uptick in the spectral density curve at monitoring station number s13, specifically for frequencies between 20 to 45 Hz.

**Table 6.40:** In Figure 6.48, the Power Spectral Density (PSD) values are presented below each curve. Upon comparison with all other stations, it becomes clear that detection of the plastic drum using the North-South component is not feasible.

S21	1.216	S16	1.308	S11	1.047	S6	0.881	S1	0.694
S22	0.599	S17	0.579	S12	0.842	S7	0.48	S2	0.221
S23	0.449	S18	0.25	S13	0.269	S8	0.193	S3	0.102
S24	0.127	S19	0.149	S14	0.264	S9	0.215	S4	0.18
S25	0.109	S20	0.231	S15	0.304	S10	0.385	S5	0.414

### 6.21 Summary of N - S Component Results

**In the concrete experiment,** the analysis focused on seismic waves recorded along the North-South component at all monitoring stations, with station s13 directly positioned above the concrete structure. Notably, there was a discernible increase in the amplitude of seismic waves at station s13 compared to other stations (Appendix I 1)), indicating a distinct response to the presence of the concrete. Figure 6.38 illustrates the PSD curves across all monitoring stations, clearly showing that station s13 recorded the highest PSD values within the frequency range of 20 Hz to approximately 55 Hz. This observation underscores the concrete's impact on

seismic wave characteristics, particularly in terms of energy distribution across different frequencies.

Table 6.29 complements Figure 6.37 by providing quantitative data on the area under the PSD curves. It confirms that station s13 accumulated the greatest amount of seismic energy compared to most other stations, although station s17 recorded higher energy, possibly influenced by local soil heterogeneity. When the seismic source was at location SB (Figure 6.44), the PSD curves revealed that station s13 continued to exhibit prominent PSD values within the frequency band of approximately 20 Hz to 35 Hz. However, Table 6.35 indicates that differentiating concrete based solely on the quantity of seismic energy recorded is challenging due to variations in local conditions.

**In the steel experiment** conducted at SA (Figure 6.40), the PSD analysis of seismic waves along the North-South component again highlighted station s13 as recording the highest PSD value. This finding suggests a clear influence of the steel drum on the seismic waves detected at this particular station. Table 6.31 corroborates this by detailing the calculated areas under the PSD curves, emphasizing the significant energy concentration observed at station s13. At SB (Figure 6.46), the PSD-frequency plot indicated that station s13 captured peak PSD values between 25 Hz and 33 Hz, indicating a concentration of seismic energy in this specific frequency range across the monitoring stations.

**plastic experiment**, Appendix I 3 showed a comparison of seismic waves across all monitoring stations, revealing no discernible effect of the plastic drum on the waves recorded at the station directly above it. However, Figure 6.42 displayed the PSD of selected seismic waves, where station s13 exhibited the maximum PSD value ranging from 20 Hz to 30 Hz, indicating a significant capture of seismic energy within this frequency range. Table 6.33 provided a closer look at the PSD values beneath each curve in Figure 6.42, highlighting station s13's notable position. At SB location, Figure 6.48 further confirmed that the plastic drum had minimal impact on the seismic waves recorded across various monitoring stations.

Figure 6.48, despite an observable increase in amplitude of PSD curve at station s13 within the frequency range of 20 Hz to 45 Hz, Table 6.39 underscored the challenge of using the North-South component to detect the plastic drum. This table compared the PSD values across stations, emphasizing the limitations in identifying the drum solely through seismic energy measurements.

## 6.22 Response of Various Materials to Seismic Waves

Consider Figure 6.49, which depicts the power spectral density of the seismic waves recorded at Station No. s13, located above these objects. It was observed that materials have a special response when seismic waves collide them. This depends directly on the mechanical properties of the materials, which are density and hardness, as well as the size and shapes of the materials. It is clear that when the recording was without an object, the recorded seismic energy was lower at station No. s13. This is because most of the seismic waves passed through and did not find an object from which they were reflected. In the case of steel, some seismic waves are reflected, and since the steel is solid and has a high density, many of the seismic waves are scattered. In the case of concrete, it was noted that a large amount was reflected and recorded at this station.

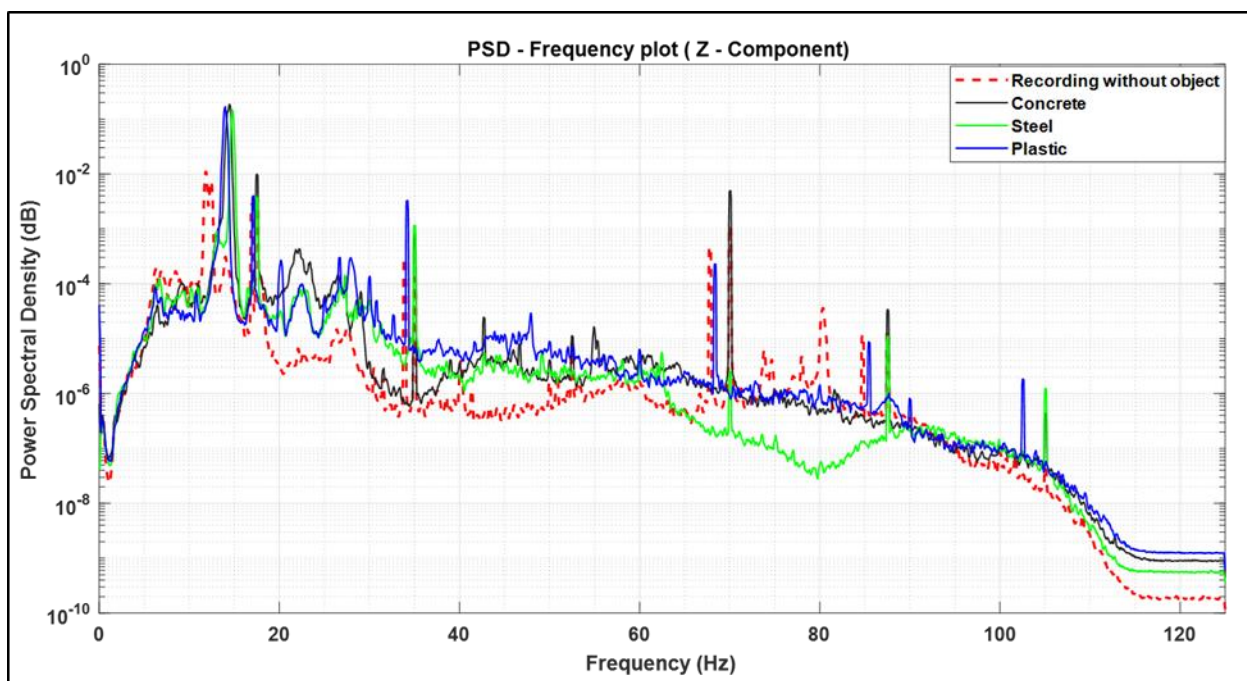


**Figure 6.49:** power spectral density of the seismic waves recorded at Station No. s13

**Table 6.41:** The table provides a summary of how seismic components perform in detecting objects with different mechanical properties near the Earth's surface. It outlines the impact of each object on the recorded characteristics of seismic waves from each seismic component conclusions from the results obtained in the field experiment.

Material name	Seismic source distance (20m)			Seismic source distance (40m)		
	Z- component	E-W component	N-S component	Z- component	E-W component	N-S component
Concrete	Effective	Effective	Low effective	Effective	Low effective	No effective
Plastic drum	Effective	Effective	No effective	Effective	No effective	No effective
Steel drum	Effective	Effective	Effective	Effective	Effective	No effective

**Colour table**

Effective	Effective
Low effective	Low effective
No effective	No effective

## Chapter 7 : Discussion

### 7.1 Introduction

The aim of this research was to develop an approach that can take advantage of the wide applicability of seismic waves in site investigation despite unfavourable geological conditions (e.g. the presence of clay) but at the same time, minimise the number of seismic sensors required and reduce the computational cost. The analysis methodology should be possible without the need of licenced software and be simple enough for non-experts to follow. Results should be easy to interpret without the need of inversion approaches that are based on models of the velocity structure at shallow depths.

The developed methodology offers a novel approach to near-surface imaging through power spectral density analysis, and was validated by field trials. The results identified a distinct pattern in which seismic peaked at two key locations: directly above the buried objects and at peripheral monitoring stations up to about 4 m away. This pattern illustrates the small-angle fall and reflection behaviour of seismic waves at such shallow depths

### 7.2 Comparison of developed microseismic reflection methodology vs existing geophysical technologies

There are key differences between existing geophysical site investigation methods and the microseismic technology and methodology analysis presented in this thesis:

1. While the developed technology utilizes an active source, as is the requirement for seismic reflection and refraction surveys, this source does not need to have specific or known characteristics (frequency, wavelength) for the method to work, neither requires expensive machinery to transfer and implement it. A simple vehicle or existing machinery, e.g. digger, that can induce ground vibrations on the site are adequate.
2. Unlike the study by Harmankaya et al. (2013), the method proposed here requires knowledge of the first arrivals of seismic waves and this attribute allows for the application of the reflection principle to surveys at the near-surface. Even 1 minute of seismic data is sufficient to provide evidence of the presence of a buried object. The parameter used for detection is the total average power (in this thesis in units of  $m^2/s^2$ ) of the seismic wave as recorded by surface geophones and this is quantified as the area below the power spectral density curve of the recorded seismic velocity (Grami, 2016).

3. Because of the small incidence and reflection angles, the distance at which the highest energy can be detected by nearby stations only depends on the object size (larger reflecting area) rather than the reflection angle.
4. For the vertical resolution, it should be made clear that, in contrast to all other geophysical methods that utilize seismic waves for imaging the subsurface, the technology developed by this research is not limited to, not dependent on the wavelength of the seismic wave to detect an object (Anderson and Akingbade, 1997). It rather depends on the size (area) of the object's top surface that reflects the seismic wave. The larger the area, the higher the power of the reflective wave and the easier it is to distinguish from the power recorded at neighboring stations. This means that if a geophone is placed directly above a buried object, this object will be detected irrespective of whether it complies with the vertical seismic resolution criterion (object height  $\geq$  seismic wavelength/4; Chopra et al., 2006). The higher the frequency of the seismic wave source, the higher the speed, and thus the waves do not spread farther. Therefore, in objects close to the source, they can be detected at close depths. The further we are, the waves spread in all directions and help more in detecting objects.
5. The analysis of the seismic data is very simple and does not require cross-correlation of recordings or inversion algorithms. For this research all analysis steps were carried out manually, but the process is not complicated and it is easy to automate making results available in near-real time in the field. However, this was out with the scope of this thesis. While licenced software like MATLAB was used for these analyses, other commonly used analysis software, such as Excel, are now capable of performing the calculations efficiently. This accessibility streamlines the process, allowing for faster data acquisition and interpretation without requiring specialized training in advanced software.
6. Overall, while traditional geophysical methods have specific advantages, they are often constrained by site conditions, labour intensity, and interpretational ambiguities. Microseismic technology provides a more versatile and cost-effective alternative, with deeper penetration, ease of deployment, and improved detection accuracy in heterogeneous brownfield environments. The work takes about four hours, which is not a long time compared to other methods, which distinguishes it from other methods.

### **7.3 Numerical simulation of seismic waves propagation through media**

To understand the changes in the properties of seismic waves, three models were built that have different mechanical properties, and these properties match a range of soils found in brown field sites. The source of the seismic waves is a sine wave with a frequency that is consistent with the mechanical properties of the model to ensure numerical stability. Since the models differ in mechanical properties, three sine waves with different frequencies were applied.

The simplified seismic source does not affect the validity of the results. The choice was based solely on the simplicity of the source that would allow easy interpretation of the numerical results. In real projects, the active seismic source is more complex and likely a sum of different frequencies, especially when the source is machinery available on site. This will only affect the amount of energy emitted, but the fact that higher energy is reflected directly above the object does not change.

The models only account for geometrical spreading as it concerns attenuation of the seismic waves. The mechanical damping was not incorporated in the modelling. While, it is typically necessary to account for energy losses in the physical system (e.g., heat, hysteresis) that are not accounted for by the numerical algorithm when conducting dynamic analysis with any numerical software, this was not applied in this research. The reason was because this study focused at depths that do not exceed 3m, and the models were also highly homogeneous and elastic, and as such, there is no high temperature to affect the seismic waves. In addition, the focus was the reflective wave rather than predicting the dynamic response of the soil to the induced vibration.

In general, the numerical simulations depended on simplifying processes to simulate seismic waves or simplifying objects underground, and this, is not entirely comparable to field work. Building large models, however, may require time consuming calculations, and this required expensive, high-computing devices. The model uncertainty, the accuracy of simulating seismic waves and obtaining accurate results is dependent on the data inputted into the programme as well as the characteristics and location of the source of the seismic waves. Because of this, simulation was not entirely accurate. Verifying the validity of simulations through field work was necessary.

#### **7.3.1 Data Analysis approach**

The Power Spectral Density (PSD) plot represents the distribution of the recorded seismic waves power over a frequency range. The smooth wide peak is due to applying the Welch

equation, which averages overlapping segments to provide a more stable spectral estimate. Unlike the Fourier Transform, which can produce a single narrow peak, Welch's method results in a wider peak as shown in figures 7.1 and 7.2. Both the FFT power spectrum and the PSD were produced using the same data and values for the window, overlap, NFFT and sampling frequency. While FFT is better in representing well defined, stationary signals consisting of a limited number of discrete frequencies, PSD is better suited for analyzing non-stationary data, such as seismic signals that change over time or represent random processes. Additionally, it helps reduce spectral leakage, improving the accuracy of seismic energy estimation by providing a clearer representation of frequency content (Claeys *et al.*, 2015).

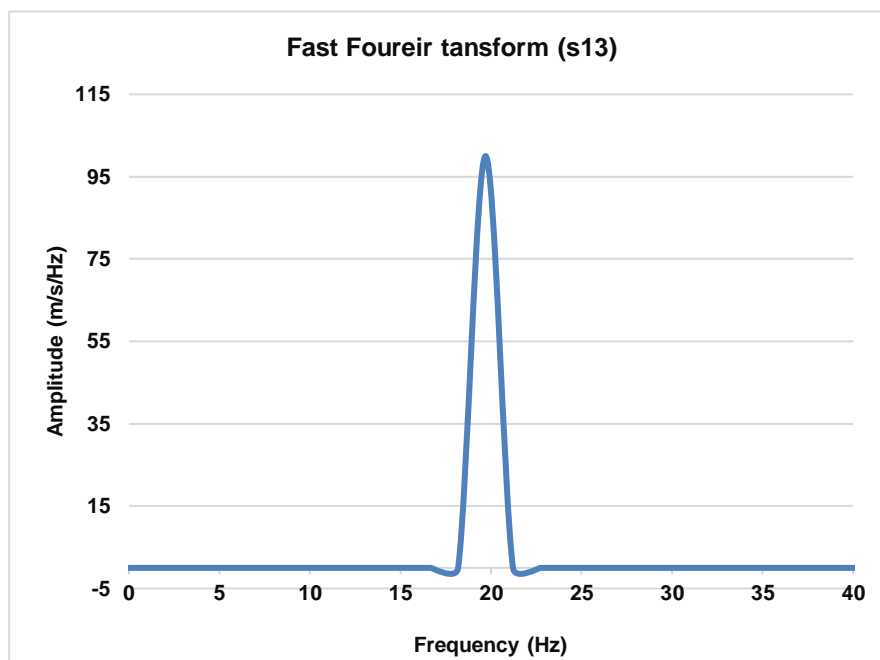


**Figure 7.1:** Fast Fourier Transform (FFT) of velocity history at s13 (Homogeneous model, Site A).

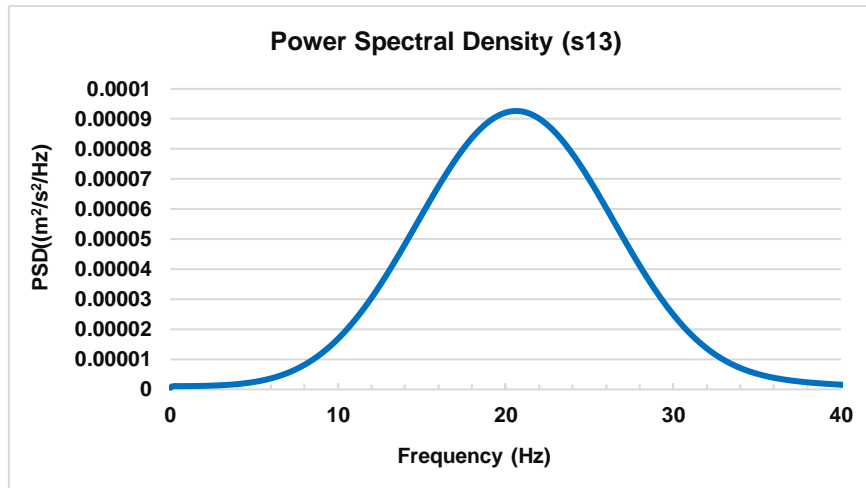


**Figure 7.2:** Power Spectral Density (PSD) of velocity history at s13 (Homogeneous model, Site A).

#### 7.4 Pilot study (chapter 6)

The generation of seismic waves was conducted at two distinct locations (SA and SB) from the buried objects to observe the variations in seismic waves behaviour. When the source of the seismic waves is close, and if the seismic waves collide with objects, the angle of incidence and reflection decrease, and when the source of the seismic waves is further, the angle of incidence and reflection increases (it was detailed in literature review chapter – Seismic Reflection).

Before burying any object, seismic data were recorded when the source was at SA location and also at SB location, to enable comparison between the changes that occurred in the characteristics of the seismic waves after the objects were buried. The result of the data analysis before burying the objects showed the lowest amount of seismic energy recorded at monitoring station No. s13, compared to the amount of energy recorded after burying the objects at the same station. From the results, it is clear that recording without burying any object means a greater amount of seismic energy passes without being reflected at a reflective surface. If there is an object, the seismic waves collide with it and a greater amount of energy is reflected.

It is understood that seismic waves lose energy as they move away from their source as a result of geometrical attenuation for example, but in the pilot study experiments, it was observed that the seismic waves recorded when the source was further away from the buried object had greater seismic energy. This was because the properties of the soil at the two locations of the seismic wave sources differ in stiffness. In the first location, which is 20m from the object (SA location), the soil under the wave source was softer, and in the second location of the wave source, which is 40m away from the object (SB), the soil was harder.

The seismic data recorded from the three components were interpreted, and it was noted that all objects affect the characteristics of the seismic waves, whether in the time or frequency domain. The study of the characteristics of the seismic waves recorded from the vertical component showed that all objects can be detected. This stands for recordings on the East – West component as well but with some exceptions; it was observed that all three objects examined in the experiments were detectable at the monitoring station directly above the buried object, when the seismic source was nearer (SA location). When the seismic source was further away, the seismic waves recorded from the East-West component successfully detected steel drums. While concrete was detectable, it exerted a less influence on the properties of the seismic waves recorded from this component. Regarding the plastic drum, there is no effect on the characteristics of the seismic waves recorded from this component, and therefore it was difficult to detect it.

The characteristics of the seismic waves recorded from the North-South component were not affected by the presence of all objects when the source of the seismic waves was 40 m away. The seismic waves in the N-S direction are seismic waves that propagate on the earth's surface in these experiments, and because the width of the deployed objects was small, most of the seismic waves passed without effect. Also, the east-west seismic component represents the seismic waves that travel on the surface in this case, but their effect is greater than the seismic waves recorded in the N - S component. This is because the E-W direction is parallel to the length of the objects, which is larger than the width and for this reason, its effect was slightly greater. As such, when applying this technology in the field, it is recommended that a source is applied into 2 directions relative to the surveyed area to address any limitations due to the object geometry and orientation with regards to the source locations.

In the field experiments, it was expected that objects would be detectable at both the monitoring station directly above the object and at side monitoring stations, similar to simulation results. However, in reality, objects were only detected at the station directly above the object. This is can be attributed to the low frequencies applied (13 to 16 Hz) and the small size of the objects.

The two horizontal components yielded unexpected results in this study. Initially, it was expected that these components would show a resultant of zero due to destructive interference observed during the simulation process.

The study accounted for changes in soil compaction during the experiments, evaluating whether these variations in compaction affected results. To confirm that the changes were due

to the objects and not the change in soil compaction due to the excavations, the author refers to the seismic simulations results as well as results from the experiment at Heriot-Watt where recordings after the end of experiments and refilling of the excavated area showed no higher energy above the excavation when no buried object was present.

Concrete and steel objects exhibited different seismic energy levels at the same monitoring station, a finding further validated by field experiments. It was observed that the deployed objects reflected varying amounts of seismic energy, with each object's response corresponding to its specific properties and size.

The depth of the objects was estimated in the chapter 4 (the simulation chapter) by detecting the first arrival of the seismic waves, but it was difficult to detect the first arrival of the seismic waves recorded in the field experiments because they contained noise and interference. This was not unexpected.

Chapter 4 introduced several questions, which included discussions on the feasibility of detecting small objects, the capability of side observation stations to detect small objects, and the examination of object detection at depths ranging from 1 to 3m. However, these investigations were not conducted in the field experiments due to time restrictions and high cost to maintain equipment and personnel for longer than 1 day.

At a few monitoring stations an unexpected increase in seismic energy was recorded, despite having introduced no buried object beneath them. This anomaly is likely due to local soil heterogeneities, i.e. subsurface conditions may have contributed to more efficient transmission or amplification of seismic waves. For example, when digging the excavation trench for the buried objects at Steps, we encountered a small buried beer cannister. The soil at Steps is man-made and as such, there is a possibility of the presence of small, unknown to us, objects or building materials in the ground. Such localized effects could explain the higher-than-anticipated localised energy levels detected in those areas.

The maximum depth of the buried object at 3m is not a limitation of the method as such, although this is the depth that the frequency content of the input signal/source in this study would allow for enough energy to be recorded at the surface. Sources of different frequency content could allow for seismic waves that disperse less at the shallow subsurface. However, in practice, this is likely a rare requirement. Originally, the choice of maximum depth was dictated by the common characteristics of buried infrastructure at brownfield sites with the vast

majority of objects being at a maximum depth of 3m. Therefore, there is no need to reach deeper depths.

The developed technology is possible to estimate the depth of the object by using arrival times of the waves but this is not a straight-forward task in most cases due to the shallow depths involved. As such, the technology is most suited in identifying areas that require further investigation with other methods, e.g. GPR - ground penetrating radar (assuming that the site conditions are favourable for their application).

### **7.5 Key contributions of this Research**

The applying of micro seismic technology in brownfield sites offers several significant contributions:

- **Unique Geophysical Approach:** The thesis presents a novel approach for the application and data analysis of an otherwise, traditional geophysical method; the seismic reflection. This approach is aimed at overcoming limitations inherent in existing methods while making use of their advantages. It can be used to complement other geophysical methods by identifying quickly and at very low-cost areas for further investigation.
- **Simplifying Micro seismic Data Interpretation:** Micro seismic data interpretation is simple, contrasting with other methods requiring complex inversion algorithms or extensive modelling, e.g. resistivity or gravity surveys.
- **Non-Invasive Approach:** Unlike traditional geophysical methods that may involve invasive procedures such as drilling or excavation, this technology offers a non-invasive approach to the shallow subsurface investigation. This minimizes environmental disturbance and reduces costs associated with site investigation and remediation.

### **7.6 Application of developed Microseismic approach as a Complementary Tool in Site Investigations: practical considerations**

The Microseismic brownfield site investigation approach developed in this research serves as an effective preliminary screening tool during site investigations, particularly for detecting subsurface anomalies warranting further exploration. Its ability to swiftly identify areas of interest within less than 2 hours (for an area of 100 m<sup>2</sup>), makes it a valuable tool in guiding the use of specialized geophysical methods, such as ground-penetrating radar (GPR) or electromagnetic (EM) surveys, in a more targeted manner. This systematic approach reduces the overall time and resources required for comprehensive surveys while ensuring efficient

allocation of investigative efforts. The proposed method allows for the initial mapping of areas with minimal site disturbance. Once potential anomalies are detected, secondary technologies are employed to refine key attributes such as depth, material composition, and dimensions, thereby minimizing redundancy and optimizing cost-effectiveness.

The deployment of microseismic sensors is contingent upon specific objectives and the expected dimensions of buried objects. For preliminary screening across large areas, a lower density of sensors, spaced at approximately 5-meter intervals, is generally sufficient to identify larger objects. However, in the case of smaller or irregularly shaped objects, closer spacing and an increased number of sensors are necessary to obtain reliable detection data. Sensor configuration can be adjusted to account for factors such as object size, depth, site-specific constraints, and budgetary considerations. A phased deployment strategy—initiating with a sparse array followed by denser sensor placement in areas of interest—effectively optimizes resource utilization.

The reflection angles in this study fall within the range of 1–5 degrees. For such angles, the surface area receiving the highest energy corresponds to the area of the object, supplemented by an approximate margin of 0.25m. Sensor spacing of 2m ensures maximum detection probability for buried objects with dimensions of at least 1m per side at a depth of 3m. For smaller objects, denser spacing is required, with recommendations suggesting sensor intervals not exceeding 1.5–2 times the smallest expected object dimension. Similar to hydrocarbon exploration, initial surveys employing wide sensor spacing provide evidence of subsurface anomalies. Subsequently, denser arrays are deployed around these target areas to better constrain dimensions before utilizing specialized techniques like GPR to precisely determine depth.

The applicability of microseismic technology varies based on site characteristics and project requirements. Favourable scenarios include preliminary screening, wherein initial surveys identify areas warranting further investigation. This approach is particularly advantageous for cost-sensitive projects, urban environments, and shallow subsurface investigations up to depths of 3 meters. Additionally, the technology offers a streamlined process suitable for locations with high electromagnetic interference or conductive materials that hinder the effectiveness of GPR or EM methods. In brownfield sites, microseismic surveys facilitate the detection of buried infrastructure without disturbing potentially contaminated soil, while construction sites benefit from subsurface obstacle identification during pre-excavation assessments.

However, the proposed approach has limitations. It is less effective for detecting deep-seated objects beyond 3 meters due to challenges associated with the spreading and reflection of seismic waves at greater depths. Similarly, areas with highly heterogeneous soils introduce significant noise, making reliable detection less feasible. Despite these constraints, this method remains particularly valuable in urban redevelopment, where it aids in identifying buried utilities or remnants of prior constructions in settings with considerable electromagnetic interference.

For the range of reflection angles covered by this research (1-5 degrees), the maximum area on the ground surface receiving the highest energy is the area of the object plus approximately a 0.25m (= 3m depth \* tan (5)) border around it. Assuming a spacing between consecutive sensors of 2m, this means that in order to maximize the chance of detection of a buried object at a depth of 3m, the minimum object dimension per side should be at least 1m. For smaller objects, a denser spacing is required. As a rule of thumb, it is recommended that the spacing of the seismic stations is maximum 1.5 – 2 times the minimum expected dimension (length or width) of the buried object.

The principle is that, in the same way as with exploration geophysics for hydrocarbons, a first survey with relatively large spacing (2m) between geophones takes place and then a denser array is deployed around the areas for which the first survey provided evidence of the presence of a buried object to better constrain its dimensions. As a final step, GPR or other suitable geophysical method is then deployed to constrain the object's depth.

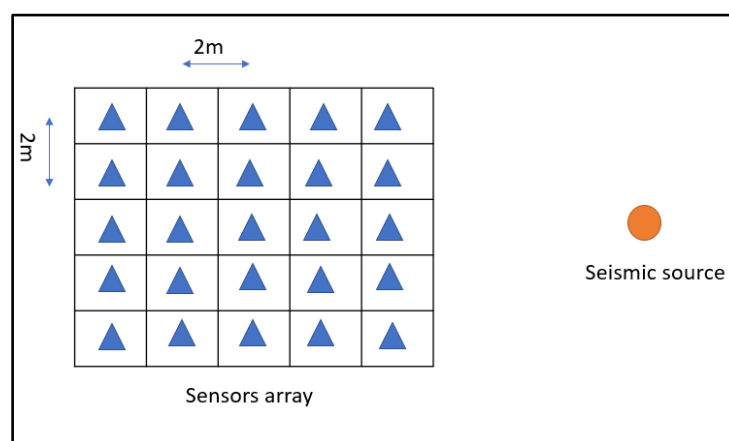


**Figure 7.3:** Seismic Source and Geophone Sensor Array

### 7.6.1 Favourable Cases:

- **Preliminary Screening:** An initial survey is conducted to identify areas of interest before applying more detailed methods. This preliminary assessment helps save time and efficiently cover larger areas in brownfield sites. More importantly, it significantly reduces costs. If any objects are detected during this phase, a more detailed survey with intensive geometry can be designed to focus on these objects, allowing for an approximate determination of their dimensions.
- **Urban Environments:** When working in areas with high-conductivity soils or dense infrastructure where GPR or EM methods face significant limitations. This is because the resistance is disturbed by the presence of conductive materials, and the GPR may lose the energy of the transmitted waves. Also, the waves transmitted by the GPR may have an effect on the environment because they have high frequencies, unlike seismic waves.
- **Shallow Investigations:** When targeting objects at depths of up to 3 meters, which aligns well with the capabilities of the technology. This is because seismic waves fall almost vertically and are reflected almost vertically when they hit objects very close to the Earth's surface, especially less than 6 meters away, which is considered a very close distance as seismic waves are not allowed to spread.
- **Cost-Sensitive Projects:** When budget constraints limit the use of expensive, high-resolution geophysical methods. This technology does not require much time and does not require a lot of equipments, which makes its application easy and fast. Also, data processing and analysis does not take time and can be done in the field.

### 7.6.2 Less favourable/not recommended Use:

- **Deep Targets:** When the buried objects are deeper than 3 meters, as the technology is optimized for shallow depths. Because the seismic waves begin to spread and expand more, the angles of incidence and reflection increase, which leads to the waves being reflected in farther places where they are recorded at other stations.
- **Highly Heterogeneous Soils:** In areas where soil variability introduces significant noise, making detection unreliable. When the soil is heterogeneous, this may lead to incorrect because seismic waves.

### 7.7 Where would it be particularly valuable?

- **Brownfield Sites:** To locate buried infrastructure, such as drums or concrete structures, without disturbing potentially contaminated ground.
- **Construction Sites:** For assessing the presence of subsurface obstacles before excavation.
- **Urban Redevelopment:** To detect buried utilities or remnants of previous construction in areas with high electromagnetic interference.

### 7.8 Future work

Further research is needed to investigate further the potential of this technology, which could deepen understanding and address the following issues:

**Depth Determination Methods:** One major area for advancement is improving the accuracy of depth determination for buried objects. Future studies should focus on developing more reliable methods for depth estimation, possibly by integrating complementary geophysical techniques like Ground-Penetrating Radar (GPR). This integration could help overcome current limitations in resolving depths, especially in complex geological environments. Also, the reduction in seismic energy with increasing object depth, as observed in seismic wave simulations, can be used to estimate target depths by analyzing the variations in signal power at different depths.

**Improved Material Identification:** Accurately distinguishing between various materials remains a significant challenge. Research should explore advanced seismic wave analysis techniques, possibly incorporating machine learning to enhance material characterization. Additionally, combining microseismic data with other geophysical methods, such as electromagnetic surveys, could provide richer data sets that improve material differentiation and classification.

**Size Estimation Techniques:** To refine object size estimation, future research should look into utilizing high-frequency seismic waves, which have the potential to offer greater resolution. Employing multi-angle data collection could also provide more precise dimensional analysis by capturing the object from different perspectives, leading to a clearer understanding of its true size and shape. The object size can be calculated approximately by creating a special model for the power spectral density, but it may require other software (like petrel or kingdom) to draw such three-dimensional models.

- **Cost-Effective Solutions:** One critical area of focus is developing cost-effective solutions that do not compromise data quality. Future work should explore ways to reduce the number of monitoring stations and sensors required by optimizing their placement or through the use of adaptive sampling techniques. Additionally, research into affordable, efficient sensor technology could make large-scale deployment more feasible while maintaining high accuracy.

## Chapter 8 : Conclusion

There is need for effective site investigation methods for brownfield sites due to limitations that are inherent in presently available geophysical methods. This work has developed a deployment and analysis methodology for identifying buried objects using microseismic technology with an active source, that overcomes the challenges of and complements existing traditional methods. More specifically, the work proposes the use of three component low cost seismic sensors (seismic nodes or geophones) in a rectangular grid formation with an active source (e.g. site machinery engine) and comparative spectral analysis as a technology that can identify buried objects at depths down to 3m from the ground surface at brownfield sites.

The site investigation method is based on the principle of traditional reflection surveys but it does not incorporate the use of seismic wave arrival times. This attribute allows for its application for imaging the near-surface. No other active or passive seismic site investigation method allows for this.

The analysis demonstrated that the reflected energy, as quantified by calculating the area below the power spectral density curve, from seismic waves can effectively identify objects from concrete, steel and plastic buried up to 3 m deep for source to object distances up to 50m. It was shown through numerical modelling that the incidence and reflection angle are almost vertical at depths down to 6m, thus confirming the observation that a seismic sensor deployed directly above a buried object could allow for its detection.

Different materials reflect different amounts of seismic energy. This study has provided field and numerical evidence that materials commonly found at brownfield sites, i.e. concrete, plastic and steel reflect enough energy to allow for their detection.

The highest amount of the energy of the reflected wave is recorded directly above the buried object. Numerical simulations have shown that detection can also be possible at seismic stations at a lateral distance from the object. This distance is dependent on the size of the object, its depth and the spacing between the seismic stations. As a rule of thumb, a maximum distance of 1.5 times the minimum dimension of the object to be detected should be maintained as the spacing between seismic stations.

Implementing this technology in the field is highly feasible by deploying a network of sensors at spaced intervals. Once an object is detected, the sensors can be positioned more densely to enhance accuracy.

This approach and analysis methodology can change the way site investigations of brownfield sites have been conducted so far. It is yet to be fully developed, but even in this form, it can be a solution when site conditions do not favour the application of other traditional geophysical methods.

## References

- Ackman, T.E. and Cohen, K.K. (1994) 'Geophysical Methods: Remote Techniques Applied to Mining-Related Environmental and Engineering Problems', *Journal American Society of Mining and Reclamation*, 1994(4), pp. 208–217. Available at: <https://doi.org/10.21000/jasmr94040208>.
- Adagunodo, T.A., Sunmonu, L.A. and Adeniji, A.A. (2015) 'an Overview of Magnetic Method in Mineral Exploration', *Journal of Global Ecology and Environment*, 3(1), pp. 13–28. Available at: [www.ikpress.org](http://www.ikpress.org).
- Adams, D., de Sousa, C. and Tiesdell, S. (2010) 'Brownfield development: A comparison of North American and British approaches', *Urban Studies*, 47(1), pp. 75–104. Available at: <https://doi.org/10.1177/0042098009346868>.
- Alamar, M.C. *et al.* (2020) 'WP T1 . D3 . 1 Benchmark report on geophysics and non- intrusive investigation techniques 15 October 2020', (October).
- Alao, J.O. *et al.* (2024) 'The studying of magnetic anomalies due to shallow underground targets and the environmental applications', *Results in Earth Sciences*, 2(January), p. 100016. Available at: <https://doi.org/10.1016/j.rines.2024.100016>.
- Anderson, N. and Akingbade, A. (1997) 'Overview of the Shallow Seismic Reflection Technique', p. 27.
- Anyanwu, T. (2021) 'Theory and Applications of Shallow Seismic Reflection Geophysical Method to Engineering and Groundwater Studies: An Overview Osita Okeke Theory and Applications of Shallow Seismic Reflection Geophysical Method to Engineering and Groundwater Studies: An Ov', *International Journal of Innovative Science and Research Technology*, 6(2), pp. 178–191. Available at: [www.ijisrt.com](http://www.ijisrt.com)178.
- ASIM HASHIMI, S.A. (2011) 'Master of Science Master of Science Master of Science Master of Science', *Thesis*, 132001(1), pp. 9707–9710.
- Awad, S., Araffa, S. and Pek, J. (2014) 'Delineating Groundwater Aquifer and Subsurface Structures Using Integrated Geophysical Interpretation at the Western Part of Gulf of Aqaba, Sinai, Egypt', *International Journal of Water Resources and Arid Environments*, 3(1), pp. 51–62.

## ***Bibliography***

---

Ayala-Cabrera, D. *et al.* (2011) 'Location of buried plastic pipes using multi-agent support based on GPR images', *Journal of Applied Geophysics*, 75(4), pp. 679–686. Available at: <https://doi.org/10.1016/j.jappgeo.2011.09.024>.

Baker, G.S., Jordan, T.E. and Pardy, J. (2007) 'An introduction to ground penetrating radar (GPR)', *Special Paper of the Geological Society of America*, 432(01), pp. 1–18. Available at: [https://doi.org/10.1130/2007.2432\(01\)](https://doi.org/10.1130/2007.2432(01)).

Beckel, R.A. (2022) *Active and passive seismic methods for investigating the glacially-triggered Burträsk fault*.

BenDor, T.K., Metcalf, S.S. and Paich, M. (2011) 'The dynamics of brownfield redevelopment', *Sustainability*, 3(6), pp. 914–936. Available at: <https://doi.org/10.3390/su3060914>.

Bohnhoff, M. *et al.* (2013) 'Microseismic monitoring of reservoir stimulation: Case studies and implications for improved geomechanical characterization', *75th EAGE Conference and Exhibition Incorporating SPE EUROPEC 2013* [Preprint], (February 2018). Available at: <https://doi.org/10.3997/2214-4609.20131178>.

Bongiolo, A. de B. e S. *et al.* (2022) 'Geophysical surveying for the detection of ferrous-based objects: possibilities for depth estimative combining analytic signal and vertical integral of the anomalous magnetic field', *Brazilian Journal of Geophysics*, 40(1), p. 43. Available at: <https://doi.org/10.22564/brjg.v40i1.2132>.

Bruno, P.P.G. (2023) 'Seismic Exploration Methods for Structural Studies and for Active Fault Characterization: A Review', *Applied Sciences (Switzerland)*, 13(16). Available at: <https://doi.org/10.3390/app13169473>.

De Carlo, L. *et al.* (2013) 'Characterization of a dismissed landfill via electrical resistivity tomography and mise-à-la-masse method', *Journal of Applied Geophysics*, 98, pp. 1–10. Available at: <https://doi.org/10.1016/j.jappgeo.2013.07.010>.

Chelminski, S., Watson, L.M. and Ronen, S. (2019) 'Research Note: Low-frequency pneumatic seismic sources', *Geophysical Prospecting*, 67(6), pp. 1547–1556. Available at: <https://doi.org/10.1111/1365-2478.12774>.

Chen, H. (2014) 'Development status of micro seismic monitoring technology in China', *IOSR Journal of Engineering*, 4(1), pp. 16–19. Available at: <https://doi.org/10.9790/3021-04131619>.

## ***Bibliography***

---

CIRIA (2018) *A Guide to Small Brownfield Sites and Land Contamination*, C773.

Claeys, T. *et al.* (2015) ‘Removing the Spectral Leakage in Time-Domain Based Near-Field Scanning Measurements’, *IEEE Transactions on Electromagnetic Compatibility*, 57(6), pp. 1329–1337. Available at: <https://doi.org/10.1109/TEM.2015.2447051>.

Coe, J.T.; *et al.* (2018) ‘STATE OF CALIFORNIA • DEPARTMENT OF TRANSPORTATION ADA Notice CA17-2111 2. GOVERNMENT ASSOCIATION NUMBER 3. RECIPIENT’S CATALOG NUMBER 4. TITLE AND SUBTITLE GEOPHYSICAL METHODS FOR DETERMINING THE GEOTECHNICAL ENGINEERING PROPERTIES OF EARTH MATERIALS Unc’, 0003.

Collaton, E. and Bartsch, C. (1996) *Industrial Site Reuse and Urban Redevelopment-An Overview*, *Cityscape*.

Cui, X. *et al.* (2021) ‘Energy Characteristics of Seismic Waves on Cardox Blasting Tube’, *Geofluids*, 2021, pp. 21–25. Available at: <https://doi.org/10.1155/2021/9919764>.

Dales, P., Audet, P. and Olivier, G. (2017) ‘for Temporal Subsurface Monitoring’, (2), pp. 863–870. Available at: <https://doi.org/10.1002/2017GL075342>.

Doick, K.J. *et al.* (2006) ‘Brownfield sites turned green: Realising sustainability in urban revival’, *WIT Transactions on Ecology and the Environment*, 94, pp. 131–140. Available at: <https://doi.org/10.2495/BF060131>.

Duguid, C., Halliday, D. and Curtis, A. (2011) ‘Source-receiver interferometry for seismic wavefield construction and ground-roll removal’, *Leading Edge (Tulsa, OK)*, 30(8), pp. 838–843. Available at: <https://doi.org/10.1190/1.3626489>.

Eissa, R. (2021) ‘Electrical Resistivity Tomography Application for Buried Foundation Investigations: Insights and Review’, *Iraqi Geological Journal*, 54(2), pp. 122–133. Available at: <https://doi.org/10.46717/IGJ.54.2E.8MS-2021-11-24>.

Ékes, C. *et al.* (2011) ‘Gpr Goes Underground : Pipe Penetrating Radar’, pp. 1–10.

Ferrari, G. (2011) ‘Three –Dimensional Earthquake Response of Slopes’.

Fkirin, M.A., Youssef, M.A.S. and El-Deery, M.F. (2021) ‘Digital filters applications on aeromagnetic data for identification of hidden objects’, *Bulletin of Engineering Geology and the Environment*, 80(3), pp. 2845–2858. Available at: <https://doi.org/10.1007/s10064-020->

## ***Bibliography***

---

02067-4.

Gehrig, M. (2004) 'Ground Penetrating Radar for Concrete Evaluation Studies', *Technical ...*, (January 2004), pp. 1–17. Available at: [http://foundationperformance.org/pastpresentations/gehrig\\_paper\\_march2004.pdf](http://foundationperformance.org/pastpresentations/gehrig_paper_march2004.pdf).

Gołębiowski, T. *et al.* (2017) 'The application of electromagnetic methods for polymetallic prospecting in mining conditions', *Geology, Geophysics & Environment*, 43(3), p. 181. Available at: <https://doi.org/10.7494/geol.2017.43.3.181>.

Grami, A. (2016) 'Signals, Systems, and Spectral Analysis', *Introduction to Digital Communications*, pp. 41–150. Available at: <https://doi.org/10.1016/b978-0-12-407682-2.00003-x>.

Guglielmetti, L. and Moscariello, A. (2019) 'Application of the gravity method to constrain geological structures of geothermal interest in the Geneva Basin', (June), pp. 11–14.

H. Karim, H., H. Ibrahim, K. and A. H. Al-Rubaye, M. (2015) 'Detection of Buried Utilities Using Electrical Resistivity Imaging (ERI) Technique', *Engineering and Technology Journal*, 33(3A), pp. 703–719. Available at: <https://doi.org/10.30684/etj.33.3a.15>.

Hammond, E.B. *et al.* (2021) 'A critical review of decision support systems for brownfield redevelopment', *Science of the Total Environment*, 785. Available at: <https://doi.org/10.1016/j.scitotenv.2021.147132>.

Heezen, B.C. and Wilson, L. (2006) *Submarine geomorphology*, *Geomorphology*. Available at: [https://doi.org/10.1007/3-540-31060-6\\_360](https://doi.org/10.1007/3-540-31060-6_360).

Itasca Consulting Group (2017) 'FLAC3D 6.0 Modelling', p. 405.

Jol, H.M. and Bristow, C.S. (2003) 'GPR in sediments: Advice on data collection, basic processing and interpretation, a good practice guide', *Geological Society Special Publication*, 211(January 2003), pp. 9–27. Available at: <https://doi.org/10.1144/GSL.SP.2001.211.01.02>.

Joshi, M. *et al.* (2020) 'Significance and limit of electrical resistivity survey for detection sub surface cavity: A case study from, Southern Western Ghats, India', *Basics of Computational Geophysics*, (February), pp. 81–93. Available at: <https://doi.org/10.1016/B978-0-12-820513-6.00004-7>.

Kayal, J.R. (2006) 'Seismic waves and earthquake location', *Geological Survey of India*, 27,

## ***Bibliography***

---

pp. 1–42.

Killeen, P.G. (1997) ‘Borehole Geophysics : Exploring the Third Dimension’, *Exploration* 97, Keynote Se, pp. 31–42.

Kisohara, M. *et al.* (2020) ‘Optimal length of R – R interval segment window for Lorenz plot detection of paroxysmal atrial fibrillation by machine learning’, *BioMedical Engineering OnLine*, pp. 1–18. Available at: <https://doi.org/10.1186/s12938-020-00795-y>.

Kumar, S., Pal, S.K. and Guha, A. (2024) ‘Combined Geophysical Study to Compare Responses from Pipe 1 and Pipe 2 in Wajrakarur Kimberlite Field’, *Mining, Metallurgy and Exploration*, 41(1), pp. 413–429. Available at: <https://doi.org/10.1007/s42461-024-00914-6>.

Li, C.F. *et al.* (2019) ‘The effect of parallel pipeline parameters on the characteristics of gravity and magnetic surveys’, *Journal of Applied Geophysics*, 166, pp. 77–88. Available at: <https://doi.org/10.1016/j.jappgeo.2019.04.023>.

Li, H. (2008) *Spectral Analysis of Signals [Book Review]*, *IEEE Signal Processing Magazine*. Available at: <https://doi.org/10.1109/msp.2007.273066>.

Likhacheva, O., Kashin, G. and Mironychev, V. (2021) ‘Use of passive seismic to identify oil-bearing reservoirs in the Udmurt Republic, Russia’, *Journal of Geotechnology and Energy*, 38(1), pp. 35–40. Available at: <https://doi.org/10.7494/jge.2021.38.1.4290>.

Liu, X. *et al.* (2022) ‘Research on the Attenuation Characteristics of High-Frequency Elastic Waves in Rock-Like Material’, *Materials*, 15(19). Available at: <https://doi.org/10.3390/ma15196604>.

Lu, J. and Wang, Y. (2010) ‘Seismic wave propagation in Kelvin visco-elastic VTI media’, *Applied Geophysics*, 7(4), pp. 357–364. Available at: <https://doi.org/10.1007/s11770-010-0256-y>.

Mari, J.-L. (2019) ‘Chapter 1 Wave propagation’, *Seismic imaging: a practical approach*, pp. 17–34. Available at: <https://doi.org/10.1051/978-2-7598-2351-2.c003>.

De Martins, J.N., Freire, E. and Hemadipour, H. (2009) ‘Applications and market of PVC for piping industry’, *Polimeros*, 19(1), pp. 58–62. Available at: <https://doi.org/10.1590/s0104-14282009000100014>.

Miller, J.T. (2016) ‘Is urban greening for everyone? Social inclusion and exclusion along the

## ***Bibliography***

---

Gowanus Canal’, *Urban Forestry and Urban Greening*, 19, pp. 285–294. Available at: <https://doi.org/10.1016/j.ufug.2016.03.004>.

Miong, S. (2008) ‘Borehole Geophysical Methods for Near-Surface Characterization’.

Mitchell, J.K. and Green, R.A. (2017) ‘Some induced seismicity considerations in geo-energy resource development’, *Geomechanics for Energy and the Environment*, 10, pp. 3–11. Available at: <https://doi.org/10.1016/j.gete.2017.01.001>.

Moss, T. (2003) ‘Utilities, land-use change, and urban development: Brownfield sites as “cold-spots” of infrastructure networks in Berlin’, *Environment and Planning A*, 35(3), pp. 511–529. Available at: <https://doi.org/10.1068/a3548>.

Murthy, C.V.R. (2002) ‘Learning earthquake design and construction earthquake tip-2 - How the ground shakes?’, *Journal of Structural Engineering (Madras)*, 29(2), p. 137.

Mutagi, R.N. (2014) ‘Understanding the sampling process’, (September 2004).

Pesaran, B. (2008) ‘Spectral Analysis for Neural Signals’, *Short Course III*, p. 1.

Del Pezzo, E. *et al.* (2013) ‘Detection of seismic signals from background noise in the area of campi flegrei: Limits of the present seismic monitoring’, *Seismological Research Letters*, 84(2), pp. 190–198. Available at: <https://doi.org/10.1785/0220120062>.

Poppeliers, C. (2007) ‘Estimating vertical stochastic scale parameters from seismic reflection data: Deconvolution with non-white reflectivity’, *Geophysical Journal International*, 168(2), pp. 769–778. Available at: <https://doi.org/10.1111/j.1365-246X.2006.03239.x>.

Poppeliers, C. and Mallinson, D. (2015) ‘High-frequency seismic noise generated from breaking shallow water ocean waves and the link to time-variable sea states’, *Geophysical Research Letters*, 42(20), pp. 8563–8569. Available at: <https://doi.org/10.1002/2015GL066126>.

Pringle, J.K. *et al.* (2024) ‘Forensic geoscience non-invasive detection and characterisation of underground clandestine complexes, bunkers, tunnels and firing ranges’, *Forensic Science International*, 359(February), p. 112033. Available at: <https://doi.org/10.1016/j.forsciint.2024.112033>.

Quinta-Ferreira, M. (2019) ‘Ground Penetration Radar in Geotechnics. Advantages and Limitations’, *IOP Conference Series: Earth and Environmental Science*, 221(1). Available at:

## ***Bibliography***

---

<https://doi.org/10.1088/1755-1315/221/1/012019>.

Rejkkjær, S. *et al.* (2021) ‘Determination of the resistivity distribution along underground pipes in urban contexts using galvanic and capacitive methods’, *Near Surface Geophysics*, 19(1), pp. 27–41. Available at: <https://doi.org/10.1002/nsg.12135>.

Roden, R. *et al.* (2017) ‘Seismic interpretation below tuning with multiattribute analysis’, *Leading Edge*, 36(4), pp. 330–339. Available at: <https://doi.org/10.1190/tle36040330.1>.

Routh, P.S. and Oldenburg, D.W. (2000) ‘Electromagnetic coupling in frequency domain IP data: A method for removal’, *2000 SEG Annual Meeting*, pp. 59–76.

Ruigrok, E. *et al.* (2010) ‘High-resolution lithospheric imaging with seismic interferometry’, *Geophysical Journal International*, 183(1), pp. 339–357. Available at: <https://doi.org/10.1111/j.1365-246X.2010.04724.x>.

Schlinger, C.M. (1990) ‘Magnetometer and gradiometer surveys for detection of underground storage tanks’, *Bulletin - Association of Engineering Geologists*, 27(1), pp. 37–50. Available at: <https://doi.org/10.2113/gseegeosci.xxvii.1.37>.

Schmischke, M. (2010) ‘Nonequispaced Fast Fourier Transform ( NFFT ) Interface for Julia’, pp. 1–19.

Shahandashti, M. *et al.* (2021) *Advanced Geophysical Tools for Geotechnical Analysis Final Report Title: Advanced Geophysical Tools for Geotechnical Analysis*. Available at: [www.ntis.gov](http://www.ntis.gov).

Shebl, S. *et al.* (2019) ‘Utilizing shallow seismic refraction in defining the geotechnical properties of the foundation materials: A case study at New Minia City, Nile Valley, Egypt’, *Egyptian Journal of Petroleum*, 28(2), pp. 145–154. Available at: <https://doi.org/10.1016/j.ejpe.2018.12.006>.

Shin, H.-C. *et al.* (2021) ‘Geophysical methods to assess soil characteristics’, (February 2022), pp. 139–174. Available at: <https://doi.org/10.19103/as.2020.0079.12>.

Sigurdsson, T. (1992) ‘Application of ground penetrating radar for shallow geological investigations’, *Journal of Applied Geophysics*, 29(1), p. 72. Available at: [https://doi.org/10.1016/0926-9851\(92\)90037-1](https://doi.org/10.1016/0926-9851(92)90037-1).

Solomon, O.M.J. (1991) ‘PSD computations using Welch’s method’, *Sandia National*

## ***Bibliography***

---

*Laboratories*, (December), pp. 1–64.

Szymko, R. *et al.* (2021) ‘Application of spatio-temporal spectral analysis for detection of seismic waves in gravitational-wave interferometer’, *Galaxies*, 9(3), pp. 1–25. Available at: <https://doi.org/10.3390/galaxies9030050>.

Tang, B. *et al.* (2022) ‘Seismic Response of Star-Type Grid Concrete Wall Structure by Numerical Modeling’, *Materials*, 15(23), pp. 1–15. Available at: <https://doi.org/10.3390/ma15238519>.

United States Environmental Protection Agency (2016) ‘Expedited Site Assessment Tools for Underground Storage Tank Sites: A Guide for Regulators.’, (Chapter V-Direct Push Technologies), p. 122. Available at: <https://www.epa.gov/sites/production/files/2014-03/documents/esa-ch5.pdf>.

Usman, F.C.A. *et al.* (2020) ‘Geophysical survey of landslide movement and mechanism in Gorontalo Outer Ring Road, Gorontalo’, *IOP Conference Series: Earth and Environmental Science*, 589(1). Available at: <https://doi.org/10.1088/1755-1315/589/1/012008>.

Volpini, C., Douglas, J. and Nielsen, A.H. (2021) ‘Guidance on Conducting 2D Linear Viscoelastic Site Response Analysis Using a Finite Element Code’, *Journal of Earthquake Engineering*, 25(6), pp. 1153–1170. Available at: <https://doi.org/10.1080/13632469.2019.1568931>.

Wahab, S. (2013) ‘ASSESSING THE CONDITION OF BURIED PIPE USING GROUND University of Birmingham Research Archive’, (August).

Watts, H. *et al.* (2022) ‘An Assessment of Geophysical Survey Techniques for Characterising the Subsurface Around Glacier Margins, and Recommendations for Future Applications’, *Frontiers in Earth Science*, 10(March), pp. 1–23. Available at: <https://doi.org/10.3389/feart.2022.734682>.

Xu, M.X., Wei, Y.X. and Li, J.J. (2021) ‘Application of a new seismic reflection imaging system TSP-SK in tunnel advanced geological prediction’, 252, pp. 0–3. Available at: <https://doi.org/10.1051/e3sconf/202125201030>.

Yang, D., Qin, Y. and Ren, X. (2015) ‘Research on the Ground Penetrating Radar Clutter Suppression Technology Based on PCA Method’, *Proceedings of the 2015 International Conference on Electrical, Computer Engineering and Electronics*, 24(Icecee), pp. 239–242.

## ***Bibliography***

---

Available at: <https://doi.org/10.2991/icecee-15.2015.53>.

Yang, L. *et al.* (2007) 'Pure S-waves in land P-wave source VSP data', *Applied Geophysics*, 4(3), pp. 173–182. Available at: <https://doi.org/10.1007/s11770-007-0035-6>.

Yang, L., Yang, D. and Yuan, Q. (2024) 'Electrical resistivity tomography through reinforced concrete floor', *Near Surface Geophysics*, 22(1), pp. 47–59. Available at: <https://doi.org/10.1002/nsg.12285>.

Yomogida, K. and Benites, R. (2002) 'Scattering of seismic waves by cracks with the boundary integral method', *Pure and Applied Geophysics*, 159(7–8), pp. 1771–1789. Available at: <https://doi.org/10.1007/s00024-002-8708-9>.

Zeckra, M. (2022) 'Sensitivity , Accuracy and Limits of the Lightweight Three-Component SmartSolo Geophone Sensor ( 5 Hz ) for Seismological Applications', (October). Available at: <https://doi.org/10.31223/X5F073>.

Zihong, G. *et al.* (2018) 'Seismic Analysis of Shallow Tunnel in Bad Ground with the Numerical Simulation Method', (Icmit), pp. 96–104. Available at: <https://doi.org/10.23977/icmit.2018.016>.

## **Appendix**

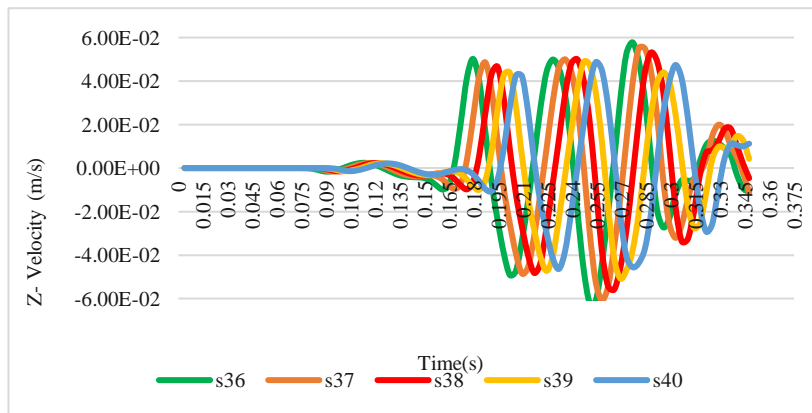
### **A Numerical simulation of seismic waves propagation through media (site B, model 2)**

This appendix includes the results obtained from the simulation of seismic waves. It details the velocities histories, PSD curves.

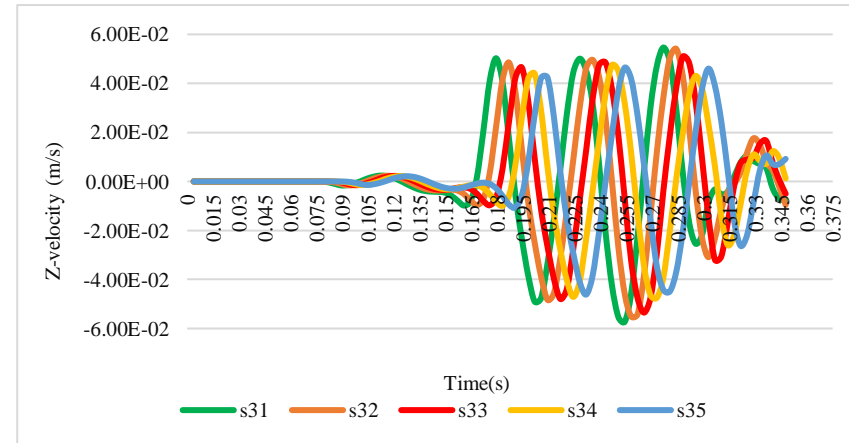
# Appendix

## A.1 Result and discussion of seismic wave simulation that was recoded from the homogenous model at site B.

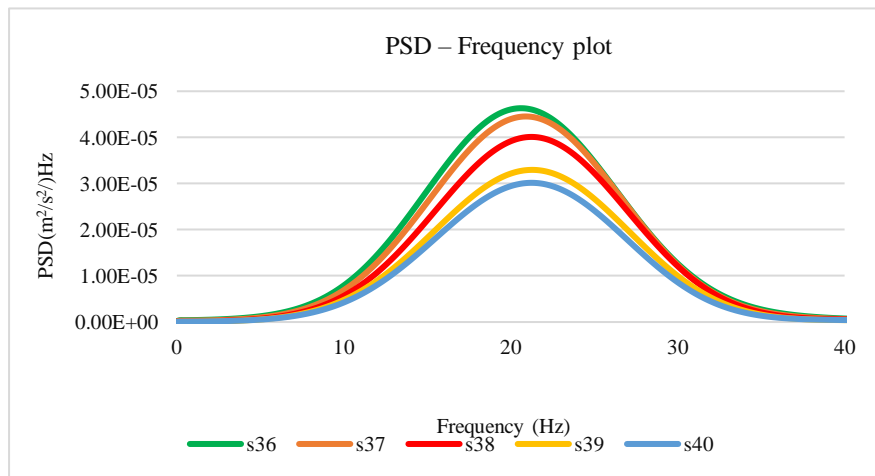
Velocity history recorded at monitoring stations s36, s37, s38, s39, and s40



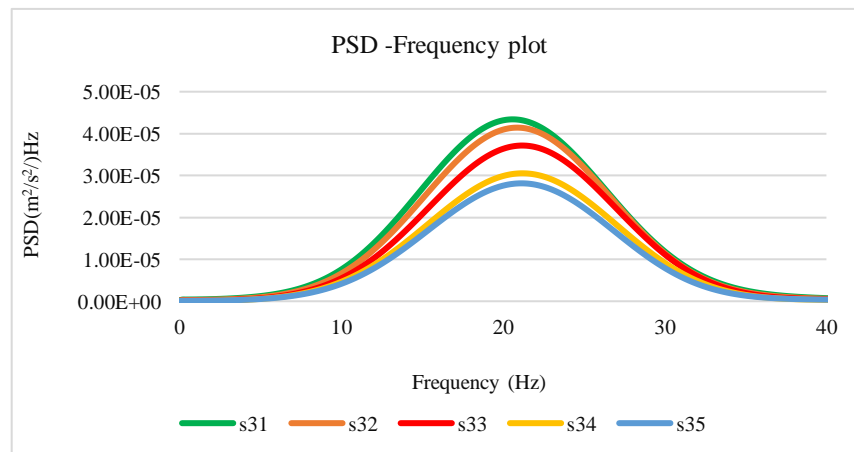
Velocity history recorded at monitoring stations s31, s32, s33, s34, and s35



PSD of the velocity history recorded at monitoring stations s36, s37, s38, s39, and s40

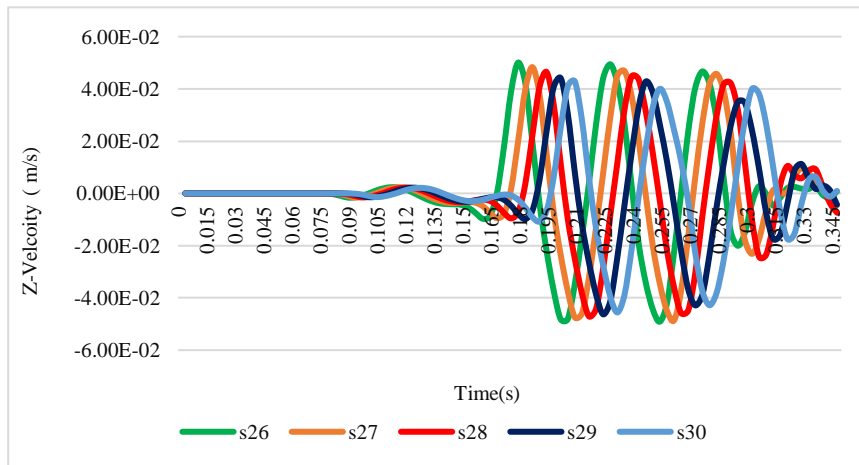


PSD of the velocity history recorded at monitoring stations s31, s32, s33, s34, and s35

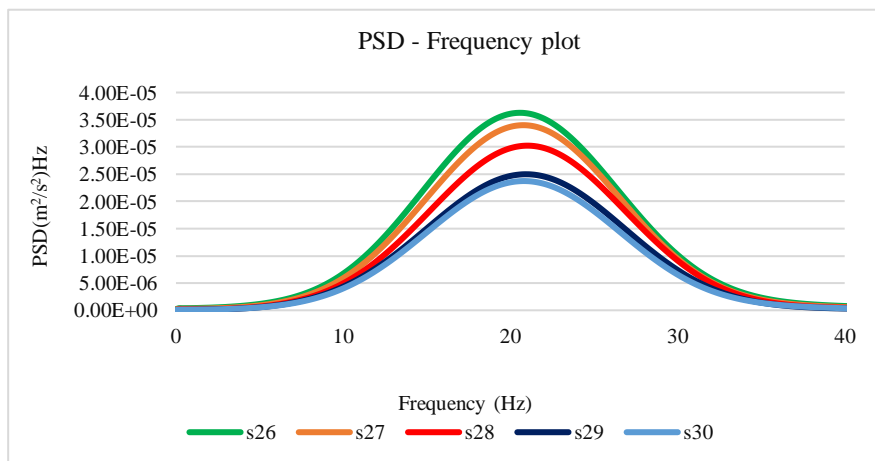


# Appendix

Velocity history recorded at monitoring stations s26, s27, s28, s29, and s30



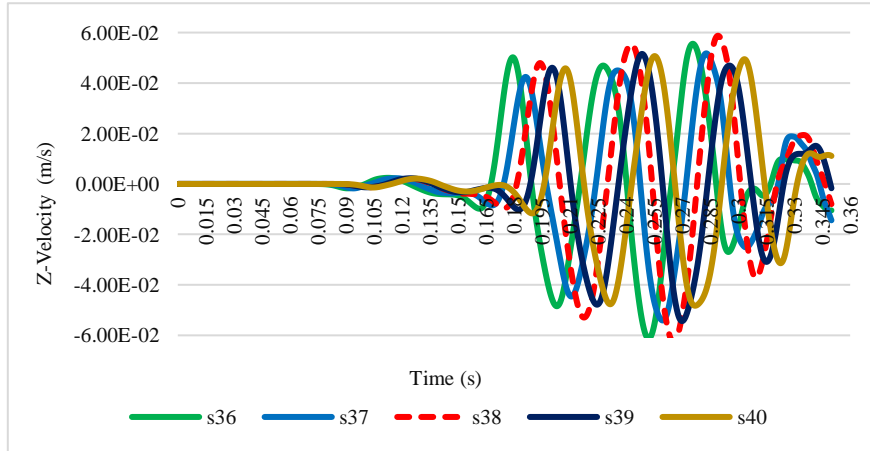
PSD of the velocity history recorded at monitoring stations s26, s27, s28, s29, and s30



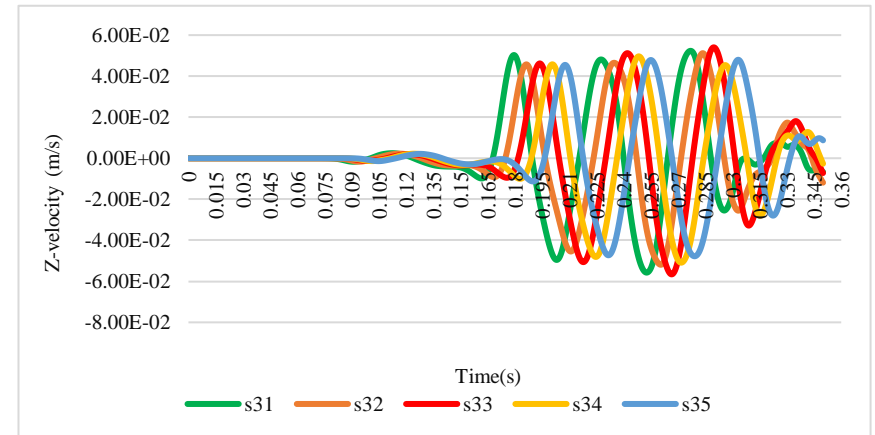
# Appendix

## A.2 First scenario (the object at 1m depth)

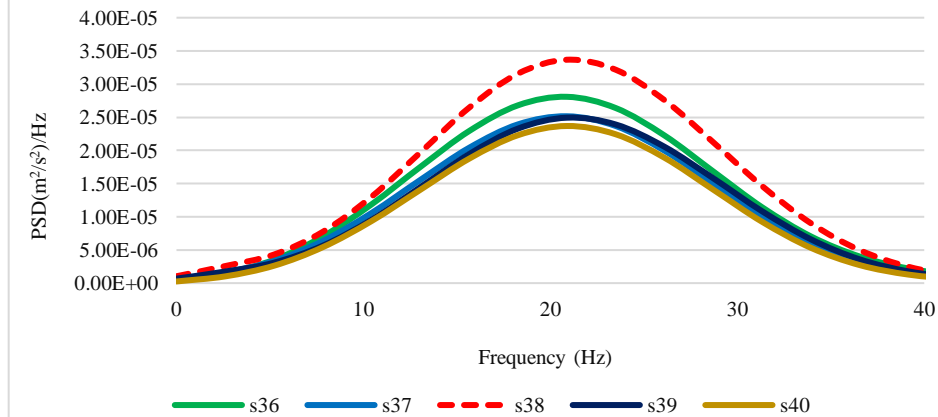
Velocity history recorded at monitoring stations s36, s37, s38, s39, and s40



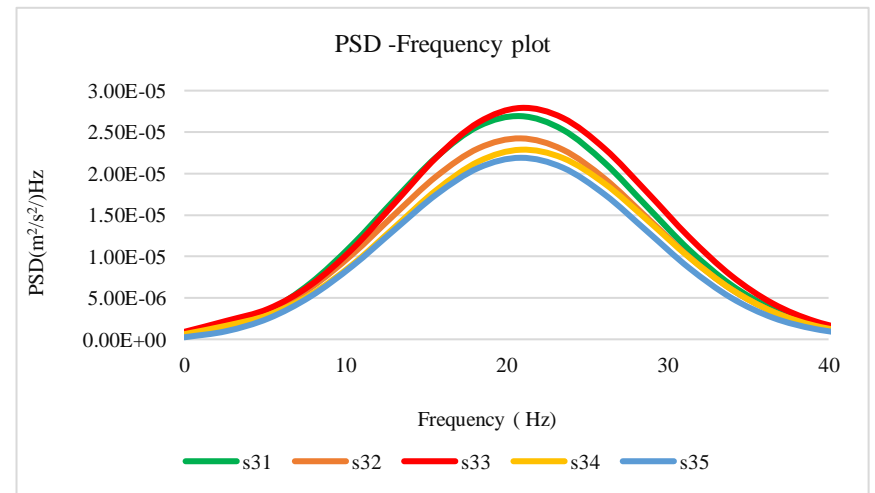
Velocity history recorded at monitoring stations s31, s32, s33, s34, and s35



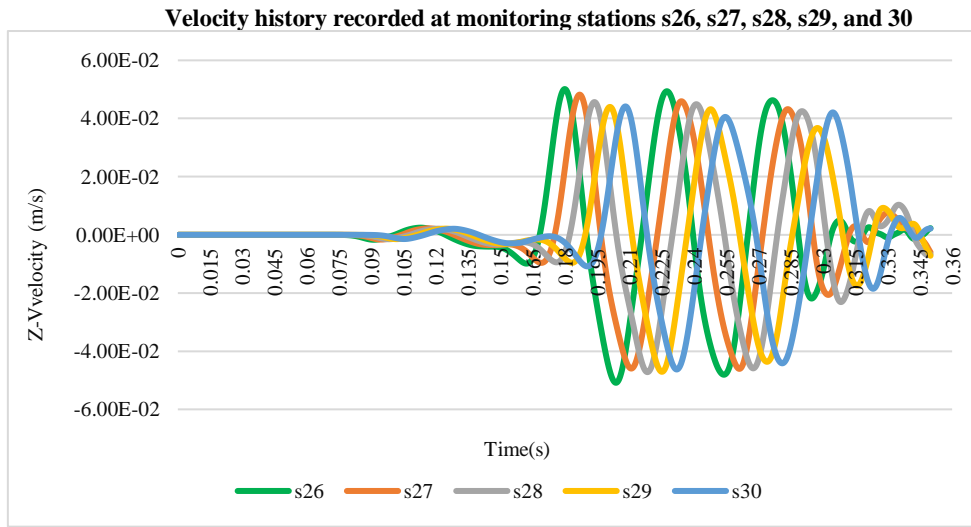
PSD -Frequency plot



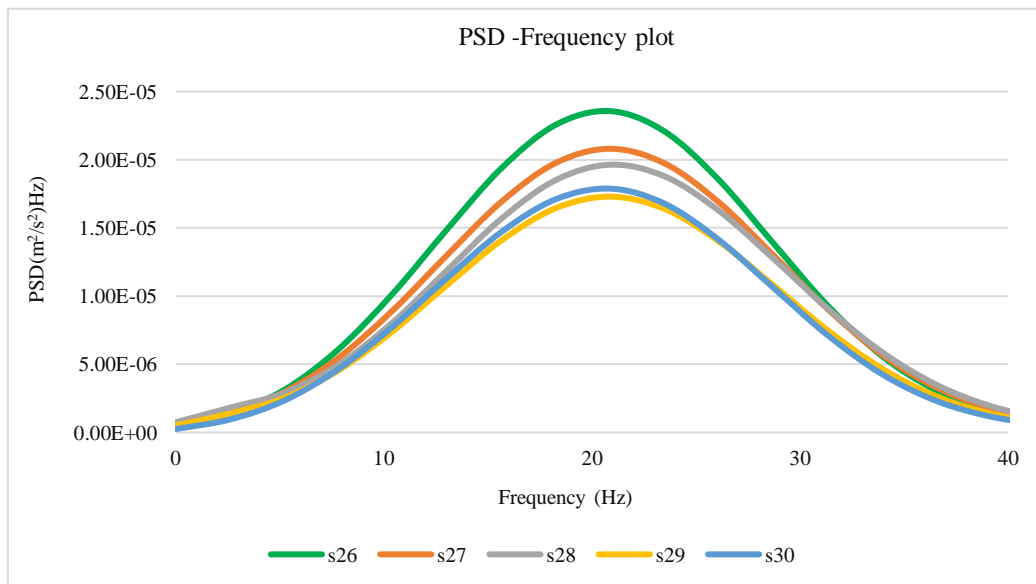
PSD of the velocity history recorded at monitoring stations s31, s32, s33, s34, and s35



# Appendix



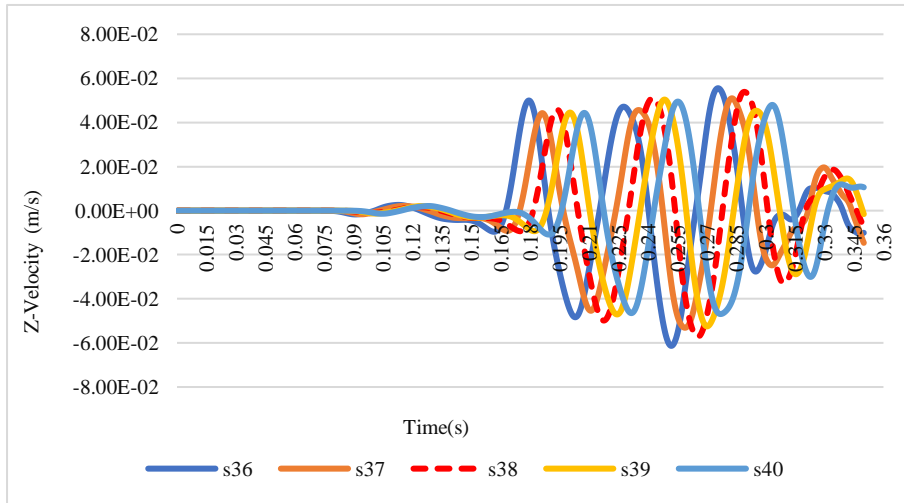
**Power spectral density of the velocity history recorded at monitoring stations s26, s27, s28, s29, and s30**



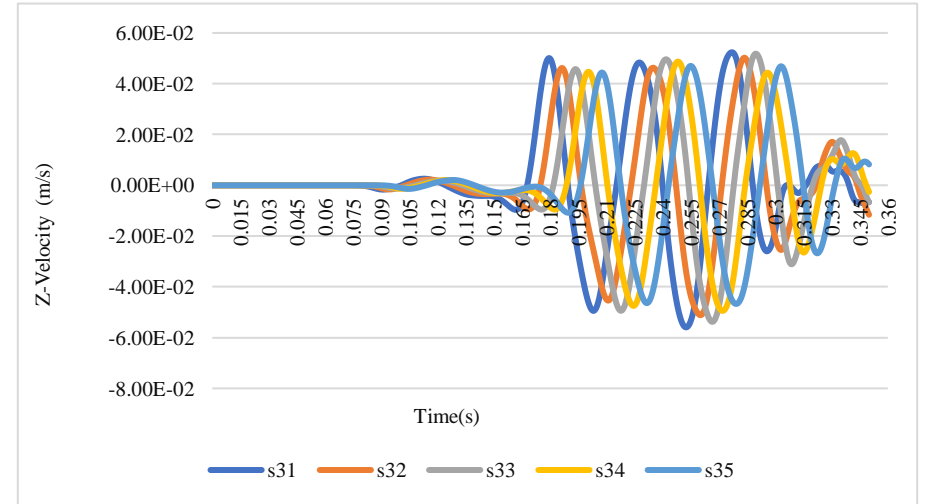
# Appendix

## A.3 Second scenario (the object at 2m depth)

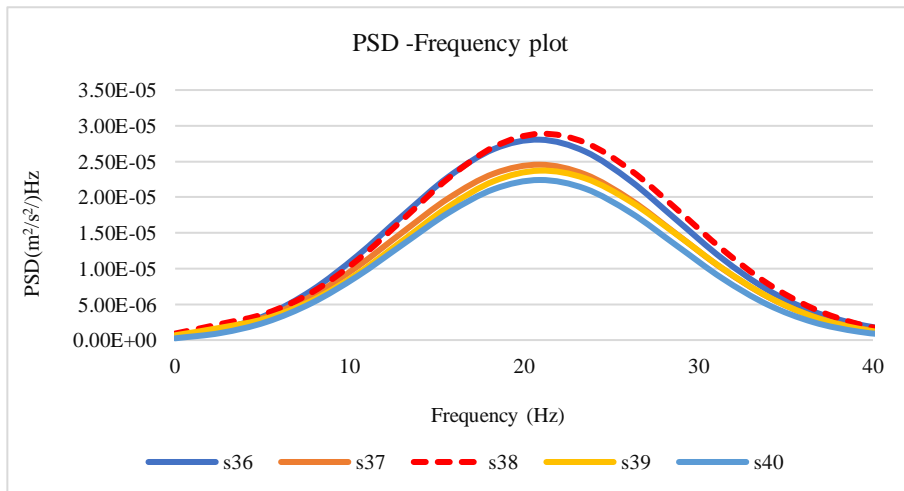
Velocity history recorded at monitoring stations s36, s37, s38, s39, and 40



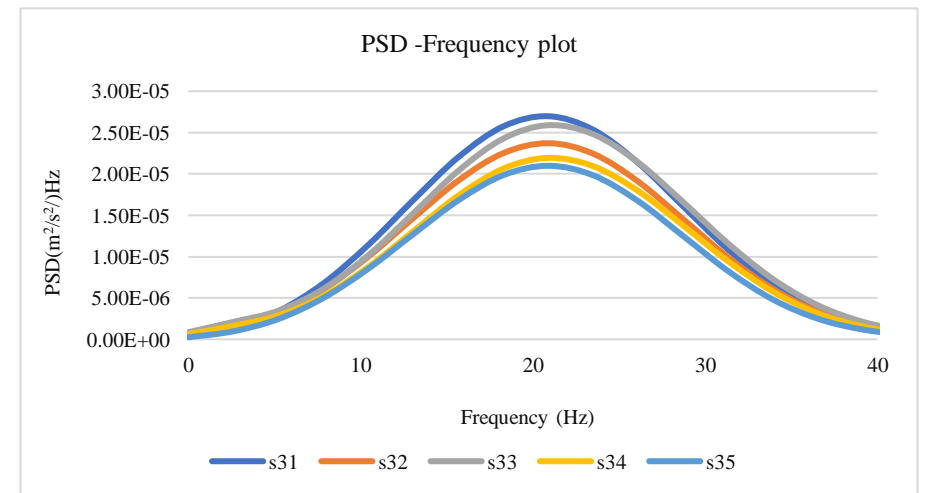
Velocity history recorded at monitoring stations s31, s32, s33, s34, and 35



PSD of the velocity history recorded at monitoring stations s36, s37, s38, s39, and s40

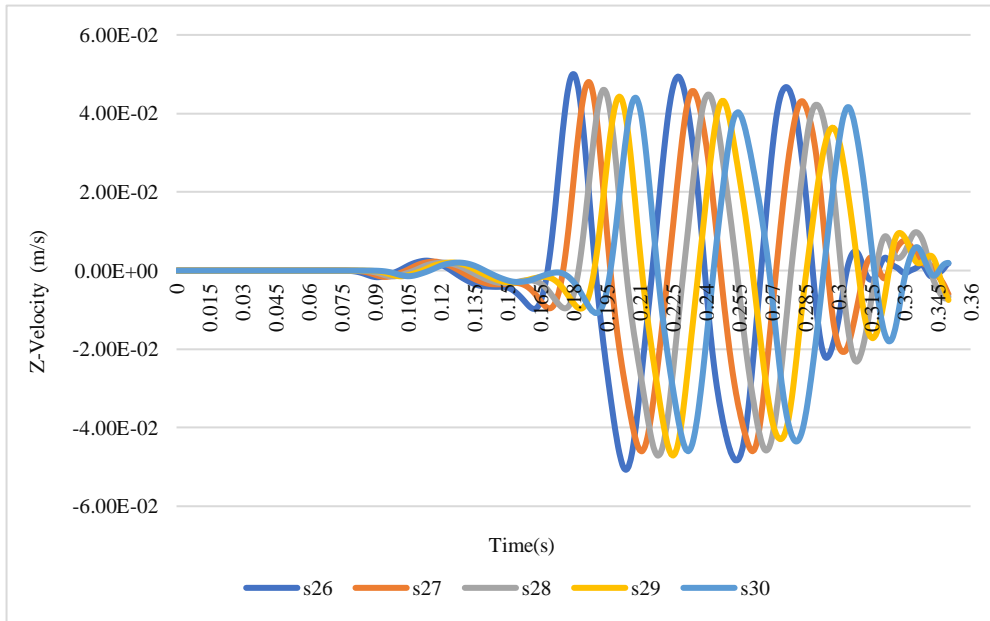


PSD of the velocity history recorded at monitoring stations s31, s32, s33, s34, and s35

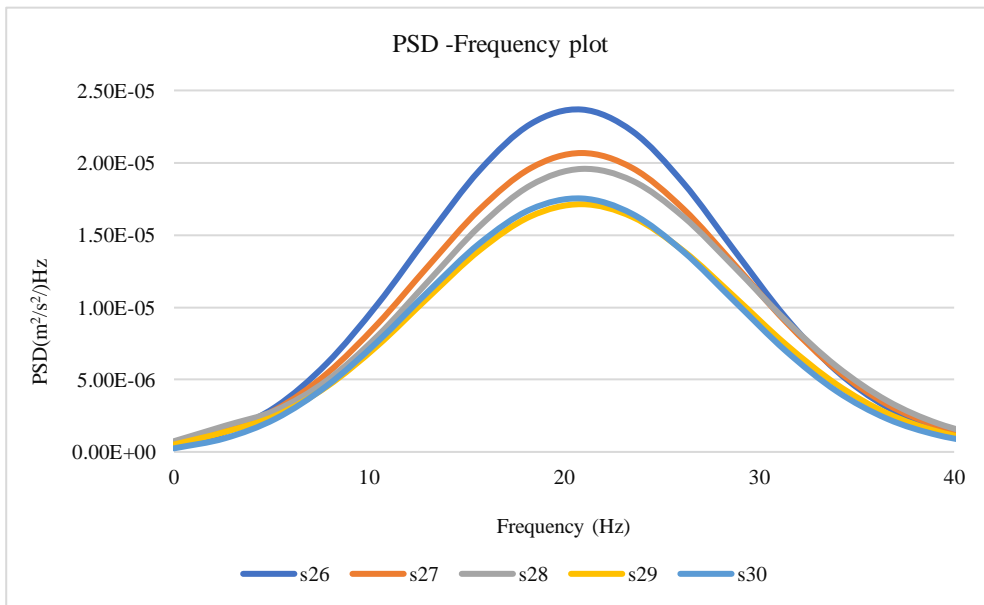


# Appendix

Velocity history recorded at monitoring stations s26, s27, s28, s29, and



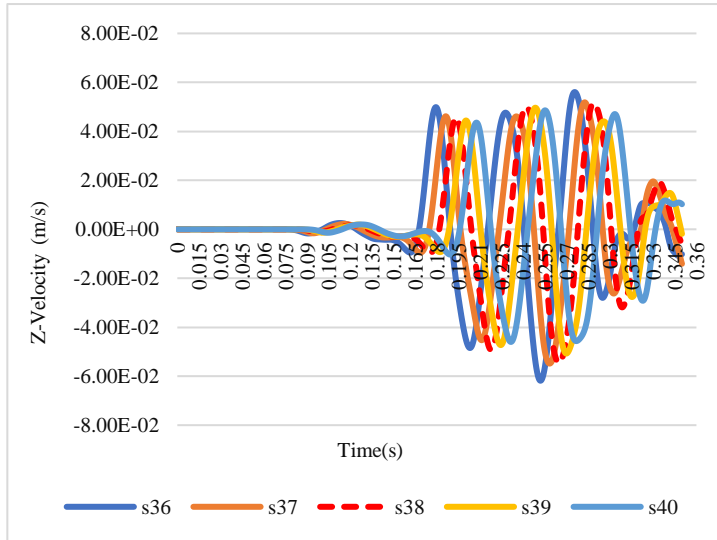
PSD of the velocity history recorded at monitoring stations s26, s27, s28, s29, and s30



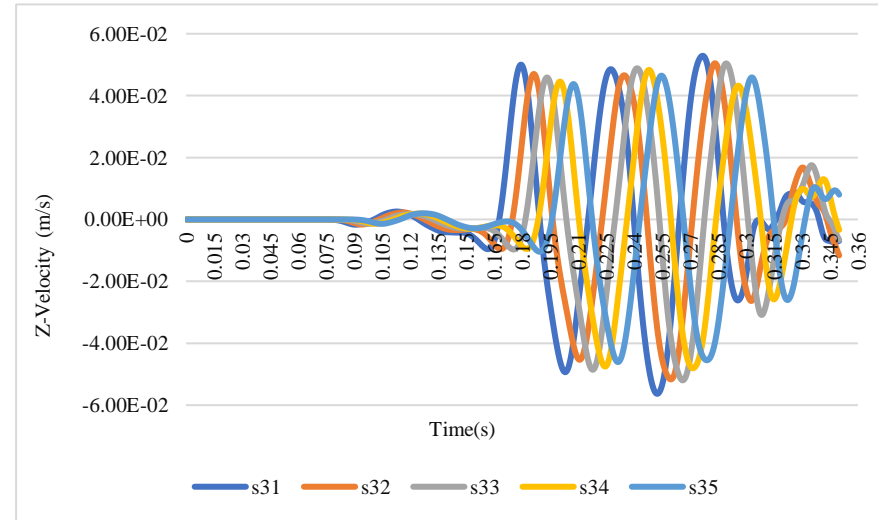
# Appendix

## A.4 Third scenario (the object at 3m depth)

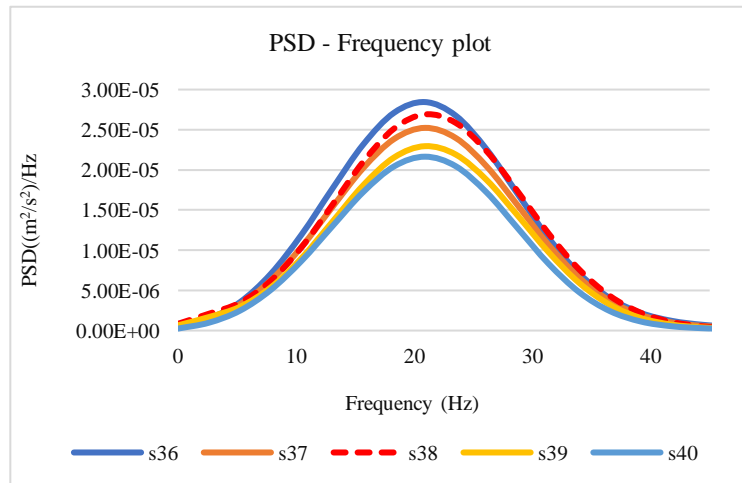
Velocity history recorded at monitoring stations s36, s37, s38, s39, and 40



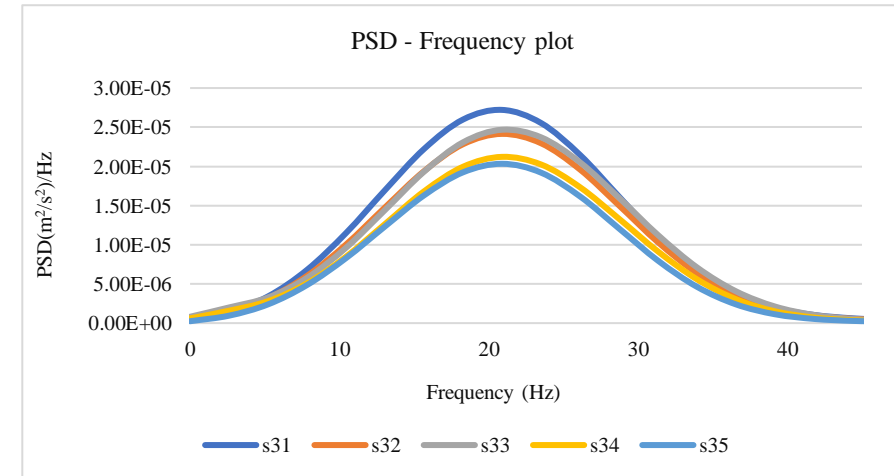
Velocity history recorded at monitoring stations s31, s32, s33, s34, and 35



PSD of the velocity history recorded at monitoring stations s31, s32, s33, s34, and s35

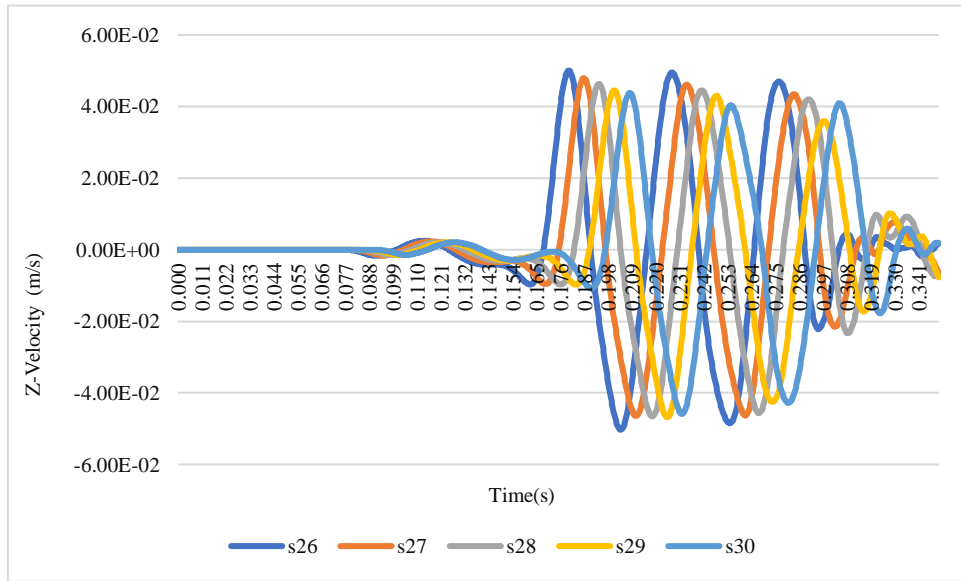


PSD of the velocity history recorded at monitoring stations s31, s32, s33, s34, and s35

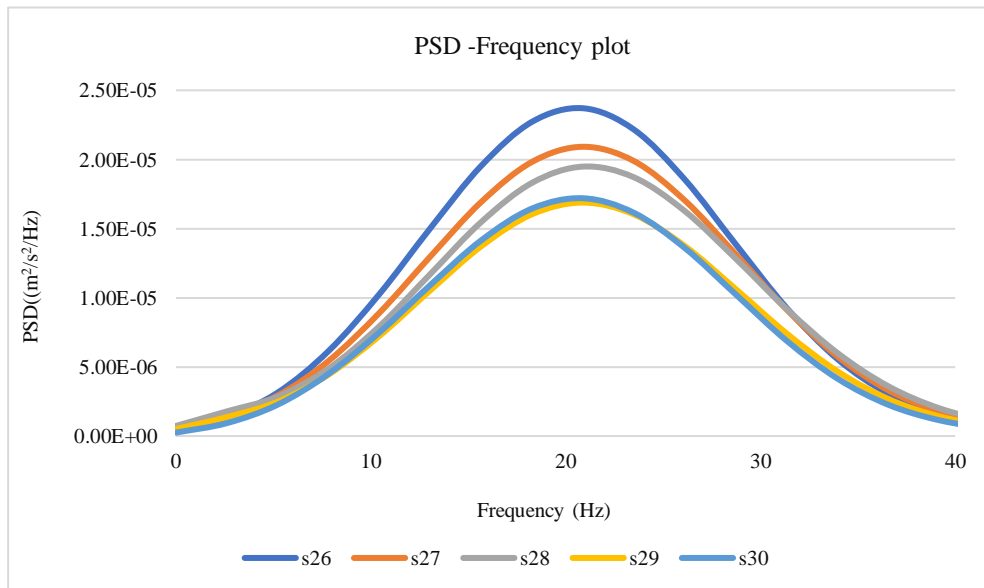


# Appendix

Velocity history recorded at monitoring stations s26, s27, s28, s29, and s30



PSD of the velocity history recorded at monitoring stations s26, s27, s28, s29, and s30



## Appendix

---

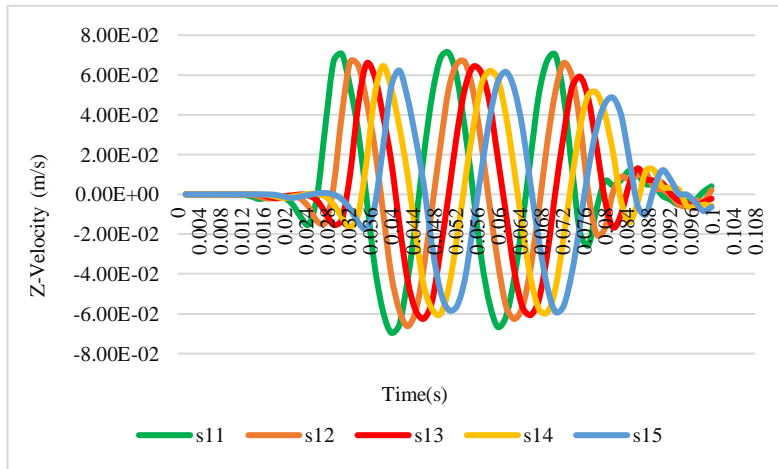
### **B Numerical simulation of seismic waves propagation through media (Model 3)**

This appendix includes the results obtained from the simulation of seismic waves in model 3. It details the velocities histories, PSD curves.

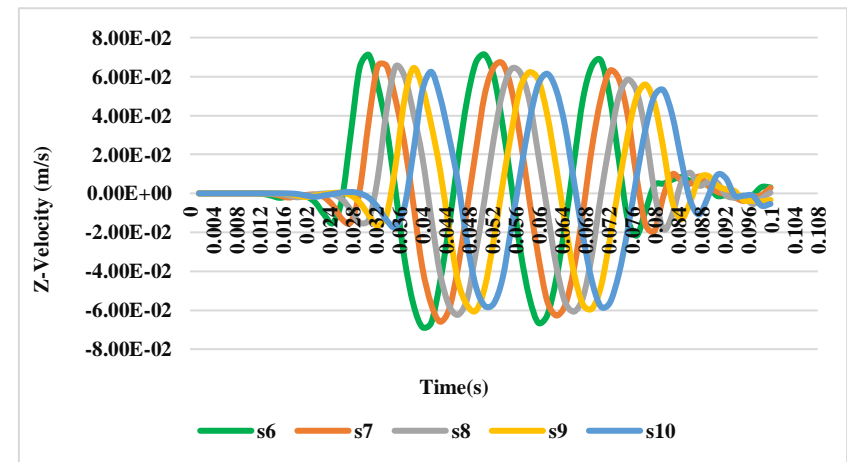
# Appendix

## B.1 Seismic wave simulation that was recorded from the homogenous model at site A.

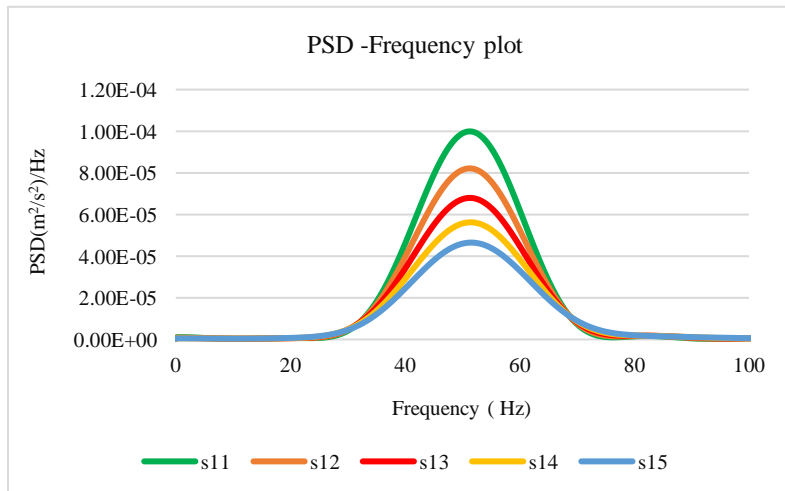
Velocity history recorded at monitoring stations s11, s12, s13, s14, and 15



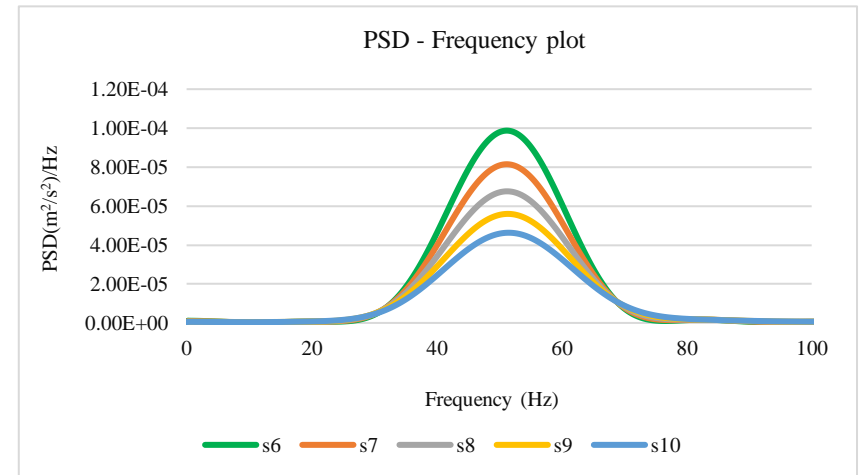
Velocity history recorded at monitoring stations s6, s7, s8, s9, and 10



PSD of the velocity history recorded at monitoring stations s11, s12, s13, s14, and s15

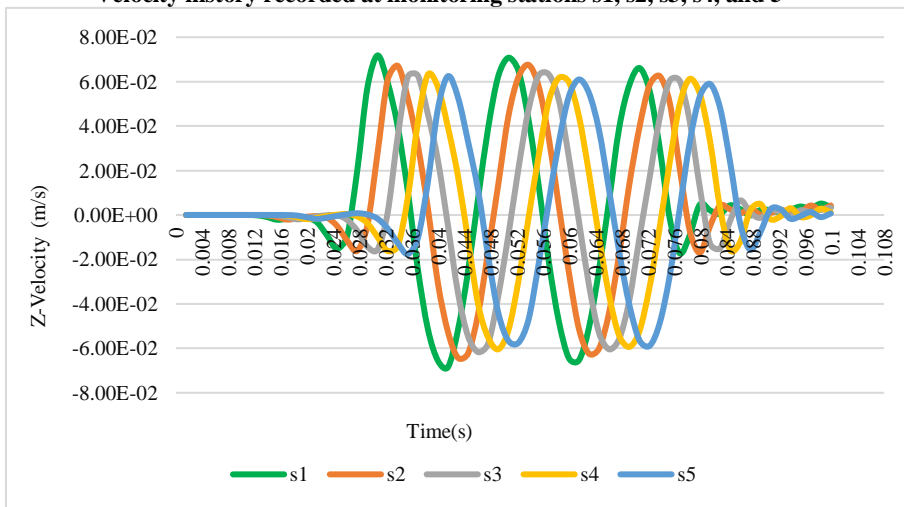


PSD of the velocity history recorded at monitoring stations s6, s7, s8, s9, and s10

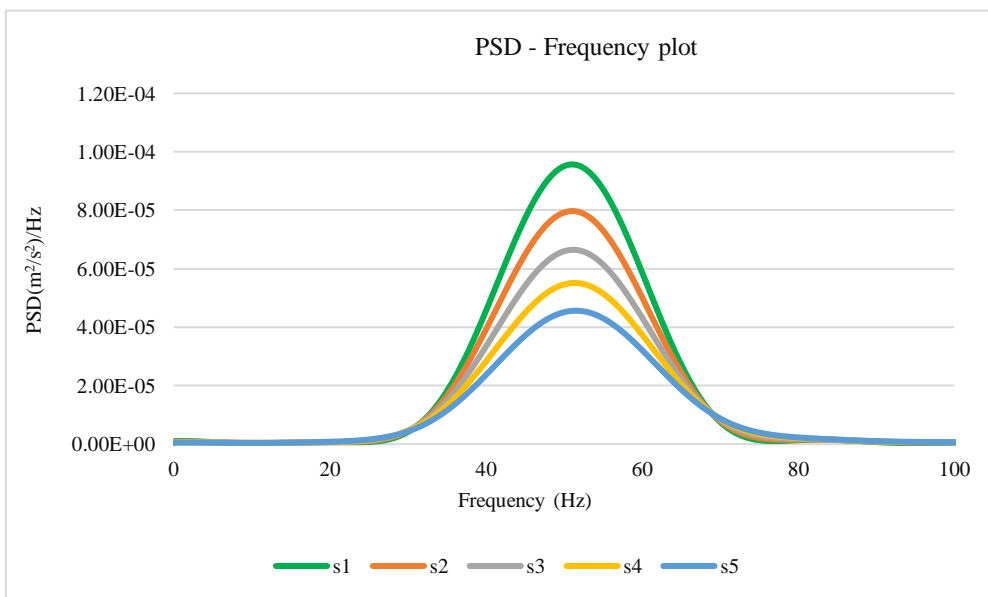


# Appendix

Velocity history recorded at monitoring stations s1, s2, s3, s4, and 5



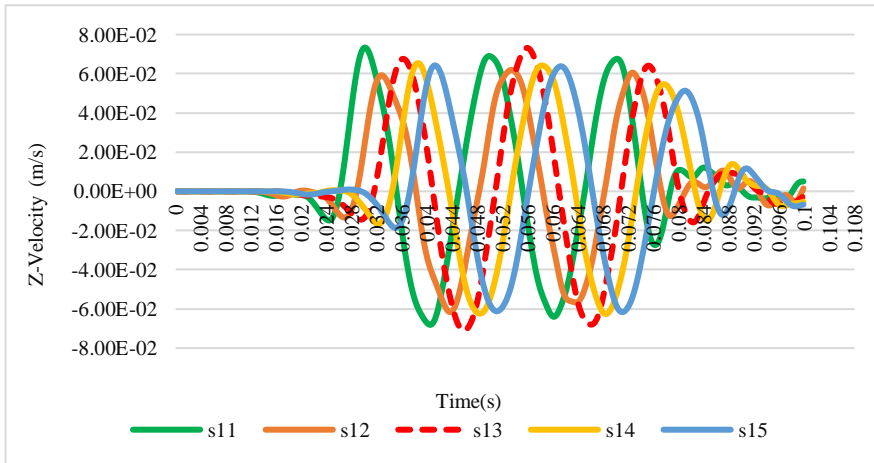
PSD of the velocity history recorded at monitoring stations s1, s2, s3, s4, and s5



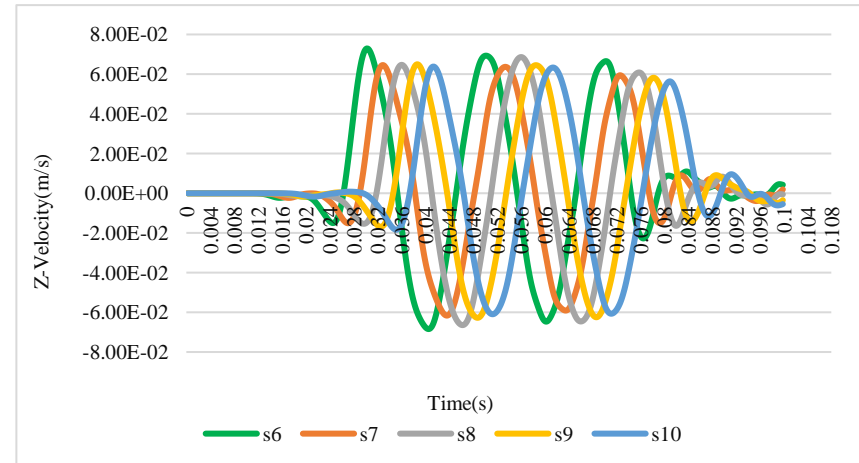
# Appendix

## B.2 First scenario (the object at 1m depth)

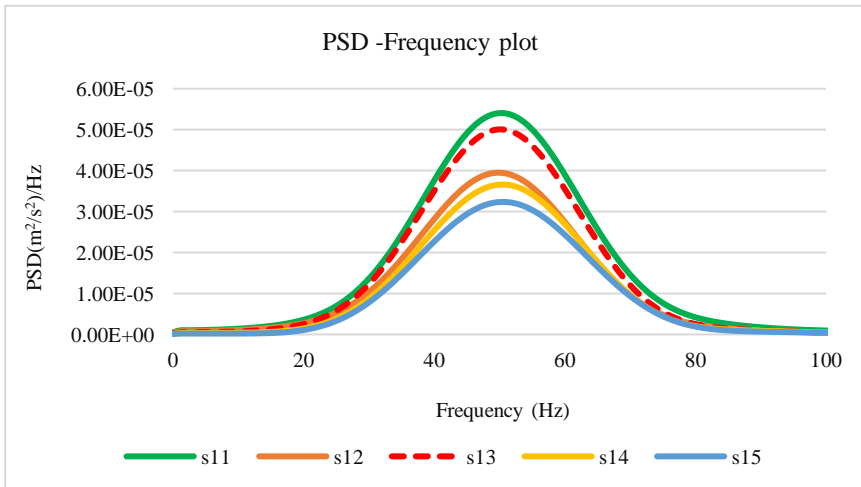
Velocity history recorded at monitoring stations s11, s12, s13, s14, and 15



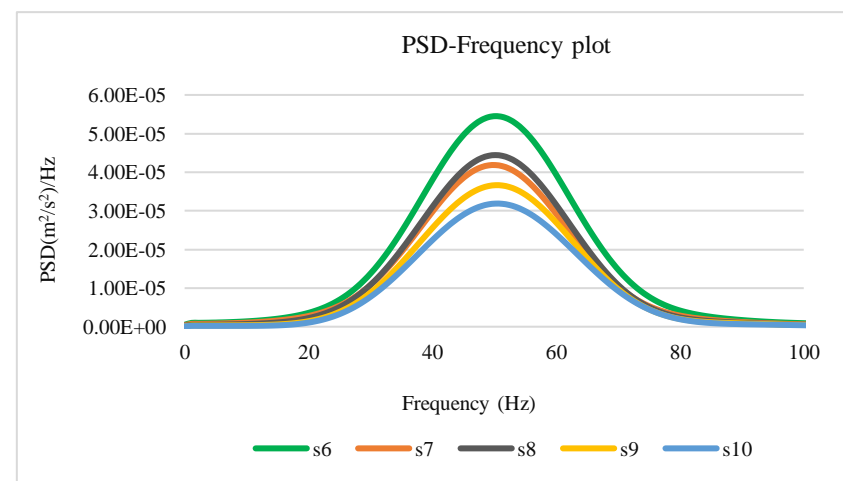
Velocity history recorded at monitoring stations s6, s7, s8, s9, and 10



PSD of the velocity history recorded at monitoring stations s11, s12, s13, s14, and s15

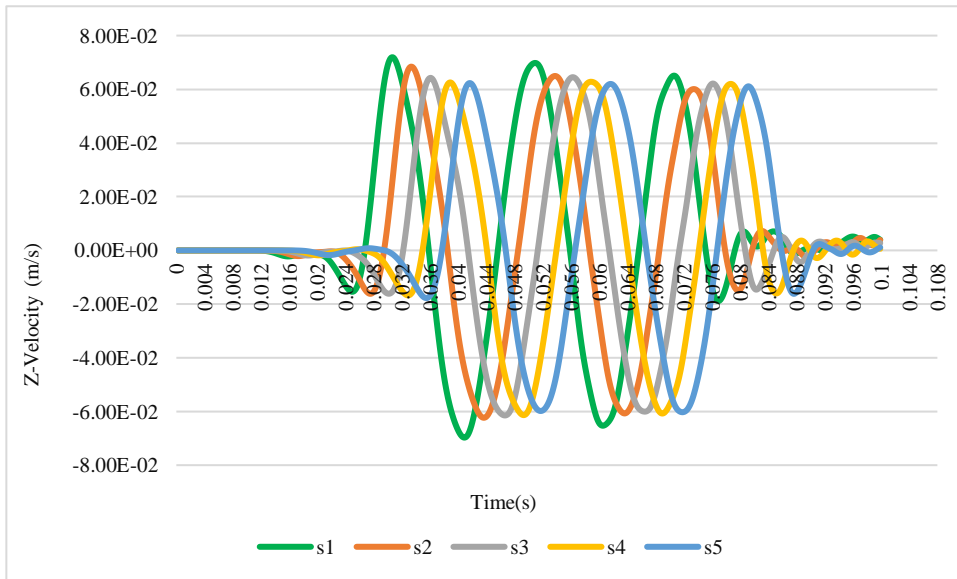


PSD of the velocity history recorded at monitoring stations s6, s7, s8, s9, and s10

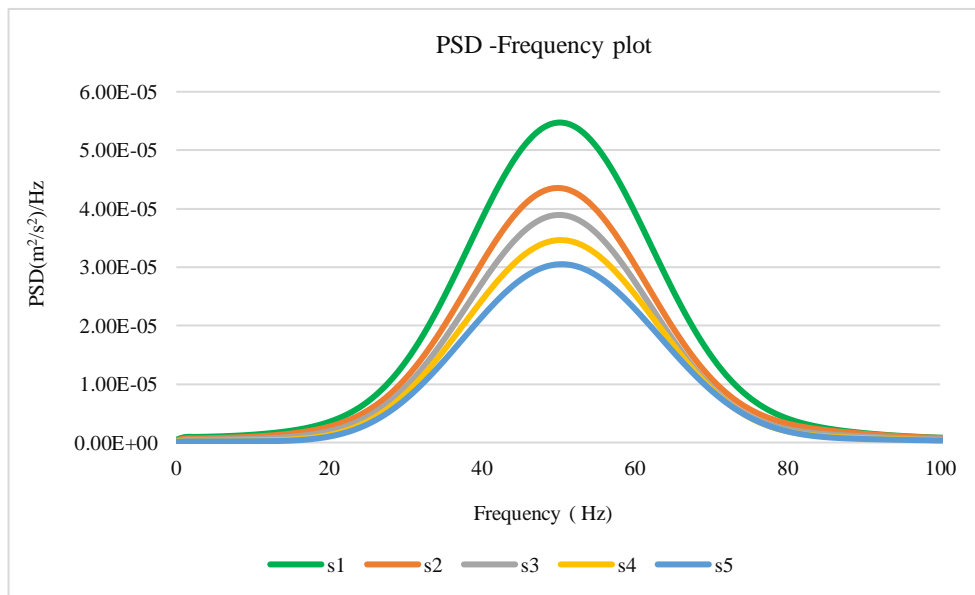


# Appendix

Velocity history recorded at monitoring stations s1, s2, s3, s4, and 5

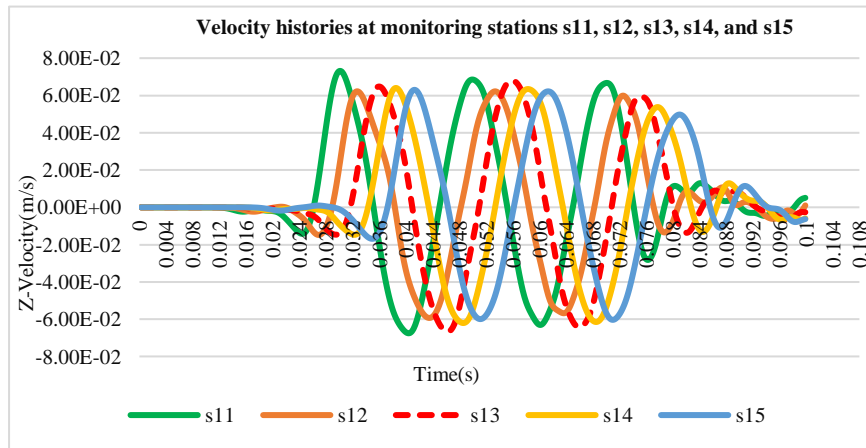


PSD of the velocity history recorded at monitoring stations s1, s2, s3, s4, and s5

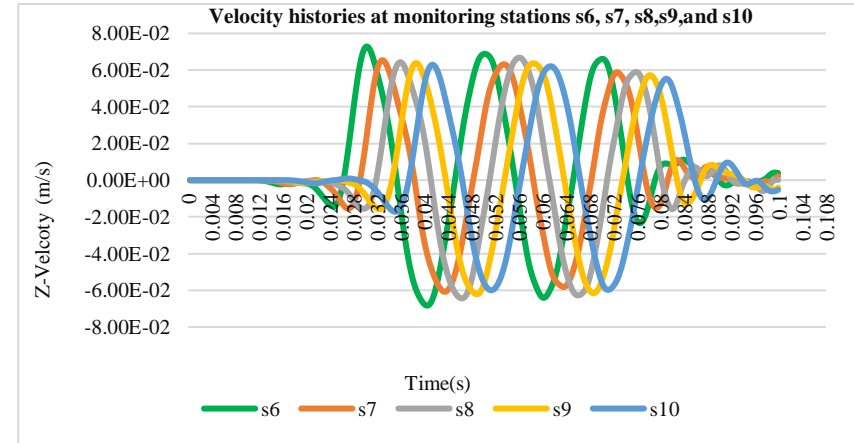
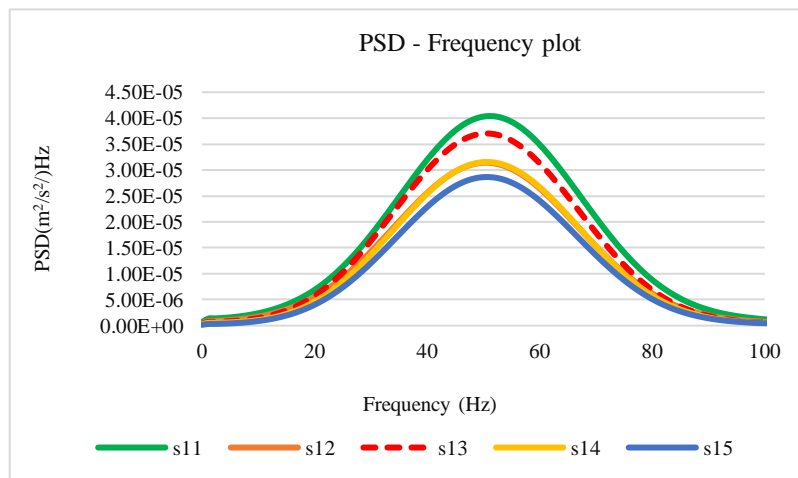


# Appendix

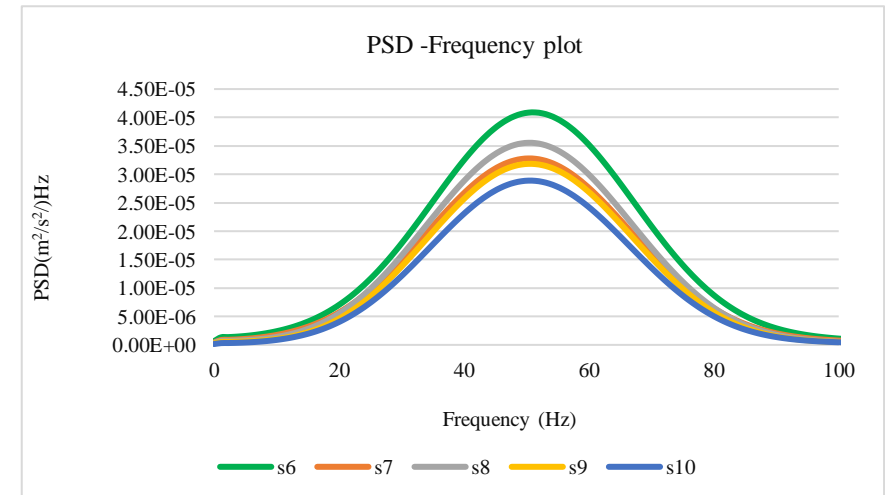
## B.3 Second scenario (the object at 2m depth)



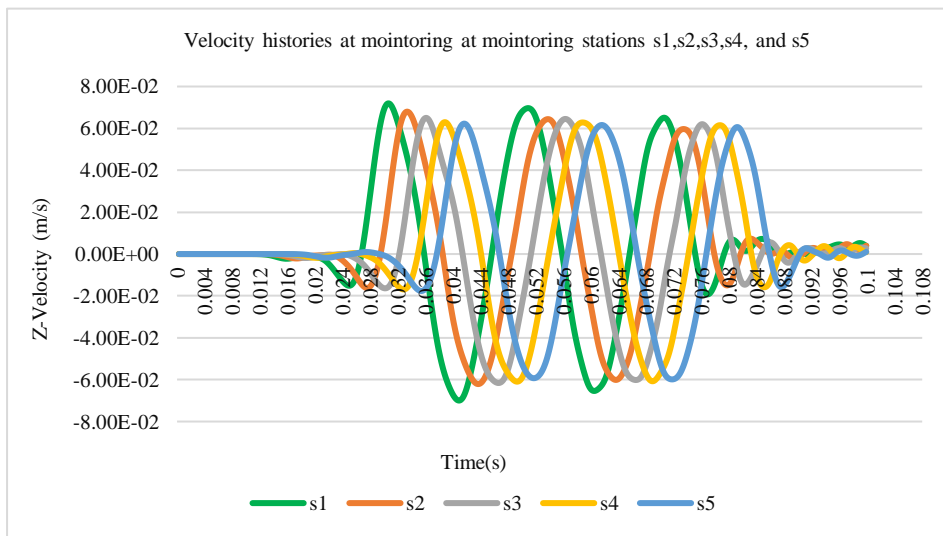
PSD of the velocity history recorded at monitoring stations s11, s12, s13, s14, and s15



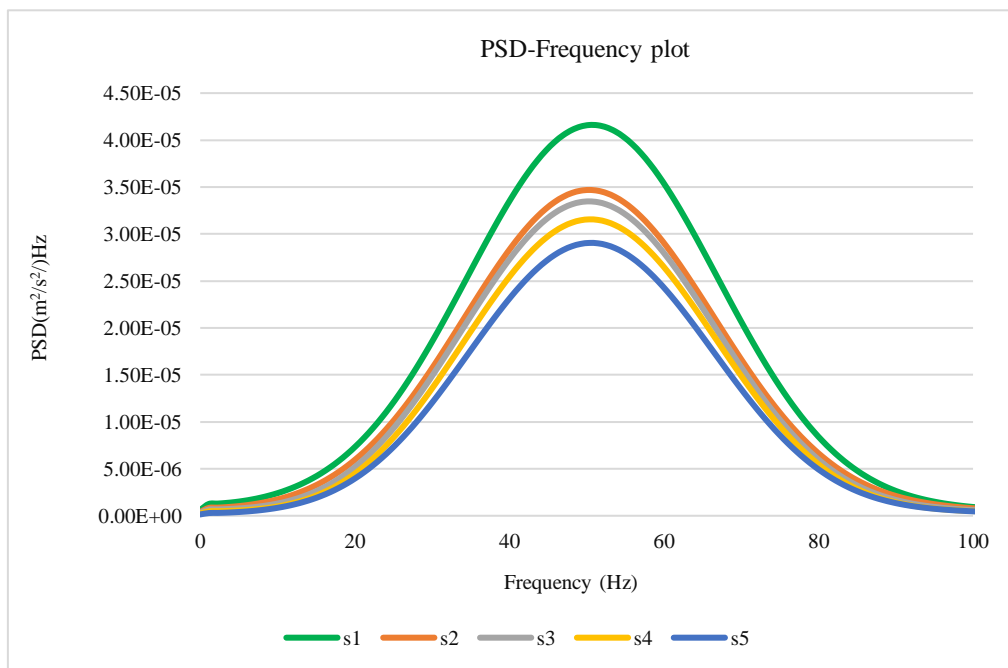
PSD of the velocity history recorded at monitoring stations s6, s7, s8, s9, and s10



# Appendix

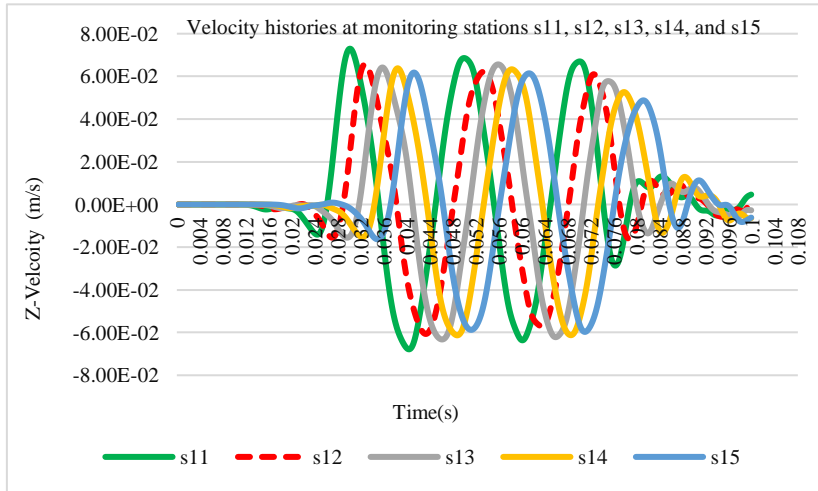


PSD of the velocity history recorded at monitoring stations s1, s2, s3, s4, and s5

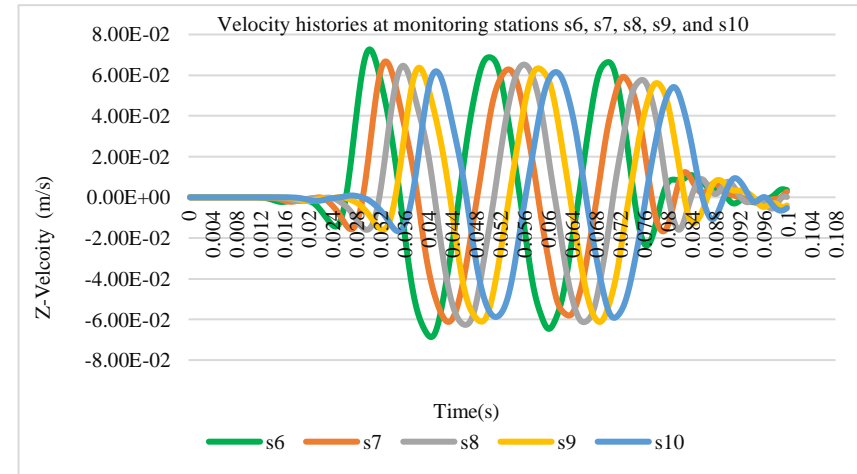
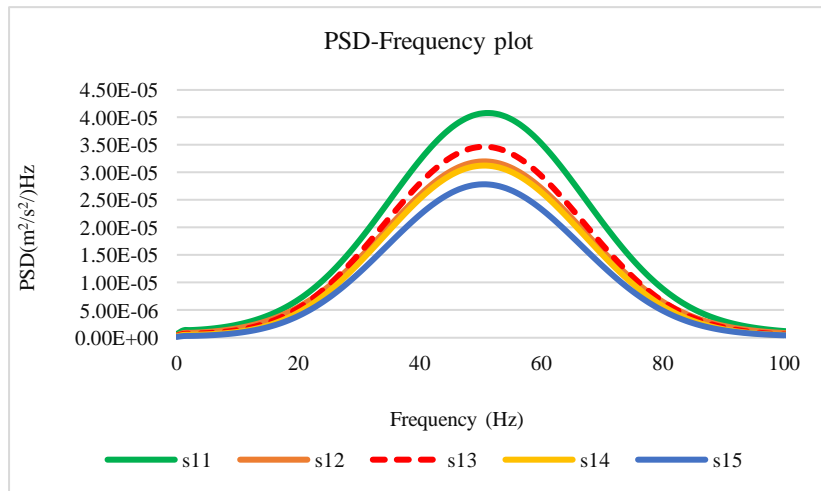


# Appendix

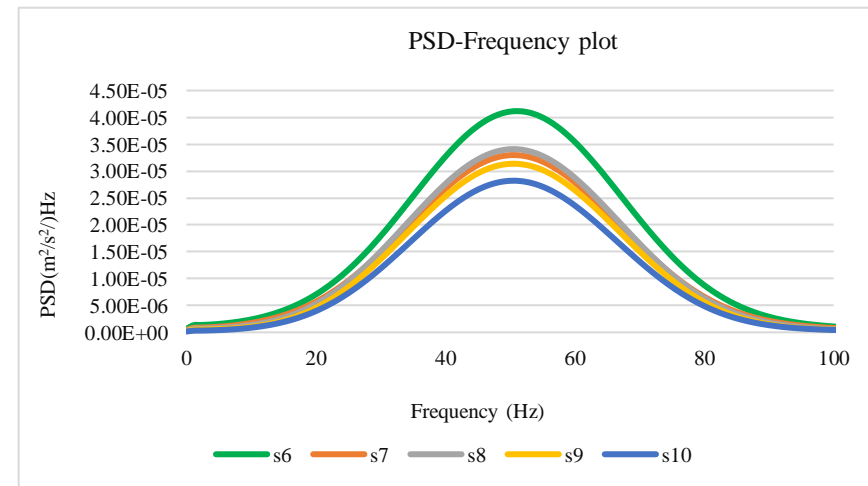
## B.4 Third scenario (the object at 3m depth)



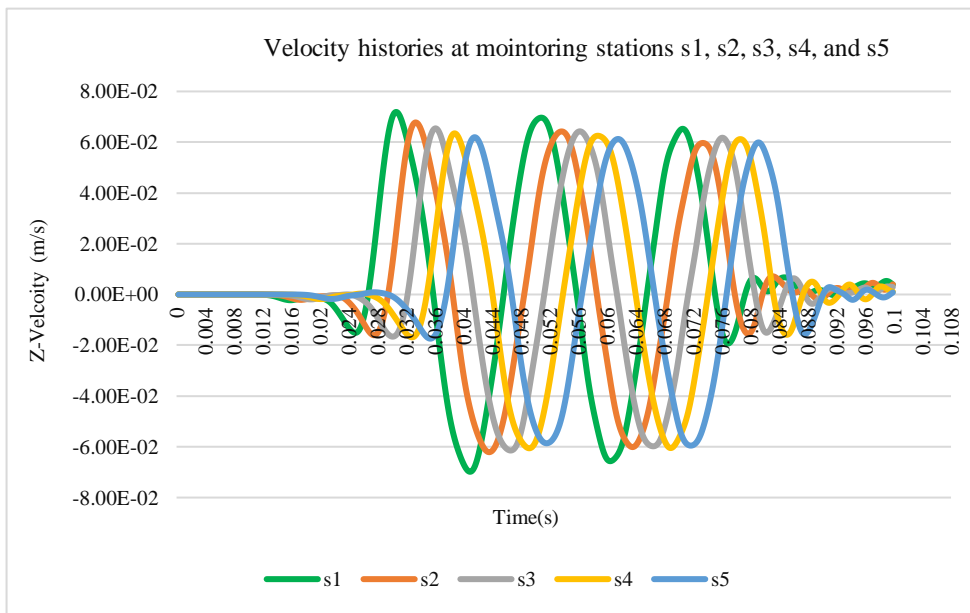
PSD of the velocity history recorded at monitoring stations s11, s12, s13, s14, and s15



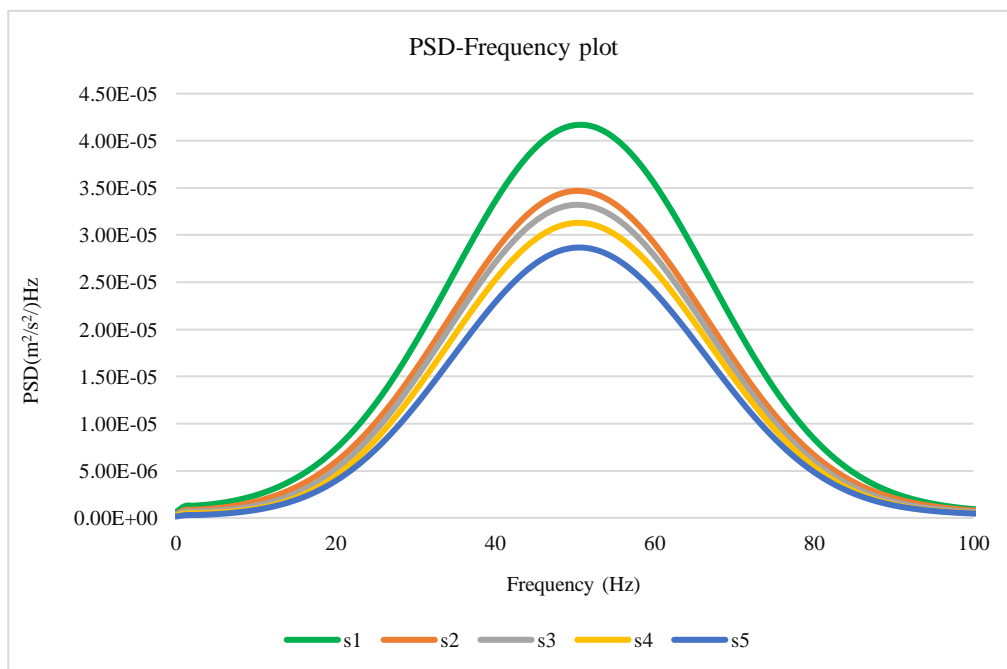
PSD of the velocity history recorded at monitoring stations s6, s7, s8, s9, and s10



# Appendix

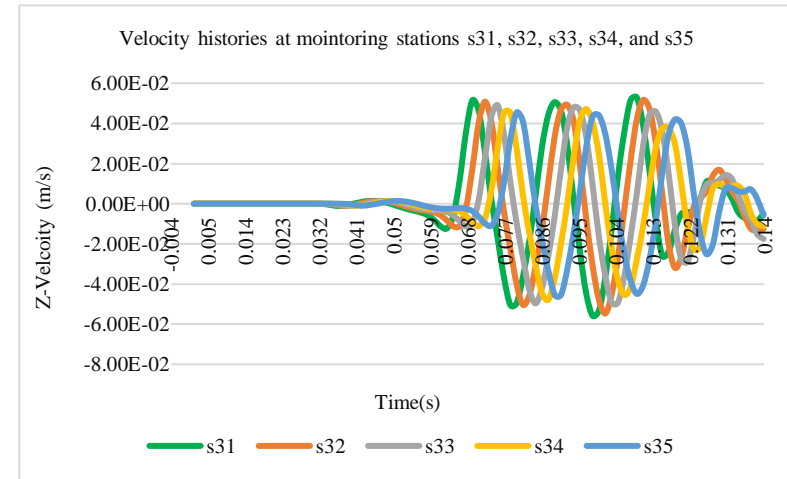
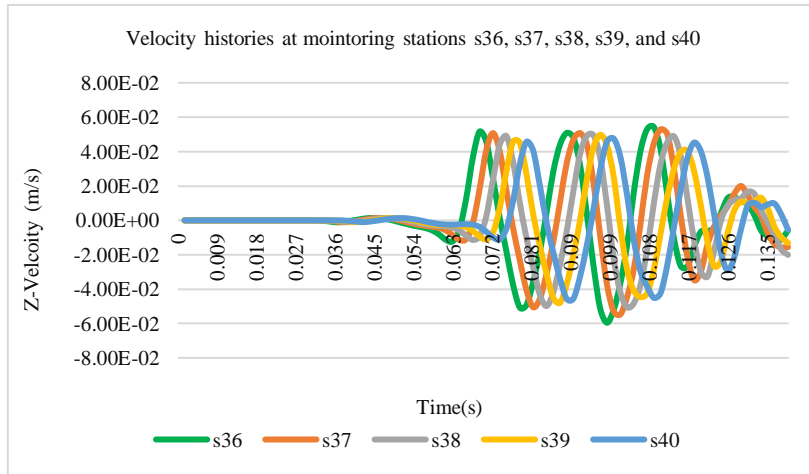


PSD of the velocity history recorded at monitoring stations s1, s2, s3, s4, and s5

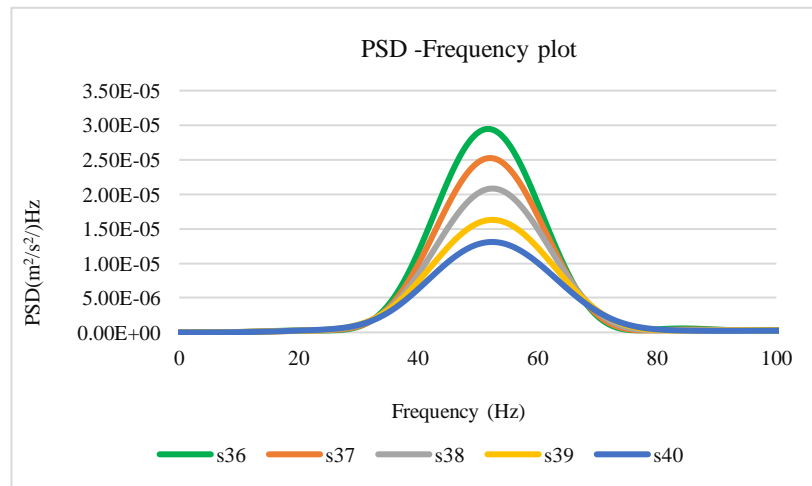


# Appendix

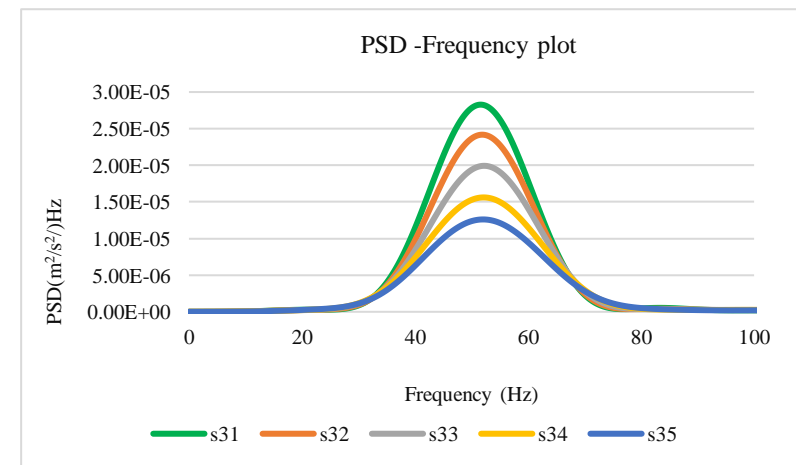
## B.5 Result and discussion of seismic wave simulation that was recoded from the homogenous model at site B.



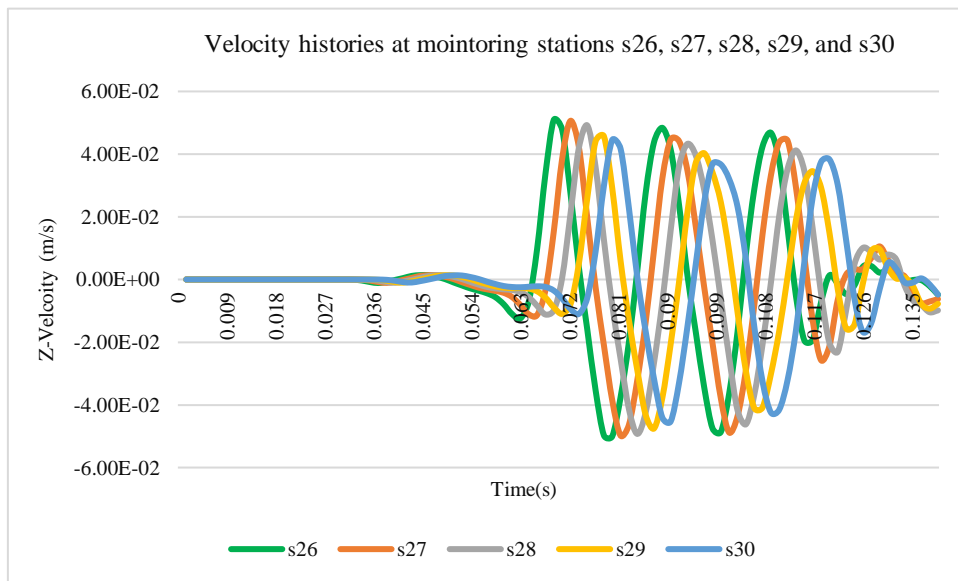
PSD of the velocity history recorded at monitoring stations s36, s37, s38, s39, and s40



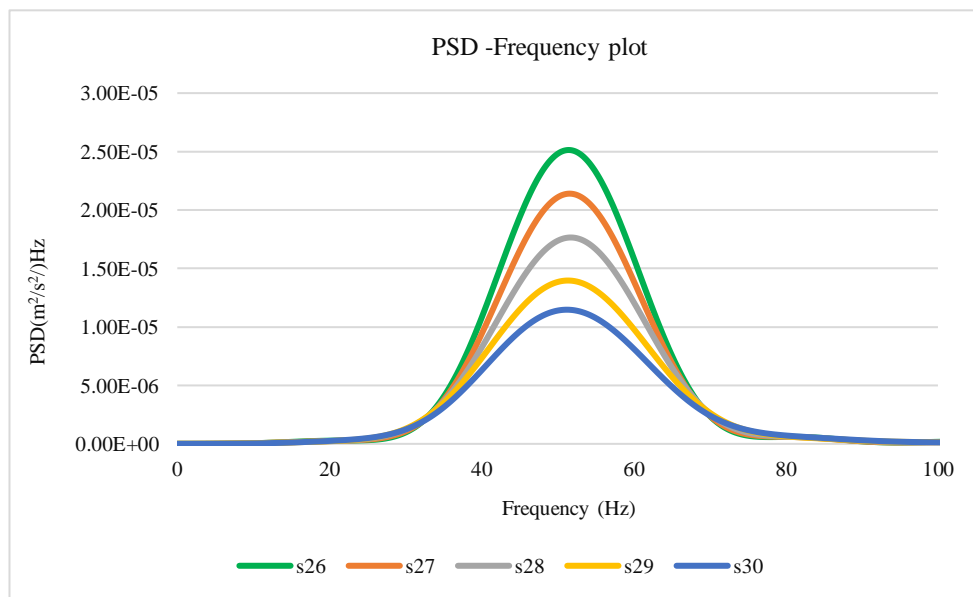
PSD of the velocity history recorded at monitoring stations s31, s32, s33, s34, and s35



# Appendix

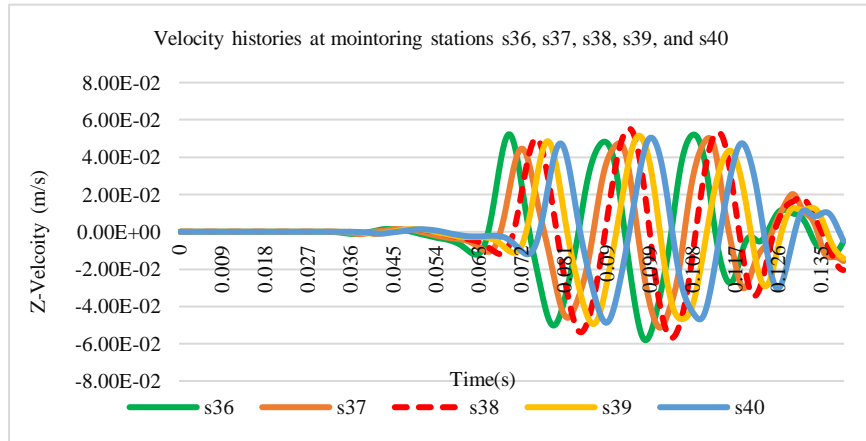


PSD of the velocity history recorded at monitoring stations s26, s27, s28, s29, and s30

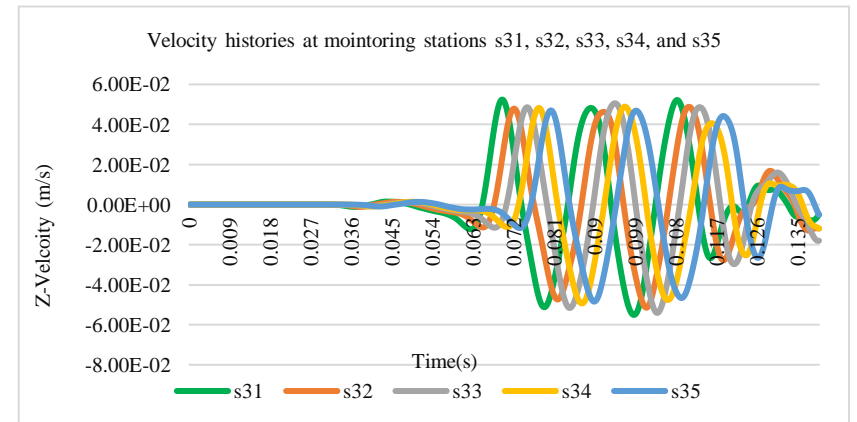
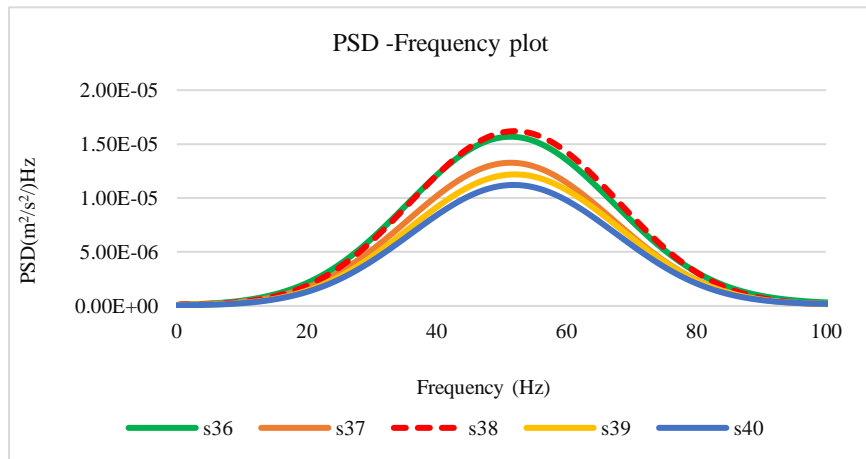


# Appendix

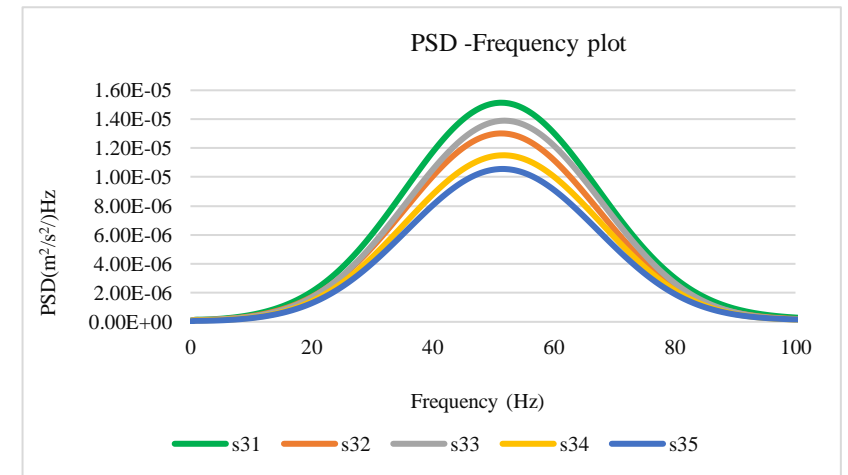
## B.6 First scenario (the object at 1m depth)



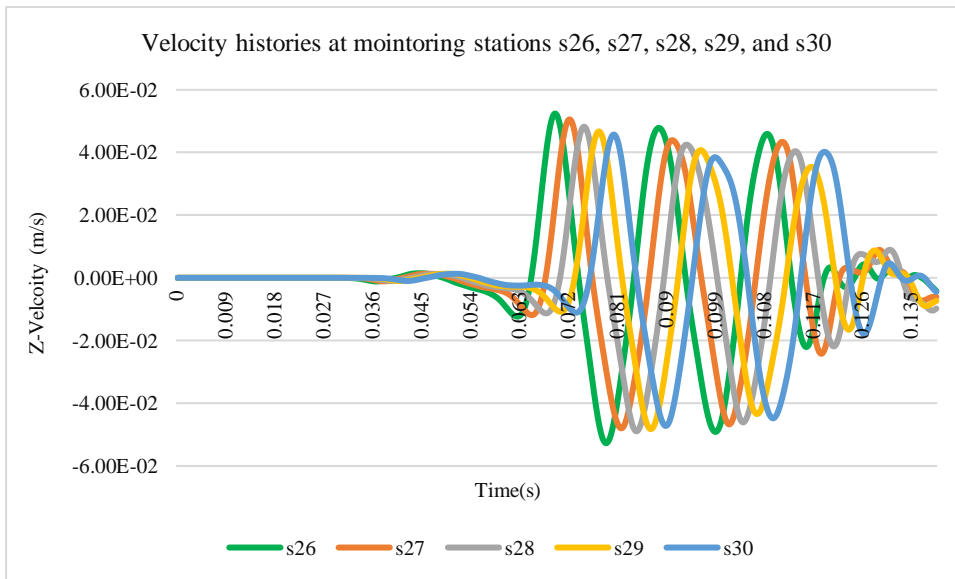
PSD of the velocity history recorded at monitoring stations s36, s37, s38, s39, and s40



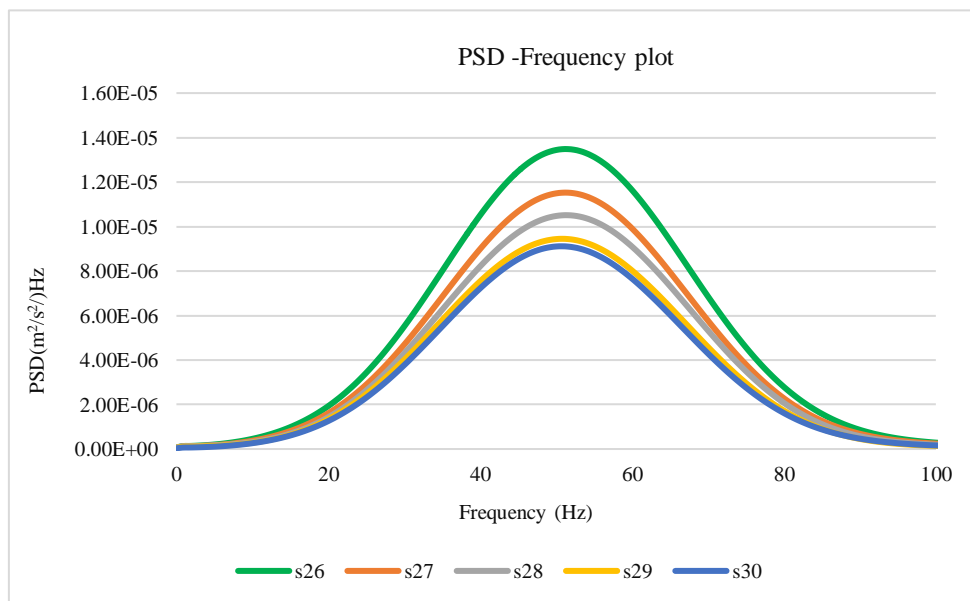
PSD of the velocity history recorded at monitoring stations s31, s32, s33, s34, and s35



# Appendix

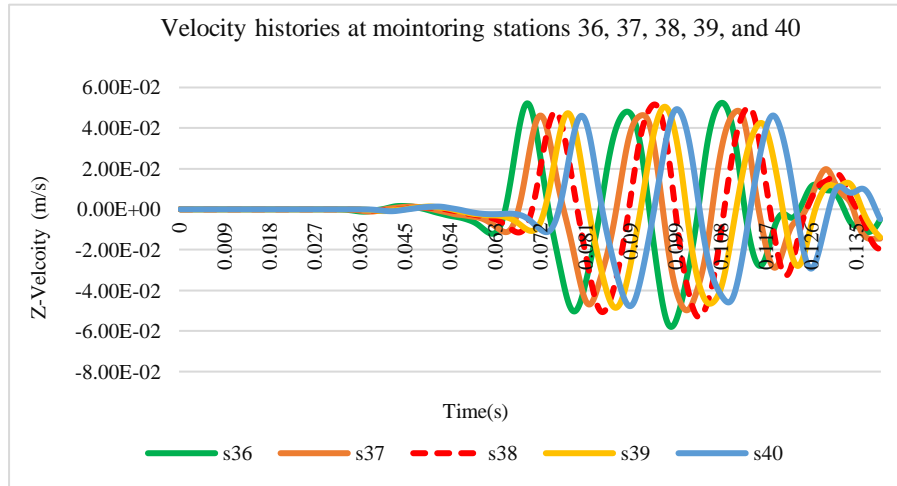


PSD of the velocity history recorded at monitoring stations s26, s27, s28, s29, and s30

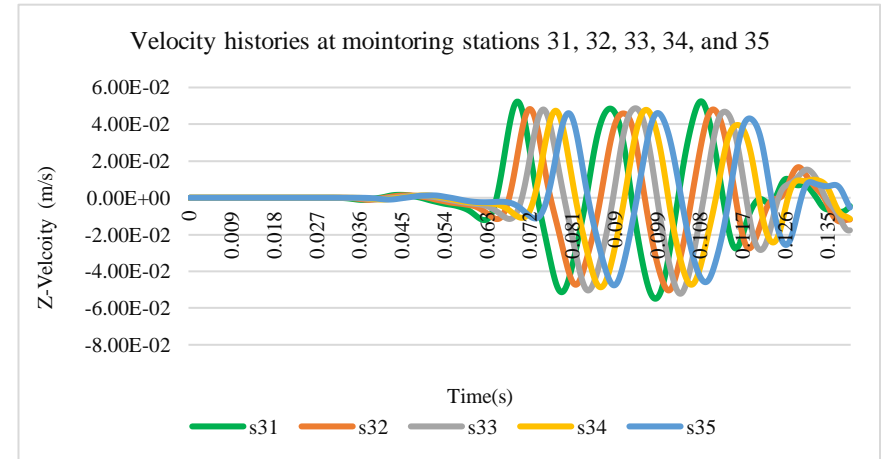
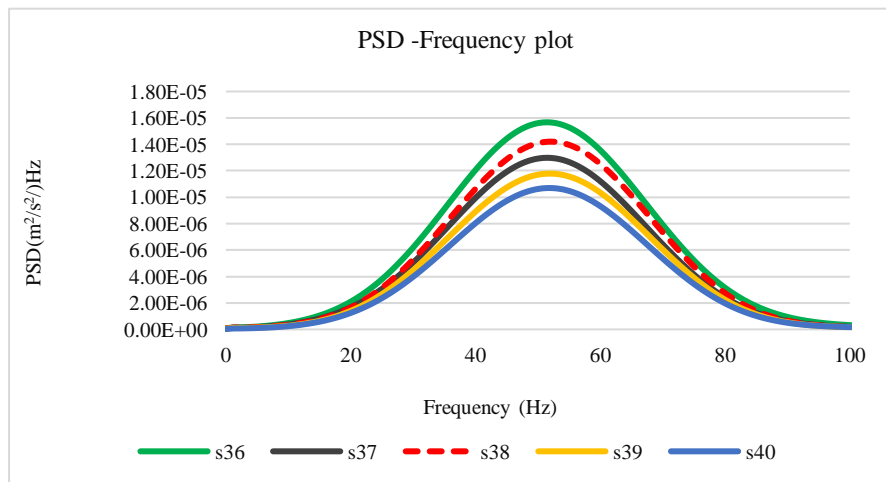


# Appendix

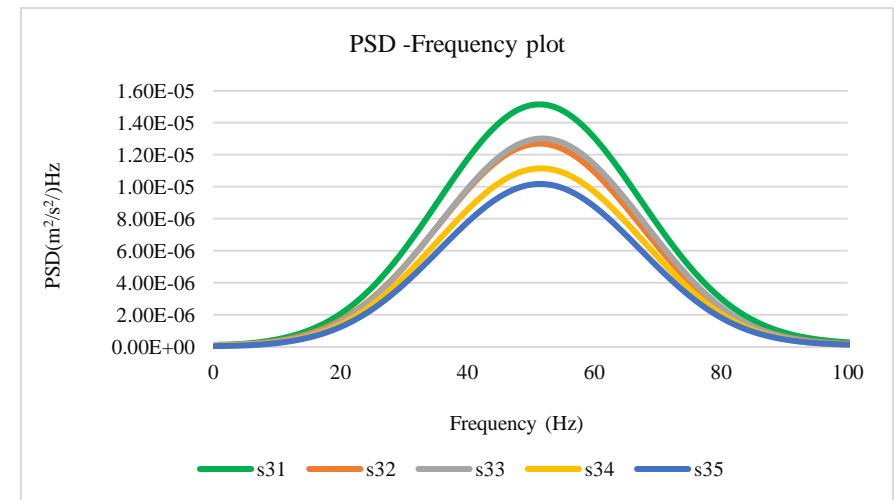
## B.7 Second scenario (the object at 2m depth)



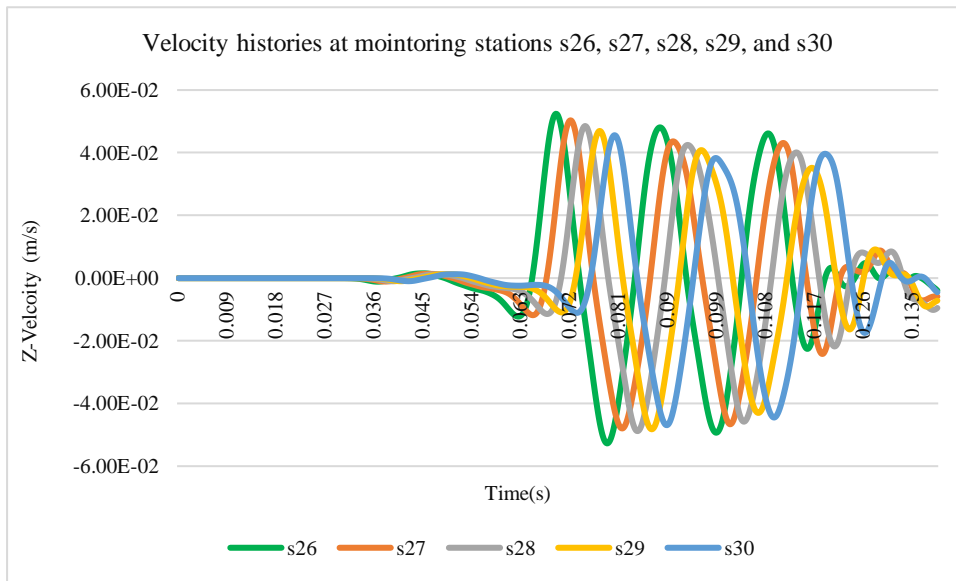
PSD of the velocity history recorded at monitoring stations s36, s37, s38, s39, and s40



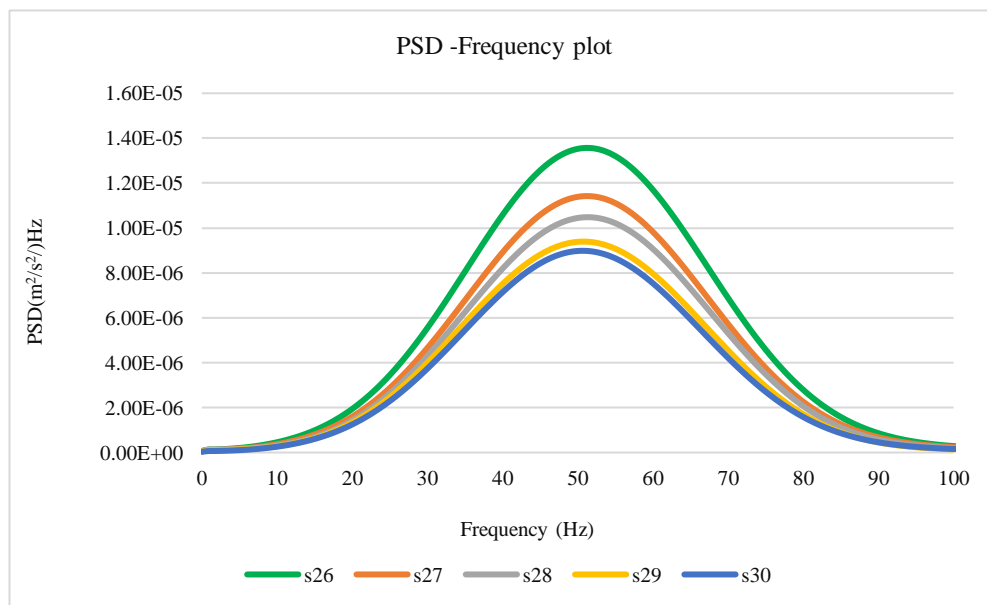
PSD of the velocity history recorded at monitoring stations s31, s32, s33, s34, and s35



# Appendix

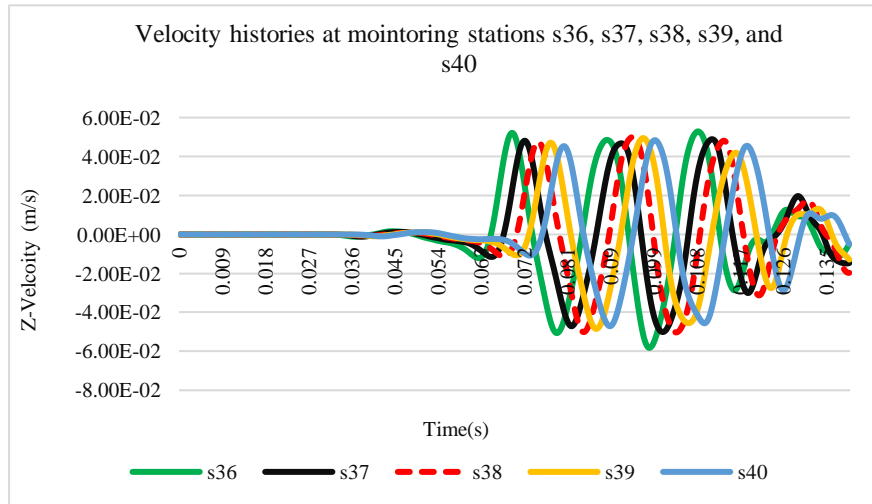


PSD of the velocity history recorded at monitoring stations s26, s27, s28, s29, and s30

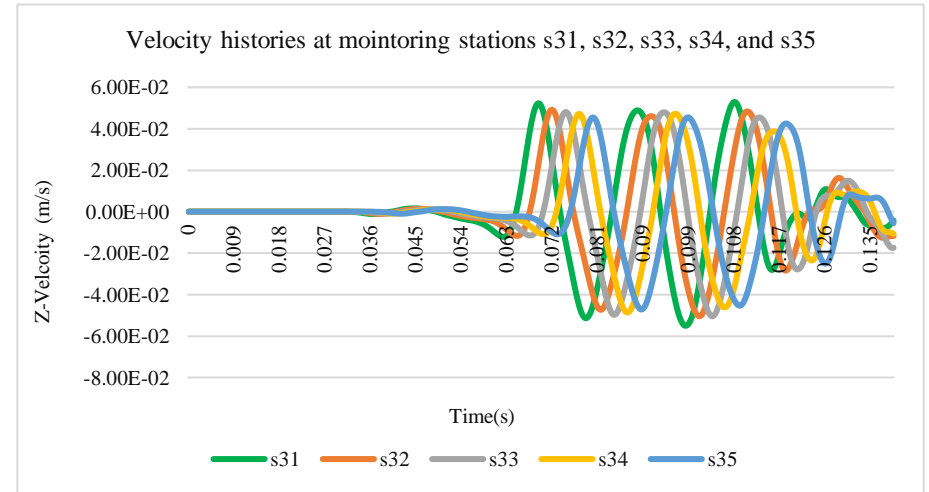
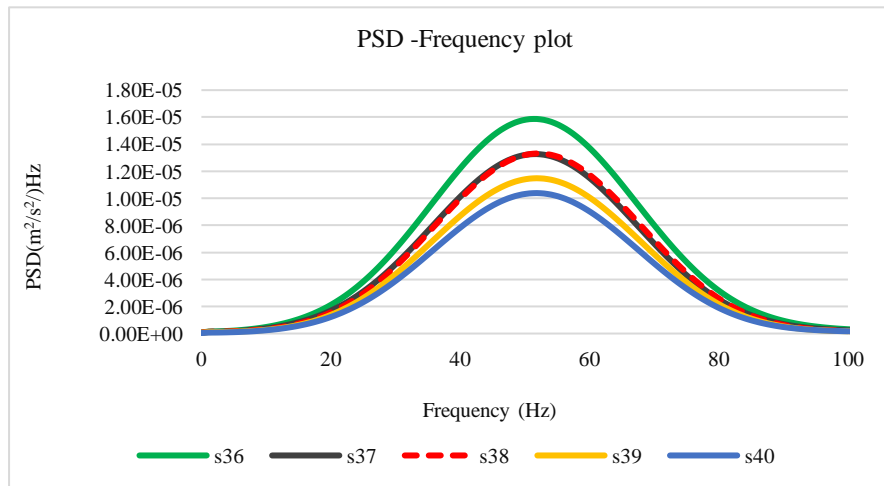


# Appendix

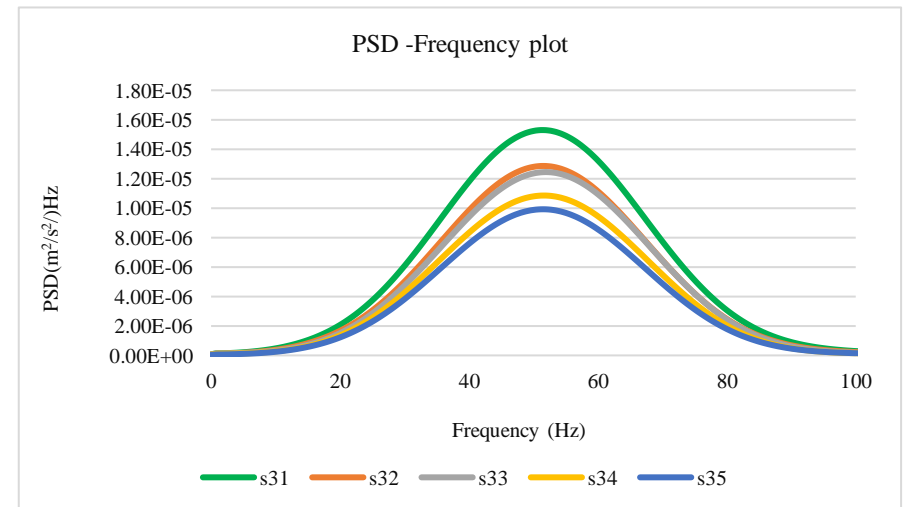
## B.8 Third scenario (the object at 3m depth)



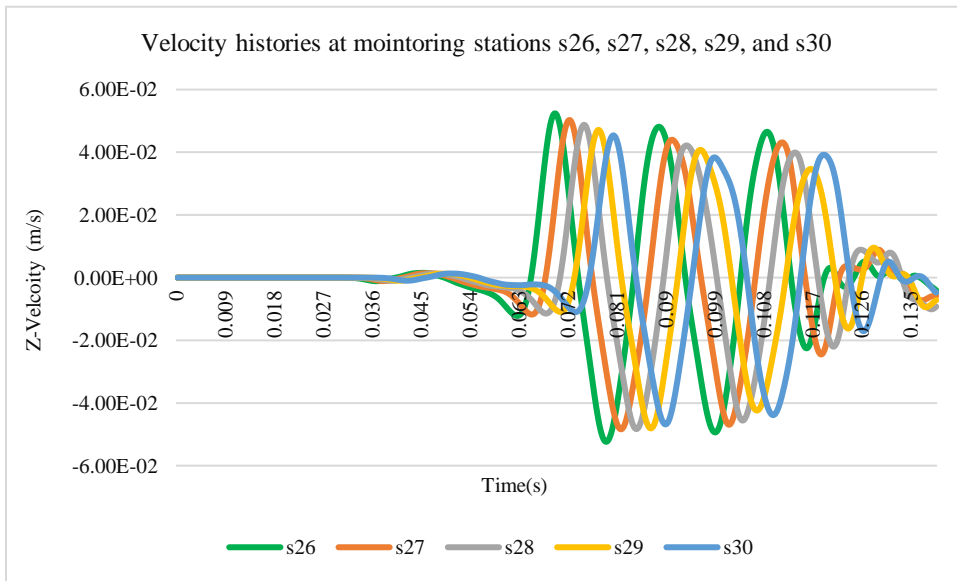
PSD of the velocity history recorded at monitoring stations s36, s37, s38, s39, and s40



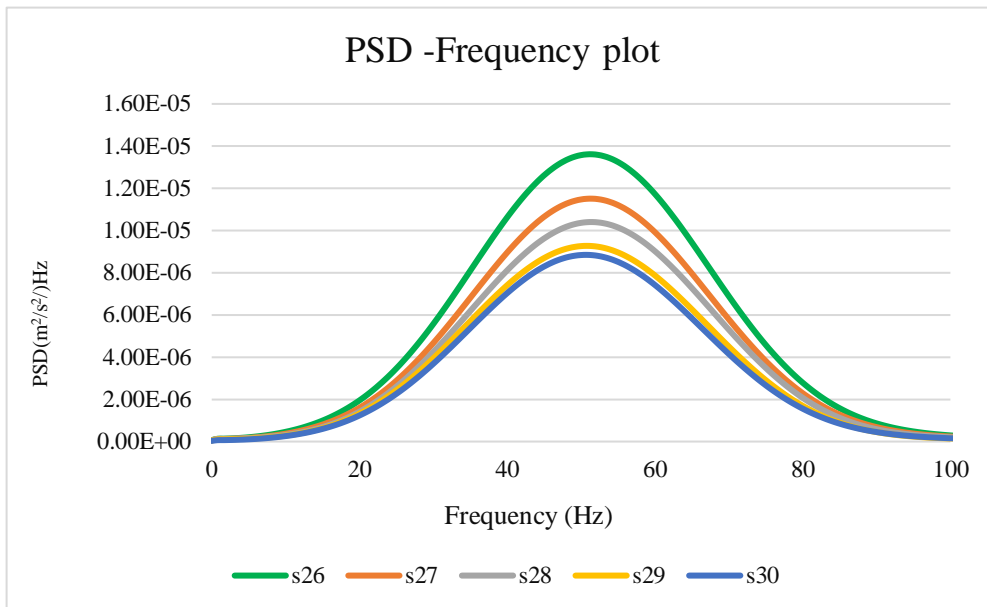
PSD of the velocity history recorded at monitoring stations s31, s32, s33, s34, and s35



# Appendix



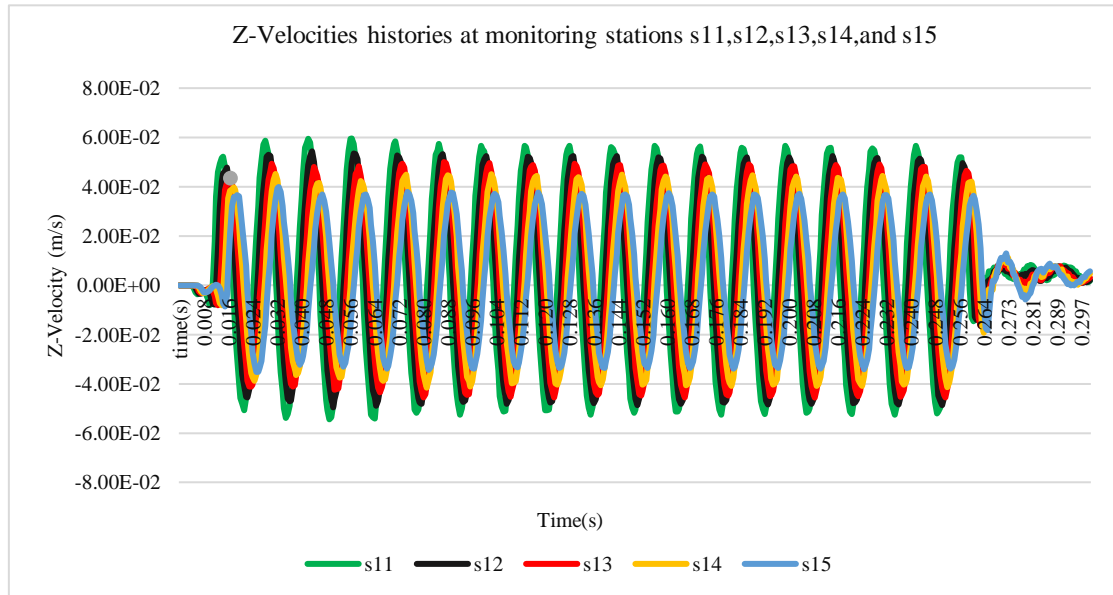
PSD of the velocity history recorded at monitoring stations s26, s27, s28, s29, and s30



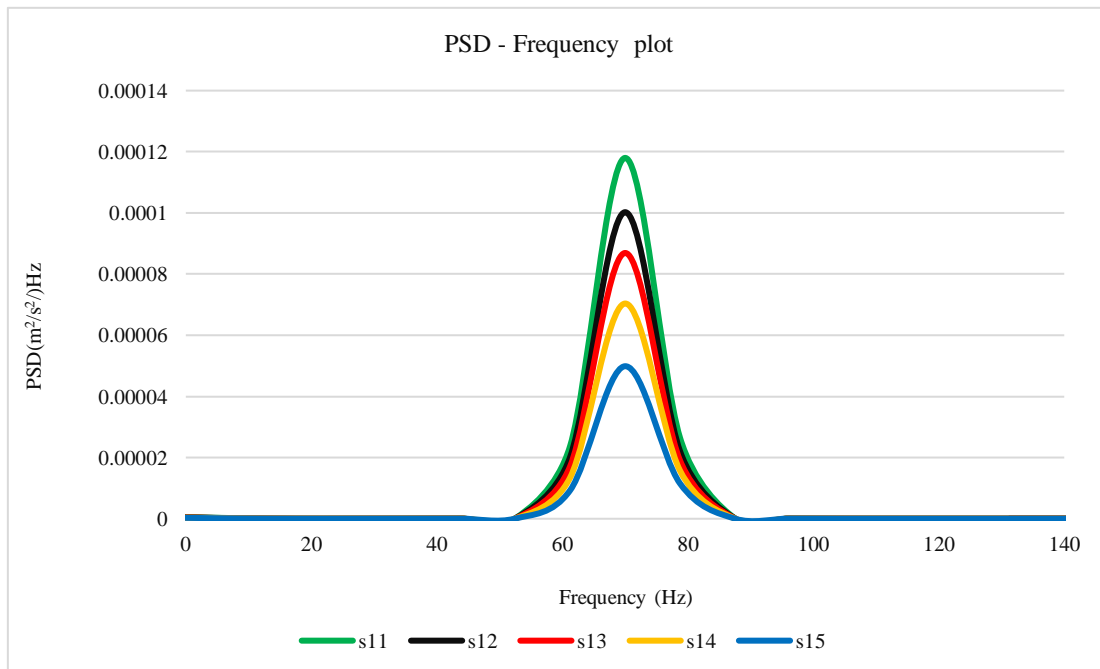
# Appendix

## C Numerical simulation of seismic waves propagation through media (Model 4)

### C.1 Seismic wave simulation that was recorded from the homogenous model at site A.

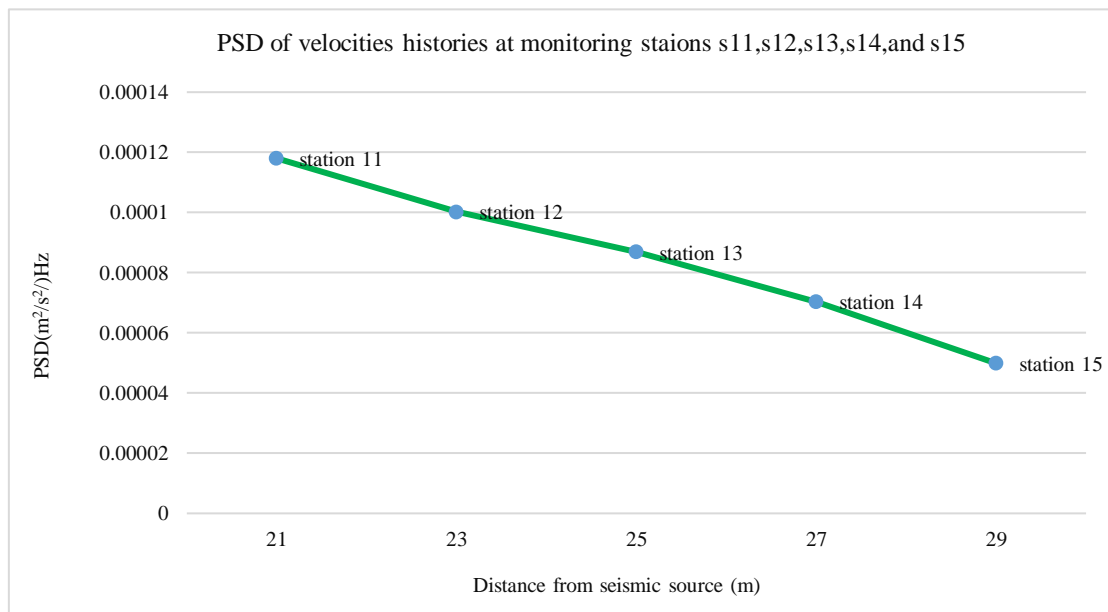


PSD of the velocity history recorded at monitoring stations s11, s12, s13, s14, and s15



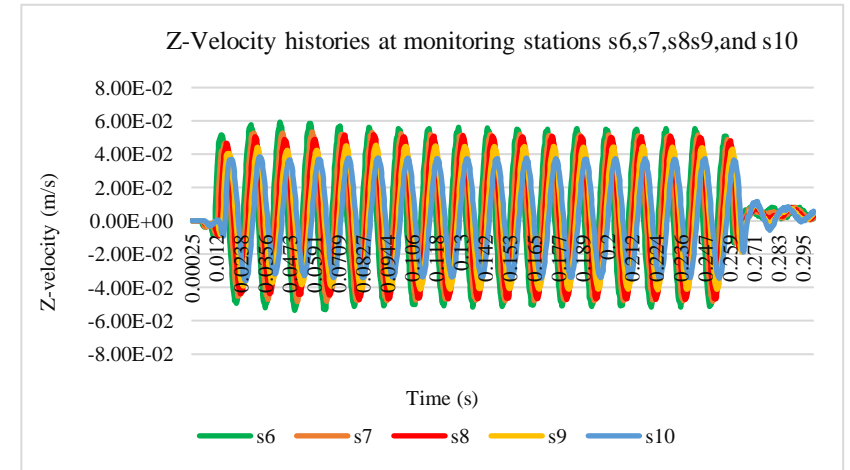
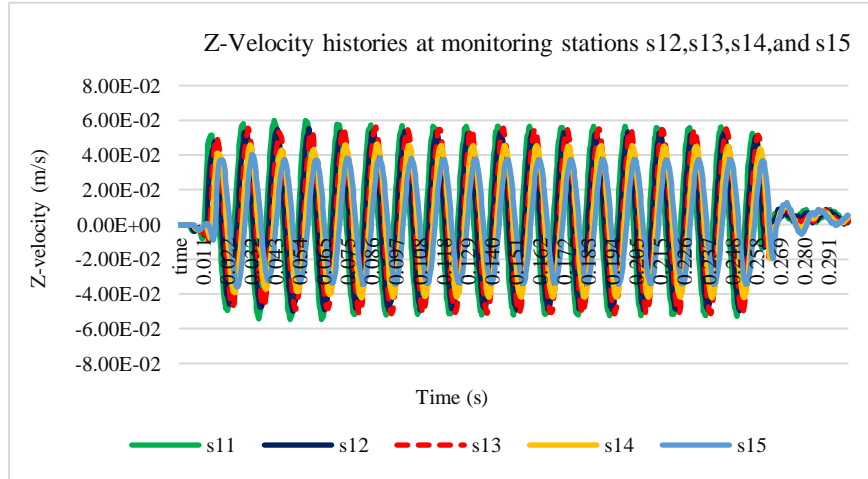
# Appendix

---

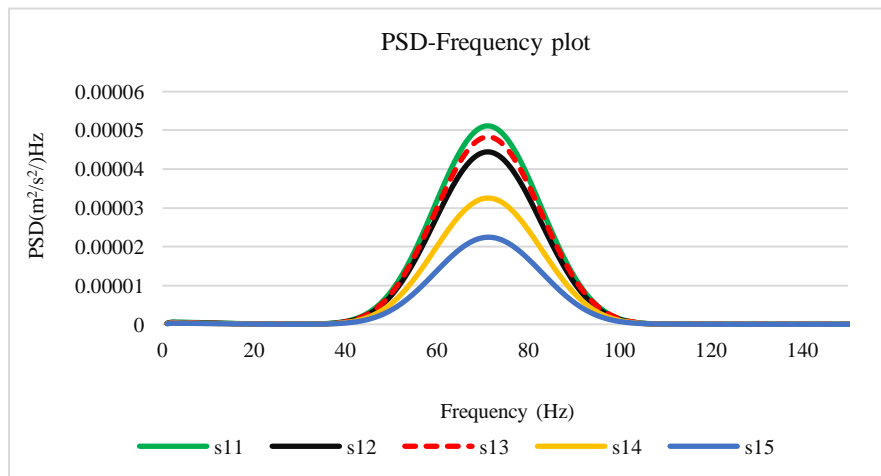


# Appendix

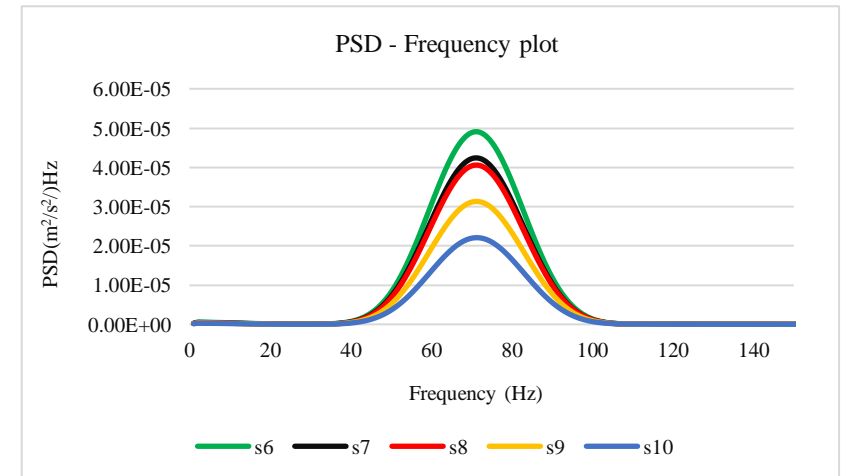
## C.2 First scenario (the object at 1m depth)



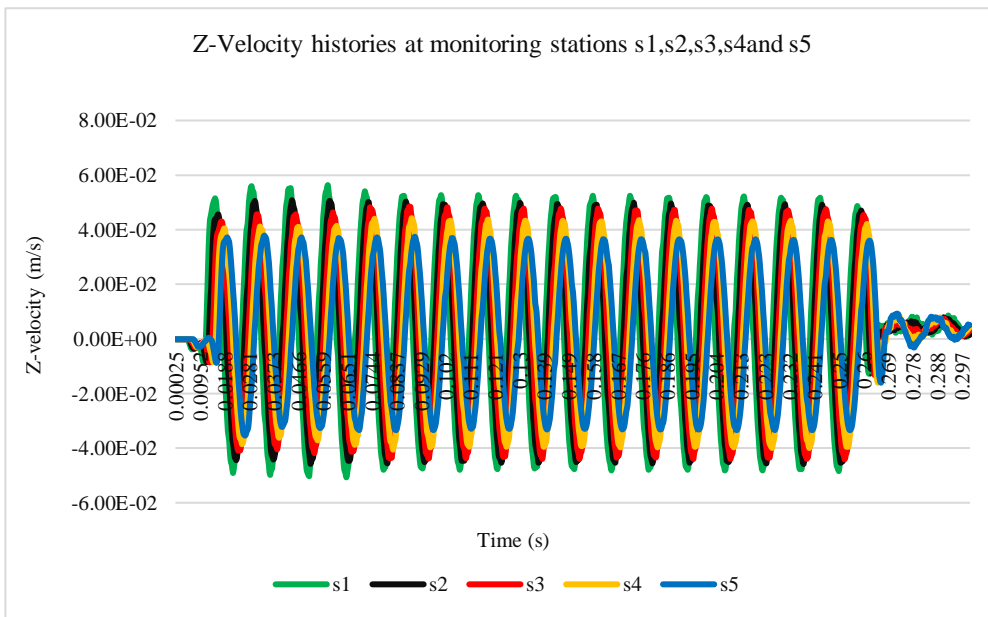
PSD of the velocity history recorded at monitoring stations s11, s12, s13, s14, and s15



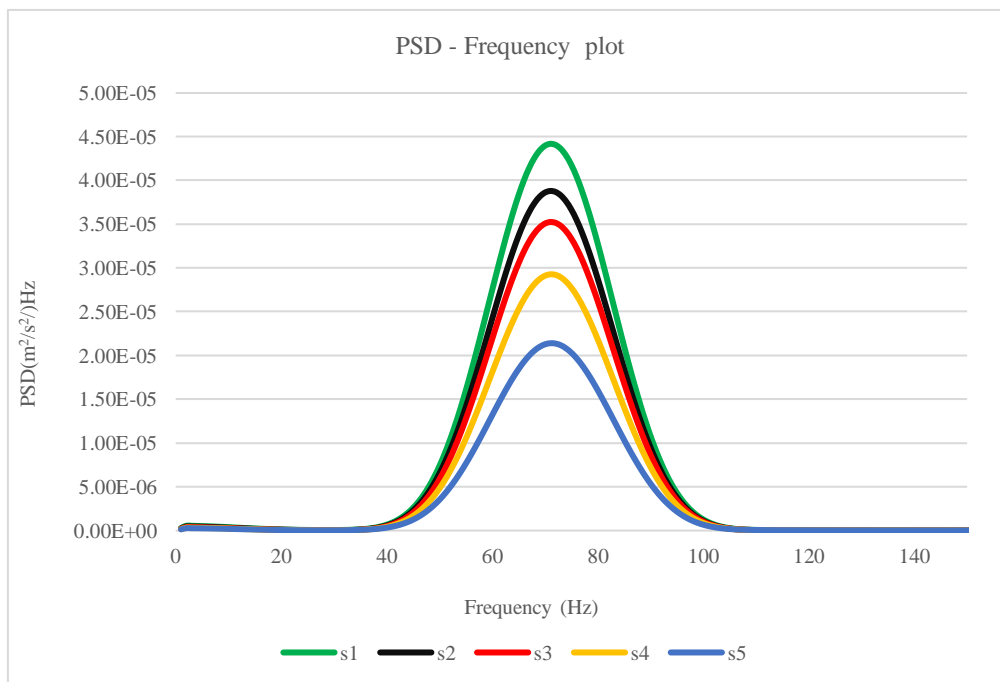
PSD of the velocity history recorded at monitoring stations s6, s7, s8, s9, and s10



# Appendix

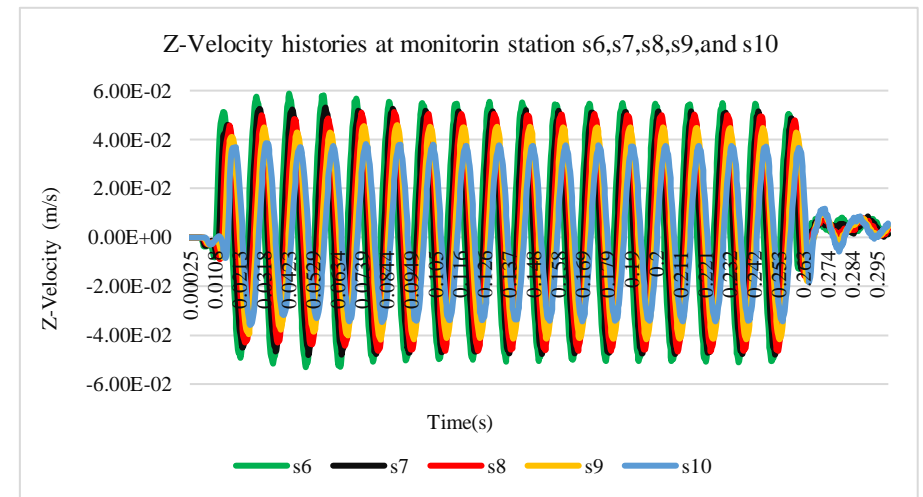
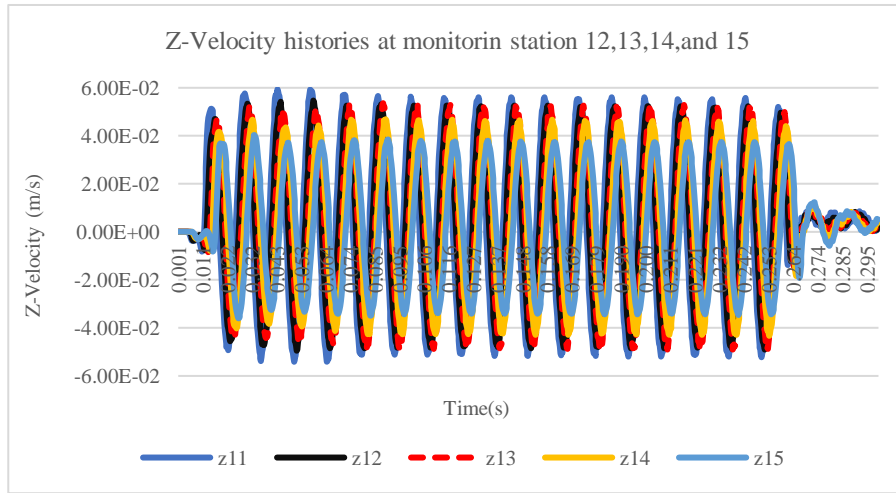


PSD of the velocity history recorded at monitoring stations s1, s2, s3, s4, and s5

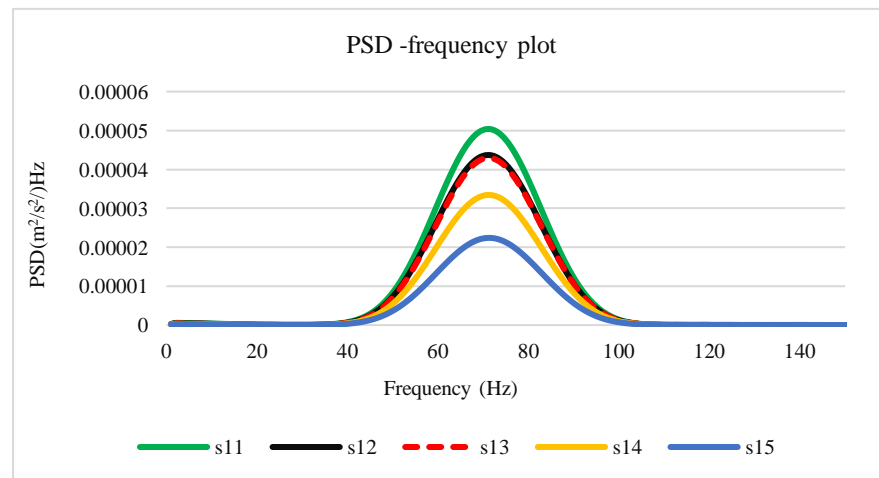


# Appendix

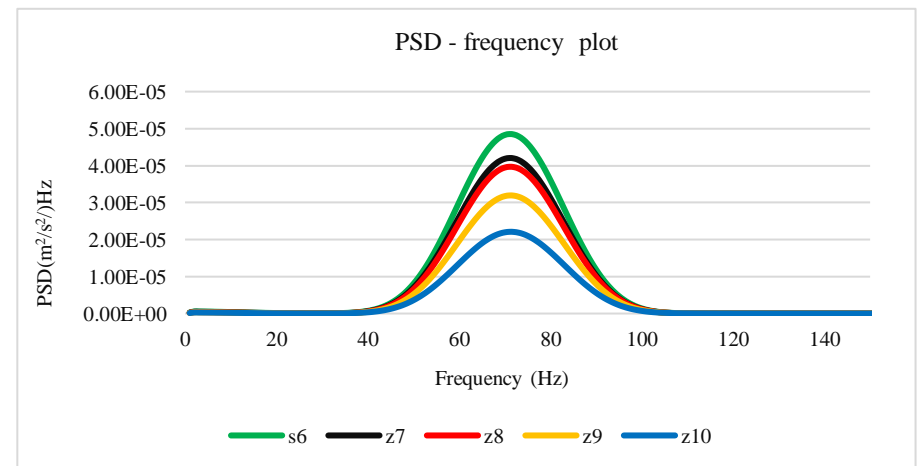
## C.3 Second scenario (the object at 2m depth)



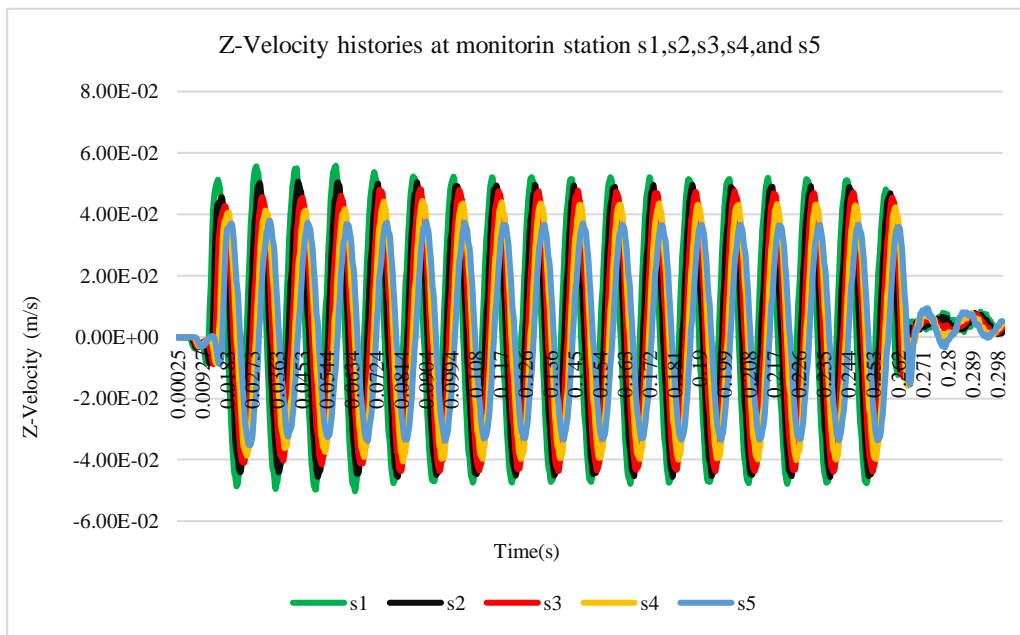
PSD of the velocity history recorded at monitoring stations s11, s12, s13, s14, and s15



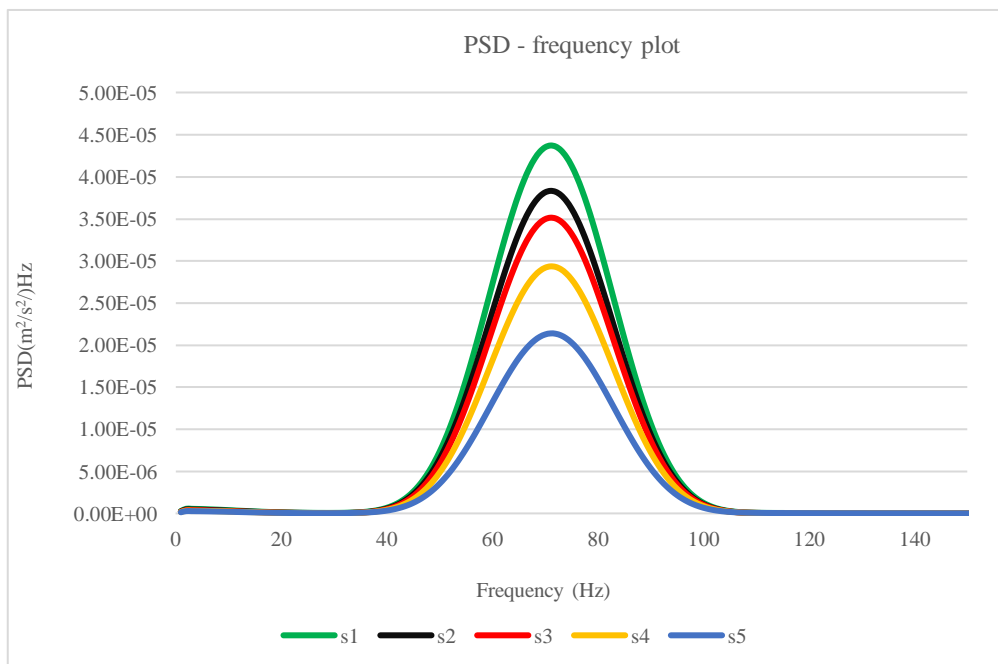
PSD of the velocity history recorded at monitoring stations s6, s7, s8, s9, and s10



# Appendix

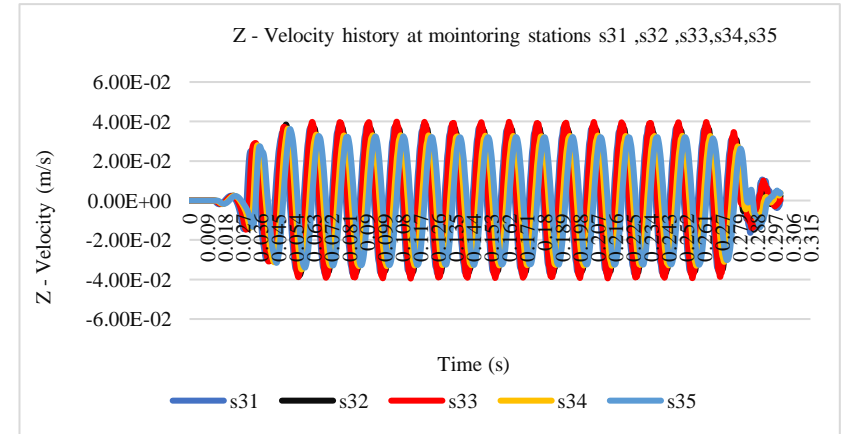
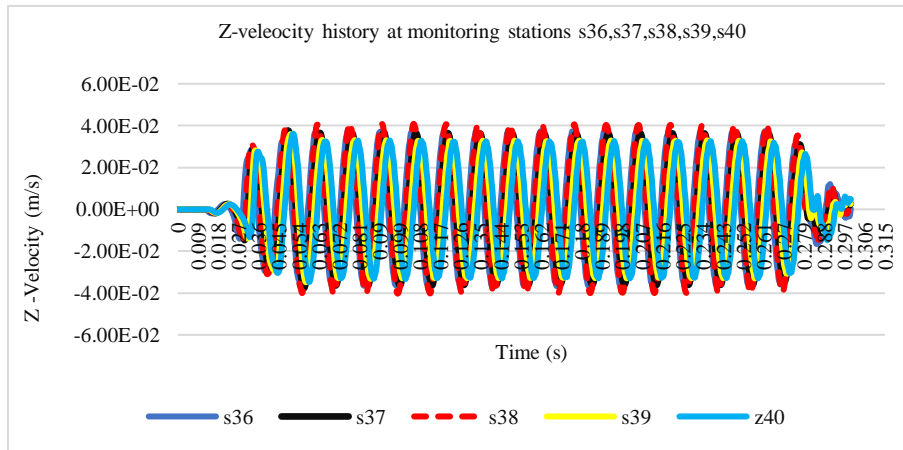


PSD of the velocity history recorded at monitoring stations s1, s2, s3, s4, and s5

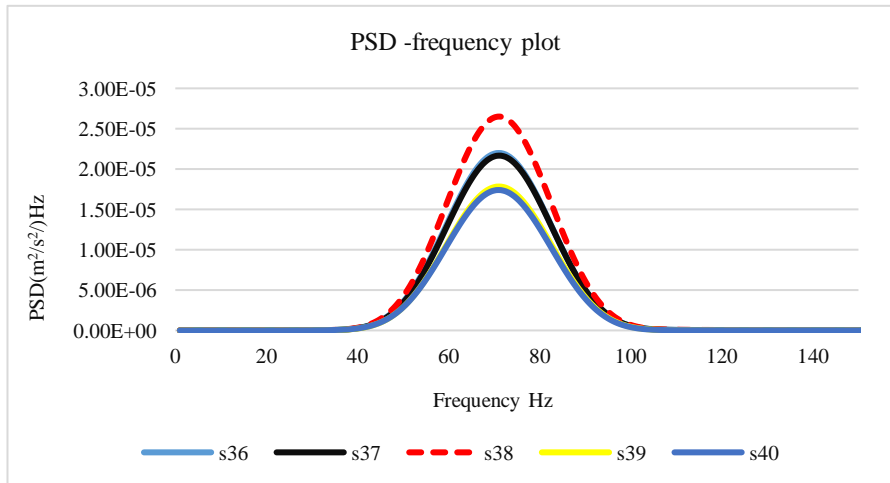


# Appendix

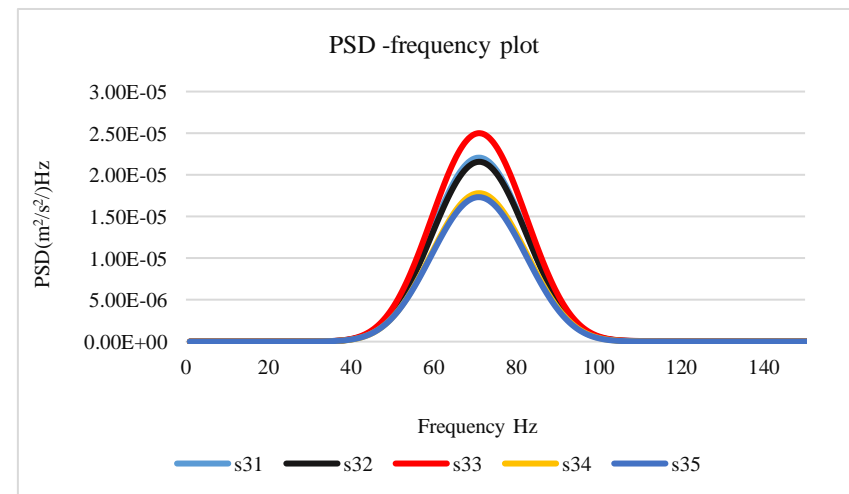
## C.4 First scenario (the object at 1m depth)



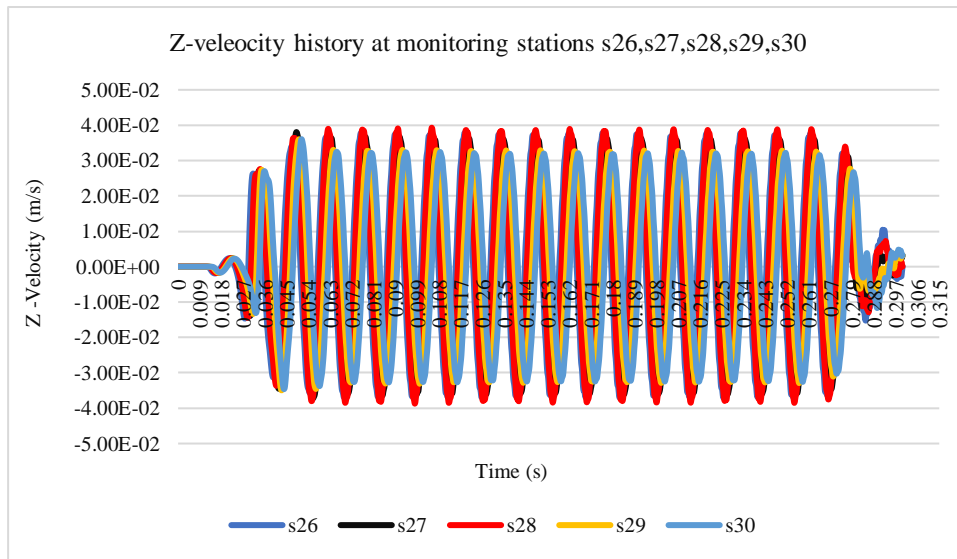
PSD of the velocity history recorded at monitoring stations s36, s37, s38, s39, and s40



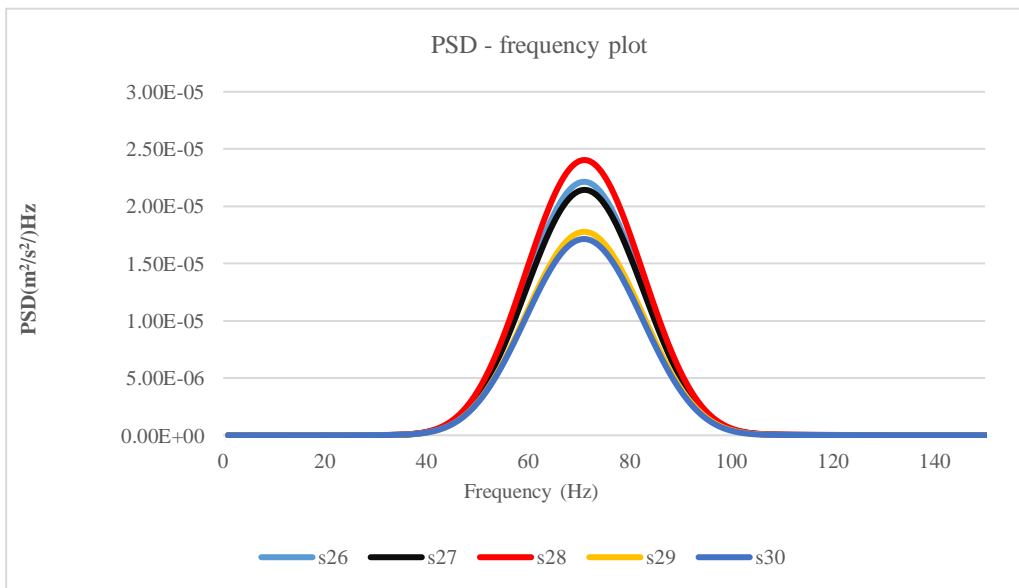
PSD of the velocity history recorded at monitoring stations s31, s32, s33, s34, and s35



# Appendix

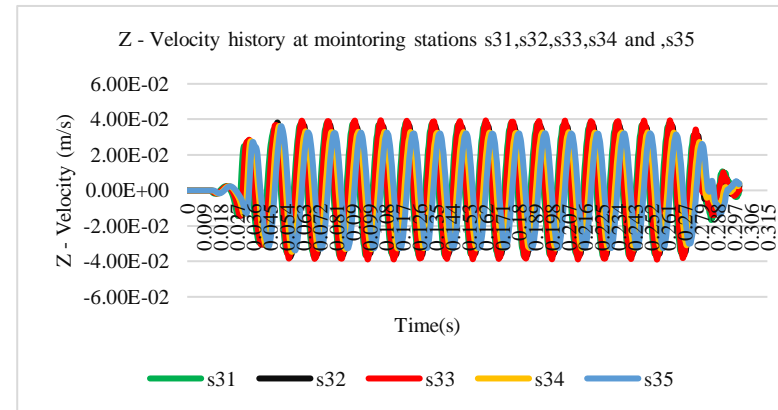
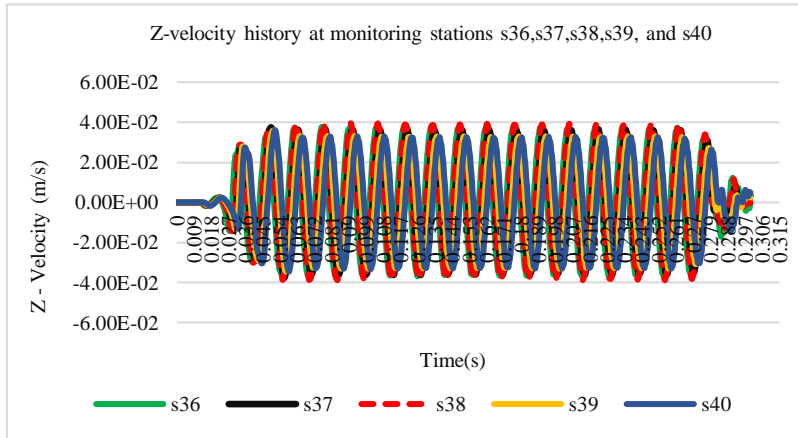


PSD of the velocity history recorded at monitoring stations s26, s27, s28, s29, and s30

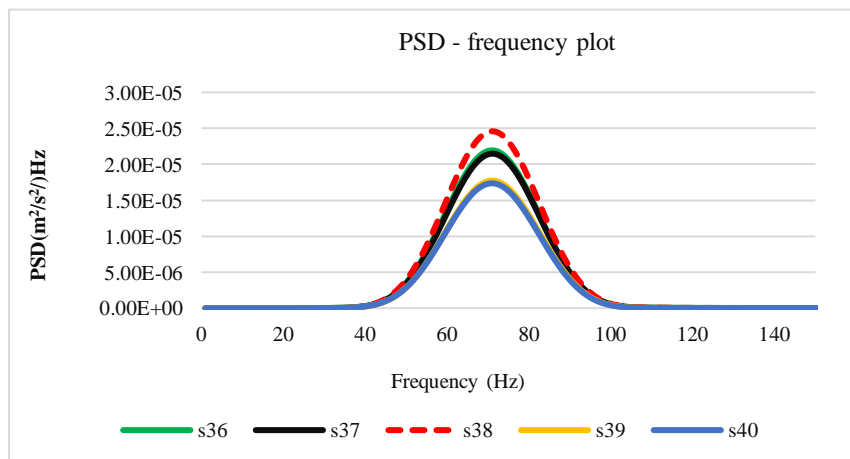


# Appendix

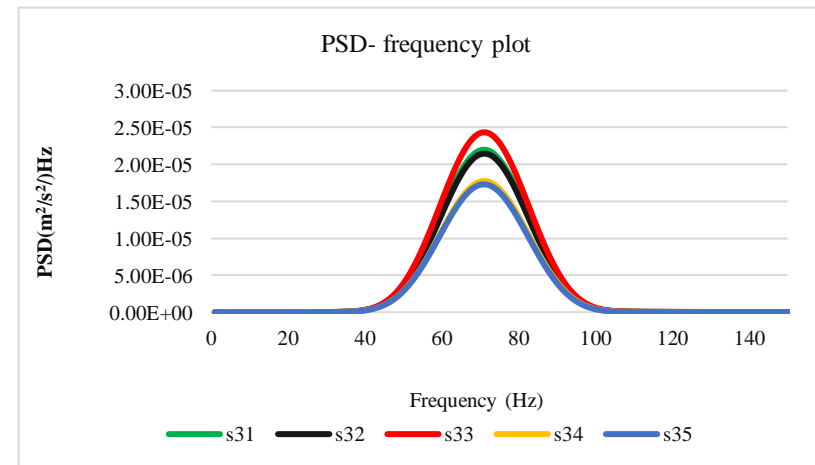
## C.5 second scenario (the object at 2m depth)



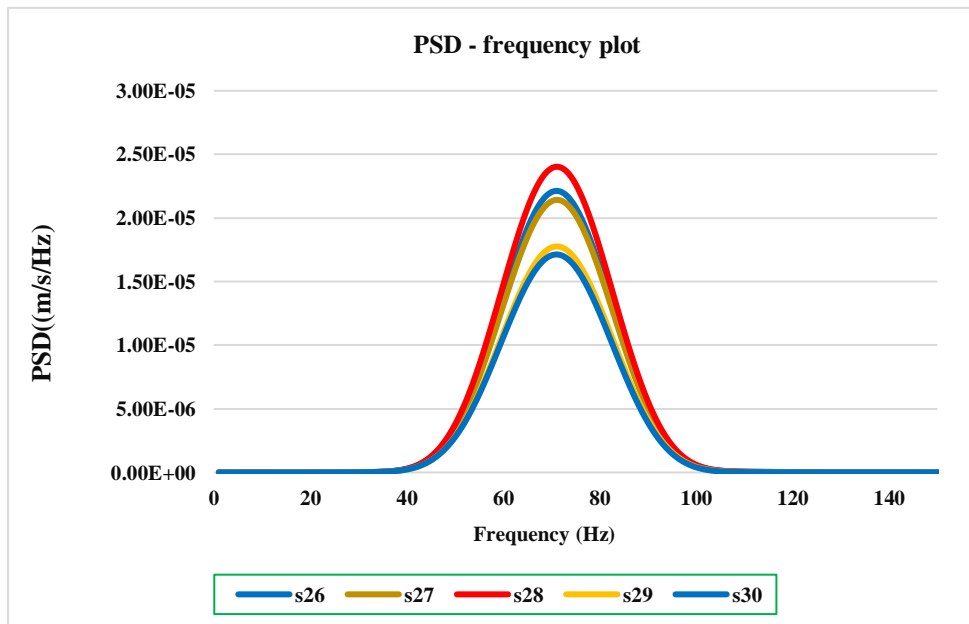
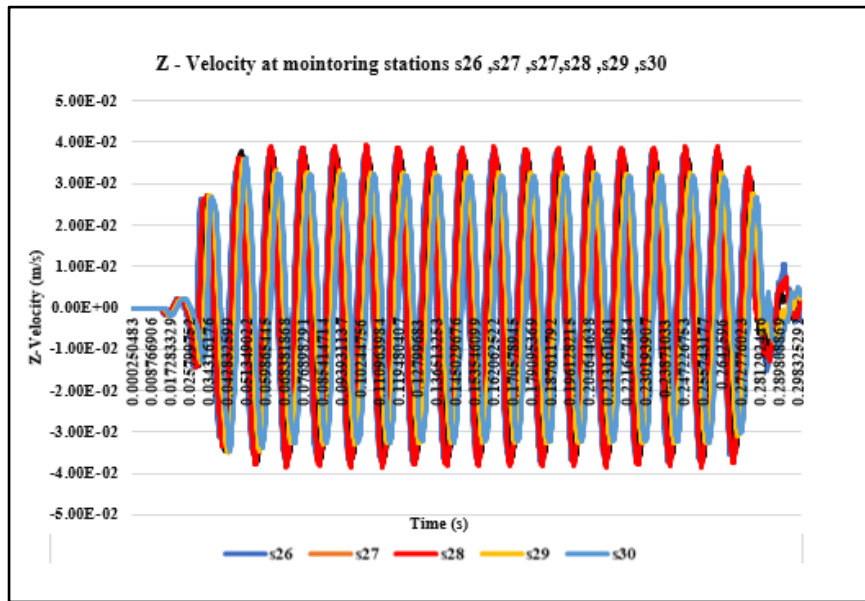
PSD of the velocity history recorded at monitoring stations s36, s37, s38, s39, and s40



PSD of the velocity history recorded at monitoring stations s31, s32, s33, s34, and s35



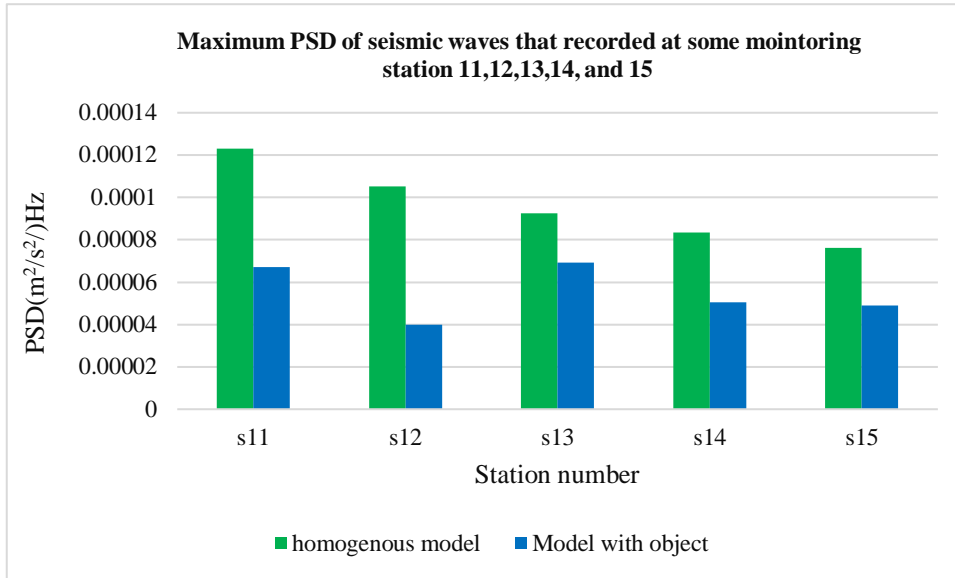
# Appendix



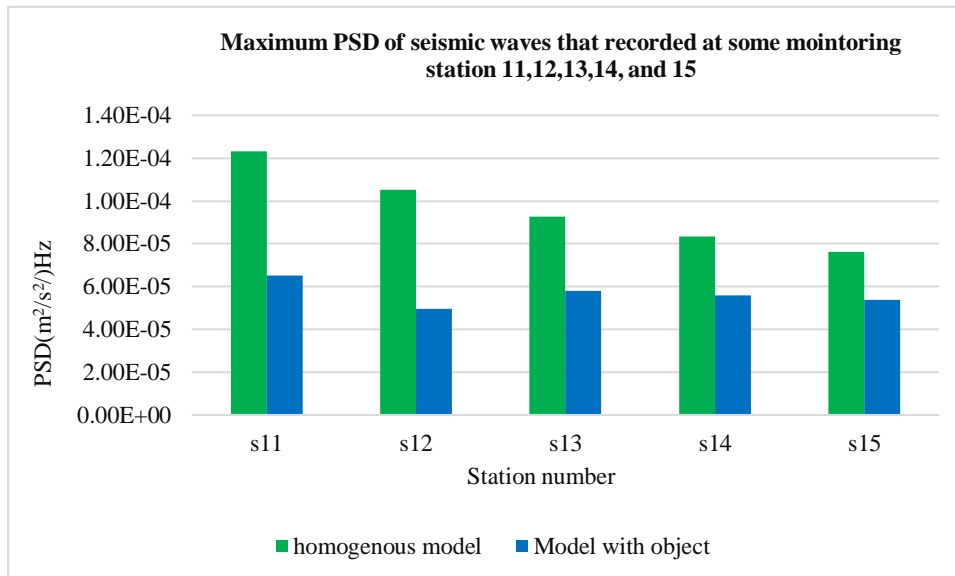
# Appendix

## D In case the object size (steel properties) is 1.5 m × 1.5 m × 1.5 m

### D.1 Object at 1m depth

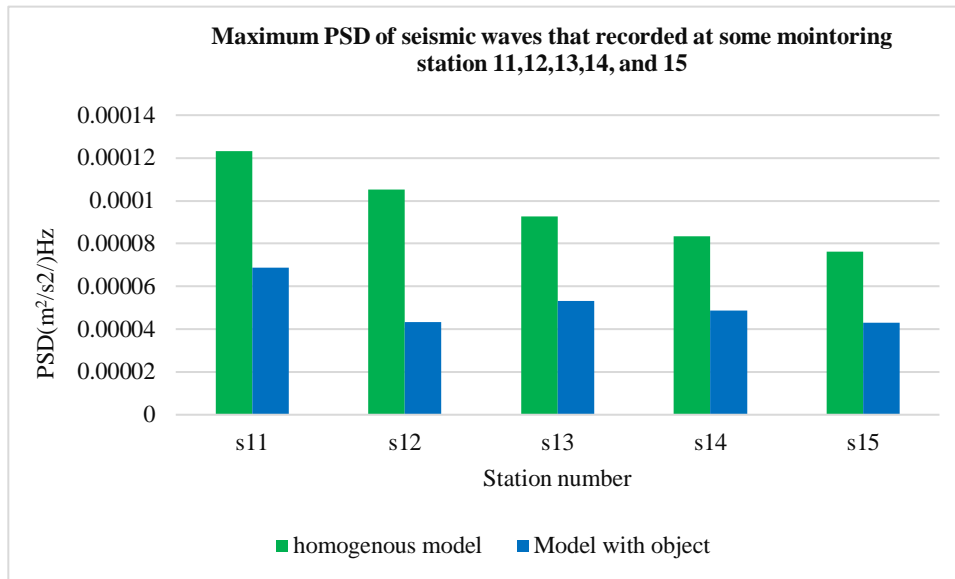


### D.2 Object at 2m depth



# Appendix

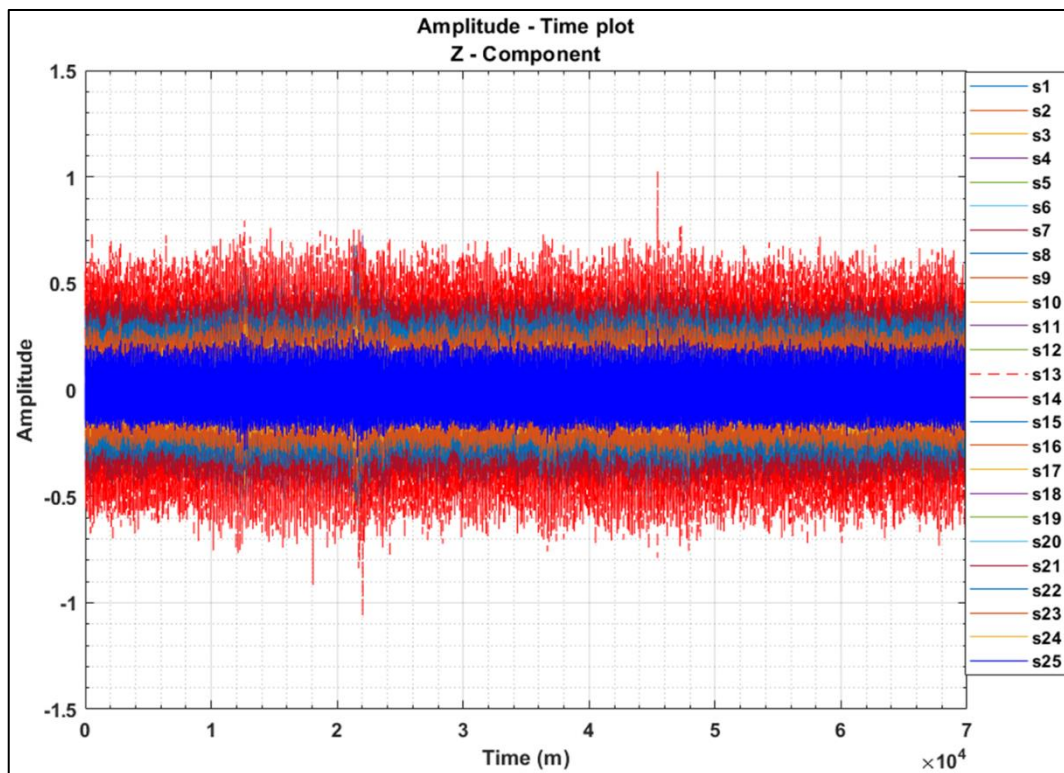
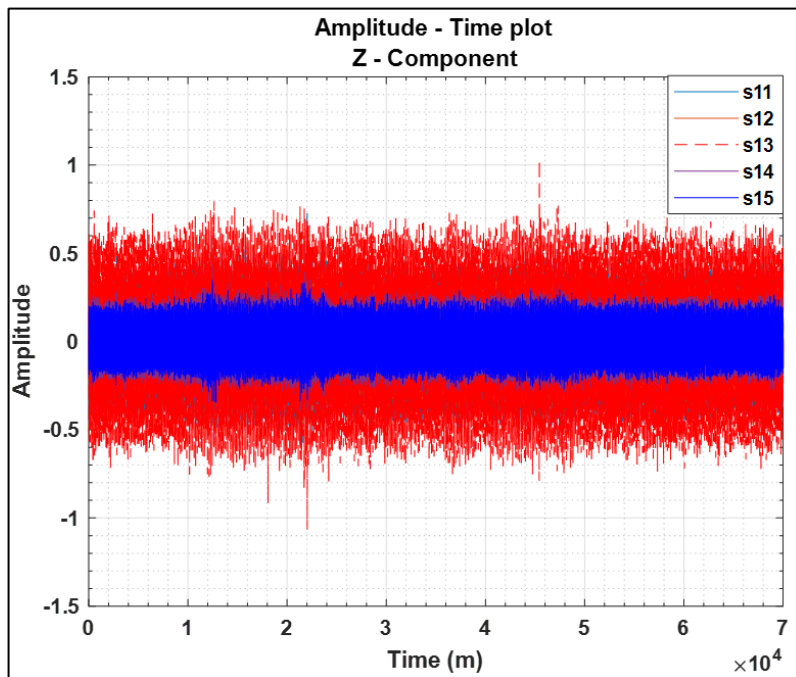
## D.3 Object at 2m depth



# Appendix

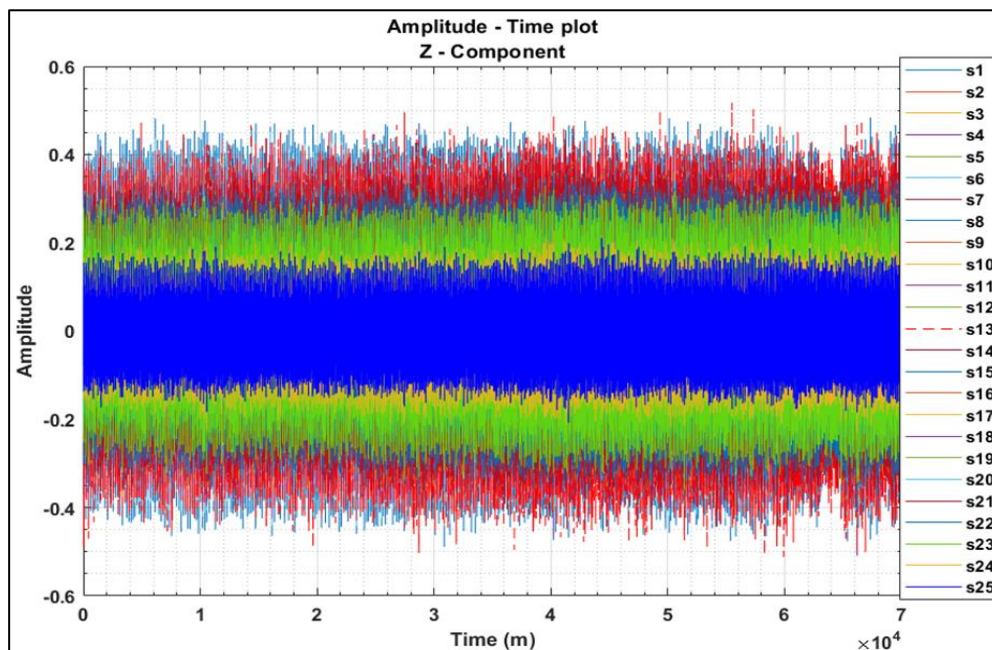
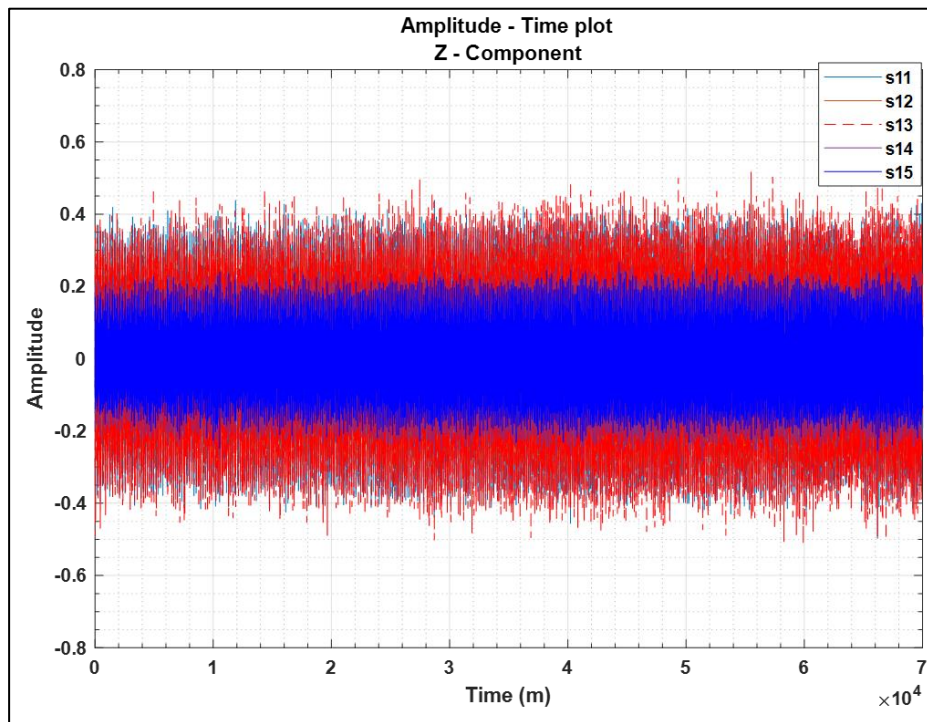
## E Vertical component (Seismic Source located at SA)

### E.1 Concrete block experiment.



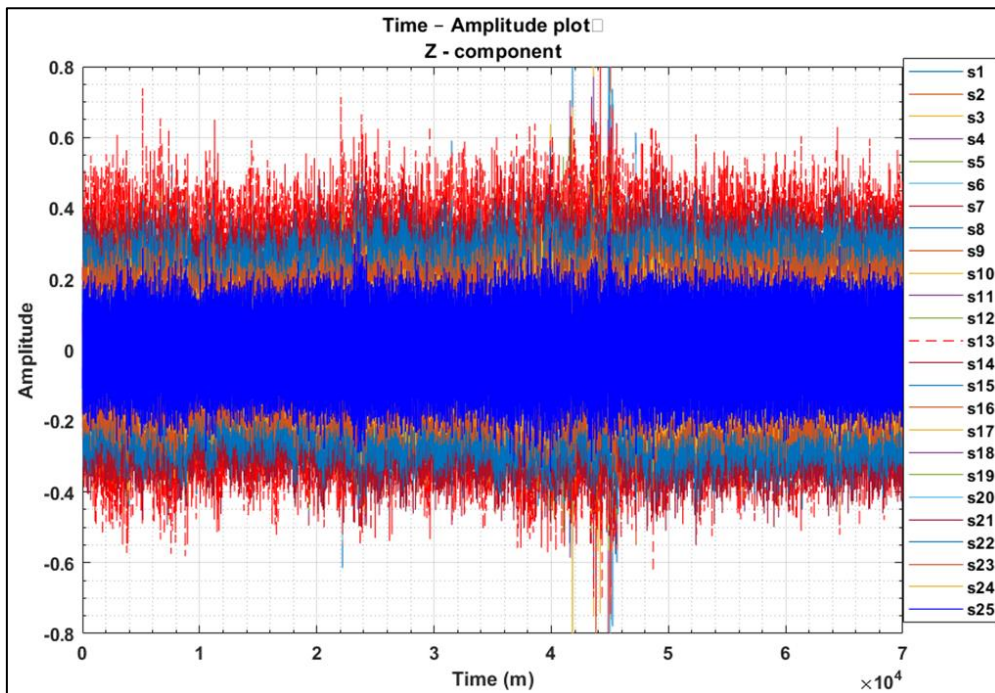
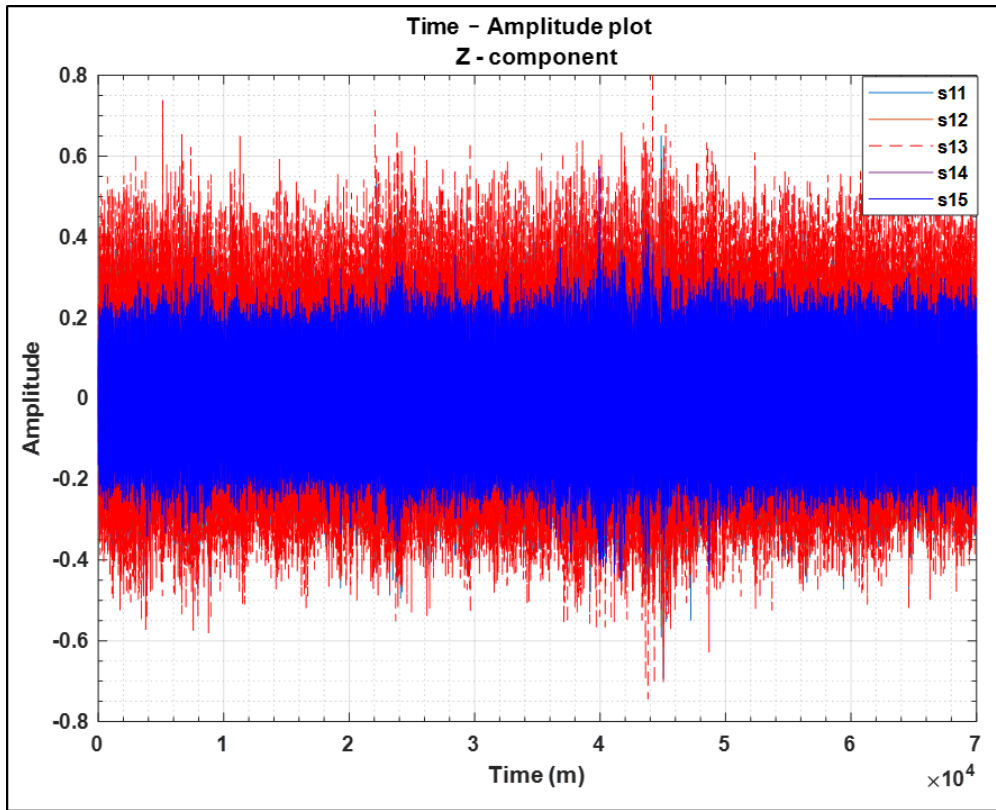
# Appendix

## E.2 Steel drum experiment



# Appendix

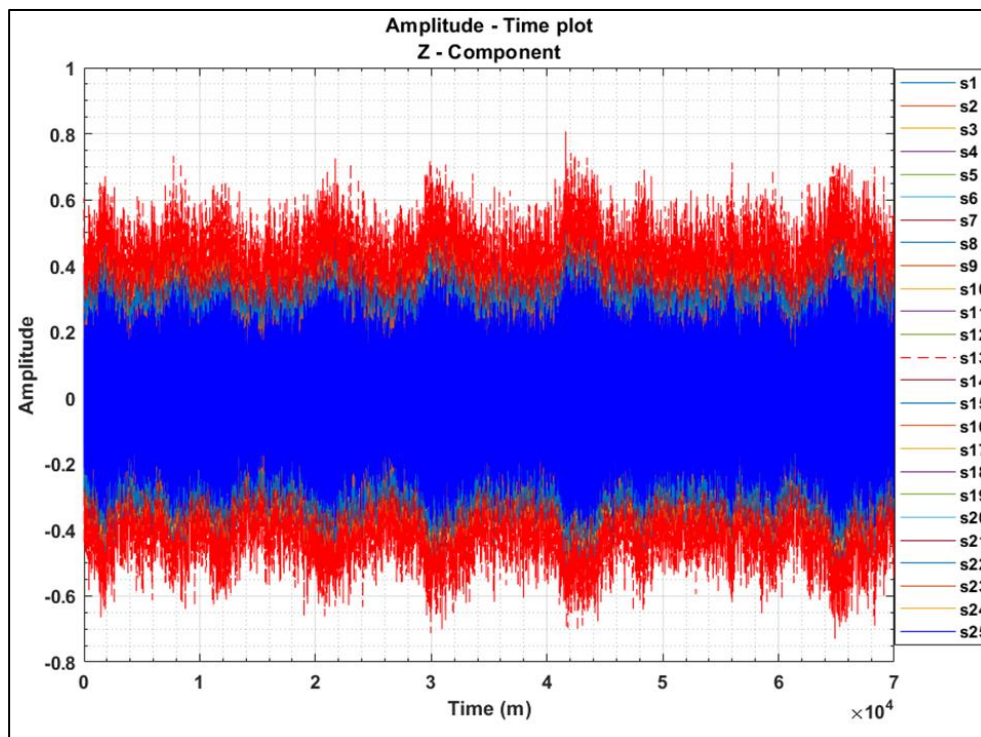
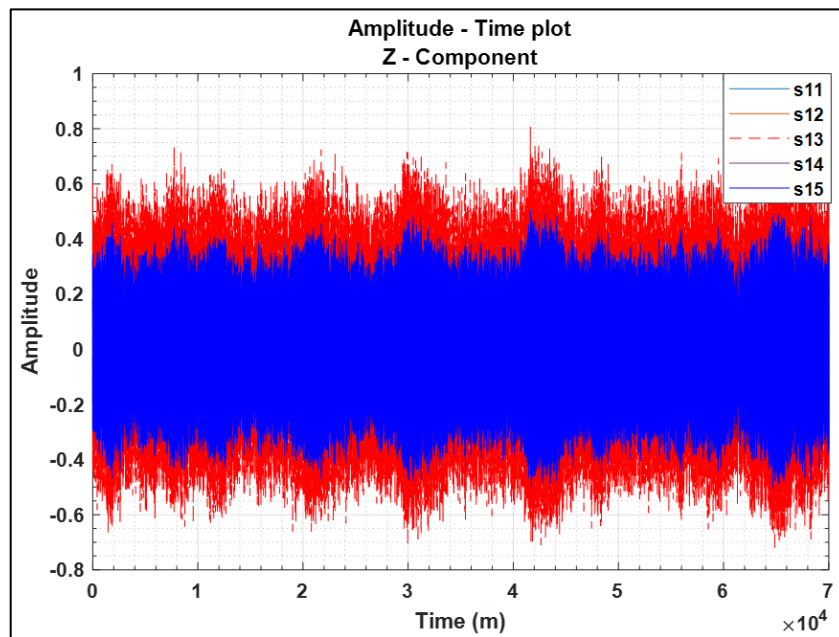
## E.3 Plastic drum experiment



# Appendix

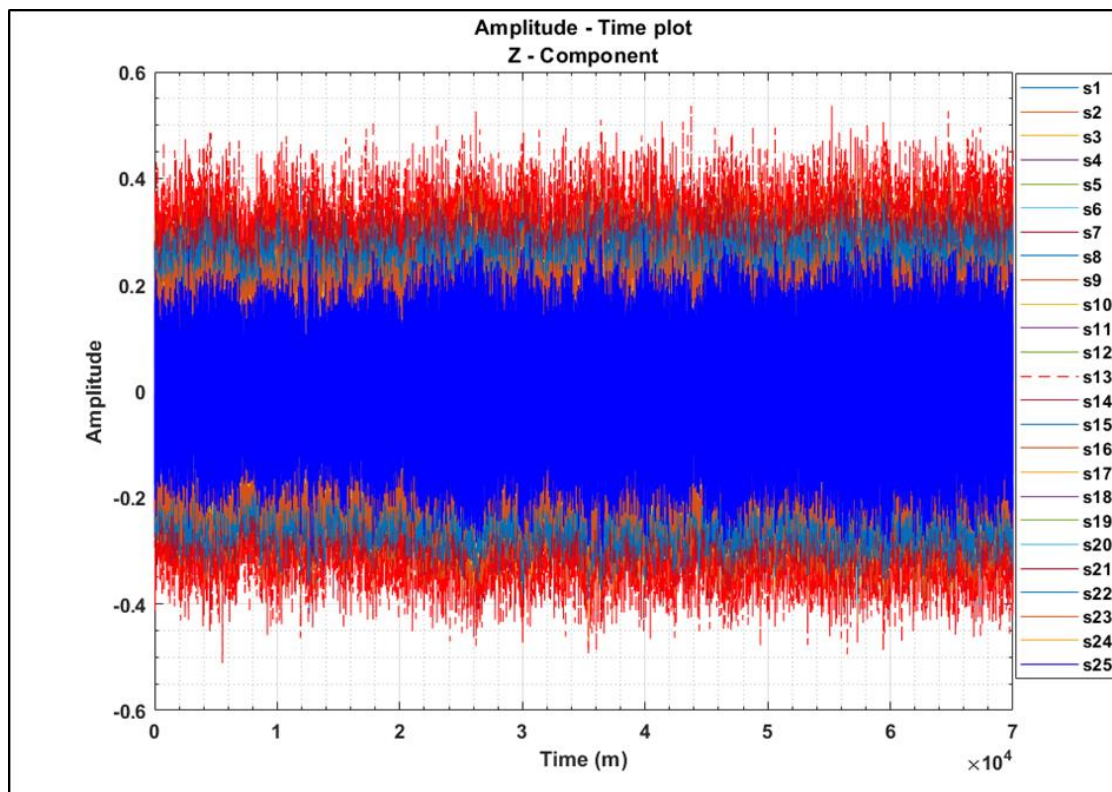
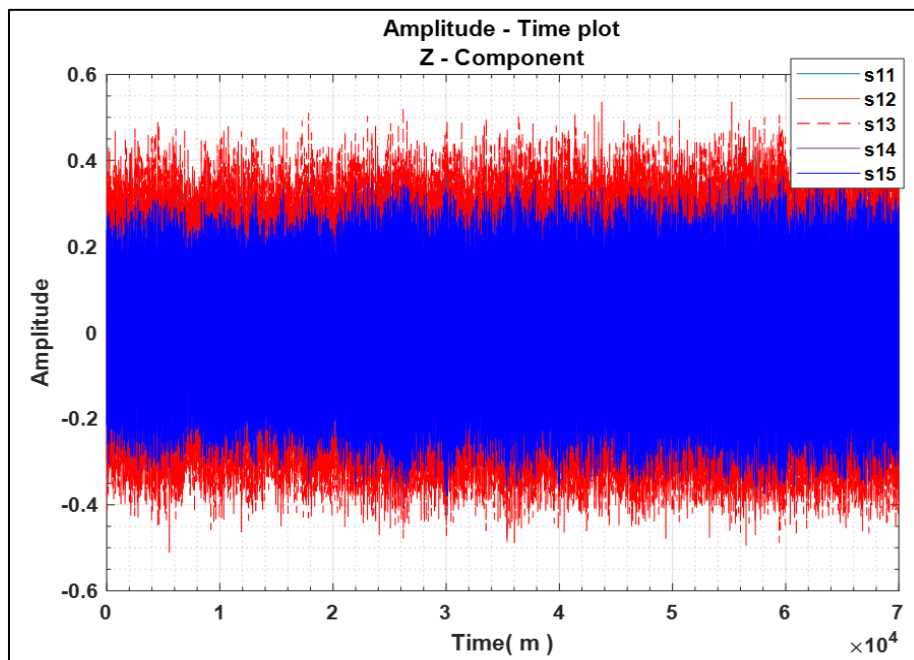
## F Vertical component (Seismic Source located at SB)

### F.1 Concrete experiment



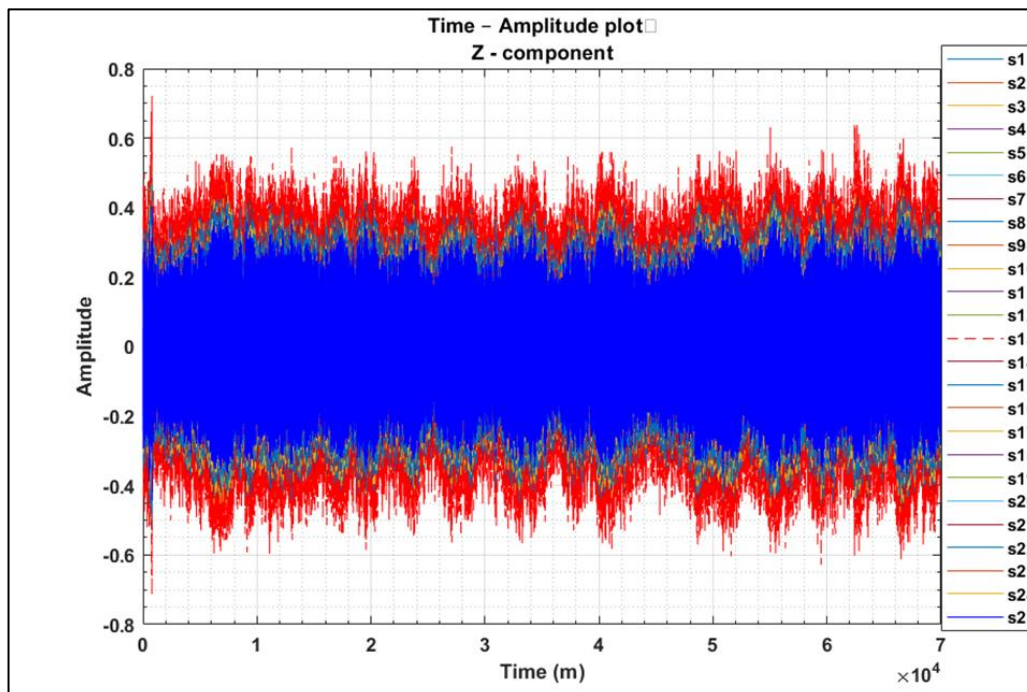
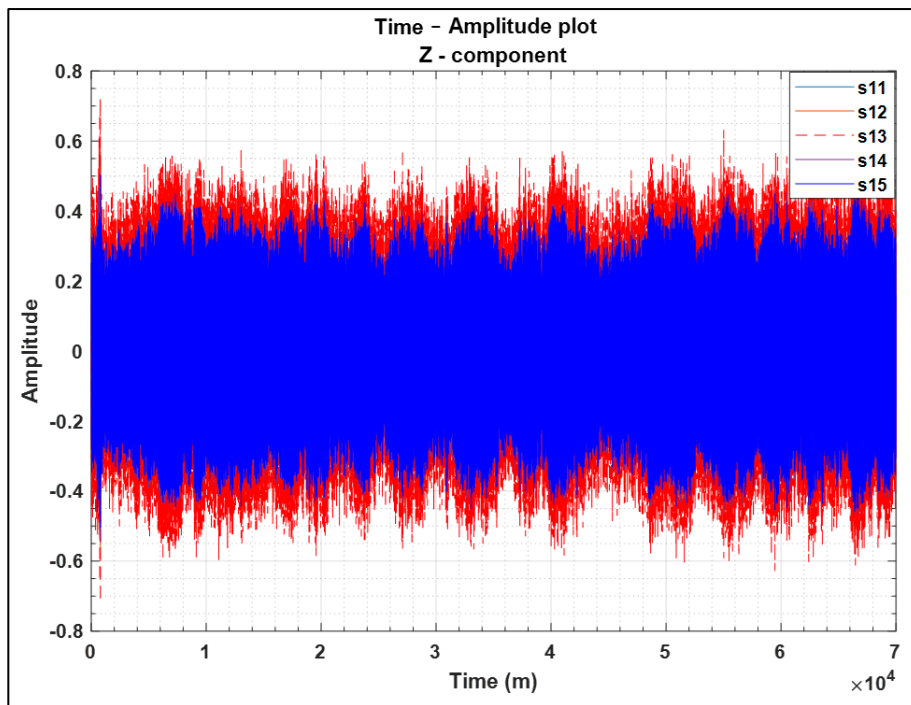
# Appendix

## F.2 Steel drum experiment



# Appendix

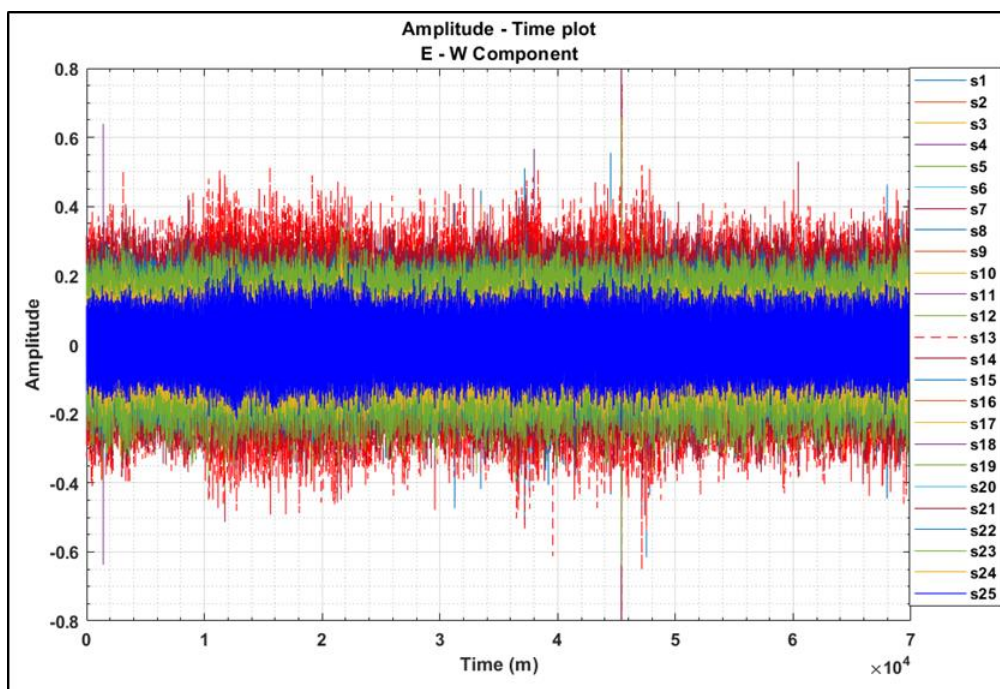
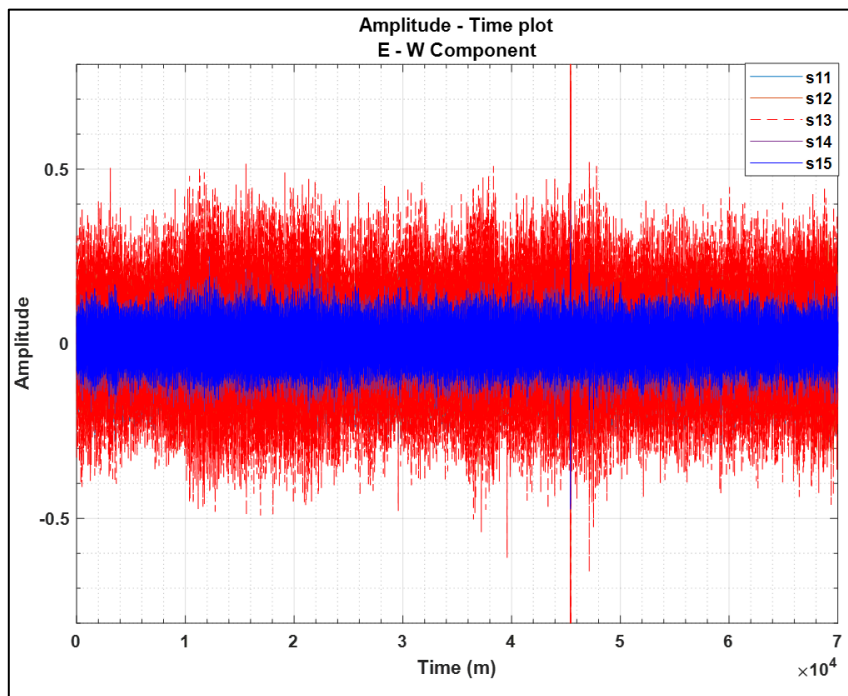
## F.3 Plastic drum experiment



# Appendix

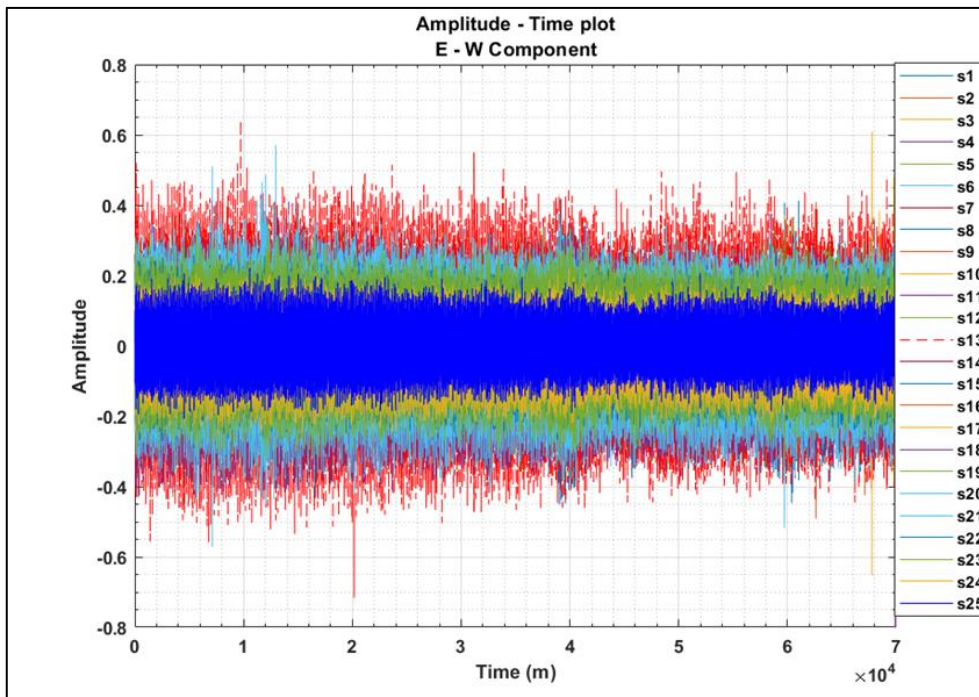
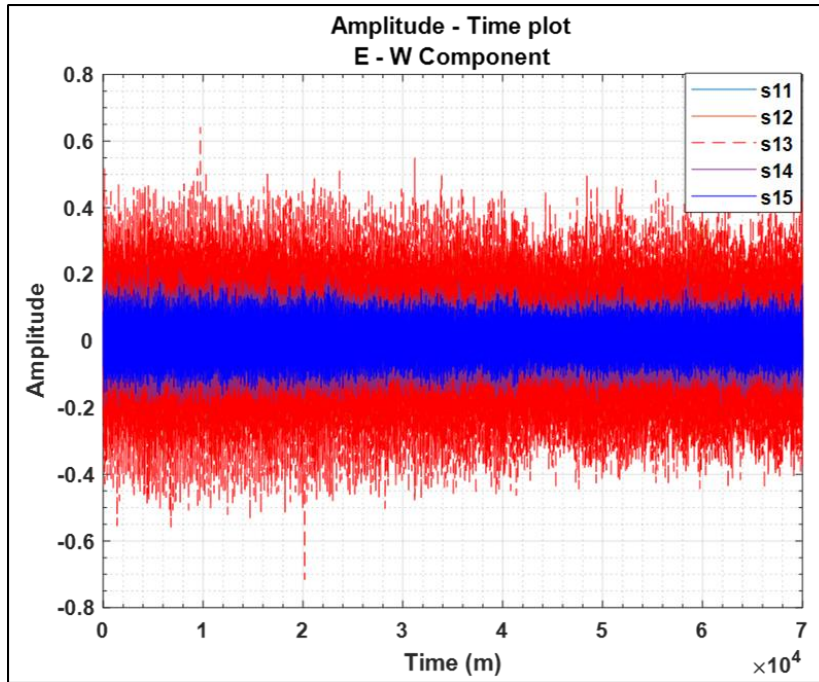
## G East – West component (Seismic Source located at SA)

### G.1 Concrete experiment



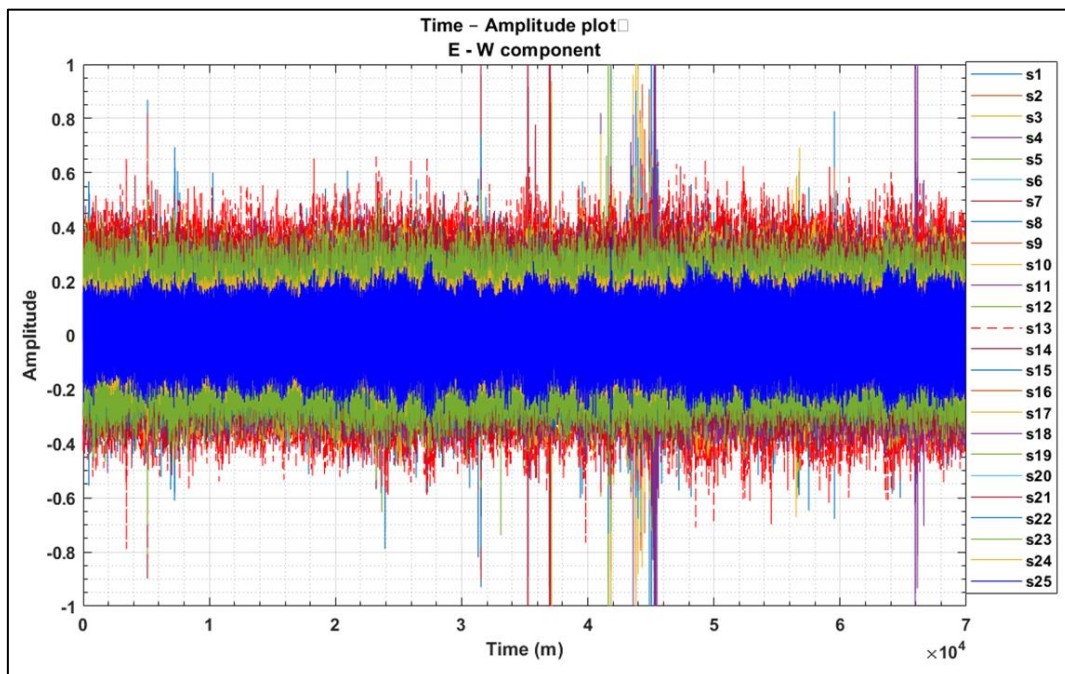
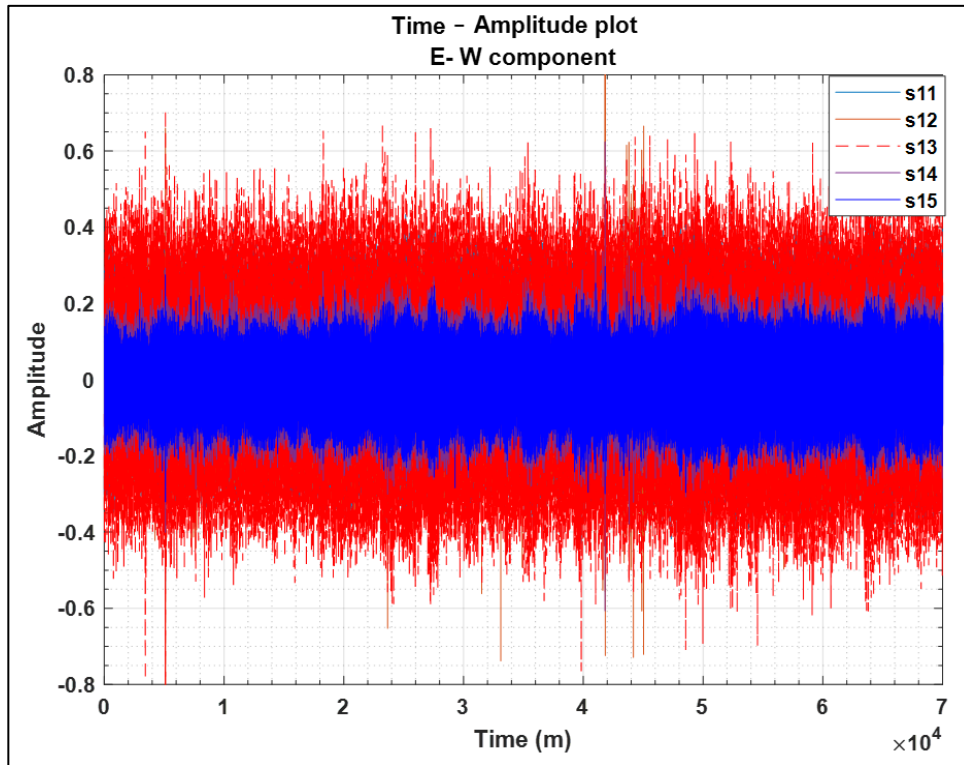
# Appendix

## G.2 Steel drum experiment



# Appendix

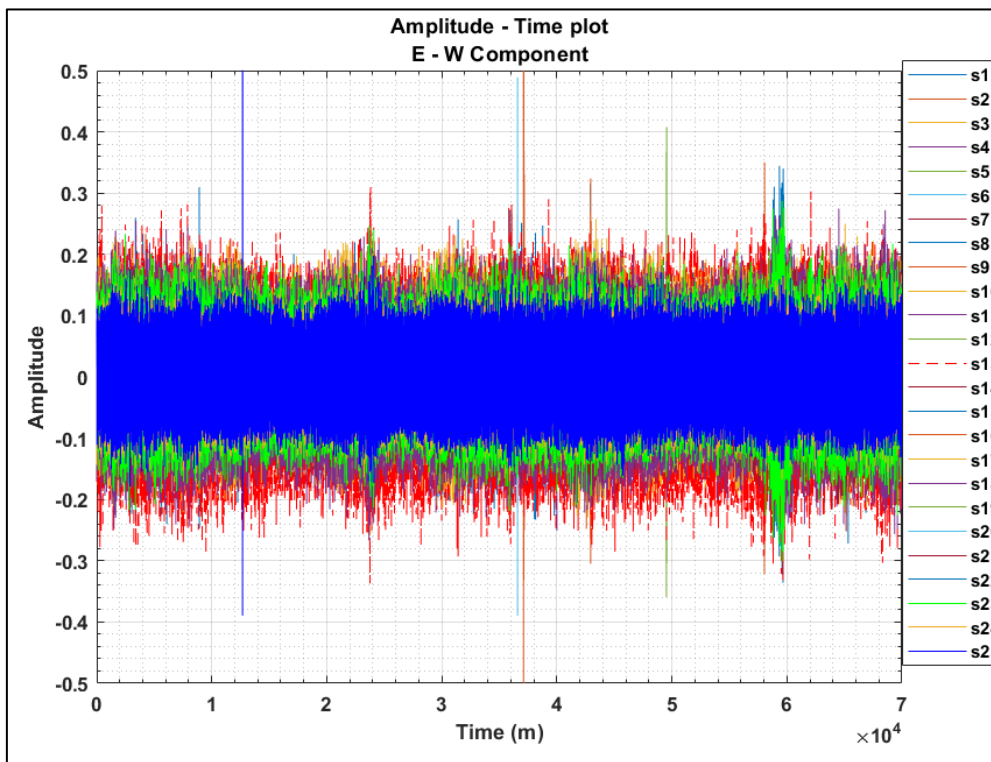
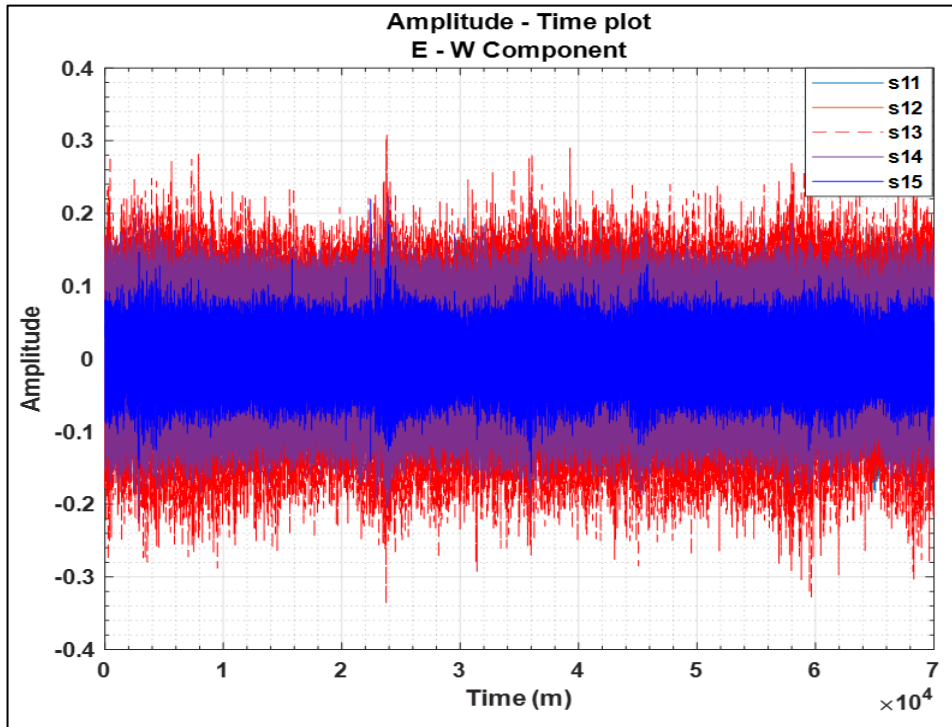
## G.3 Plastic drum experiment



# Appendix

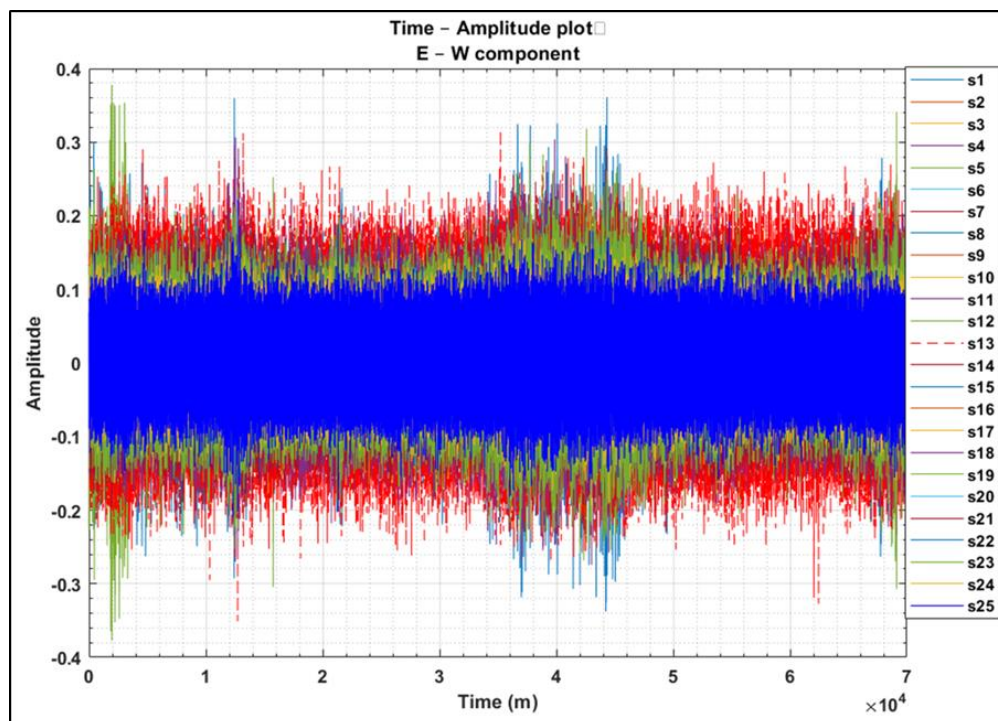
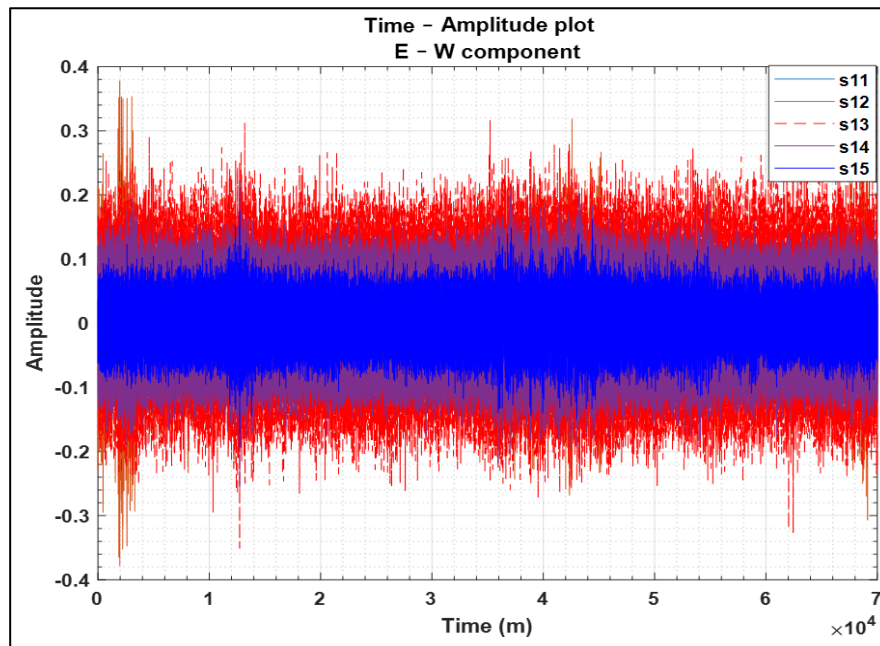
## H East – West component (Seismic Source located at SB)

### H.1 Concrete experiment



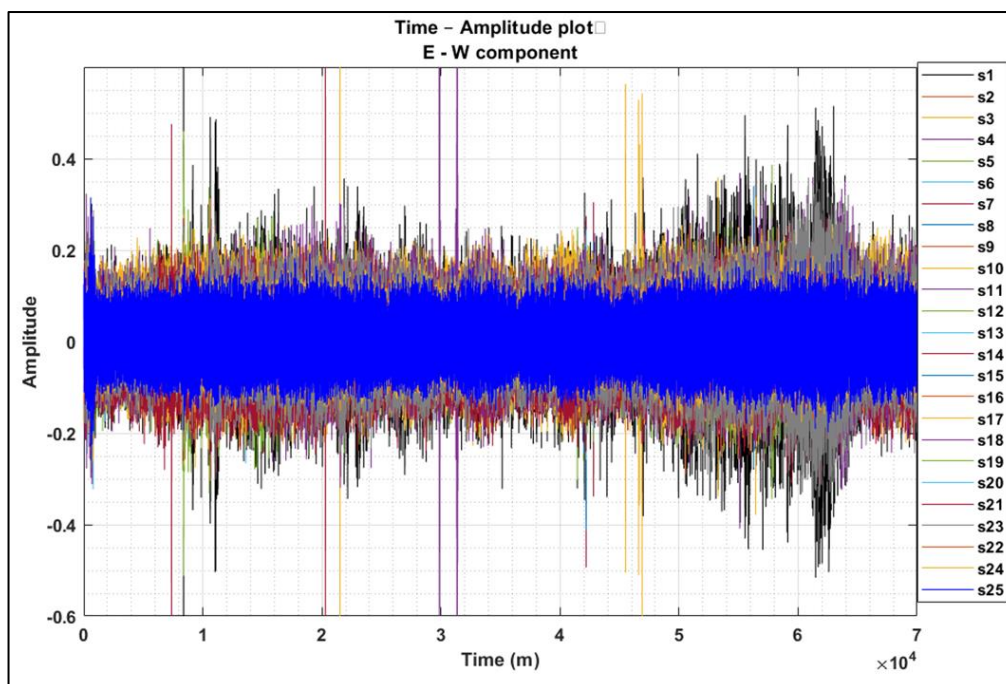
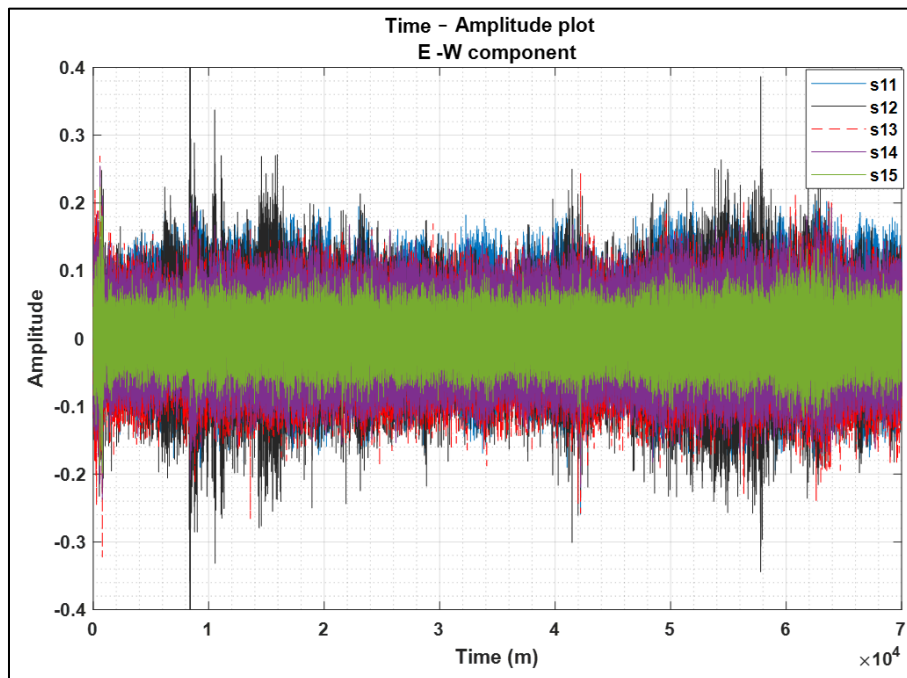
# Appendix

## H.2 Steel experiment



# Appendix

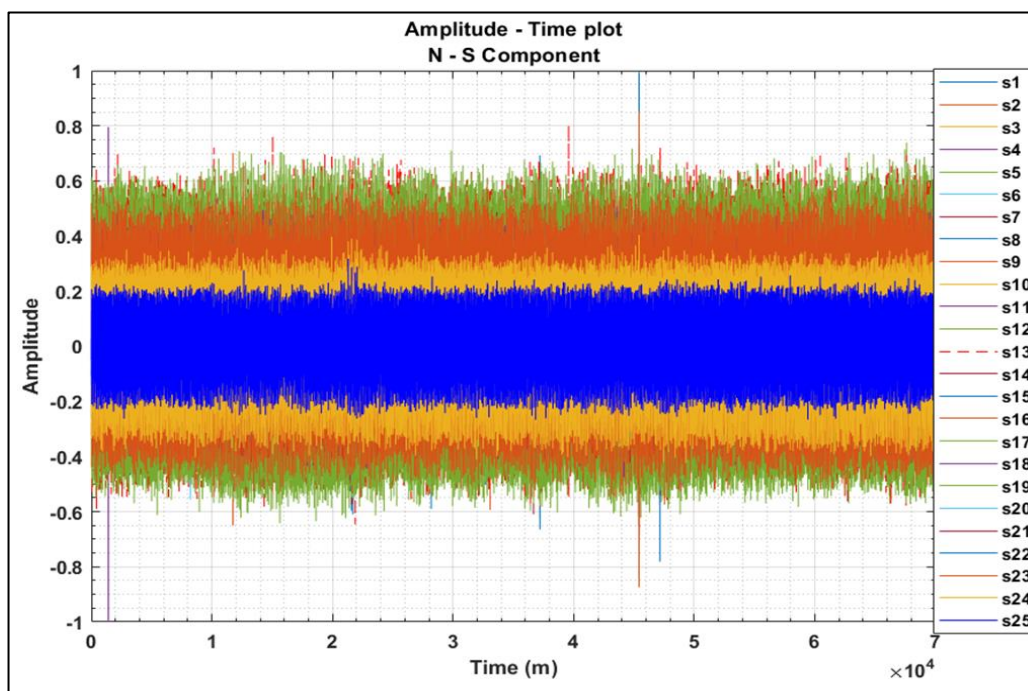
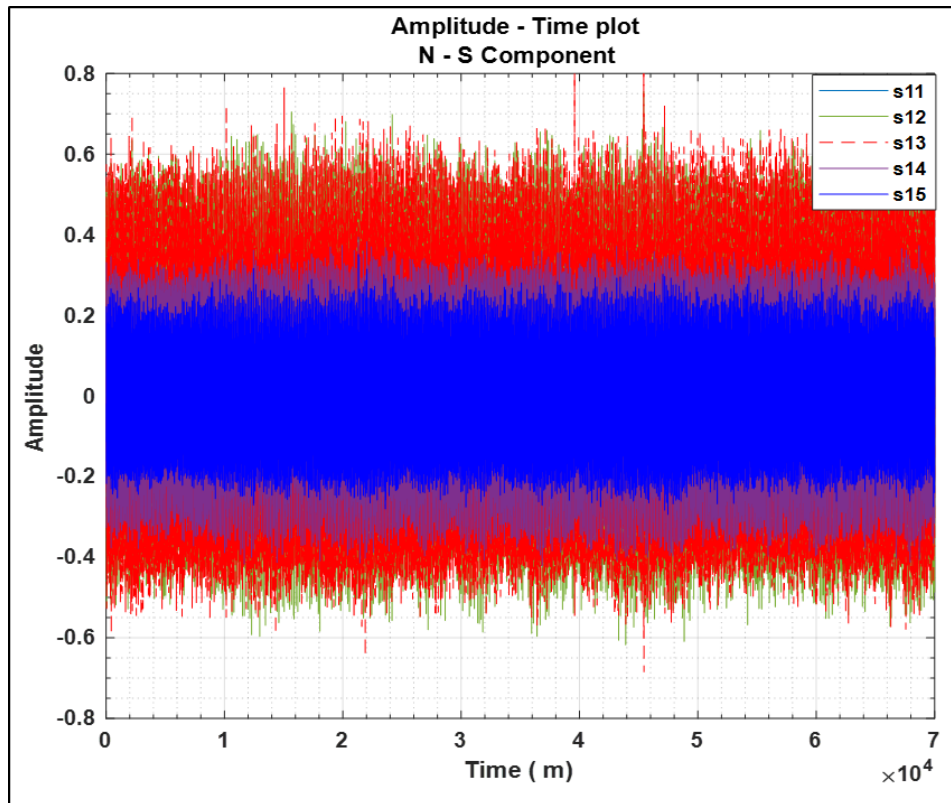
## H.3 Plastic drum experiment



# Appendix

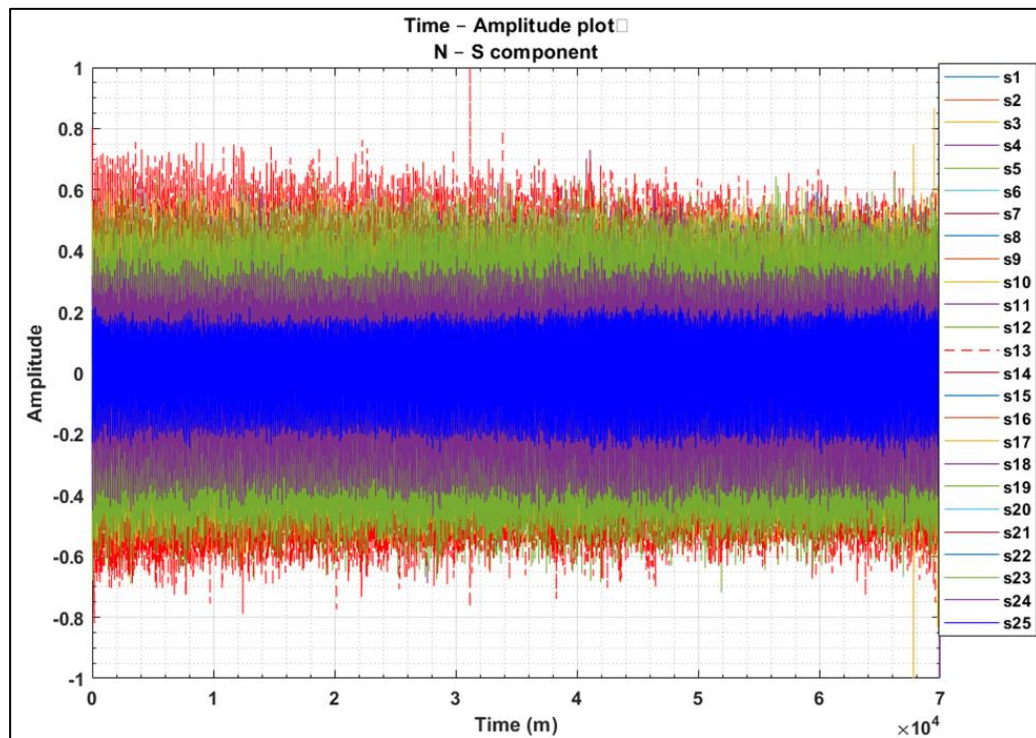
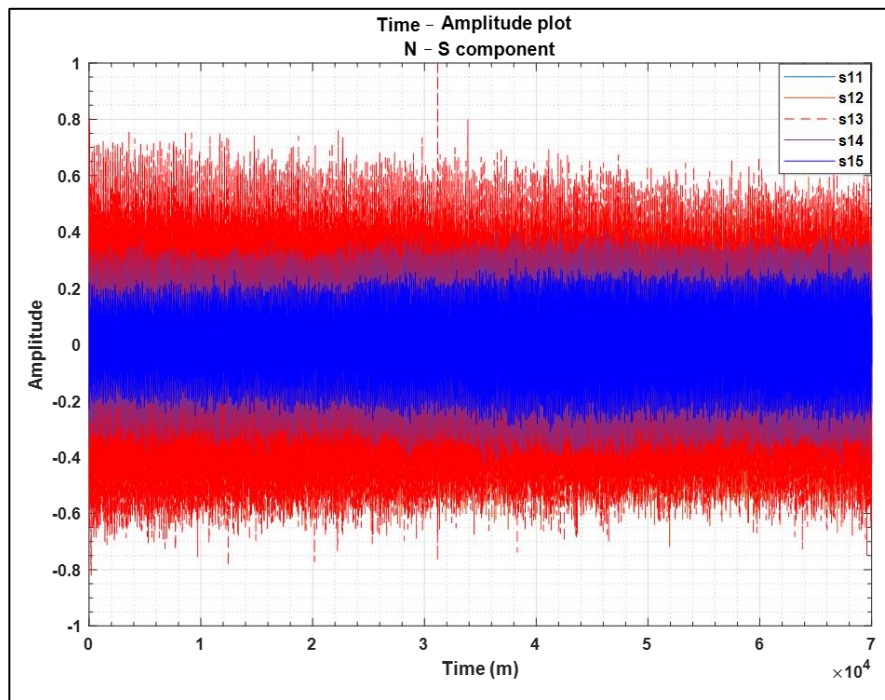
## I North – South component (Seismic Source located at SA)

### I.1 Concrete experiment



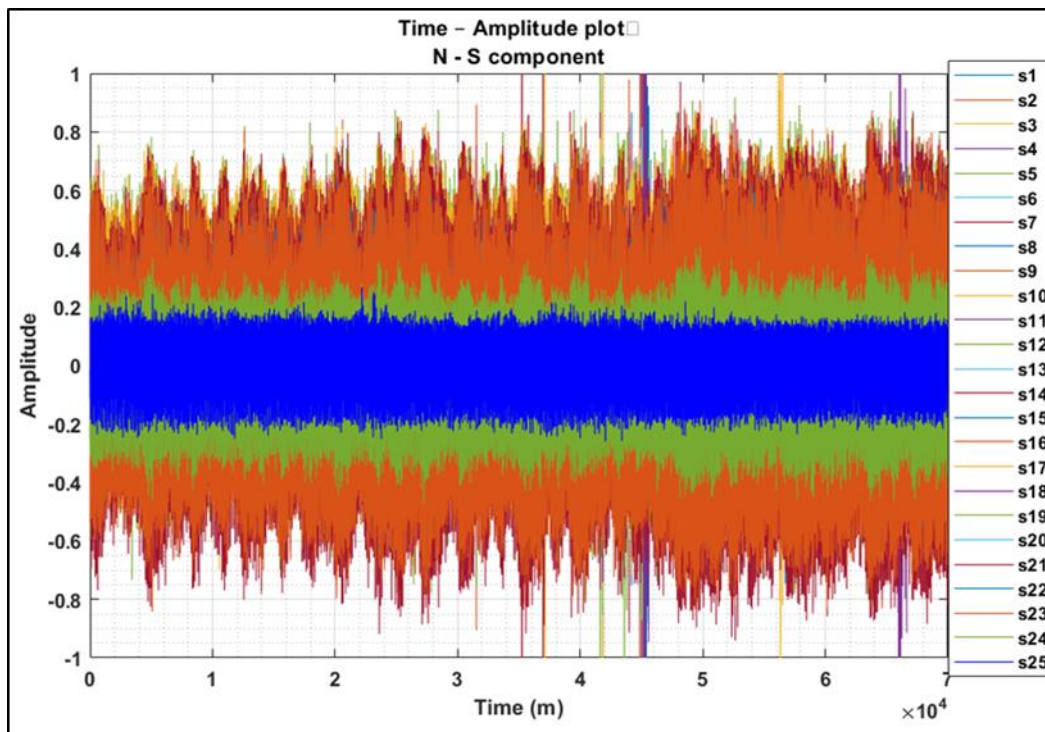
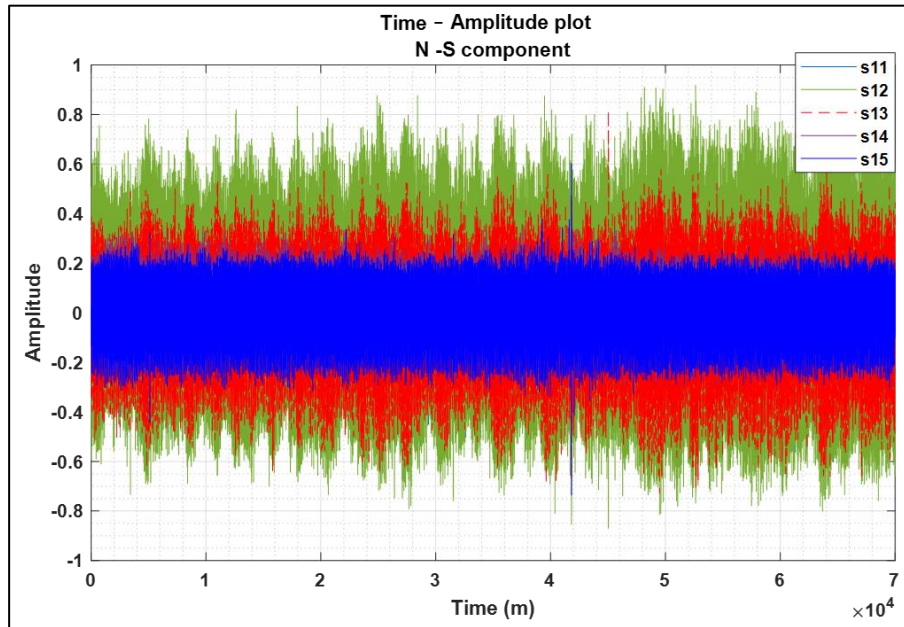
# Appendix

## 1.2 Steel experiment



# Appendix

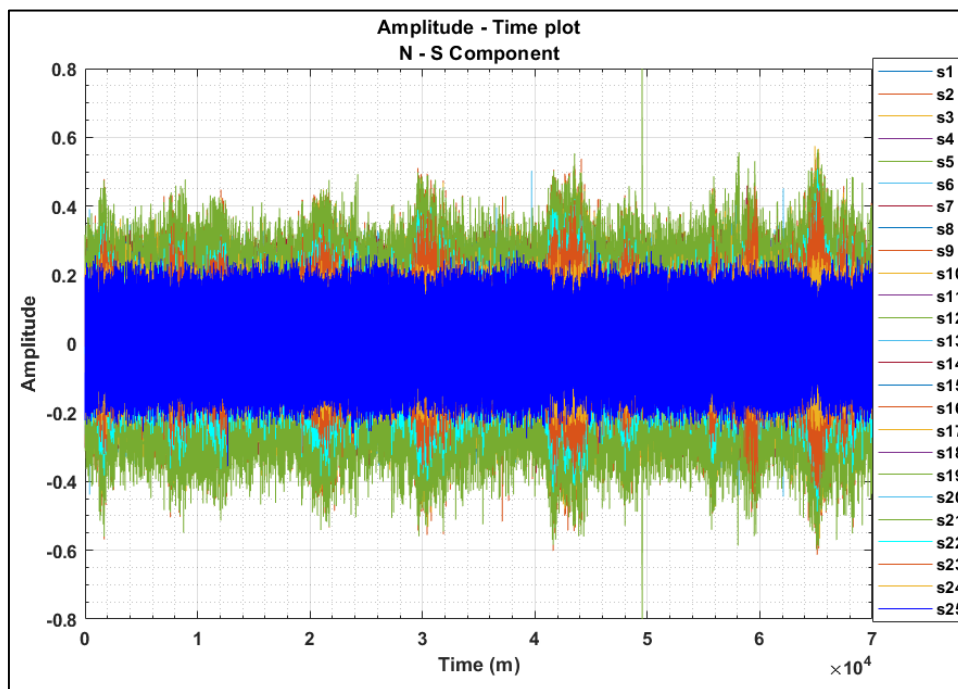
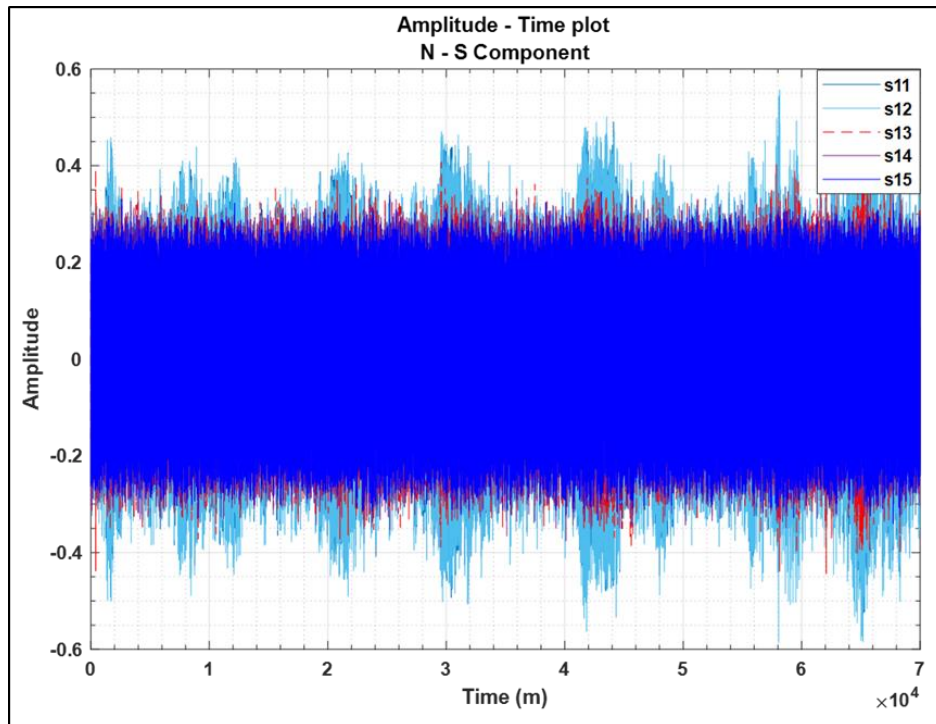
## I.3 Plastic drum experiment



# Appendix

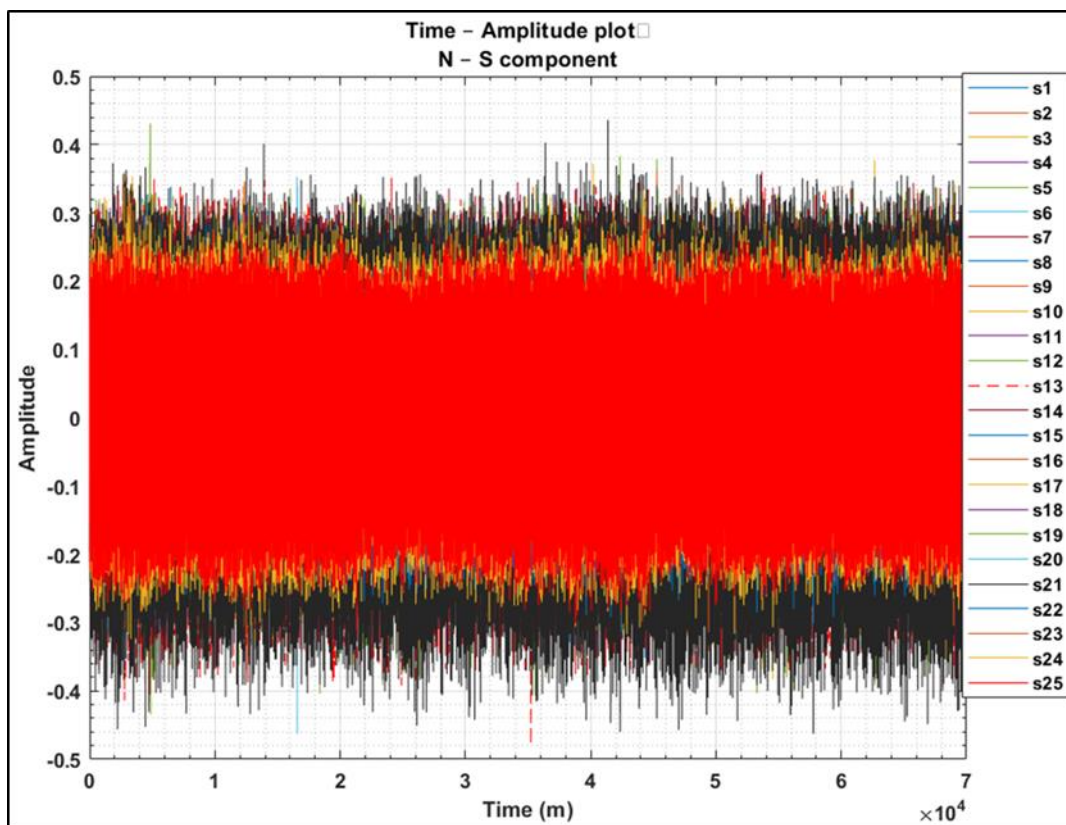
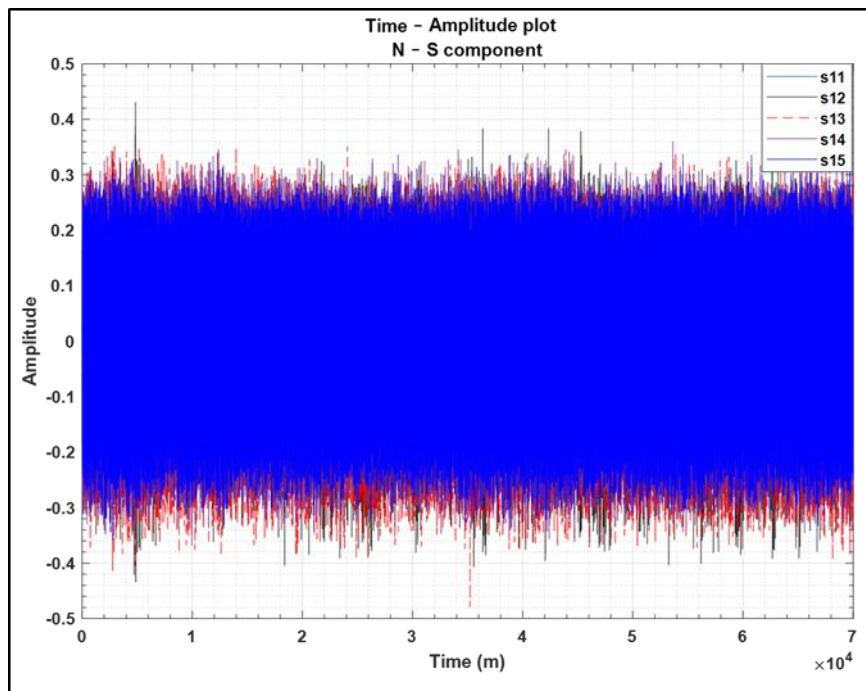
## J North – South component (Seismic Source located at SB)

### J.1 Concrete experiment



# Appendix

## J.2 Steel experiment



# Appendix

## J.3 Plastic drum experiment

